The Venice Lagoon Study (F-ECTS) Field Results - February, 1999

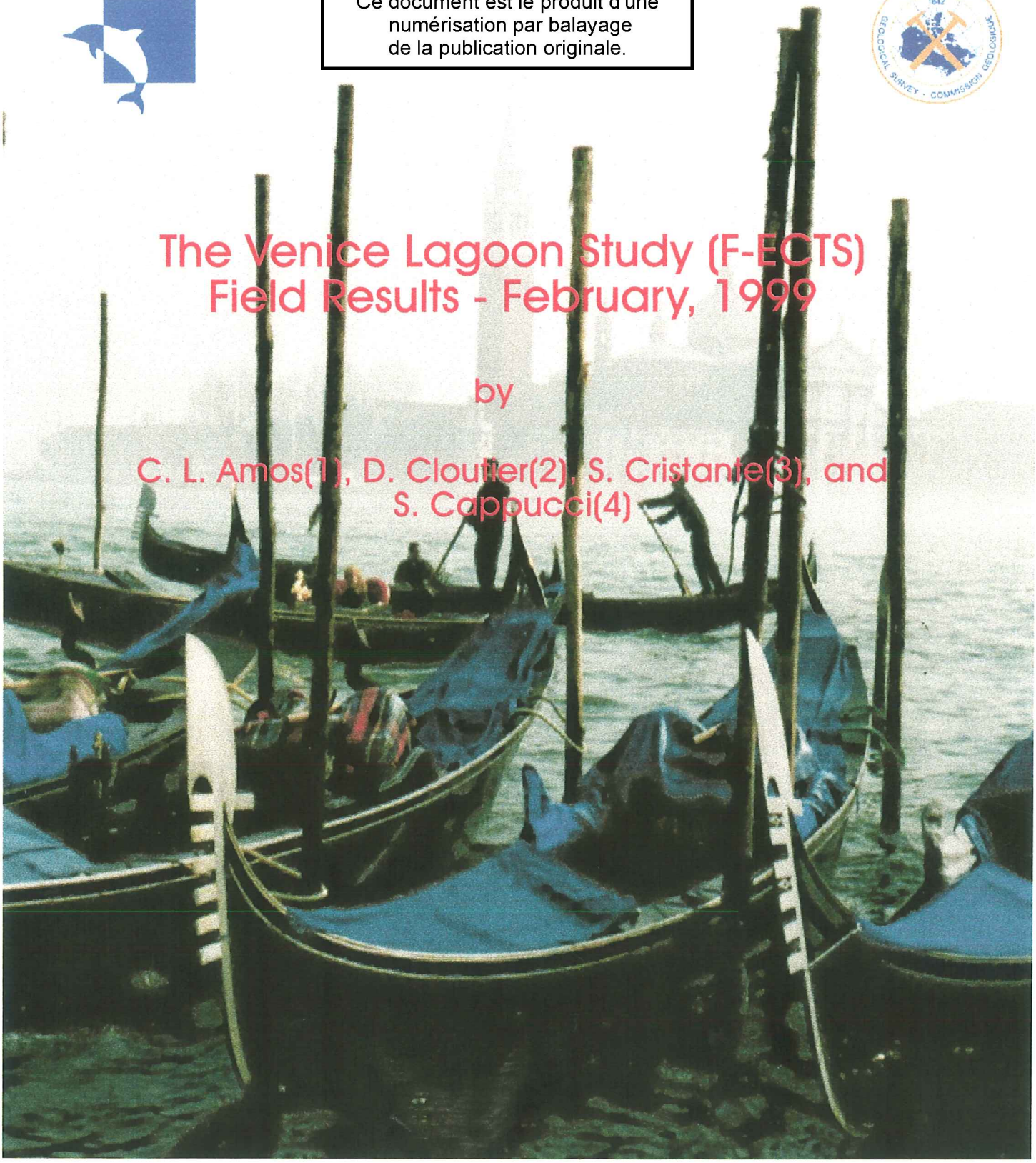

by

C. L. Amos(1), D. Cloutier(2), S. Cristante(3), and S. Cappucci(4)

Geological Survey of Canada Open File Number 3904

Natural Resources Canada | Ressources naturelles Canada

Canada

2000

The Venice Lagoon Study (F-ECTS)
Field Results - February, 1999

by

C. L. Amos[1], D. Cloutier[2], S. Cristante[3], S. Cappucci[4] and M. Le Couturier[4]

1. Geological Survey of Canada (Atlantic),
Bedford Institute of Oceanography, Dartmouth
Nova Scotia, CANADA ,
present address: Southampton Oceanography Centre
Empress Dock, Southampton, Hants, UK
2. INRS- Oceanologie
Universite de Quebec, Rimouski, Quebec, CANADA
3. Dipartimento di Scienze della Terra
Universita di Parma, Parma, Italy
4. Southampton Oceanography Centre
Empress Dock, Southampton, Hants, UK

a report prepared for:

Thetis SpA
Castello 2737/F30122
Venezia, Italia
(F-ECTS, contract # MAS3-CT97-0145)

Geological Survey of Canada Open File Report No: 3904

2000

ACKNOWLEDGMENTS

This work was carried out with the support of a wide variety of experts without whose effort, the project would not have succeeded. In particular, we wish to thank Robert Murphy (Geological Survey of Canada - Atlantic) for his technical help during field operations.

The work has been heavily supported by THETIS SpA, Venice. We are indebted to Alessandro Bergamasco for overall coordination, Luca de Nat for logistical support, Roberto Marescalchi and Carlo Piovesan for technical support, Roberto Cattelan for laboratory support, and Sergio Bomben for Pontoon maintenance, safety and design. Luca de Nat produced the site location diagram of Venice and is thanked for making it available to us.

Thanks also go to Mogens Flindt (University of Odensa, Denmark) for the support provided to the pontoon activities, and for general discussions about project logistics.

Alessandro Bergamasco provided the over-arching co-ordination to the project and, as project leader, provided the leadership so important to this kind on multi-disciplinary project. Our special thanks go to him for his never failing support, and for the effective delivery of the project.

This report is dedicated to the memory of Dr Adrian Cramp, supervisor of Sergio and great friend to us all. We will miss his dry humour, good sense, and companionship.

FRONT COVER

A photograph taken by Danielle Cloutier of Isola San Georgio across the Canale Grande, Venezia. The gondolas in the foreground are almost at the pavement level of Piazza San Marco and attest to rising sealevel. The waves in the lagoon around Venice are typically force 3 due to the constant and intense boat traffic which create bow waves that echo and re-echo within the lagoon creating a complexity of cross seas.

EXECUTIVE SUMMARY

In the context of the MAST-III programme, the European Community Directorate General XII has co-funded a multi-national study of Venice Lagoon, Italy, coordinated by THETIS SpA, Venice. The study, titled Feed-back of Estuarine Circulation and Transport of Sediments on Phytobenthos (F-ECTS, contract # MAS3-CT97-0145), was to examine the benthic flux of organic and inorganic material to the water column, and the controls placed on this flux by the micro- and macro-algae which colonize the Lagoon.

The study comprised two major field studies (August, 1998 and February, 1999) and a subsequent application of the field results to a numerical simulation of the Lagoon. The main participants in the field program were: THETIS SpA; Geological Survey of Canada Atlantic (GSCA); University of Copenhagen, Denmark; Cardiff University, Wales; Universita di Ferrara, Italy; Universita di Parma, Italy; University of Algarve, Portugal, and Hydraulics Research Limited, UK. This report describes results collected by Geological Survey of Canada Atlantic (GSCA) during the winter field survey of 1999.

The majority of the work was carried out aboard a pontoon that was mobilized by THETIS SpA. This pontoon was equipped with the GSCA Sediment Dynamics container, a wet lab, and a small davit and hand winch. The draft of the pontoon was 0.8 m which was sufficiently small to provide access to the widespread tidal flats where this study was focused. Aboard the pontoon, the activities of the GSCA and the University of Copenhagen were concentrated. The GSCA activities included: programming and deployment of a nearbed InterOcean® S4 current meter and a Cyclops (turbidity sensor) at site V40 (paludine della Rosa); Sea Carousel benthic flume surveys; Mini Flume benthic surveys; water sampling; and bottom sediment sampling. These studies were complimented by controlled analyses of bottom sediment bulk samples used in the Lab Carousel which was set up at THETIS SpA.

The main purpose of this part of the F-ECTS program was to determine the stability and benthic flux of bottom sediments of the various bottom types of the lagoon during the period of minimum benthic biological activity. Thereafter, to compare these results with those of the summer (maximum benthic biological activity) and to examine the differences resulting from changing physical and biological setting. Sea Carousel and Mini Flume were used for this purpose. Water samples were pumped from Sea Carousel and analyzed onboard for suspended solids concentration, O_2 content, chlorophyll and dissolved carbohydrate content, and organic content. As well, syringe cores and bulk samples were collected in order to define the physical and biological properties of each site. Samples were also taken for bacterial and diatom productivity.

The field campaign began on 21st February, 1999 and ran till 6th March, 1999. In that period, 13 sites were re-occupied of the 24 sites occupied during the previous summer survey. The study focused on the region north of Venice where 8 sites were surveyed. A further 5 sites were dispersed across the south and central parts of the lagoon. Results showed that the tidal flats were still protected by eel grass (Zostera sp. and Cymodosia sp.) and filamentous bacteria which populated the shallow tidal flats but to a lesser extent.

The results of this survey showed that the mean stability of the Lagoon bed was significantly lower (55%) than during the summer period. This we attribute to the diminished influence of biostabilization during the winter period. The stability of the lagoon thus more than doubles during the summer period yielding strength values that are amongst the highest ever detected by Sea Carousel. The stability is largely the result of filamentous bacteria and sea grasses.
Slight differences in results were evident between Sea Carousel and Mini Flume. However, the mean value of the critical erosion threshold for the Lagoon was the same (0.69 Pa). The inference of this is that scale effects induced by the devices (such as the structure and magnitude of turbulence or wall effects) are unimportant, and that heterogeneity of bed properties at the scale of metres is accounted for through the integration of results over multiple sites. The turbidity was highest in the inner Lagoon, intermediate throughout the central parts and lowest in the north (which was the site of highest turbidity during the summer). Sediment bulk density was still highest in the region adjacent to the sandy barrier islands fronting the Lagoon. The pattern of erosion thresholds in the Lagoon had not changed from the summer; highest values were still evident in the northeast. The greatest friction coefficients (highest consolidation rate) showed significant differences from the summer survey being found in the southwest and northeast. Minimum values of friction coefficient had not changed with season and were located around the Island of Venice. This, perhaps, reflects anthropogenic effects such as discharges of material, boat traffic resuspension and redeposition of bottom material. The settling rates (W_s) showed no trend with suspended sediment concentration (S) at sites north of Venice. However, settling rates of "fluff" material eroded at the onset of deployments were up to 30% less than material eroded from the bed. South of Venice, the results were quite different; there were distinct trends between W_s and S, yet pre-erosion and post-erosion settling rates were the same (diagnostic of an absence of the "fluff" layer). Differences in synthetic cores were seen north and south of the City of Venice. To the north, a surface layer of rapidly increasing strength prevailed; south of Venice, this layer was largely absent. These results suggest that there are fundamental differences in bed properties to the north and south of Venice. This, we suggest, is the result of differences in exposure of the two regions to wind waves which are the major cause of bed erosion. The region south of Venice is relatively exposed. The sediments of this region demonstrate clearly the characteristics of continued bed erosion.

The loss of habitat experienced within Venice Lagoon over the last 30 years has taken place largely south of Venice. Our observations suggest that the region to the north is not in immediate danger of disappearing. While one cannot change the degree of wave exposure of the two regions, there are other fundamental differences between them which may offer a viable, natural solution to the continued losses to the south (i.e. river input of material). These should be explored as a possible alternative to the present practice of re-charging.

LIST OF CONTENTS

1.0 INTRODUCTION

A study of Venice Lagoon was proposed by THETIS SpA, Venice, Italy. This study was called Feed-back of Estuarine Circulation and Transport of Sediments on Phytobenthos (F-ECTS). The project is described in the proposal Technical Annex as...."**F-ECTS main focus is the interdisciplinary investigation of the ecosystem loops in estuarine environments involving phytobentos communities, hydrodynamics, nutrient cycling and sediment transport, with the aim of integrating some of the aspects already investigated in the INTRMUD and BENFLUX Mast Projects and in the ROBUST Environment project.**"

The purpose of F-ECTS was to examine the benthic flux of organic, chemical and inorganic materials from the floor of the Lagoon as a consequence of physically-induced stresses, and the factors which control this benthic flux. The study is multi-national and multi-disciplinary and comprises two major parts: a field component; and a modeling component. The field component involves monitoring seabed response to forcing *in situ* and the bio-physical attributes of the bed which affect this response. As well, a parallel objective was to measure the biodiversity of the Lagoon floor and the productivity resulting from this biodiversity. The field component involved groups from THETIS SpA, University of Copenhagen, University of Algarde, Portugal, University of Ferrara, Italy, University of Southampton, UK, University of Parma, Italy, University of Quebec at Rimouski, Canada, and the Geological Survey of Canada - Atlantic (GSCA). Two field campaigns were planned: the first during mid-summer (August, 1998); the second during mid-winter (February, 1999). The data gathered in these campaigns form the basis of input and calibration of a numerical model (SEDTRANS) of the benthic flux of the Lagoon. It is this modeling which forms the second component of the F-ECTS study.

Specific scientific objectives of this part of F-ECTS was: (1) to determine the factors controlling the erosion/sedimentation parameters (the benthic flux of sediment) in Venice Lagoon ; (2) to determine the effects of dispersal from Sea Carousel by comparison with a sealed system (Mini Flume); (3) to determine the scale effects of benthic flumes by comparing Sea Carousel with Mini Flume; (4) to compare *in situ* results on erosion and deposition with those derived using Lab Carousel; (5) to derive a data set on which to evaluate the evolution of a typical tidal flat in Venice Lagoon (to form the basis of Ph.D. thesis undertaken by Sergio Cappucci, University of Southampton, UK); (6) to compare the nature of the stability of sediment with microfabric, mineralogy, and granulometry of the seabed (to be undertaken by Samanta Cristante, Universita di Parma, Italy); (7) to determine the processes which lead to (i) sediment resuspension and (ii) sediment export from Venice Lagoon; (8) to examine the role of bed roughness on flow turbulence (to form part of a Ph.D. thesis of Magali Le Couturier, University of Southampton, UK); and (9) to examine the role of suspended sediment concentration on flow turbulence reduction (to form part of a Ph.D. thesis of Danielle Cloutier, Universite de Quebec at Rimouski, Quebec).

This report deals with the work carried out by GSCA within the second (winter) campaign. The field work was undertaken between 21st February and 6th March, 1999 aboard a pontoon mobilized by THETIS SpA. A total of 7 major sites were selected to describe the diversity of the

Lagoon. These sites were a sub-set of those occupied during the summer survey and are designated as V20 (and V21), V30 (and V31), V40 (and V41), V50 (and V51), V60 (and V61), V70 (and V71) and V80. The field work was complimented by controlled laboratory analyses to evaluate the effects of consolidation time on stability. The laboratory experiments were carried out on remoulded material from site V40 at THETIS using Lab Carousel. All sites occupied during this survey were muddy and free of sea grasses.

The field program comprised the following operations:

- 13 Sea Carousel deployments, to determine the erosion and sedimentation parameters of the Lagoon bed;
- 13 Mini Flume deployments to examine deposition thresholds and to look into the influence of scale of the instruments on the results so derived;
- 26 syringe cores, to determine the grain size analyses and physical properties (bulk density) of the surface sediments at each Sea Carousel site;
- 4 InterOcean® S4 current meter moorings at site V40 in order to examine the currents of the water mass flooding pallude della Rosa; and
- 2 Cyclops deployments placed adjacent to the InterOcean® S4 current meter to examine the suspended sediment concentration of the water mass flooding pallude della Rosa

The stations occupied in this study are listed in Table 1.1 and shown in Figure 4.1.

STATION	LAT	LON	NAME
V20	45° 28" 31'	12° 23" 11'	S. Giacomo
V21	"	"	"
V30	45° 30" 30'	12° 23" 12'	Cona
V31	"	"	"
V40	45° 29" 40'	12° 26" 23'	Centrega
V41	"	"	"
V50	45° 30" 34'	12° 28" 28'	Saline
V51	"	"	"
V60	45° 19" 58'	12° 18" 13'	S. Maria del Mare
V61	"	"	"

STATION	LAT	LON	NAME
V70	45^0 21" 25'	12^0 15" 45'	S. Leonardo
V71	"	"	"
V80	45^0 24" 08'	12^0 20" 10'	S. Spirito

Table 1.1. A summary of the Sea Carousel and Mini Flume sites occupied during the winter field campaign in Venice Lagoon.

2.0 METHODS and DEFINITIONS

Most of the sedimentation/erosion parameters needed to simulate sediment transport in Venice Lagoon may be determined from time-series of measurements from the Sea Carousel, Mini Flume and Lab Carousel. We sub-divide these parameters into: (1) cohesive (muddy); and (2) non-cohesive (sandy) responses.

The effects of consolidation and the deposition threshold cannot, at present, be determined using Sea Carousel, and so are determined on bulk samples placed within a laboratory equivalent of the Sea Carousel called Lab Carousel. We have attempted in this study to examine, *in situ*, sedimentation rates and dispersal using a new benthic instrument - Mini Flume. The results of this new instrument will also be presented.

2.1 Definitions of seabed erodibility and stability

The stability of sandy beds and the methods by which sand transport may be calculated is reviewed by Li and Amos (1995). In order to define this transport we need the following parameters:

- **threshold for traction (surface creep) τ_{sc} (Pa);** this defines the beginning of sand motion at the onset of a current. It is usually defined visually as the continuous motion of 10 grains (Yalin, 1977)

- **threshold for saltation/suspension τ_{ss} (Pa);** this defines the decay of ripples and the beginning of sand motion into the water column from the bed (Bagnold, 1966);

- **threshold for the onset of sheet flow τ_s (Pa);** this defines the motion of the bed as a liquefied traction carpet without the presence of bedforms (Bagnold, 1966);

- **bedload transport rate as a function of applied bed stress (kg/m/s);** this defines the mass transport rate per unit width per unit time (kg/m/s) moving along the bed with grain-to-grain contact; this is calculated from the video imagery which gives bedform height (H), bedform wave length (L), and bedform migration rate (D_r). The mass transport rate (G_s) as

bedload = 0.5 γ_b HL/D_r., where γ_b is the sand bulk density (assumed to be 1800 kg/m^3) (van den Berg, 1987);

- **suspension profile with height above the bed;** this defines the distribution of material suspended in the vertical, and is necessary in order to compute the suspended sediment transport rate. It is also a measure of turbidity, and the suspended mass. This parameter may be used as a proxy for organic carbon suspension, nutrient fluxes, and O_2 balance of the water column (van Rijn, 1993);

- **suspended sediment flux (kg/m/s);** the depth integration of the suspension profile times the mean flow velocity (kg/m/s); it is determined from the OBS measures of suspended mass (S) per unit volume times the mean current speed (U_y) = S.U_y kg/m/s (van Rijn, 1993); and

- **bedform type;** this defines the type and size of ripples (in sand) or scour patterns (in mud). It is used as an input parameter in the estimation of bed shear stress and defines the bed roughness (Allen, 1982).

The erodibility of a cohesive bed may be defined as the benthic flux from that bed due to hydrodynamic forces.Those parameters which define the benthic flux are reviewed by Dyer (1986). The stability of a cohesive bed, by contrast, may be defined as the resistance of a bed to hydrodynamic forces. The stability of cohesive sediment is often expressed as a single index: the erosion threshold. This index defines the resistance of the bed surface to fluid motion, but does not take into account what takes place once the erosion process has begun, nor does it account for the rate of change in strength with time and the duration over which the erosion event prevails once initiated. Furthermore, bed stability is the time-product of the upward (erosional) and downward (depositional) benthic fluxes, and so we must also account for the type of bed erosion (Villaret and Paulic, 1986), the nature (size, shape, and density) of the eroded material, and the associated sedimentation properties (mass settling rate, ballistic momentum flux, and mode of transport). The evolution of a cohesive bed is the sum of the responses to all stabilizing and destabilizing forces applied to that bed. The stabilizing forces impact the sedimentation character of a bed sediment; the destabilizing forces influence the erodibility of that bed. We may describe the erosion character of a bed in terms of the following attributes:

- **the erosion threshold (cohesion),** $\tau_c(0)$ (in Pa); interpreted as the point at which the surface of the bed begins to erode. There are several criteria by which this threshold is defined (see Sutherland *et al.,* 1998). In the past we choose to express it as the intercept of the sediment failure envelope with the sediment surface (Amos *et al.*, 1992b). In this report, we define it as the value of bed stress at which S reaches ambient values in a regression plot of S and shear stress (Sutherland, 1996). As a proxy to erodibility, $\tau_c(0)$ is rather poor because of the large variations in strength just below the surface layer. Indeed, some contend that an erosion threshold doesn't exist;

- **the erosion threshold as a function of sediment depth**, $\tau_c(z)$ (in Pa); interpreted as the sediment failure envelope (Lambe and Whitman, 1969). It defines the changes in sediment strength (to fluid erosion) throughout the erosion process. It is based on the assumption that, at an applied bed shear stress (τ_o), bed erosion will stop when the bed has eroded to a depth (z) wherein the strength equals the applied stress: $\tau_c(z) = \tau_o$ (Mehta and Partheniades, 1982). By definition, therefore, it is applicable to type I erosion only; that is, asymptotically decaying erosion with time;

- **the friction coefficient**, ϕ (in degrees); adapted from Terzaghi and Peck (1967) is: $\phi = \tan^{-1}(\tau_c(z)/\sigma')$. Depth is transformed to an effective stress (σ') from a knowledge of sediment bulk density (ρ_b): $\sigma' = \rho_b gz + U'$ where g is the gravitational acceleration and U' is the ambient pore pressure (usually unknown, but assumed to be zero in this study). ϕ is used to define the relative stability of a bed, its consolidation state, and bed sedimentary macro-structure (Amos *et al.* 1998);

- **the peak erosion rate**, E_p (in kg/m^2/s), as a function of applied bed shear stress and eroded depth; erosion rate shows a distinct maximum within the first 60 seconds of an applied eroding stress. This peak then diminishes with time in a fashion that defines the erosion type;

- **the mean erosion rate**, E_m (in kg/m^2/s), as a function of applied bed shear stress and eroded depth; it is defined as a function of the difference in the starting and final S within any velocity increment: $E_m = \delta M/\delta t = (S_{end} - S_{start})V/\Delta t\alpha$, where M is the eroded dry mass, V is the Sea Carousel volume (0.218 m^3), α is the flume bed area (0.873 m^2) and Δt is the duration of the applied eroding bed shear stress; for the Mini Flume V = 0.0114 m^3 (fully inundated) and α is 0.0324 m^2;

- **the type of erosion** as a function of time (erosion type) and excess bed shear stress (in kg/m^2/s); it may be either asymptotically diminishing with time (type I) or constant (type II) (after Villaret and Paulic, 1986). The two types of erosion results in vastly differing final S' as well as eroded depths. We suppose it is controlled by the change in bed strength with depth, but not enough information is available to prove this, or to accurately predict when either type of erosion will occur;

- **the size spectra and modes of transport** of material eroded from the bed: type I erosion is characterised by the release of flocs and small pellets (surface erosion), and the mode of transport is largely in suspension; whereas type II erosion occurs through the release of rip-up clasts and large (8 mm) aggregates (mass erosion). In this latter case, the mode of transport is largely through saltation and surface creep, with a significant portion of the eroded material moving within 2 cm of the bed. We presume that this bedload fraction has a large impact on the nature of the erosion process itself through the delivery of momentum to the bed (the solid-transmitted stress of Bagnold, 1936). Also, sedimentation

of material eroded in type II fashion will be much more rapid than that of material derived from type I erosion; and

- **the effect of consolidation** on the erosion threshold (Pa/s); this is a time-dependent attribute of the sediment which is largely unknown due to its complexity. We may chart its evolution in terms of changes in sediment bulk density with sediment depth and with time.

We define sedimentation character in terms of:

- **the deposition threshold**, τ_d (Pa): that is, the applied stress at which material begins to drop back to the bed. It is dependent on S (through the influence on water density and viscosity), and the still-water mass settling velocity of the particles in suspension (W_s). We determine it in settling experiments within the Lab Carousel using "fresh" sediment and local water. We transform the mass settling equation of Krone (1962) as follows: $\delta M/\delta t = W_s S(1 - \tau_o/\tau_d)$; and $\tau_d = \tau_o/(1 - [\delta M/\delta t.1/S.W_s])$. In Mini Flume, the deposition threshold was evaluated by fitting an exponential decay equation to each stage of settling: $S(t) = S_o - k.\ln(t)$. τ_d is determined by plotting k versus applied stress, and solving for $k = 0$. τ_d cannot be determined using Sea Carousel at present because of the uncertainties resulting from dispersion (leakage). Consequently, it was determined within Lab Carousel using bulk samples collected in Venice Lagoon and from settling under know applied flows within Mini Flume;

- **the mean mass deposition rate**, D_m (kg/m^2/s); under an applied stress below the critical for deposition, we may determine D_m per unit area of bed from the rate in change in S: $D_m = \delta M/\delta t = (S_{start} - S_{end})V/\Delta t\alpha$. This was determined from results of Mini Flume;

- **the still water mass settling rate**, W_s (m/s); measured at the end of some Sea Carousel erosion experiments, the still-water mass settling rate may be defined as $D_m = S_t.W_s (1 - \tau_o/\tau_d)$; where $W_s = \delta M/\delta t.\ 1/S_t$, where S_t is the mean suspended sediment concentration for the settling period under consideration; and

- **the degree of retention,** S_{eq}, that is, the amount of material remaining in suspension at a given current speed below an initial deposition threshold (Mehta and Partheniades, 1975) expressed as:

$$S_* = \frac{S_o - S}{S_o - S_{eq}} = \frac{1}{\sqrt{2\pi}} \int_{-\infty}^{T} e^{-0.5W^2} dW$$

$$T = \frac{1}{\sigma} \log\left[\frac{t}{t_{50}}\right]$$

where σ is the standard distribution of the suspended material, S_* is a dimensionless sediment concentration, t is the time from onset of deposition, and w is a dummy variable. O' Brien (1998) has shown that the degree of retention is important in accurate prediction of the long-term evolution of tidal flats.

2.2 Catscan analysis for bulk density

Bulk density was evaluated using x-ray computed tomography, which offers advantages over standard methods of analysis by being digital (yielding spectra of the Hounsfield Unit), three-dimensional, and able to resolve to a voxel volume of 0.06 mm^3 anywhere within the sample. The Hounsfield Unit (HU) for any voxel is defined as $\mathbf{HU = 1000(\mu_s - \mu_w)/\mu_w}$, where μ_s and μ_w are the x-ray linear attenuation coefficients of sediment and fresh water, respectively. According to Beer's Law, μ_s is a function of sediment bulk density, ρ_s. Thus for a constant photoelectric effect, HU should vary in direct proportion to ρ_s. To eliminate negative numbers, and to approximate bulk density, Orsi (1994) transformed HU into a computed tomographic number CT with the expression $\mathbf{CT = 1 + (HU/1000)}$ so that air has CT $\approx$ 0, water has CT $\approx$ 1, and natural, fine-grained sediment has CT between 1 and 3. The transform from CT to fresh-water wet bulk density was: $\rho = \mathbf{390 + 670(CT)}$ kg/m^3; $r^2 = 0.992$; n = 11 (Amos *et al.*, 1996).

Syringe cores were analysed in a frozen state, wet bulk densities were therefore corrected to equivalent densities at 25°C (the water temperature at the time of sampling) from the following relationship: $\rho_{s25} = \rho_{s0}\ (\rho_{w25} / \rho_{w0})$, where ρ_{s25} = wet bulk density at 25°C, ρ_{s0} = wet bulk density at 0°C, ρ_{w25} = water density at 25°C, and ρ_{w0} = water density at 0°C.

Sediment volume (V_s) is determined as: $\mathbf{V_s = (\rho_{s25} - \rho_{w25})/(2650- \rho_{w25})}$, that is the wet sediment bulk density minus the water density divided by the sediment buoyant density. Once V_s is known, porosity (η) can be found: $\eta = (1 - V_s)$, from which the dry weight bulk density (ρ_{bs25}) may be determined: $\rho_{bs25} = (1 - \eta\rho_s)$ and the water content (W) of the sediment is: $\mathbf{W = \eta\rho_{w25} /(1- \eta\rho_s)}$. Cores were analyzed at 1.5 m intervals from the core top to a depth of 15 mm. Thereafter, analyses were made each 5 mm of depth. At each increment, approximately 14,000 independent analyses were made across a 1.5 mm thick tomographic slice of the core. These analyses were illustrated on radiographs in the form of (1) histograms of frequency distribution of x-ray attenuance, (2) the estimated standard deviation of the distribution, and (3) imagery of the tomographic slice in terms of HU intensity. The mean and standard deviation were plotted against core depth for each sample to produce the core profile.

Sample analysis at intervals corresponding to the tomographic slices were made in an attempt to correlate HU frequency types to (1) grain size distributions, and (2) macrofabric.

3.0 INSTRUMENTATION and CALIBRATIONS

3.1 Sea Carousel instrumentation and deployment

Sea Carousel is a benthic annular flume designed for field use in subaqueous settings. The carousel is 1.0 m in radius with an annulus 0.15 m wide and 0.30 m high. It weighs approximately 150 kg in air and 40 kg in water and is made of aluminum (Plate 3.1.1A). Flow in the annulus is induced by rotating a movable lid which is driven by a 0.75 HP digital stepping motor that is powered from the surface. Eight small paddles, spaced equidistantly beneath the lid, induce a flow of water in the annulus. The Carousel is equipped with three optical back scatter sensors (OBS's; Downing, 1983). Two of these are located non-intrusively on the inner wall of the annulus at heights of 0.03 and 0.18 m above the skirt (the skirt is a horizontal flange situated around the outer wall of the annulus 0.04 m above the base; it is designed to standardize penetration of the flume into the seabed). The third OBS detects ambient S outside the annulus, or it may be used to detect internal sediment concentration at a height between the other two. A Seapoint® fluorometer is installed at a height of 0.20 m above the bed in order to monitor chlorophyll through fluorescence. A sampling port, through which water samples may be drawn, is situated in the outer wall of the annulus at a height of 0.2 m above the skirt. It is used to calibrate the three sensors under the assumption of well mixed conditions, for the calibration of the fluorometer, and for the collection of biological and chemical samples. Water samples are collected through a rubber tubing connected to a sample port in the side of the flume (See Plate 3.1.1A). They are pumped to the surface using a Gusher® foot-pump.

Mean flow within the Sea Carousel is determined from a relationship betweemos, *et al.* (1992a) and later verified in laboratory measurements made using a Laser-Doppler flow sensor (Fung, 1995). Mean tangential lid rotational speeds are detected through a shaft end-coder resting on the lid. Tangential (U_y) and vertical (U_w) current speeds are also detected by a Marsh-McBirney® EM flow meter (model 512) situated *circa* 0.18 m above the bed. A Sontek® ADV current meter is installed at a height of 0.15 m above the bed and is situated mid-flow. It logs three components of flow (azimuthal, radial, and vertical) at 25 Hz continuously throughout the deployments. Controller boards for each sensor and operating power (12 VDC) are derived from an underwater pod located above the annulus (Plate 3.1.1A). Output voltages from all sensors are digitized and transformed to engineering units on a Campbell Scientific® CR10 data logger and are stored on a Campbell Scientific® SM192 storage module (storage capacity of 96,000 data values) also located in the underwater pod. The data logger is interrogated and programmed from the surface using a micro-computer linked to the data logger through an RS232 interface. This link operates at 9600 baud, data are transferred as 8-bits including 1 stop bit, and no parity. The sampling rate of all channels was 2 Hz; time stamps (yearday and time) were written to the data file each minute. The structure of the resulting file is: 120 lines of 104, OBS1 (mV), OBS2 (mV), OBS3 (mV), Uw (mV), Ux (mV), LR (counts), P (m), PP (degrees), PR (degrees), and F (mV), where Uw is the vertical component of flow, Ux is the azimuthal component of flow, LR is lid rotation recorded by the shaft end-coder, P is water depth measured by the pressure transducer (calibrated during the survey), PP and PR are pitch and

roll of the Sea Carousel, and F is fluoresence; and 1 line of 304, xxx, yyyy, where xxx is the yearday and yyyy is the time taken from the PC clock. The data are written to a circular buffer capable of storing about 45 minutes of results. These data are uploaded to the PC each 60 seconds and stored to a file named "logger.dat". A memory pointer in the data logger ensures that the data transfer is seamless. At the end of each experiment the data file is renamed to its site designated name Vxx-99.dat.

All channels may be monitored and displayed on the surface computer allowing the operator to control experiments interactively. Bed shear stress is varied in time through a series of script commands issued to the digital motor through a surface controller. The script file used in this survey is as follows: MC, A0.1, V0.5, G, T300, V1.0, G, T300, V1.5, G, T300, V2.0, G, T300, V2.5, G, T300, V3.0, G, T300, V3.5, G, T300, V4.0, G, T300, V5.0, G, T300, V6.0, G, T300, V7.0, G, T300, V8.0, G, T300, V9.0, G, T300, V0, G (where A defines the acceleration rate, V the rotational speed of the motor, T the duration in seconds, and G the "go" command).

A window is located in the inner flume wall for purposes of observing and recording the mechanics of bed failure. Visual observations are made using a Sony® Handycam "super-8" video recorder model CCD-Vxx held in an Amphibico®, Amphibian V11 underwater housing. Light is provided by two Amphibico® 75-Watt underwater lights powered from the surface. The housing has a lens that corrects for underwater geometric distortions and so is suitable for accurate image scaling. Continuous imagery of each deployment is recorded onto the Hi-8 tape in the camera. These tapes are then transferred to SVHS format for further analysis. A scale is placed in the field of view for purposes of measurement.

A second black and white video camera (Panasonic) was placed next to the Hi-8 camera. It was housed in a purpose built pressure housing with a plane perspex face. This camera was used to monitor the experiment real-time through a co-axial cable connected to a surface black and white monitor and VHS recorder. These videos were stored on VHS tapes for reference purposes. The videos are useful in providing information about (1) the type of bed at each site, (2) the mechanism of bed failure (floc, rip-up clasts, undercutting, etc.), (3) the effects of any in fauna trapped in the flume, (4) the presence of a bedload component, (5) any leakage from the flume base, (6) movement of the flume by dragging, etc. Sequential video images may also be digitized for particle trajectories at varying heights above the bed. From these, velocity profiles may be constructed. From such profiles, thicknesses of the logarithmic part of the benthic boundary layer may be determined and friction velocities computed. These latter values may then be compared with laboratory measures as a check.

The principal behind benthic flumes is that we may solve for the benthic flux through a concise definition of the mass balance equation, which may be stated as:

$$\frac{\partial m}{\partial t} + U\frac{\partial m}{\partial x} + V\frac{\partial m}{\partial y} + (W - W_s)\frac{\partial m}{\partial z} + W_b m_b + F_n = 0$$

where term (1) is the rate of change in the suspended mass, the next three terms express the advection of the horizontal and vertical mass concentration gradients (where U, V, and W are the advective mean velocities), the fifth term is the benthic flux and the last term represents any changes in sediment supply from n possible sources. Within the context of the Sea Carousel, we may eliminate the horizontal advective terms because the system is closed. We may also consider the system well mixed during erosion and $W >> W_s$ (the mass settling rate). Furthermore, due to the brevity of each experiment, other external forcing functions such as changing ambient S are neglected, thus $F_n = 0$. In our case the sediment continuity equation becomes the following:

$$\frac{\partial m}{\partial t} + w_b m_b + \mu \frac{\partial m}{\partial x} = 0$$

where the first term is the measured changes in suspended mass through time, the second term is the benthic flux from the bed, and the third term is the dispersion of material from the flume through leakage. The first term is measured *in situ*, the third is determined though experimentation and so the benthic flux ($w_b m_b$) is derived. This may be transformed into an eroded depth through application of Exner's equation:

$$\gamma_b (1 - p) . \frac{\partial z}{\partial t} = w_b m_b$$

where γ_b is the sediment unit weight, p is sediment porosity, and z is bed elevation. The benthic flux is a balance between sediment deposition (D) and erosion (E):

$$w_b m_b = D - E$$

The deployment and operation of the Sea Carousel in this study were held as constant as possible for comparability. The Carousel was lowered to within 1 m of the bed. Thereafter it was lowered at a slow rate of 5-10 cm/s (subsequently found to be below the threshold for erosion). After landing, the Carousel data logger was initialized to log for about 10 minutes under still-water conditions. This initial period was used to determine the current meter zero offsets, and to clear the water of any material suspended by the instrument landing. The experiment consisted of subjecting the seabed to 13 increments of flow, each increment lasting 5 minutes. The instantaneous azimuthal current speeds were quite variable due to: (1) macro-turbulence; (2) variations in lid speed; and (3) changes in bed roughness. Finally, the flow was stopped for a 10-minute period and still-water settling of eroded material was monitored. After retrieval of the Carousel, the site was fixed with GPS which was considered accurate to ± 50 m.

Motor settings (M) were used as the standard input to control flow in the Sea Carousel. These settings showed a perfectly linear relationship to lid rotation (rot) of the form: **rot = 0.160(M)** m/s, $r^2 = 0.99$, n = 7 (Figure 3.1.1). The index azimuthal velocity is also linearly related to motor setting in the form: $\mathbf{U_y = 0.096(M)}$ m/s, $r^2 = 0.99$, n = 96 (Figure 3.1.2). Bed shear stress (τ_o)

varies with lid rotation as a power function that approximates the quadratic stress law: τ_o = $\mathbf{0.43M^{1.57}}$, $r^2 = 0.99$, n = 14.

The effect of the suspended sediments on suppression of the bed shear stress is complex. It can cause fluid stress reduction through (1) turbulence dampening due to changes in the Richardson's number (density stratification), (2) consumption of momentum in maintaining material with finite W_s in suspension, and (3) fluid momentum transfer to accelerating saltating aggregates. Nominal experiments on this subject are inconclusive. Nevertheless, a stress reduction algorithm has been applied to our data on the basis of results in Amos *et al.* (1992a) and Li and Gust (in press). This algorithm is: $\sqrt{(\tau_s/\rho)} = \sqrt{(\tau_o/\rho)} - \mathbf{[0.2267(\log_{10}(S)).((\sqrt{(\tau_o/\rho)}/6.35))]}$ cm/s (S evaluated in mg/L).

The calculation of mean mass settling rate comes from the transform of the equation: $\mathbf{W_s = \delta M/\delta t.\ 1/S_t}$. By using Gibbs *et al.* (1971), W_s is transformed into an equivalent sedimentation radius (RAD, in cm) as follows:

- $\mathbf{RAD = (P1 + \sqrt{(P2 + (P5(P3 + P4)))})/P5}$, where
- $\mathbf{P1 = 0.055804(\rho W_s^2)}$,
- $\mathbf{P2 = 0.003114(\rho^2 W_s^4)}$,
- $\mathbf{P3 = 4.5\mu W_s}$,
- $\mathbf{P4 = 8.704 \times 10^{-3} (\rho W_s^2)}$, and
- $\mathbf{P5 = 981(\rho_b - \rho)}$

(where μ is the viscosity of sea water at the relevant temperature and salinity, and ρ_b is the aggregate bulk density equated with the sediment bulk density at the equivalent eroded depth; all evaluated in cgs units). The fluid density, ρ_w, was also corrected for suspended solids as follows: $\rho_w = (\rho_o(1-V) + \rho_s V)$, where ρ_o is the clear water bulk density (1026 kg/m^3), V is the suspended sediment volume, and ρ_s is the assumed sediment bulk density (2650 kg/m^3).

The size spectrum was evaluated by binning the diameters evaluated each 20 seconds into a series of 22 size classes ranging from 10 to 300 microns and writing the output to file *.dia.

The raw data from Sea Carousel is processed in order to produce the calibrated plots for interpretation. The processing involves the following:

- define date and time for each record;
- read record and despike the data (± 2 standard deviations);
- time-average the 1Hz data (usually over 20 seconds);
- transform time-averaged OBS output to S (mg/L) and suspended mass (kg);
- transform current meter output to azimuthal and vertical flow (m/s);

- compute the clear water friction velocity (m/s) and bed shear stress (Pa);
- determine stress reduction due to S;
- compute fluid density and flow Reynolds number;
- determine lid rotational speed (m/s);
- compute diffusion rate out of flume (kg/s);
- compute corrected suspended mass (kg) and erosion rate ($kg/m^2/s$);
- compute mean eroded depth (mm);
- compute still water mass settling rate (m/s) and equivalent particle diameter (m);
- compute the size spectrum of the suspended material; and
- write output files for plotting results (*.asc; *.dia; *.set).

Estimates of bed shear stress have been made using the ADV burst-sampled data (25 Hz) using the inertial-dissipation method (Stapleton and Huntley, 1995). The results of this work is well beyond the scope of this study and forms part of the post-graduate studies of a Ph.D. student (Magali Le Couturier, School of Ocean and Earth Sciences, Southampton University, UK). The purpose of this work is to verify the estimates of bed shear stress made using other, simpler methods, and to assess changes in bed roughness throughout the Lagoon on flow dynamics.

A summary of the Sea Carousel stations is given in Table 3.1.1.

SITE	DEPTH (m)	TEMP (C)	SAL (‰)	DENSITY (kg/m^3)	DESCRIPTION
V20	2.0	6.5	35	1024	muddy smooth site - 50 m from major shipping channel, ship wakes
V21	1.6	6.5	35	1024	well developed biofilm of filamentous algae (~3 cm long)
V30	1.6	6.5	20	1015	east channel margin
V31	1.4	7.8	20	1015	adjacent to marsh inshore of V30 (= V33, Aug 98)
V40	1.2	9.0	33	1025	inner lagoon mudflat, biofilm of filamentous brown algae on channel edge; gradient of biofilm

SITE	DEPTH (m)	TEMP (C)	SAL (‰)	DENSITY (kg/m^3)	DESCRIPTION
V41	1.2	9.0	32	1025	adjacent to V40, top west flank of tidal channel, no biofilm
V50	1.4	5.3	36	1028	inner lagoon, western edge of tidal channel - continuous macroalgal cover
V51	1.2	5.3	36	1028	replicate of V50
V60	2.5	7.2	36	1028	smooth muddy bottom surrounded by eel grass
V61	2.7	6.8	38	1028	eel grass cover
V70	2.5	7.7	37	1028	adjacent to Margera shipping channel - large wakes
V71	2.9	7.5	37	1028	edge of main shipping channel - ship wakes
V80	1.7	7.3	36	1028	central lagoon mudflat

Table 3.1.1 A summary table of the Sea Carousel and Mini Flume deployments of the winter campaign.

3.2. Current meters

An InterOcean® S4 current meter (SN: 07581590) was used in this project. This meter was equipped with sensors to monitor two horizontal components of flow and hydrostatic pressure. Note that this meter was not equipped with temperature and salinity sensors, so these data were not collected in this project. The current meter was programmed to log current speed and direction and hydrostatic pressure at varying sampling protocols indicated in Table 3.2.1. The meter was set to a height of 0.3 m above the seabed on a stainless steel rod pushed into the bed. A summary of the meter deployments is given in Table 3.2.1. ON refers to the logging period of the meter, while OFF defines the cycle period including the logging time.

SITE	ON (mins)	OFF (mins)	RECORDS	START	END
V40-99s	5	30	115484	1243@04/02/99	1245@08/02/99
V40-992s	5	30	115484	1508@22/02/99	1510@26/02/99
V60-99	C	C	115484	1157@03/03/99	0359@04/03/99
V40-99	C	C	107530	0001@06/03/99	1457@06/03/99

Table 3.2.1 A summary table of the InterOcean® S4 current meter deployment of the winter campaign. (C denotes continuous recording).

3.3 Mini Flume

The Mini Flume is an annular benthic flume made of acrylic (Plate 3.1.1B). It is 30 cm in diameter and stands 30 cm high. The flume width is 4.5 cm and the flow volume is about 7 litres. The flume is open at the base and totally enclosed at the top. The flume is mounted on a tubular frame which supports a digital Sony® video camera, a 70 watt light, two battery pack housings and an electronics housing. The flume is designed to be lowered into a cohesive bed encapsulating the local bed properties as well as those of the nearbed waters. It is mounted with springs that maintain a downward pressure on the flume (about 10 kg force) once on the bed. Flow is induced by 4 square paddles spaced equidistant beneath a rotating circular lid. The speed and acceleration of the paddles are controlled by a Parker Compumotor® digital DC stepping motor which are powered by a bank of 90 D-cell (1.5 volt) batteries. The motor is controlled by a Tattletale® 7 and Compumotor Indexer which are located in the electronics housing and which are connected to it through a RS232 serial link. The relationship between motor voltage (M), lid rotation (rot), and azimuthal current speed 10 cm above the bed (U_{10}) is: $\mathbf{rot = 1.222 \times 10^{-4} (M)}$ m/s (Figure 3.3.1), and $U_{10} = 0.54$ (rot). Notice that the minimum speed of the flume lid is 0.16 m/s. This is the result of non-linear responses of the motor for a given gear ratio. In most cases, this minimum speed is below the threshold for erosion and so has not been a major concern in this study. The flow structure in the flume, the thickness of the boundary layer and the wall effects have been examined in a series of Laser doppler flow measures under various bed roughness (Fung, 1997). These results show a well-developed benthic boundary layer about 1 cm thick to within 1 cm of the walls. The gradient of flow in this boundary layer was used to define the friction velocity (U_*) which is linearly related to U_{10}: $\mathbf{U_* = 0.141\ U_{10}}$ m/s, and $\tau = \mathbf{1.50 \times 10^{-3} \rho\ U_{10}^2}$ Pa, where τ is the bed shear stress and ρ is fluid density. A Seapoint® Optical Backscatter Sensor (OBS) monitors turbidity at a height of 12 cm above the base. The OBS is interfaced to the Tattletale® 7 which logs and stores data on a 20 Mbyte hard drive at a rate of 1 Hz. A sample port is situated at the height of the OBS for purposes of sensor calibration. A Digital Sony® video camera was used to monitor the erosion process at the bed. The camera is capable of storing about 1 hour of imagery on internal memory.

Operation in time is defined by an ASCII script file downloaded to the motor. The program we used was kept for the duration of the project. This program consisted of three phases: (1) an initial period (5 mins) of still-water to equilibrate conditions in the flume; (2) an erosion period, in which flow is increased in a series of 8 steps (of 5-10 mins duration). The magnitude of the steps was dependent on the final lid speed which was selected on the expected erosion characteristics of each site; and (3) a settling period of 5 decreasing steps in speed, the last being still-water (each 20 minutes in duration). Between each settling step, the lid was accelerated to a maximum speed for 5 minutes in order to resuspend settled material.

The Mini Flume offers advantages over Sea Carousel in that it is stand-alone, easier to operate, suffers no dispersion to the ambient water, and monitors erosion over a much smaller area of bed

(0.0324 m^2). It was used to compare results on erosion in order to define any scale effects and to assess the validity of the dispersion algorithm used to correct data from the Sea Carousel.

The Mini Flume was deployed next to the Sea Carousel and was operated concurrently with it. Table 3.3.1 summarizes the operating parameters of the Mini Flume during this survey.

SITE	MAX SPD (m/s)	MIX TIME (mins)	START (UTM)	END (UTM)
V20	0.40	0.3	10:23	12:24
V21	0.40	0.3	13:00	14:56
V30	0.40	0.3	11:34	13:13
V31	0.40	no settling	11:22	12:27
V40	0.40	0.3	15:50	17:29
V41	0.40	0.3	16:15	17:54
V50	--	--	14:15	--
V51	0.40	0.3	14:35	16:14
V60	0.40	0.3	12:22	14:20
V61	0.53	0.6	11:27	13:36
V70	0.53	1	14:09	18:12
V71	0.66	1	11:28	13:36
V80	0.40	0.3	12:12	14:18

Table 3.3.1. A summary table of the Mini Flume deployments during the winter campaign. MAX. SPD is the maximum rotational speed of the paddles. The settling time under an applied flow in all cases was 5 minutes.

The calibration of the OBS installed in Mini Flume was completed during this phase of the program (Figure 3.3.2), and hence the results of the summer campaign are included for completion. The summer report shows uncalibrated plots, and no erosion thresholds or erosion rates could be calculated at the time of its production.

3.4 Lab Carousel

The Lab Carousel is a mobile, laboratory version of the Sea Carousel. Its prime function is to compliment field results obtained by Sea Carousel through more accurate, more controlled simulations of individual attributes of the field site which operate in concert, but which can be manipulated individually in the laboratory. Its main purpose is to evaluate the effect of consolidation time on erosion resistence and to determine (1) deposition threshold as a function of S, and (2) to define the degree of retention (S_{eq}) at a given shear stress.

Lab Carousel has the same dimensions and mode of flow generation as Sea Carousel. It is 1.0 m in radius and has a flume width of 0.15 m. Flow in the flume is controlled by a digital stepping motor which is powered by a 1000 watt Xantrex® power supply. The motor is controlled by a PC which downloads a script file of pre-programmed acceleration rates, rotational speeds, and durations to ensure replication between experiments. The flume is equipped with three OBS sensors at heights of 0.02, 0.10, and 0.20 m above the base. It also contains a Marsh-McBirney® EMCM model 513 which measures azimuthal and radial flow rates at a height of 0.15 m above the base. The relationship between lid rotational speed (R) and motor voltage input (M) is: $\mathbf{R = 1.17 \times 10^{-4} M}$ m/s. The relationship of R to azimuthal speed (U_y) is: $\mathbf{U_y = 0.574R}$. The relationship of the azimuthal velocity to bed shear stress has been evaluated by Fung (1995) using a Laser Doppler Velocimeter to measure the flow structure in the benthic boundary layer of the flume. This layer was about 10 mm thick and showed a logarithmic velocity profile from which shear stress was derived. The relationship has the form: $\mathbf{U_* = 0.097U_y + 0.0167}$ m/s.

Data from all sensors are logged to a Campbell Scientific® CR10 data logger at 2 Hz. Data from the OBS's are converted to mass concentration from analysis of samples taken from one of the three ports situated in the side of the flume at the heights of the OBS's.

3.5 Cyclops

Cyclops was used in this study to measure turbidity of the waters flooding pallude della Rosa (site V40). Cyclops is a self contained, self logging turbidity sensor. It logs backscatter within the water column and stores the intensity of backscatter on an Onset® data logger. Backscatter is logged using a Seapoint® Optical Backscatter Sensor mounted on the endcap of the underwater housing. The housing was mounted on a stainless steel rod which was injected into the seabed. The sensors were set up to log time-averaged turbidity at varying intervals. The sensors were situated about 0.20 m above the seabed. The location and duration of the Cyclops deployment are given in Table 3.5.1.

SITE	SAMPLE RATE (s)	RECORDS	START	END
V10	60	15997	09:44@01/08/98	00:32@16/08/98

SITE	SAMPLE RATE (s)	RECORDS	START	END
V22(susp)	0.5	24254	09:21@13/08/98	12:42@13/08/98
V60	60	25526	11:23@17/08/98	13:37@19/08/98
V70	12	15071	11:30@17/08/98	10:14@20/08/98
V70(ship)	12	21222	08:48@21/08/98	13:12@21/08/98
V90	0.5	32520	13:42@19/08/98	10:47@22/08/98
V40	93	16793	12:27@04/02/99	14:17@22/02/99

Table 3.5.1. A summary of the Cyclops deployment during the summer (98) and winter (99) campaigns.

The calibration of the OBS sensor on Cyclops was completed during this part of the campaign (Figure 3.5.1) and so results from the summer deployment are included for completion. Voltage of the OBS (mV) was a linear function of S in the form: **S = 0.159(mV) - b**; $r^2 = 0.99$; n = 14. The plots of Cyclops shown in the summer report are tentative, and have been updated in this report.

3.6 Bottom sampling and grain size analyses

Bottom sediment samples were collected using an Eckman grab sampler. Sub-samples were collected for: (1) grain size analysis and sediment textural analysis; (2) organic content (loss on ignition); and (3) bulk density profiles (on syringe cores). In many cases, sampling was done by hand where the water depths were less than 0.5 m. This minimized sample disturbance and ensured that samples were collected from undisturbed parts of the seabed. No gravity cores were collected having been collected in the summer. No seabed photographs were taken due to the opacity of the water.

4.0 RESULTS

4.1 Summary of results

In general the Sea Carousel and Mini Flume were deployed simultaneously from the pontoon in shallow intertidal parts of the Lagoon. The Lagoon was characterized by regions of submerged rooted vegetation (Zostera marina, Zostera noltii and Cymodosia sp., Flindt *et al.* 1997) and intertidal plants of Spartina alterniflora. Wide stretches of salt marsh (pallude) were evident in the northernmost sites interspersed with bare mudflats (barene). Ulva rigida (macroalgae) was evident throughout the Lagoon and moved in large amounts as bedload. Some sites were dominated by soft mud with the algae Cladophora sp. predominating (V30, V40 and V50), whereas at other sites the bed was composed of mats of Entermorpha sp. (V30). Another algae (Chaetomorpha aerea) was prevalent at sites V60 and V100 (M. Flindt, personal communication,

1999). Natural and artificial channels dominated the landscape of the Lagoon and cut through the shallow tidal flats. These channels showed evidence of erosion of the banks through undercutting by wave motion.

4.1.1 Summer summary: The turbidity of the waters of Venice Lagoon showed a strong gradient from a maximum (around 100 mg/L) in the north to a minimum (around 10 mg/L) in the south. The region around Venice was characterised by concentrations around 50 mg/L (Figure 4.1.1.1). This trend reflects the wind patterns of the region that were prevalently from the SW. The surface erosion thresholds were greatest in the north (> 2.0 Pa) and least around the City of Venice (< 0.5 Pa, Figure 4.1.1.2). The high values in the north reflect strong biostabilization by bacteria. The low values around Venice perhaps reflects resuspension effects due to heavy boat traffic or perhaps local discharges from the open sewer system. The central and southern Lagoon was characterised by intermediate values reflecting the effects of (1) reduced biostabilization, and (2) increased erosion of the bed. The friction coefficient (an index of consolidation rate and hence bed stability) was generally greatest adjacent to the sandy barriers (> 50°) of the Lagoon and decreased landwards towards the inner Lagoon (< 5°, Figure 4.1.1.3). This in part reflects the fact that sedimentation is highest in the inner lagoon and currents are lower. Higher sedimentation rates are usually associated with a lower friction coefficient. We suspect that the bottom sediments are finer in grain size in the inner Lagoon, a fact which would also influence consolidation. The highest values are found near the entrance to the Lagoon at Cavallino and may reflect input of sand. Bed erosion rates (above threshold) are highest in the northwest (> 8 x 10^{-3} $kg/m^2/s$) and decrease southwards (< 2 x 10 10^{-3} $kg/m^2/s$, Figure 4.1.1.4). Values are least adjacent to the sandy barrier islands. The high bulk densities in this region (> 1800 kg/m^3, Figure 4.1.1.5) may be the cause of lower erosion rates. The trends of bulk density no doubt reflect sedimentation patterns and show lowest values (< 1400 kg/m^3) over the inner marshes and mudflats.

4.1.2 Winter summary: The turbidity of the bottom waters of Venice Lagoon again show a spatial gradient but the direction of this gradient is 90° to that of the summer (Figure 4.1.2.1). Highest concentrations (> 100 mg/L) are found over the inner salt marshes and mud flats while the lowest concentrations (< 20 mg/L) are situated in the northeast. The range of concentrations (20 - 100 mg/L) is similar to that found in the summer, and signifies that if wave erosion is taking place due to Bora winds (which occur throughout the winter), material is removed from the system quickly. The surface erosion threshold is, as during the summer, greatest in the northeast (> 1.0 Pa). Minima are found in the central Lagoon around Venice (< 0.50 Pa), and are intermediate in the southern parts (Figure 4.1.2.2). Bulk density follows the same trends as those seen during the summer. That is, highest values (> 2000 kg/m^3) are found adjacent to the sandy barrier islands, while the lowest values are located over the inner salt marshes and mudflats (< 1800 kg/m^3, Figure 4.1.2.3). Winter values are higher than summer ones suggesting either lower deposition rates or even winter erosion. The friction coefficients show a similar trend to the summer survey. That is, the highest values (most stable material, > 30°) are found in the northernmost and southernmost parts, while the lowest values (least stable material, < 10°) are found around the City of Venice (Figure 4.1.2.4). The still water settling rates show fascinating trends with location. North of Venice, settling rate (W_s) appears independent of S,

whereas to the south W_s is linearly proportional to S. We interpret the difference due to biological effects; to the north adhesion by organic matter reduces the dependency of W_s on size (the material being aggregated or flocculated; to the south material appears to be suspended over a broad range of sizes being less adhesive). Supporting evidence is to be found in the synthetic cores. To the north these cores show the development of a surface layer (10 mm thick) of rapidly increasing bed strength, whereas to the south this layer is absent. The surface layer we attribute to syn-sedimentation effects (primary consolidation) which are absent to the south due to prevalent erosion.

SITE	SUMMER98		WINTER99		
	S (mg/L),	$\tau_{c(0)}$(Pa)[1]	S (mg/L),	$\tau_{c(0)}$(Pa)[1]	$\tau_{c(0)}$(Pa)[2]
V20	64	0.35	32	1.08	1.16
V21	19	0.22	12	0.49	0.57
V30	51	0.80	103.4	0.30	0.36
V31	74	1.90	37.8	0.76	0.75
V40	9	3.06	21.4	0.84	0.73
V41	74	1.51	15.2	1.16	1.29
V50	7	1.42	19.8	0.99	0.68
V51	67	1.51	12.4	0.48	0.62
V60	10	0.36	64	0.53	0.68
V61	--	--	63	0.62	0.68
V70	42	0.59	94	0.61	1.00
V71	--	--	72	0.71	0.58
V80	14	0.85	89	0.38	0.51

Table 4.1.1 A summary table comparing the summer (98) and winter (99) ambient suspended sediment concentrations and threshold stresses. $\tau_{c(0)}{}^1$ was determined from trends in S, whereas $\tau_{c(0)}{}^2$ was evaluated from trends in the erosion rate (E).

Good results were obtained from the 13 sites occupied throughout Venice Lagoon. These sites are illustrated in Figure 4.1.1. The time-series for each station are shown in Figures 4.1.2 to 4.1.14. A consistent time-series of flow was applied in each case. This corresponded to lid speeds of 0.084, 0.166, 0.249, 0.332, 0.416, 0.50, 0.58, 0.67, 0.83, 1.00, 1.17 and 1.33 m/s. Each flow speed was held for 300 seconds. Acceleration rate was constant between each speed increment.

Current and lid speeds were relatively constant from site to site but a mean variation of ± 5 cm/s was evident (Figure 3.1.2).

The relationship between OBS output and S was determined from 13 samples pumped from the Sea Carousel at each increment of lid speed. The regressions of these results are plotted in Figure 4.1.15 for the upper (OBS1) and lower (OBS3) sensors respectively. In view of the overlap in results and the wide scatter at any site, a constant set of calibration equations was used for all sites. These took the form:

$$\mathbf{S1 = 4.82(OBS1) - b_1}\ \text{mg/L};\ r^2 = 0.97$$

$$\mathbf{S3 = 3.19(OBS3) - b_2}\ \text{mg/L};\ r^2 = 0.92$$

where b_1 and b_2 are offsets which depend on the ambient sediment reflectivity and so are site specific. These values are close to those values derived from the summer experiments and suggest that sediment colour and size are not a contributing factor to changes in OBS response to sediment concentration (Sutherland *et al.* 1999).

Plots of corrected S and erosion rate (E) versus applied bed shear stress are given for all sites in Figures 4.1.16 to 4.1.28. In almost all cases, log(S) shows an increase in proportion with log(t). The data show little scatter, and so the derivation of erosion threshold ($\tau_{c(0)}$), using the regression of log(S) with log(t) is considered reliable to ± 0.05 Pa. However, the critical value requires a knowledge of the ambient turbidity (S_o) in each case which is taken as the mean pre-erosional turbidities. The ambient erosion rate (E_o) is taken as either the inflection point in the plot of E versus bed shear stress, or as a mean value of 1.2×10^{-5} kg/m^2/s (see section 5.5.1). The solid dots in each figure illustrate the data which were used to determine the erosion thresholds and erosion rates. The open dots are considered to be pre-erosion measurements and were not used in the regression. Differences between $\tau_{c(0)}{}^1$ and $\tau_{c(0)}{}^2$ reflect the errors in evaluating the threshold condition which have a mean value of 0.13 Pa. The trends in the two methods are, however, similar.

4.2 Sea Carousel - erosion thresholds and erosion rates

A clearly defined erosion threshold was evident at all stations. A summary of the results on erosion threshold is given in Table 4.2.1. All stations were on mud The highest erosion thresholds were found at sites V20 and V41, i.e. in the northeastern part of the Lagoon. This corresponds to the pattern found during the summer, though the values are only half those detected at that time. The region around the City of Venice was the site of the lowest strength; bed material here was more easily eroded, but still possessed high strength by comparison to other estuaries.

SITE	EROSION THRESHOLD (Pa)	FRICTION COEFF. (degrees)	MEAN BULK DENSITY (kg/m^3)	AMBIENT TURBIDITY (mg/L)
V20	1.08	51,8	1900	32.0
V21	--	--	--	68
V30	0.30	33,8	--	103.4
V31	0.76	8,9	1850	37.8
V40	0.84	13,6	1750	21.4
V41	1.16	24,4	1850	15.2
V50	0.99	45,20	1700	19.8
V51	0.48	30	1900	12.4
V60	0.53	34	1750	64
V61	0.62	30	--	63
V70	0.61	57	1750	94
V71	0.71	33	--	72.4
V80	0.38	21	2000	89

Table 4.2.1 A summary of the Sea Carousel results and sediment composition for the summer campaign. The mean bulk density was taken from core depths of 20 - 100 mm, where in general, values were constant. Above 20 mm, density often showed rapid increases with depth.

There was no relationship between erosion threshold and sediment bulk density largely because of the dominating influences of macrobenthos which resulted in a surface layer about 10 mm thick in which a rapid increase in density was evident. This layer was found only at sites north of the City of Venice.

SITE	EROSION RATE ($kg/m^2/s$)
V20	$\log_{10}E = -5.241 + 3.706\ (\log_{10}\tau_o)$
V21	$\log_{10}E = -5.453 + 2.230\ (\log_{10}\tau_o)$ $\log_{10}E = -5.735 + 5.297\ (\log_{10}\tau_o)$
V30	$\log_{10}E = -4.187 + 2.230(\log_{10}\tau_o)$
V31	$E = 1.397 \times 10^{-4} + 1.058 \times 10^{-3}(\log_{10}\tau_o)$
V40	$\log_{10}E = -4.531 + 3.387(\log_{10}\tau_o)$

SITE	EROSION RATE (kg/m^2/s)
V41	$\log_{10}E = -5.556 + 5.040(\log_{10}\tau_o)$
V50	$\log_{10}E = -5.406 + 3.608(\log_{10}\tau_o)$
V51	$\log_{10}E = -4.607 + 1.910(\log_{10}\tau_o)$
V60	$\log_{10}E = -4.650 + 2.080(\log_{10}\tau_o)$
V61	$\log_{10}E = -4.635 + 2.227(\log_{10}\tau_o)$
V70	$\log_{10}E = -5.007 + 2.051(\log_{10}\tau_o)$
V71	$\log_{10}E = -4.601 + 1.710(\log_{10}\tau_o)$
V80	$\log_{10}E = -4.379 + 2.157(\log_{10}\tau_o)$

Table 4.2.2. A summary of the erosion rates as a function of applied bed shear stress

Synthetic cores have been created from the Sea Carousel time series. These plots map the changing applied stress against eroded depth. The locus joining the minima in stress is interpreted as the failure envelope. The macrostructure of the surface sediment is evident as changes in the slope of the failure envelope. These plots are illustrated in Figures 4.2.1 to 4.2.13. In most cases, the erosion resistence increases with depth. A surface layer (about 10 mm thick) is evident for the stations north of Venice. In this layer, the friction coefficient is very high (up to 51°) and, we feel, reflects biostabilization. Beneath this layer of rapid consolidation rate is found a layer of lower friction coefficients (between 6 and 30°) in which strength appears to increase monotonically with depth. We suggest that the surface layer reflects primary consolidation whereas the lower layer is the region of secondary consolidation. Note that the friction coefficient of the lower layer increases from the Lido entrance northwards. In the central and southern Lagoon the pattern of bed density is quite different from that of the north. The surface layer is ubiquitously absent (probably due to a lack of sedimentation and prevalent erosion) and the friction coefficient is considerably higher (> 30°). The inference of this is that the tidal flats south of Venice are more resistant to erosion than those to the north despite having *lower* erosion thresholds.

Samanta Cristante (as part of a thesis at Universita di Parma, Italy) is attempting to relate the synthetic core plots to results from the Catscan analyses and to SEM analyses of syringe cores in order to explain and verify the derived macrofabric. SEM micrographs of the syringe cores show a general decrease in pore size with depth as well as a decrease in density of worm tube galleries. A thesis describing this work is expected during 2000.

4.3 Sea Carousel - mass settling, deposition rates and sediment size

The still water mass settling rate was determined for each station by analysis of S time series during a 10-minute period at the end of each experiment. Plots of these time series are shown in Figures 4.3.1 to 4.3.9. A summary of results is given in Table 4.3.1.

SITE	MEAN W_s (m/s)	MEAN diam (m)	MAX diam (m)	S_0 (mg/L)
V20	1.91×10^{-4}	2.19×10^{-5}	16.32×10^{-5}	1032
V21	8.34×10^{-4}	4.66×10^{-5}	8.23×10^{-5}	730
V30	4.20×10^{-4}	3.08×10^{-5}	5.01×10^{-5}	1413
V31	1.56×10^{-4}	2.34×10^{-5}	4.43×10^{-5}	787
V40	2.64×10^{-4}	3.55×10^{-5}	18.43×10^{-5}	644
V41	5.25×10^{-4}	4.33×10^{-5}	15.29×10^{-5}	1002
V50	5.15×10^{-5}	1.85×10^{-5}	5.50×10^{-5}	566
V51	2.59×10^{-4}	2.85×10^{-5}	4.79×10^{-5}	227
V60	2.22×10^{-4}	2.00×10^{-5}	4.95×10^{-5}	333
V61	2.69×10^{-4}	2.48×10^{-5}	5.88×10^{-5}	315
V70	1.73×10^{-4}	2.17×10^{-5}	4.28×10^{-5}	248
V71	2.89×10^{-4}	2.66×10^{-5}	6.30×10^{-5}	310
V80	1.98×10^{-4}	1.97×10^{-5}	4.04×10^{-5}	521

Table 4.3.1. A summary of the settling rates, mean particle diameters of settling material, and starting S, determined from Sea Carousel at selected muddy sites.

Mean mass settling rate varied between 10^{-4} and 10^{-3} m/s, which is within the range of normal sedimentation rates in estuaries. The highest settling rates were found at site V41 and the lowest at site V50 (an opposite trend to the summer). In general, the northern region produced the highest settling rates. W_s is independent of suspended sediment concentration and has an estuary-wide average value of 2.78×10^{-4} m/s (Figure 4.3.10). This is about 40% of that determined during the summer campaign and shows a much slower mean settling rate during the winter season (7.12×10^{-4} m/s). This fits with trends of the organic content derived from LOI (section 4.10) was higher during the summer thus lowering the material density. Also, processes of flocculation due to increased biological activity during the summer season may well be the cause of the observed rapid settling rate at the time. The lack of correlation between W_s and S_0 was also observed in the summer data. These findings conflict with generally accepted trends

published in the literature (Dyer, 1986). Milligan and Hill (unpublished data, Bedford Institute of Oceanography), who have measured settling rates of natural estuarine flocs, have also found similar results to ours.

The grain size of suspended material is derived on the assumption that the density of the eroded aggregates is that of the bed from which they are derived. Based on this assumption we see that grain size of material settling at sites south of Venice generally diminishes with settling time: the largest grains settling first. Figure 4.3.9 shows a good example of the trend of settling of aggregates for site V60 which starts in the coarse silt size range and ends in the medium silt size range. This example appears to typify sites south of Venice. Sites north of Venice are typified by a constant size in the medium silt range (Figure 4.3.4).

On recommendations of S. Rolinski (Institut fuer Meereskunde, University of Hamburg) we analysed the settling of material that was, in some cases, resuspended on landing of the Sea Carousel. The purpose of this was to see if there were differences in magnitude and type (floc, mass or hindered) of settling of the surface "fluff" layer (which perhaps is more representative of quiescent conditions in the Lagoon; the argument was made that Sea Carousel simulates only storm events) versus the magnitude of settling of material eroded at high stresses (which may reflect conditions after storms). Initial resuspension was seen at sites V30, V40, V41, V50, V51, V70, V71 and V80. The results are summarised in Table 4.3.2.

SITE	W_{s1} (pre-erosion)	W_{s2} (post-erosion)	FUNCTION of W_{s2} with S
V20	--	1.91×10^{-4}	constant
V21	--	8.34×10^{-5}	constant
V30	3.06×10^{-4}	4.20×10^{-4}	constant
V31	--	1.56×10^{-4}	constant
V40	1.69×10^{-4}	2.64×10^{-4}	constant
V41	2.37×10^{-4}	5.25×10^{-4}	constant
V50	5.09×10^{-4}	5.15×10^{-5}	constant
V51	2.67×10^{-4}	2.59×10^{-4}	constant
V60	--	2.22×10^{-4}	$4.07 \times 10^{-6}(S) - 3.88 \times 10^{-4}$
V61	--	2.69×10^{-4}	constant
V70	8.53×10^{-5}	1.73×10^{-4}	$5.25 \times 10^{-6}(S) - 6.76 \times 10^{-4}$
V71	2.29×10^{-4}	2.89×10^{-4}	constant
V80	8.28×10^{-5}	1.98×10^{-4}	$2.74 \times 10^{-6}(S) - 6.15 \times 10^{-4}$

Table 4.3.2. A summary table of the estimated settling rates for the periods before and after the erosion cycle.

The settling rates of the fluff material are plotted against S in Figures 4.3.11 to 4.3.23. Pre-erosion results are shown for sites V30, V40, V41, V50 and V51 in order to show the large scatter in the data and the general lack of trend with S, The remaining examples show post-erosional trends for sites V70, V71, and V80. Of the post-erosion settling, only sites V60, V70,and V80 showed a correlation of instantaneous W_s with S(t); all are situated to the south of Venice. The relationships are listed in Table 4.3.2.

The fluff layer (pre-erosion) mean settling rate (W_{s1}) was 26% less than the mean settling rate of the material suspended in the erosion process (W_{s2}). The two settling rates appeared to be related (Figure 4.3.24) in the form: $\mathbf{W_{s2} = 1.26W_{s1}}$. This relationship is logical as the fluff layer would be expected to contain more organic material and hence be of a lower density and settling rate.

4.4 Bulk density profiles

Bulk density profiles of the topmost 10 cm of sediment at each of the mud dominated stations were derived from frozen syringe cores collected from the topmost part of the bed at each site. These profiles are plotted in Figures 4.4.1 to 4.4.9. The plots show the mean bulk density and the standard deviation of about 14,000 individual measures derived from each tomographic slice (1.5 mm). The standard deviation is thus a measure of the heterogeneity of the sediment, not the error in measurement. The greatest rate of change and largest heterogeneity was found in the surface 10 mm in each case (see Figure 4.4.1) and was most prevalent in the depositional region north of Venice. Below the surface layer, bulk density appears steady with depth and varies between 1600 and 2000 kg/m^3. The greatest bulk density appears to be adjacent to the sandy barrier island and least on the inner salt marshes and mudflats. Also, the winter surface densities are generally higher than those detected during the summer survey perhaps reflecting bed erosion.

4.5 Current meter measurements

Four deployments of the InterOcean® S4 current meter were made between 4 February and 6 March, 1999 (Figures 4.5.1 to 4.5.4). The longest deployments were at station V40 (two at 4 days each). The current meters yielded measures of mean tidal flow speed and direction 30 cm above the bed, and tide height. Results from V40 showed semi-diurnal currents peaking at 25 cm/s. The tides showed strong diurnal inequalities, and the resulting currents reflected this having only one strong peak each day. Currents were largely rectilinear (NE-SW) reflecting the location and orientation of the tidal channel adjacent to V40. There were strong irregularities in the flow, but the ebb current was generally twice that of the flood. The site is thus strongly ebb dominant.

4.6 Cyclops measurements

4.6.1 Summer: Six deployments of Cyclops are presented for the summer period between 1 and 22 August, 1998 (Figures 4.6.1.1 to 4.6.1.6). Site V10 shows a mean concentration of around 15 mg/L which is modulated by winds (see first 2 days in Figure 4.6.1.1). Wind events mask the effects of tidal modulations which are evident at this site during the latter half of the record. The data show strong diurnal inequalities in turbidity related to tidal flow. Peaks in turbidity reach no more than 40 mg/L. Similar trends were seen at site V60 though here a strong asymmetry (short flood - long ebb) was evident (Figure 4.6.1.3). Spikes in the data are the result of the passages of sheets of Ulva sp. Records at site V70 were very short (Figures 4.6.1.4 and 4.6.1.5) and are presented to illustrate the effect of ship passage on sediment resuspension. Peaks in the time series, which reach 70 mg/L are evident throughout the record and correspond to the passage of the bow waves of large vessels passing through the Margera Shipping Canal. Similar effects were seen in data from V90 (Figure 4.6.1.6) where the mean value was around 20 mg/L.

4.6.2 Winter: Cyclops recorded 18 days of data from site V40 during the winter campaign (Figure 4.6.2.1). The data was heavily contaminated by biofouling of fronds of floating Ulva sp. Background levels of turbidity are very low and no clear tidal signal (such as seen during the summer at site V10) was apparent. A major peak in turbidity occurred at hour 144 of the record. This we suspect is the effect of strong winds (though not verified). The peak in turbidity (270 mg/L) was the highest detected by Cyclops and illustrates the dominating effects of winter storm events on resuspension in the Lagoon. The event lasted about 36 hours and so must result in sediment export from the site, given its strong ebb dominance.

4.7 Lab Carousel - Erosion thresholds and erosion rates

Six Lab Carousel experiments were undertaken during the course of this study to examine the effects of consolidation time on the erosion threshold of surface remoulded material from site V42. Consolidation times were 6, 16, 24, 46, 72 and 264 hours. Summary plots of the analyses are shown in Figures 4.7.1 to 4.7.6. A summary of the results is given in Table 4.7.1. The three OBS's were calibrated during the summer campaign by sampling the flume water mass at each speed increment (Figure 4.7.5). The calibrations are as follows:

$$\mathbf{S(1) = b1 + 0.529(OBS1)\ mg/L;\ r^2 = 0.76;\ n = 140}$$

$$\mathbf{S(2) = b2 + 0.432(OBS2)\ mg/L;\ r^2 = 0.66;\ n = 140}$$

$$\mathbf{S(3) = b3 + 0.582(OBS3)\ mg/L;\ r^2 = 0.74;\ n = 140}$$

The sensor offsets (b1, b2 and b3) differed slightly with each experiment and were consequently adjusted to fit the initial concentration during data processing. No attempt was made to remove organic matter from the raw bulk samples. Seawater from Arsinale at room temperature (about 25°C) was used in all experiments.

The time series showed type I (after Villaret and Paulic, 1986) erosion once the yield resistence of the bed was exceeded. This erosion type was superceded by type II erosion at higher speeds,

and stopped once the sediment supply from the bed was exhausted (evident as flat trends on S plots).

CONSOLIDATION TIME (hours)	EROSION THRESH (Pa)	EROSION RATE(E) ($kg/m^2/s$)
6	0.21	--
16	0.17	$E = 1.02 \times 10^{-4} + 7.29 \times 10^{-5} (\log_{10}Tau)$
24	0.42	$E= 1.36 \times 10^{-4} + 1.28 \times 10^{-4} (\log_{10}Tau)$
46	0.56	--
72	0.68	$E= 6.84 \times 10^{-5} + 5.49 \times 10^{-5} (\log_{10}Tau)$
264	0.35	--

Table 4.7.1. A summary of the erosion threshold of surface sediment from site V42 carried out in Lab Carousel at THETIS SpA.

Results indicate that the erosion threshold in Lab Carousel is generally a small fraction of that found *in situ*. This is due to the effects in the field of biostabilization and solar radiation (for the intertidal sites). As these effects were absent in the lab, the impact of consolidation time only could be evaluated. There was a clear trend in bed strengthening with consolidation time in the form of: $\tau_{crit} = \mathbf{0.011(t)}$ Pa, where t is time in hours (Figure 4.7.7). Bed erosion rates were about 1 to 2 orders of magnitude higher than field equivalents even after 11 days of consolidation.

4.8 Mini Flume - Summer

The sensors on Mini Flume were calibrated at THETIS SpA in February, 1999 under controlled laboratory conditions. Results in the summer field report (Amos, Cloutier *et al.* 1998) were thus tentative and incomplete. Consequently, the summer results are presented here and will be compared with the equivalent Sea Carousel results and also with the results obtained from the winter deployments of Mini Flume (section 4.9). Summary plots of results from the Mini Flume are shown in Figures 4.8.1 to 4.8.16. The first panel gives the mean current speed (U_y) within the flume. This speed was pre-programmed before each deployment and varied between 0.4 and 0.8 m/s.

Results from site V43 Figure 4.8.9) show the effect of battery failure. The irregular OBS response is due to deceleration and stopping of the paddles during operation. All other experiments worked well and the OBS sensor showed (1) a measurable erosion threshold, (2) type I erosion rates, (3) a measurable deposition threshold, and (4) deposition trends similar to those seen in Lab Carousel. The peak lid speed was pre-set before each experiment in order to minimize the risk of sensor saturation. Nevertheless, sites V20, V21, V30, V31, V42, V44, V52 and V70 showed sensor saturation at peak flows. The responses at V41, V60 and V62 indicate

dispersion from the base of the flume due to leakage. These results indicate that while stand-alone systems have their advantages in ease of deployment they suffer from degradation in data quality over supervised systems such as Sea Carousel.

SITE	DEPLOYMENT DATE	EROSION THRESHOLD (Pa)
V20	11/08/98	0.31
V21	12/08/98	0.31
V22	12/08/98	0.43
V30	08/0898	0.59
V31	10/08/98	0.23
V32	10/08/98	0.18
V40	04/08/98	2.36
V41	05/08/98	0.34
V42	05/08/98	0.31
V43	06/08/98	0.29
V44	07/08/98	0.29
V53	02/08/98	1.98
V60	18/08/98	0.38
V62	19/08/98	0.65
V70	19/08/98	0.56
V80	14/08/98	0.62
V100	19/08/98	1.61

Table 4.8.1. A summary table of the Mini Flume deployments during the summer campaign.

4.8.1 Erosion thresholds and erosion rates

Clearly defined erosion thresholds were evident in the Mini Flume time series data. The trends in sediment concentration with applied bed shear stress appear linear and regression has been carried out on this basis. The erosion threshold results so derived are listed in Table 4.8.1. There is a large variation in values within short distances between replicate sites suggesting

patchiness related to channels. The greatest strength is in the regions between channels and the lowest strength is found in the channel beds. Sites V30 and V40 are good examples of this variability. Despite this uncertainty, maximum strength values show a pattern similar to that of the Sea Carousel. Maximum values (> 2 Pa) are found in the northern part of the Lagoon, minimum strengths are situated around the City of Venice, and intermediate values are situated in the southern and central Lagoon south of Venice. The mean strength of the Lagoon measured by Mini Flume was 0.67 (± 0.25) Pa.

4.9 Mini Flume - Winter

The Mini Flume provided results from all sites except V50. These results are shown in Figures 4.9.1 to 4.9.12. At sites V30 and V41, the lack of response in the OBS sensor suggests that the paddles were not turning, and hence no results can be derived. At site V31, data were logged for the first 65 minutes of the experiment only; though an erosion threshold was evident, no information on deposition was recorded. Trends in signal at sites V61, V70 and V71 suggest losses of material from the flume. This could only occur at the base, and suggests that the flume was not well seated in the sediments at these sites. These sites were too deep for a visual inspection, or to adjust flume penetration by hand. At the remaining sites this was possible, and as a result, no dispersion took place. Remaining sites yielded good data on which the stability of bottom material could be evaluated. Type I erosion was prevalent and is best illustrated in Figures 4.9.7 (V51) and 4.9.9 (V61). In general a 10 minute increment was sufficient for the erosion process to equilibrate. Deposition, by contrast, was far from completed within the 10 minutes or so allocated to settling. Consequently it was not possible to define the degree of retention at each increment of settling, although the duration was long enough to define a settling decay constant, k.

SITE	DEPLOYMENT DATE	EROSION THRESHOLD (Pa)	DEPOSITION THRESHOLD (Pa)	MEAN W_s (m/s)
V20	27/02/99	0.73	--	6.96×10^{-5}
V21	27/02/99	1.12	--	7.74×10^{-5}
V30	25/02/99	--	0.47	3.35×10^{-4}
V31	26/02/99	0.69	0.46	--
V40	23/02/99	1.16	0.24, 0.71	1.86×10^{-4}
V41	24/02/99	--	--	--
V50	21/02/99	--	--	--
V51	22/02/99	0.58	0.57, 0.99	1.24×10^{-4}
V60	02/03/99	0.60	--	6.85×10^{-5}
V61	03/03/99	0.74	0.76	1.37×10^{-4}

SITE	DEPLOYMENT DATE	EROSION THRESHOLD (Pa)	DEPOSITION THRESHOLD (Pa)	MEAN W_s (m/s)
V70	04/03/99	0.37	--	5.86×10^{-4}
V71	05/03/99	0.62	0.42	5.69×10^{-4}
V80	01/03/99	0.70	0.74	1.40×10^{-4}

Table 4.9.1. A summary table of the Mini Flume deployments during the winter campaign.

4.9.1 Erosion thresholds and erosion rates

The erosion thresholds and erosion rates were derived from data plotted in Figures 4.9.1.1 to 4.9.1.9. The solid dots in each figure were taken to represent conditions of erosion and were thus used to fit the first order regression fit to calculate the erosion threshold. In most cases, the data showed linear trends in S with applied stress (above the critical stress) which was similar to trends measured during the summer campaign. A summary of the erosion thresholds for this survey is given in Table 4.8.1. The highest values of strength were found in the northern part of the Lagoon though no trend was evident. The values in the central and southern Lagoon were consistent and similar to the summertime values. The mean erosion threshold for the Lagoon was 0.73 Pa; a value higher than that recorded during the summer. This contrasts with the Sea Carousel findings (in which the summer thresholds were higher than the winter ones). We have checked for sources of error (i.e. changes in OBS sensitivity or changes in lid rotational response) and no clear discrepancy was found.

4.9.2 Deposition thresholds and deposition rates

The deposition thresholds and deposition decay constants (k) were evaluated from the data presented in Figures 4.9.2.1 to 4.9.2.10. A summary of results is given in Table 4.9.1. The estimated deposition thresholds were of the same magnitude, if not larger, than the erosion thresholds. The reason for this is due, we suggest, to the fact that the material in suspension is of a variety of sizes and settling rates, and hence of a variety of depositional thresholds. Because of the nature of the test (resuspending material between each speed increment) we derive the maximum value (presumably resulting from the periods of erosion at the highest bed stresses). We suspect that the depositional thresholds reflect the applied bed shear stresses as there appears to be a degree of retention of material in suspension at the highest settling speeds. This is, however, hard to prove given the short period of settling. A good test in the future would be to extend the settling time, and not to resuspend material between speed increments.

The trends in mass settling (as indicated by the decay constant, k) should indicate higher values at lower flow speeds, and be at a maximum in still water. This is not the case. In most cases, the still water mass settling is less (lower k-value) than under an applied flow (Figures 4.9.2.2, 4.9.2.5,). In other cases, the trend is reversed (Figure 4.9.2.1, 2.9.2.2); here we suspect that differences in

S for each speed increment is dominating the trend (i.e. resuspension between speeds was not efficient enough to ensure a constant starting S). A comparison between still water settling (W_s) measured in Sea Carousel has been made with that of Mini Flume. Despite considerable scatter, there is a great degree of overlap with no clear differences in values.

4.10 Loss on ignition of suspended samples pumped from Sea Carousel

The material lost on ignition (LOI) of suspended matter pumped from the Sea Carousel at each increment of current speed was measured at selected stations during the summer and winter surveys. The results of these analyses are plotted in Figures 4.10.1 to 4.10.11. In general, highest values (100 %) were found at the early stages of erosion, and are diagnostic of the suspension of an organic rich, surface "fluff" layer. LOI decreased throughout the deployments in response to the erosion of inorganic material typically found in cores within the bed. Curiously, the winter survey appeared to show many examples of higher LOI values than during the summer (Figures 4.10.1, 4.10.2, 4.10.7) which contradicts the supposition of the growth of a well-developed biofilm during summer months. Furthermore, high values of LOI were found at all locations in the Lagoon, even in the central and southern parts where cores showed a general absence of a biofilm. We suggest that the suspended organic matter is fugative and constitutes a mobile bedload layer of organic detritus such as measured by Flindt *et al.* (1997).

5.0 DISCUSSION

5.1 Trends of the winter results within Venice Lagoon

Spatial trends in the results are difficult to recognise as only 13 sites were occupied during the winter survey. Nevertheless, some trends appeared to emerge. Ambient turbidity increased from east to west and ranged from 20 - 100 mg/L. The highest turbidities were in the shallower parts of the Lagoon and perhaps reflect wave resuspension from NE winds. These values are normal for estuaries and typify values where floc settling would be expected. The bed strength (erosion threshold) showed similar patterns to those found in the summer survey. That is, strengths were greatest in the northermost part of the Lagoon, were minimum in the central part (around Venice and off the international airport) and were intermediate in the southern parts. The lowest strengths may reflect anthropogenic effects (boat traffic) which is greatest around the City of Venice). The high values in the north appear to be the result of biostabilization on the tidal flats of this region. The intermediate values are from regions which are largely sub-littoral and hence less subject to intermittent resuspension events. This is apparent in the distribution in friction coefficient which may be viewed as a proxy of the depositional history. The low values in the central Lagoon correspond to the low erosion thresholds. Similarly, the high values in the north reflect the resistant material of the region.

The surface sediment wet weight bulk density were generally high (1700 - 2000 kg/m^3) for recent marine, fine-grained sediment. The inference is that the Lagoon material is well consolidated and so resistant to mobilization. The highest values are located in the east near the sandy barrier islands which separate Venice Lagoon from the Adriatic. Lowest values were found on the

fringing tidal flats in the western Lagoon. We suppose that the higher flows, and lower deposition rates have an influence on deposition rates. The trends in bulk density do not follow the trends in sediment stability. We conclude that this physical property does not have a primary control on bed stability. Rather, it is the colonization of plants, and biostabilization by bacteria and algae which appear to have the most significant effect on bed stability.

An interesting finding worthy of note is the trends in settling rate (W_s) with S. Sites north of Venice showed no obvious trends, whereas sites south of Venice showed a clear linear relationship. We suspect that the difference is related to biological influences, but beyond this we have no explanation. Insofar as settling rate is an extremely important parameter in the numerical simulation of Lagoon evolution, a study to expand on these findings would be valuable.

5.2 Comparison between results obtained during the summer and winter surveys

The ambient turbidities of the waters of the Lagoon measured during the winter and summer surveys varied over similar ranges. We expected higher values in the winter due to greater wave activity. However, we suspect that tidal flushing may well prevent the mean turbidity levels from climbing above 100 mg/L. The distribution in turbidity varied with season. During the summer, highest values were found in the north, and the lowest in the south. We suspect that changes in local wind patterns are responsible for changes in these trends. The most significant aspect of this work was the changes in erosion threshold between the summer and winter surveys (Figure 5.2.1). During the summer survey the mean (Lagoon-averaged) value was 1.10 (± 0.20) Pa. This value is within the range of values found in other coastal environments around the world, although it is quite high in response to the high water temperatures found there (25 - 30^{0}C). During the winter, this value had dropped to 0.69 (± 0.25) Pa (about 42% drop), which we suspect is the consequence of a lowering in the biostabilization resulting from the cooler water temperatures (between 6 and 10°C). This was most evident in the northern part of the Lagoon only. The central and southern parts showed values of erosion threshold similar to those of the summer. Values of bulk density were greater in the winter (Figure 5.2.2). The friction coefficient showed trends that were similar to those of the summer; that is, values were lowest in the central Lagoon, and greater to the north and south.

5.3 Comparison between Sea Carousel and Mini Flume

The Sea Carousel and Mini Flume were deployed simultaneously side-by-side at each site. There are major differences in instrument scale, operational characteristics and foot-print size which could provide insight into experimental errors. The results obtained on erosion threshold from the two instruments showed very similar values for the winter survey (Figure 5.3.1). Though differences were evident, the Lagoon-averaged mean value for both instruments was 0.69 Pa. The comparison of results from the two instruments during the summer survey were not so good (see Figure 5.3.1). The Lagoon-averaged erosion thresholds from Sea Carousel and Mini Flume were 1.10 (± 0.20 Pa) and 0.67 Pa (± 0.25 Pa) respectively. The Mini Flume during the summer survey was still being developed and it was its first field test. Unfortunately, seawater bled into the end bearings due to failure of a seal. This would have strongly influenced the rotational

speeds for a given motor setting. As a result, we view the Mini Flume results from the summer with caution.

5.4 Comparison between Sea Carousel and Sederode (summer, 1998)

The SedErode was used to examine the erosion threshold of a sub-set of those examined herein. SedErode was used both in situ during mudflat exposure, as well as on box cores collected at the time (Feates and Mitchener, 1999). The two surveys overlapped, but were not synchronous. As well Mini Flume and Sea Carousel were used during tidal inundation, SedErode was used sub-aerially. Finally, the sites of the deployments were within about 50 m only and so differences in results were to be expected due to patchiness.
The results of the summer survey are shown in Figure 5.3.1. SedErode resulted in the lowest erosion threshold of 0.22 (± 0.11) Pa (n = 16), Mini Flume yielded intermediate values of 0.67 (± 0.65) Pa (n = 17), and Sea Carousel gave the highest result of 1.10 (± 0.70) Pa (n = 23). The standard deviation of results reflects more the spatial variability over deca-metres (from the tidal flats to the channel bases), as well as km-scale trends in the Lagoon. We suggest that differences between Sea Carousel and SedErode result from the fact that (1) the instruments were used at different times, (2) they were used at slightly different locations, (3) they were used under different conditions, and (4) the tests were undertaken in different ways. As a result, it is not possible to evaluate the differences. The main point to be made is that very large differences can be derived from *in situ* instrumentation and caution should be used when interpreting results from them.

5.5 Input parameters to the numerical simulation of Venice Lagoon

Accurate numerical simulation of the benthic flux of material in Venice Lagoon can only be achieved provided that the coefficients and constants of sedimentation specified to any predictive model be accurate. Below, we attempt to synthesise the relevant coefficients and constants for application to the second phase of this study.

5.5.1 Erosion thresholds and erosion rates

The recommended erosion thresholds for the study should be neither constant in time nor space. We suggest that a summer and winter set of extremes be used in simulations which should be run separately. These values are illustrated in Figures 4.1.1.2 and 4.1.2.2 respectively. A typical mean summertime erosion threshold is 1.10 Pa and a typical winter value is 0.67 Pa. These are the values derived from surveys using the Sea Carousel. The erosion rates for the Lagoon are presented in Table 4.2.2. The summer results were presented as a log-linear relationship. The winter results were presented as a log-log relationship between erosion rate and applied bed shear stress. These rates appear to vary by an order of magnitude across the Lagoon. Note that the minimum erosion rate detectible appears to be $E_0 = 1.2 \times 10^{-5}$ kg/m^2/s. This practical limitation was largely constant. A Lagoon wide relationship of erosion rate for the summer was $\mathbf{E = E_0 + 3.78 \times 10^{-3}(\log_{10}\tau_0)}$ kg/m^2/s, and for the winter was $\mathbf{Log_{10}(E) = \log_{10}(E_0) + 2.89(\log_{10}\tau_0)}$ kg/m^2/s.

Tests carried out during the summer survey show that diel variations in erosion threshold were not evident. This was not re-evaluated during the winter survey. We suggest that a further study of time-variability in bed strength over a tidal exposure would be a valuable adjunct to this work.

5.5.2 Deposition thresholds and settling rates

The deposition threshold was determined for a limited number of sites using Mini Flume. Only the wintertime values have been presented due to uncertainties with the instrument functioning during the summer. We found that the depositional threshold was almost equivalent to the erosion threshold and varied between 0.24 and 0.99 Pa. This we suspect is because the threshold is dependent on the preceding applied bed shear stress and erosion history. That is, more energetic events suspend larger (faster settling) material, a proportion of which will deposit as energetic conditions diminish. Bagnold (1966) suggested a relationship of $\mathbf{W_s = 0.64U_*}^2$ which we recommend for application to Venice Lagoon. The proportion of material assigned to this settling rate is that proportion eroded at the equivalent level of stress during the erosion phase. Assuming no aggregate attrition, the degree of retention would be that portion of material eroded from the bed at all lower values of stress. The settling rates are independent of S north of the City of Venice, whereas they are dependent on S to the south of the City. These values (derived from Mini Flume) are given in Table 4.9.1. The Lagoon-averaged mean rate of winter settling was 2.78×10^{-4} m/s which is about 50% that of the summer survey (7.12×10^{-4} m/s).

5.5.3 Degree of retention

We were unable to evaluate this through the data from Mini Flume as the time intervals for settling were far too short. We expect that at least 1 hour of settling would be required at each speed interval resulting in deployments lasting 8-10 hours. Given the nature of this survey that was not possible. We suggest that a further study could be undertaken to answer the question of the degree of retention, and the results compared to the incremental erosion masses described above (section 5.5.1).

5.5.4 Increase in strength with sediment depth

The increase in sediment strength with sediment depth (the friction coefficient, ϕ) was not constant, but showed variations dependent on (1) position in the Lagoon, and (2) degree and nature of the biofilm. The distribution in surface ϕ in Venice Lagoon is shown in Figures 4.1.1.3 and 4.1.2.4. The values typically vary between 10 and 50^0. North of Venice there is the added complication that there is a surface layer wherein the friction coefficient is higher than below. South of Venice this surface layer is absent. A summary of friction coefficients for the winter survey are given in Table 4.2.1. These values are similar to those measured during the summer in both magnitude and spatial distribution.

6.0 CONCLUSIONS AND RECOMMENDATIONS

6.0 CONCLUSIONS AND RECOMMENDATIONS

The results of the February, 1999 field campaign have been presented in this report. The data collected were abundant, and the quality of the results was very high. In general, all objectives of the project were met and the analyses undertaken to date suggest that the results will be suitable for input to a numerical prediction of the processes controlling the organic and inorganic benthic flux.

In summary, 13 Sea Carousel sites were occupied. The sites were a sub-set of those occupied during the previous summer. As well, 12 deployments of Mini Flume were carried out simultaneously with Sea Carousel. Cyclops and the S4 current meter were deployed for several periods of time and resulted in 2 records each four days long at site V40. The results from this survey have been summarised, and several points of conclusion are evident. These are as follows:

- the winter gradient in S for the bottom waters of the Lagoon showed a gradient from west to east; the highest values (around 100 mg/L) were over the inner mudflats and marshes, and the lowest (< 20 mg/L) near the mouths

- the range in turbidities overlapped those found during the summer survey and suggest that if resuspension due to waves is taking place, the material is either redeposited rapidly elsewhere or it is lost from the Lagoon;

- bed responses in the region north of Venice are different from those found to the south of the City; in particular, we found that a 10 mm surface layer of rapidly increasing strength was present to the north but absent to the south and W_s was independent of S to the north, but dependent on S to the south;

- bulk density showed trends which were similar in both surveys; that is, they were high near the coastal sandy barrier islands and lowest in the inner (western) part of the Lagoon; density was highest overall in the winter, perhaps reflecting erosion of the tidal flats;

- erosion rates varied by an order of magnitude across the Lagoon; however, the mean relationship was $\mathbf{Log_{10}(E) = log_{10}(E_0) + 2.89(log_{10}\tau_0)}$ kg/m^2/s;

- mass settling rate varied between 10^{-3} and 10^{-4} m/s which is within the normal range for aggregated particles in estuaries; there was no trend in mean mass settling rate and S;

- the settling rates of surface (pre-erosional) material and bed (post-erosional) material were very similar, suggesting that aggregation/flocculation dominates over the relative proportions of disaggregated size classes;

- the data from Cyclops and the S4 current meter at site V40 was short-lived and was insufficient to make any statements about the flux of material to the tidal flats of that region; we recommend a further 30 days data collection at this site in order to provide the

suitable open boundary conditions to the perceived 1-D tidal flat model to be implemented by S. Cappucci as part of his Ph.D. studies;

- Lab Carousel was used to evaluate the effects of consolidation time on erosion threshold; the results showed no relationship; settling rates determined from the Lab Carousel were 10% of those determined in the field. We suggest that disaggregation of the remoulded laboratory material has caused the under-estimation of settling rate;

- Mini Flume results from the summer survey are considered inaccurate due to system failure (leakage) at the time. The winter survey, however, was much better and resulted in very good agreement with Sea Carousel;
- Sea Carousel and SedErode gave very different values of erosion threshold. This we attribute to differences in operation, calibration, and interpretation of results;

- the degree of retention could not be determined in this study; we recommend that a further study be undertaken in order to define this value as it has a strong influence on the prediction of sedimentation rates as well as sediment fluxes;

- the deposition thresholds were found to be about the same as the erosion thresholds. We feel that there is a continuum of thresholds which is controlled by the prior erosional history. Larger events would, therefore, lead to a higher depositional threshold. We recommend an analysis of this through longer settling *in situ* time series and through numerical simulations;

- the lack of a relationship between W_s and S goes against published ideas on the subject. The reasons for the lack of a relationship needs to be examined further;

- no clear diel trends in bed strength were found, However, only two day/night relicates were carried out, and so this conclusion is tentative; and

- bed strengthening due to consolidation was measured in Lab Carousel and showed a linear increase in strength with time (t) of the form: $\tau_{crit} = \mathbf{0.011(t)}$ Pa, where t is measured in hours.

7.0 REFERENCES

Allen, J.R.L. 1982. Sedimentary Structures: their character and physical basis. Publ. Elsevier, Amsterdam. 2 vols.

Amos, C.L., Grant, J., Daborn, G.R. and Black, K. 1992a. Sea Carousel - a benthic annular flume. Estuarine, Coastal and Shelf Sciences 34: 557-577

Amos, C.L., Daborn, G.R., Christian, H.A. Atkinson, A. and Robertson, A. 1992b. *In situ* erosion measurements on fine-grained sediments from the Bay of Fundy. Marine Geology 108: 175-196.

Amos, C.L., Sutherland, T.F., Radzijewski, B. and Doucette, M. 1996. A rapid technique to determine bulk density of fine-grained sediments by X-ray computed tomography. Journal of Sedimentary Research 66(5): 1023-1039.

Amos, C.L., Brylinsky, M. Sutherland, T.F., O'Brien, D., Lee, S. and Cramp, A. 1998. The stability of a mudflat in the Humber estuary, South Yorkshire, UK. In Black, K., Paterson, D.M., and Cramp, A. (eds), Sedimentary Processes in the Intertidal Zone. Geological Society of London Special Publication 139: 25-43.

Amos, C.L., Cloutier, D., Cristante, S., Cappucci, S. and Levy, A. 1998. The Venice Lagoon Study (F-ECTS). Field Results - August, 1998. Geological Survey of Canada Open File Report 3711.

Bagnold, R.A. 1936. The Physics of Blown Sand and Desert Dunes. Publ. Chapman & Hall, London: 265p.

Bagnold, R.A. 1966. An approach to the sediment transport problem from general physics. U.S. Geological Survey Professional Paper 4421: 37p.

Downing, J. P. 1983 An optical instrument for monitoring suspended particulates in ocean and laboratory. Proceedings of Oceans'83: 199-202.

Dyer, K. 1986. Coastal and Estuarine Sediment Dynamics. Publ. John Wiley & Sons, Chichester: 342p.

Feates, N.G. and Mitchener, H.J. 1999. SedErode measurements in Venice Lagoon. HR Wallingford Report TR90.

Flindt, M., Salomonsen, J., Carrer, M., Bocci, M. and Kamp-Nielsen, L. 1997. Loss, growth and transport dynamics of *Chaetomorpha aerea* and *Ulva rigida* in the Lagoon of Venice during an early summer field campaign. Ecological Modelling 102: 133-141.

Fung, A. 1995. Accurate calibration measurements of flow in Lab Carousel under varying lid rotations. Unpublished Contract Report 23420-5-M083 to Geological Survey of Canada.

Fung, A. 1997. Calibration of flow field in Mini Flume (Order 23420-7-M339). Unpublished Contract Report to Geological Survey of Canada

Gibbs, R.J., Matthews, M.D. and Link, D.A. 1971. The relationship between sphere size and settling velocity. Journal of Sedimentary Petrology 41: 7-18.

Krone, R.B. 1962. Flume studies on the transport of sediment in esturial shoaling processes. Final Report Hydraulic Engineering Laboratory and Sanitary Engineering Research Laboratory. University of California, Berkeley.

Lambe, W.T. and Whitman, R.V. 1969. Soil Mechanics. Publ. John Wiley & Sons, Inc. New York.

Li, M. Z. and Amos, C.L. 1995. SEDTRANS92: a sediment transport model for continental shelves. Computers & Geosciences 4: 533-554.

Li, M.Z. and Gust, G. in press. Boundary layer dynamics and drag reduction in flows of high cohesive sediment suspension.

Mehta, A.J. and Partheniades, E. 1975. An investigation of the depositional properties of flocculated fine sediments. Journal of Hydraulic Research 13: 361-381.

Mehta, A.J. and Partheniades, E. 1982. Resuspension of deposited cohesive sediment beds. Eighteenth Conference Coastal Engineering: 1569-1588.

O'Brien, D. 1998. The Sediment Dynamics of a Macrotidal Mudflat on Varying Timescales. Unpublished Ph.D. Thesis. Cardiff University, Wales: 140p.

Orsi, T. 1994. Computed tomography of macrostructure and physical property variability of seafloor sediments. Unpublished Ph.D. Thesis, Texas A&M: 183p.

Stapleton, K.R. and Huntley, D.A. 1995. Seabed stress determination using the inertial dissipation method and the turbulent kinetic energy method. Earth Surface Processes and Landforms. 20: 807-815.

Sutherland, T.F. 1996. Biostabilization of estuarine subtidal sediments. Unpublished Ph.D. Thesis, Dalhousie University, Halifax: 179p.

Sutherland, T.F., Amos, C.L. and Grant, J. 1998. The erosion threshold of biotic sediments: a comparison of methods. In Black, K., Paterson, D.M., and Cramp, A. (eds), Sedimentary Processes in the Intertidal Zone. Geological Society of London Special Publication 139: 295-307.

Sutherland, T.F., Lane, P.M., Amos, C.L. and Downing, J. 1999. The calibration of optical backscatter sensors for suspended sediment of varying darkness levels. Journal of Sedimentary Research.

Terzaghi, K. and Peck, R.B. 1967. Soil Mechanics in Engineering Practice. Publ. John Wiley & Sons, New York: 729p.

Van den Berg, J.H. 1987. Bedform migration and bed-load transport in some rivers and tidal environments. Sedimentology 34(4): 681-698.

Van Rijn, L.C. 1993. Principles of sediment transport in rivers, estuaries and coasts. Publ. Aqua Publications.

Villaret, C. and Paulic, M. 1986. Experiments on the erosion of deposited and placed cohesive sediments in an annular flume. Report to Coastal and Oceanographic Engineering Department, University of Florida, Gainesville.

Yalin, M.S. 1977. Mechanics of Sediment transport. Publ. Pergamon Press, Oxford: 298p.

8.0 ITINERARY

DATE	OPERATION
31 January, 1999	Leave Canada for Venice, Italy
1 February	Start consolidation tests (Lab Carousel), calibration of Cyclops'
2 February	Rebuilding Mini Flume due to corrosion internally
3 February	Function tests of Mini Flume; public seminar at THETIS
4 February	Deployment of S4/Cyclops1 at site V40
	Lab Carousel experiment V42-E6 (6-hour consolidation)
5 February	Lab Carousel experiment V42-E16 (16-hour consolidation)
6/7 February	Drive to Cardiff University from Venice, Italy
8 February	Setting up Cardiff Lab Carousel for turbulence experiments
9/12 February	Turbulence measures versus turbidity carried out
13/14 February	Drive to Venice from Cardiff, Wales
15 February	Preparing GSCA container, mobilizing Sea Carousel
16 February	Lab Carousel experiment V42-E264 (11-day consolidation)
	Loading container on THETIS pontoon
17/20 February	Mobilizing pontoon at THETIS
18 February	Lab Carousel experiment V42-E46 (46-hour consolidation)
19 February	Lab Carousel experiment V42-E24 (24-hour consolidation)
20 February	Pontoon sails for site V50
21 February	Sea Carousel site V50, no Mini Flume experiment (broken winch)
22 February	Sea Carousel site V51, Mini Flume (F053a13.99d)
	Lab Carousel experiment V42-E72
	Recovered/redeployed S4/Cyclops1 at site V40
23 February	Moving pontoon to V40, strong winds prevent access to site
24 February	Sea Carousel sites V40 and V41, Mini Flume (F055a15.99d, F055a16.99d)
25 February	Sea Carousel site V30, Mini Flume (F056a11.99d)
26 February	Sea Carousel site V31, Mini Flume (F057b11.99d)
27 February	Sea Carousel site V20, Mini Flume (F058a10.99d)
27 February	Sea Carousel site V21, Mini Flume (F058a12.99d)
1 March	Sea Carousel site V80, Mini Flume (F060a11.99d)
2 March	Sea Carousel site V60, Mini Flume (F061a12.99d)
	Calibration of OBS on Mini Flume (low gain)
3 March	Sea Carousel site V61, Mini Flume (F062a11.99d)
4 March	Public lecture at THETIS, Sea Carousel site V70
	Mini Flume (F063a14.99d)
5 March	Sea Carousel site V71, Mini Flume (F064a11.99d)
6 March	Pontoon returns to THETIS, end of field program
6/7 March	Data analysis and demobilization of equipment
8 March	Recovery of S4/Cyclops1, packing equipment
	Recovery of Cyclops2 (Lido inlet)
9 March	Packing container

10 March	Container shipped to Canada
11 March	Public lecture at THETIS
12 March	End of survey

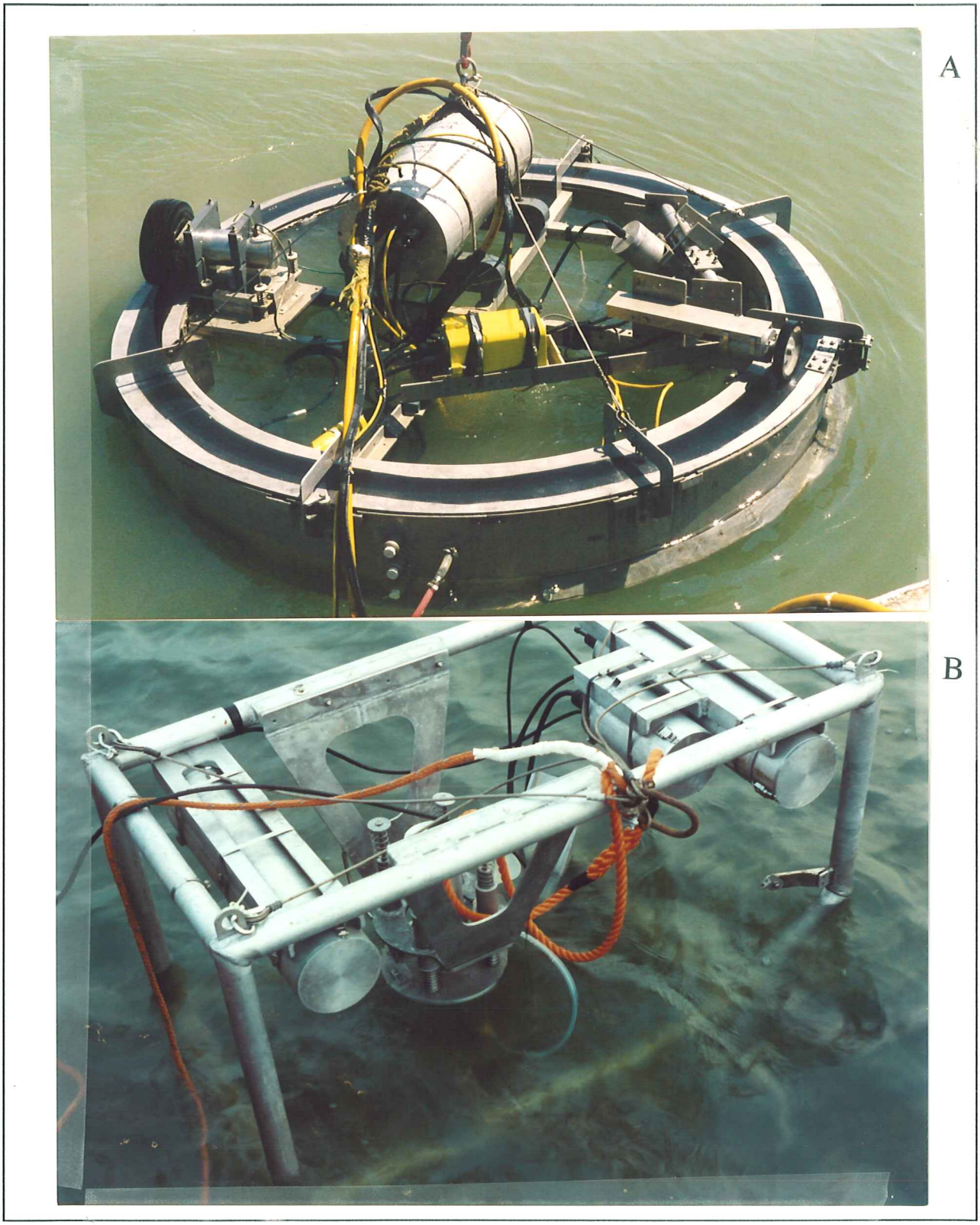

Plate 3.1.1: (A) The Sea Carousel benthic flume; (B) the Mini Flume system in operation.

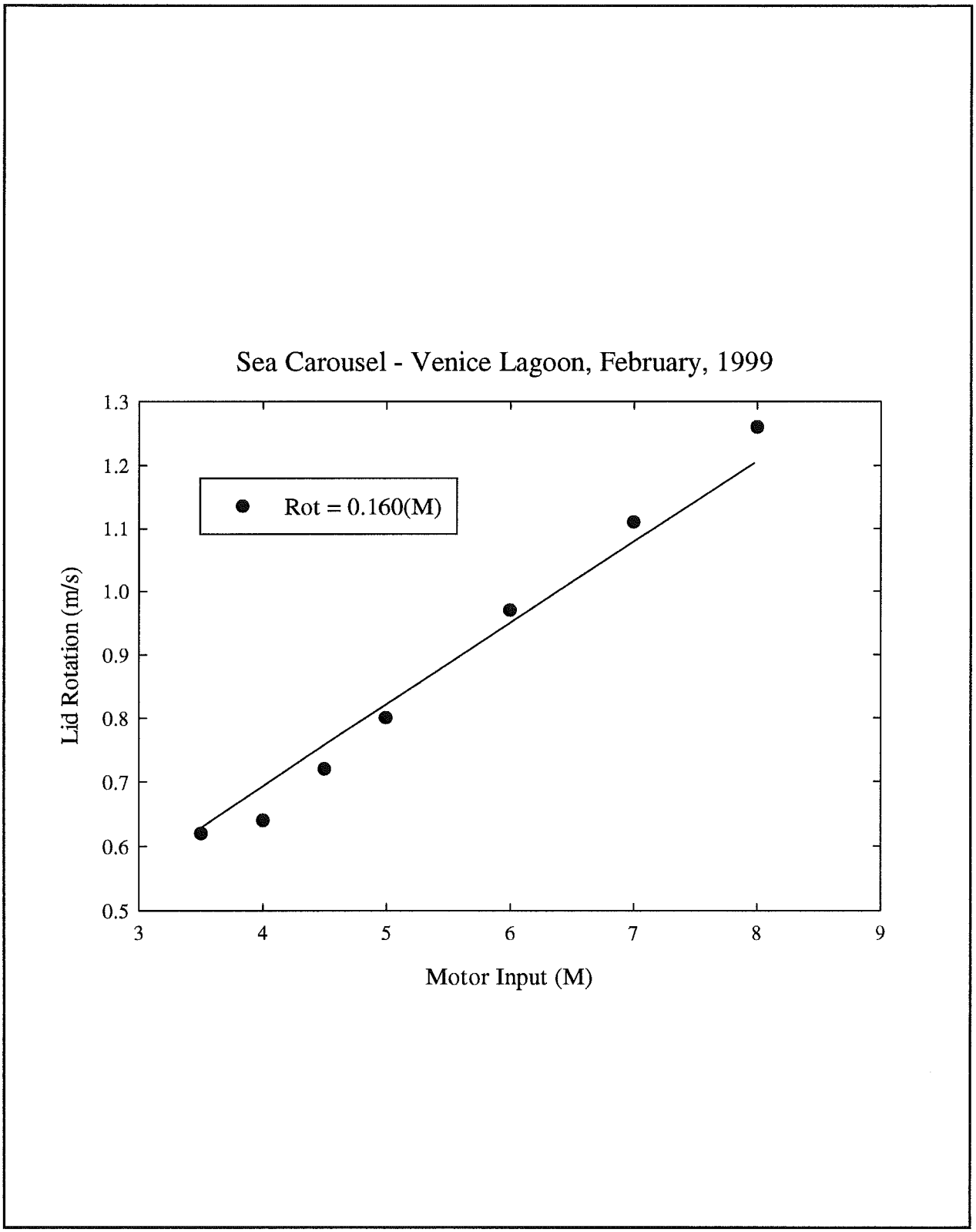

Figure 3.1.1 : The calibration of lid speed measured aboard the pontoon against motor input value loaded during Sea Carousel experiments. The results are strongly linear and show that the system is stable.

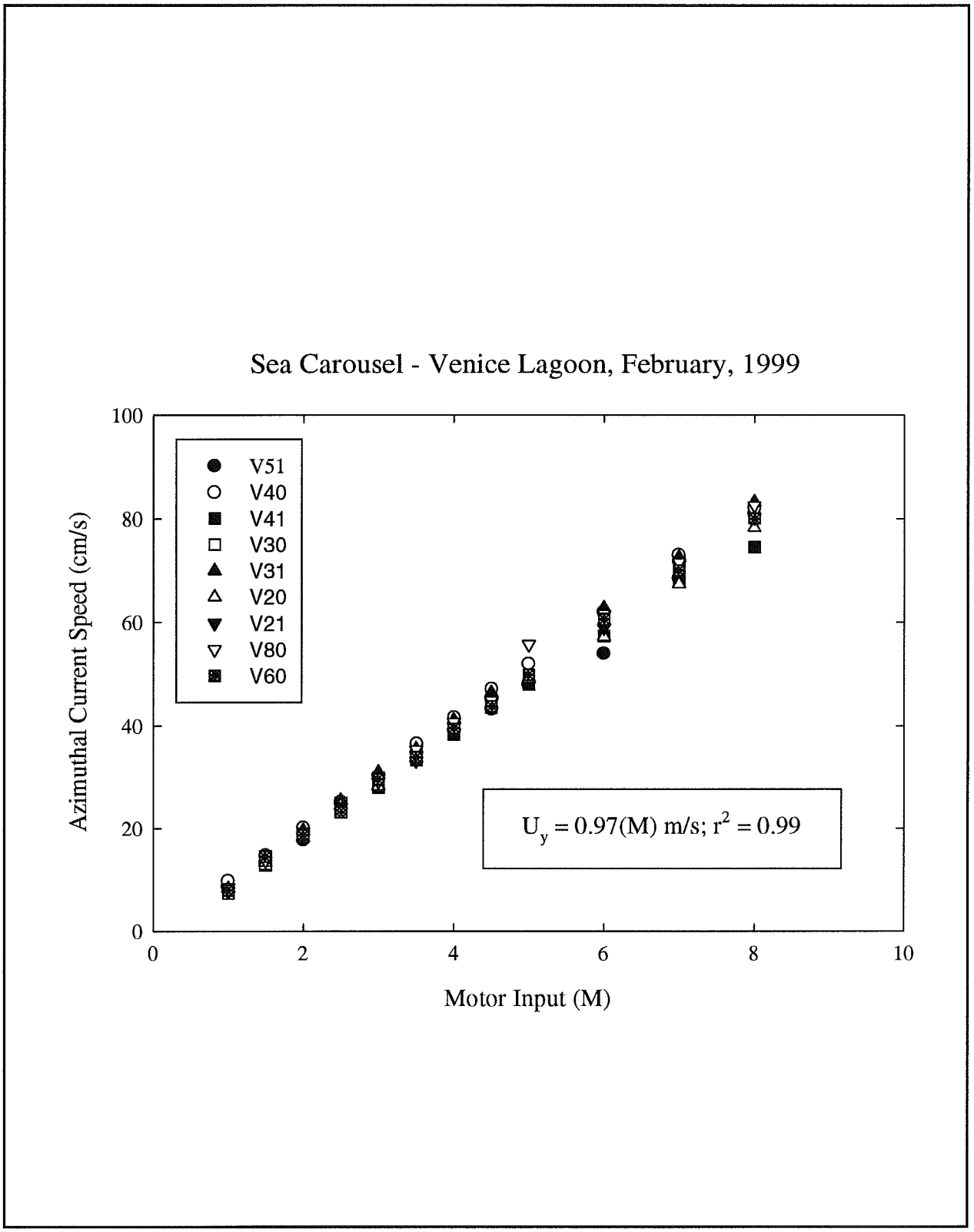

Figure 3.1.2 : The calibration of azimuthal current speed in Sea Carousel against drive motor input value. The results are strongly linear and show little variation from site to site.

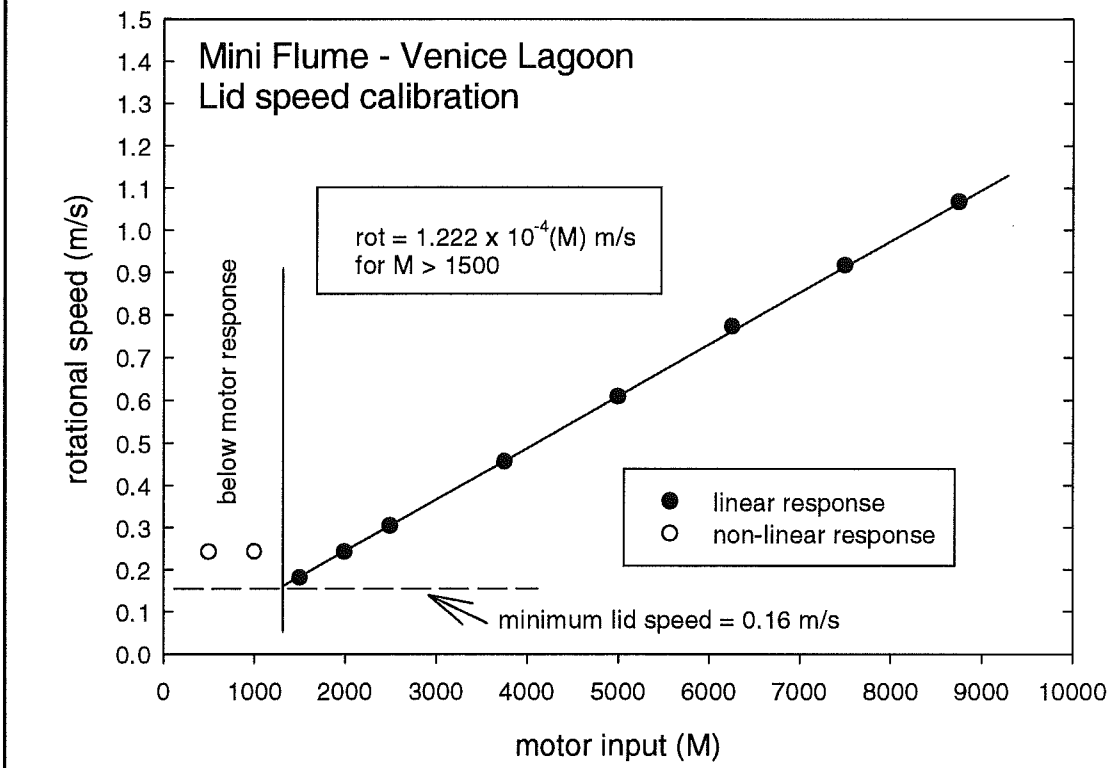

Figure 3.3.1 : The calibration of lid speed measured aboard the pontoon against motor input value loaded during the Mini Flume experiments.

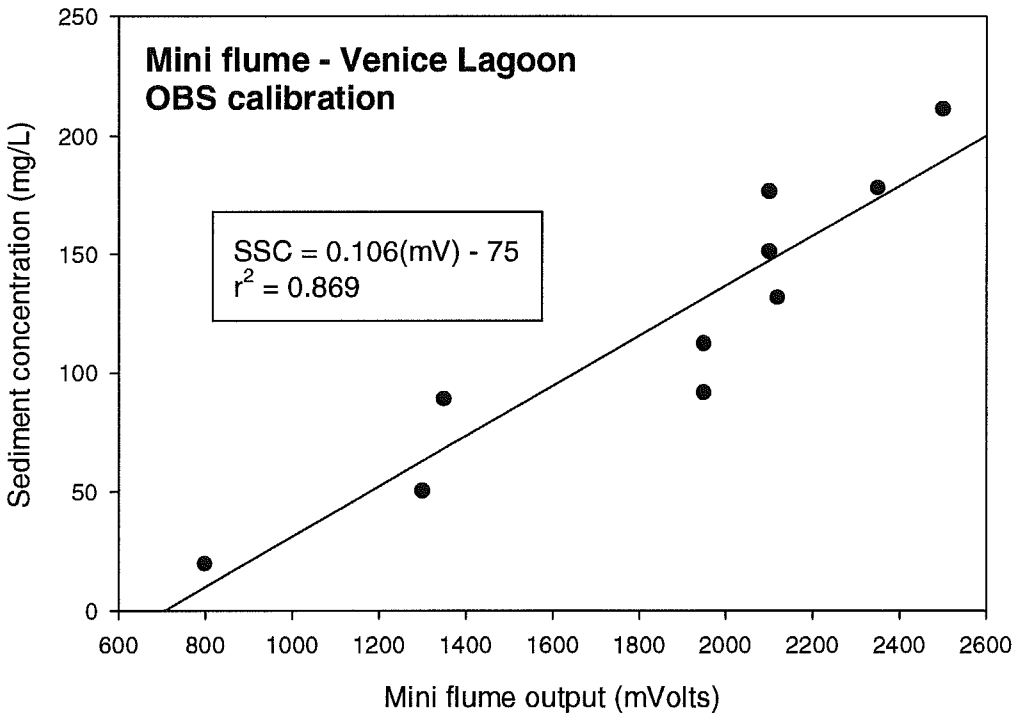

Figure 3.3.2 : The calibration of the Mini Flume OBS to suspended sediment concentration derived from samples pumped from the flume at each lid speed.

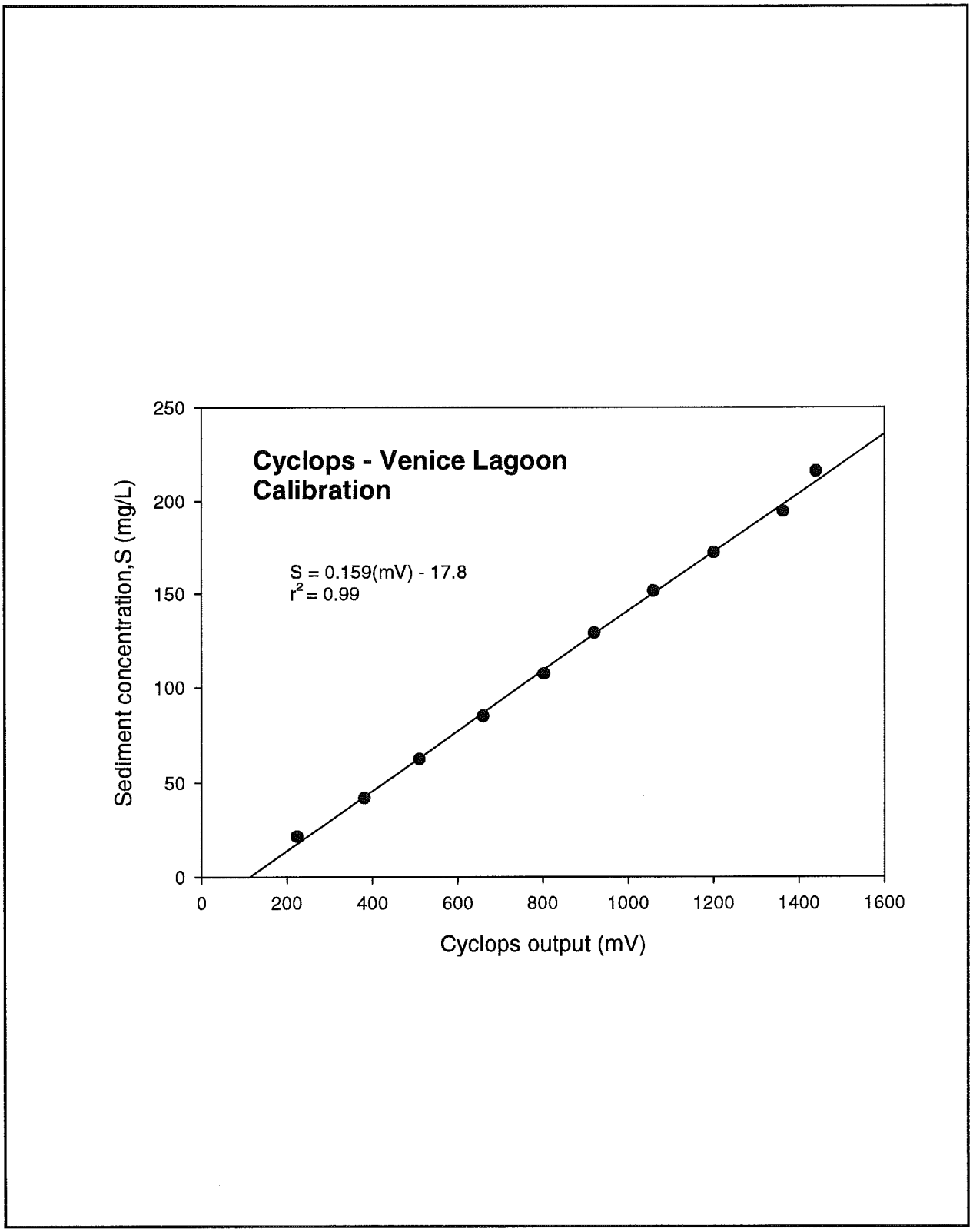

Figure 3.5.1 : The calibration of Cyclops sensors to suspended sediment concentration.

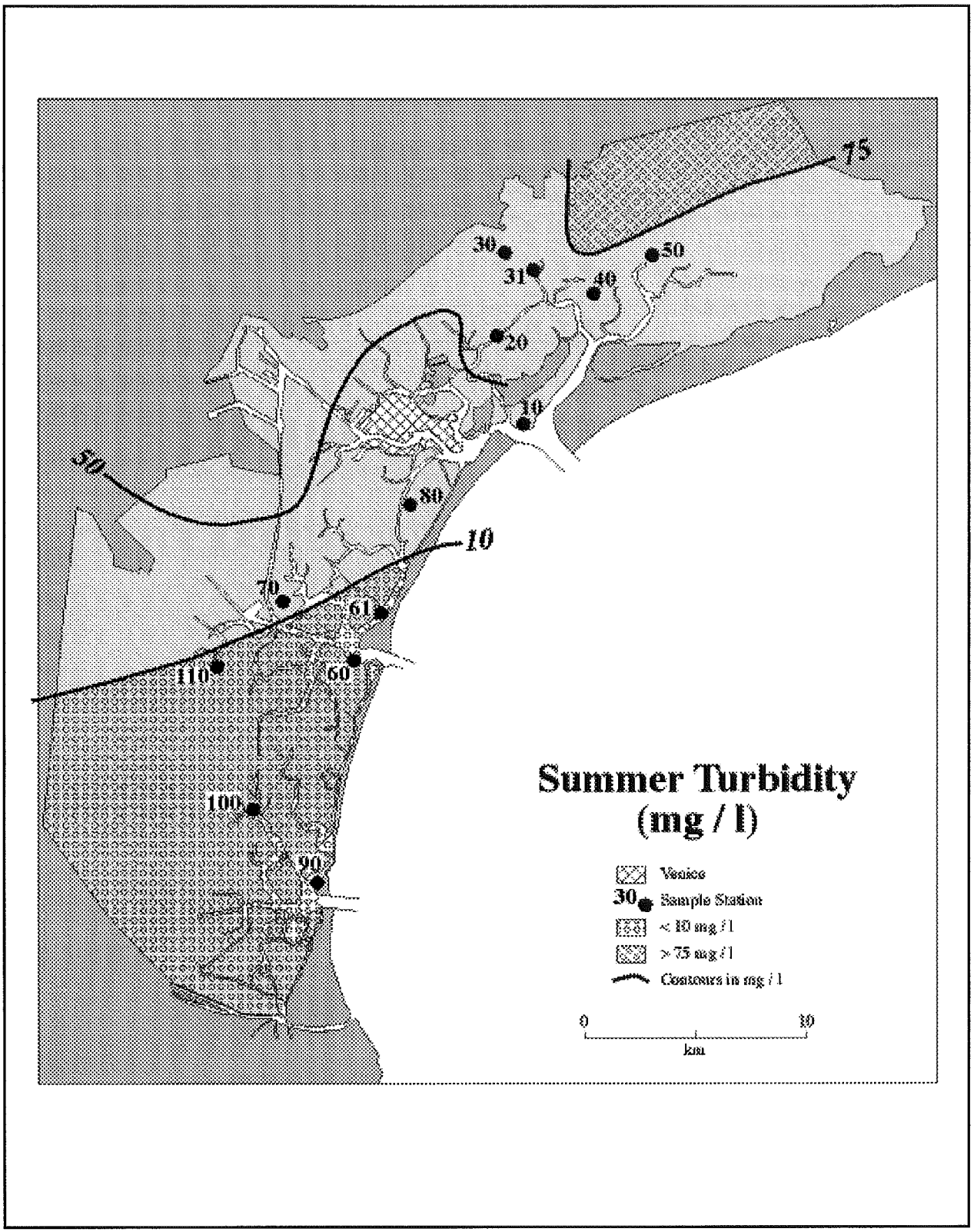

Figure 4.1.1.1: A summary of the near bed turbidity measured during the summer, 1999.

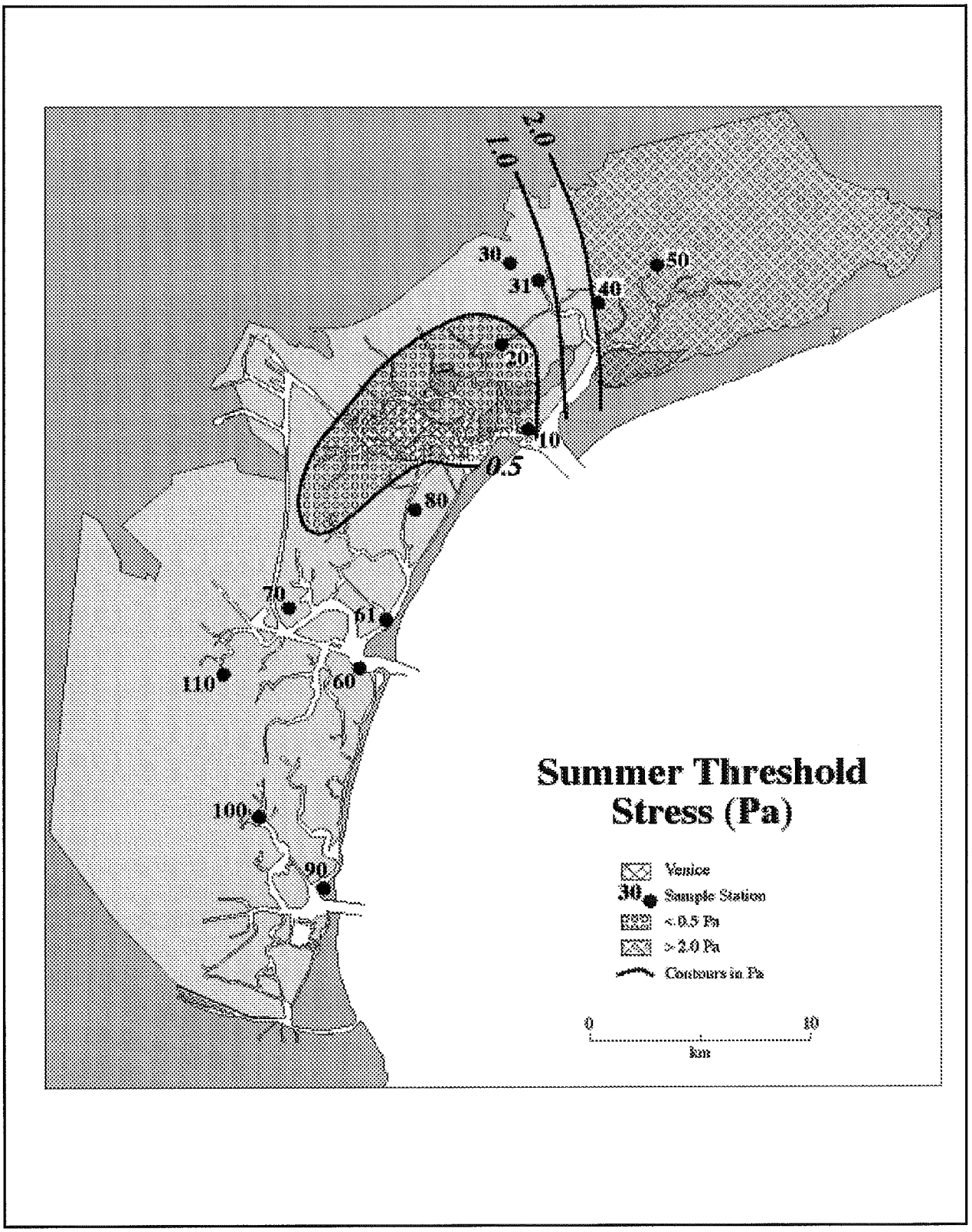

Figure 4.1.1.2: A summary of the erosion threshold for the summer, 1999.

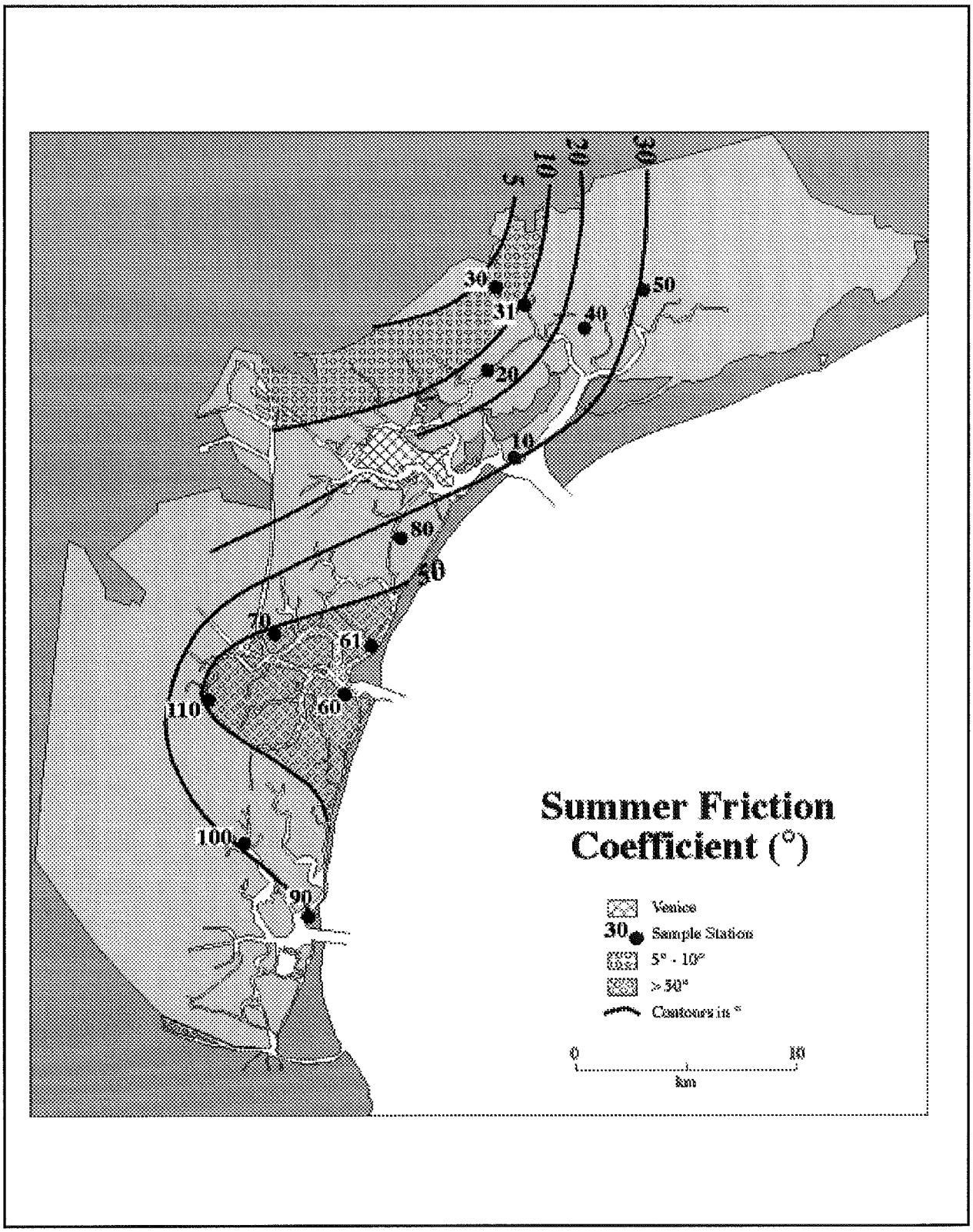

Figure 4.1.1.3: A summary of the friction coefficients measured during the summer, 1999.

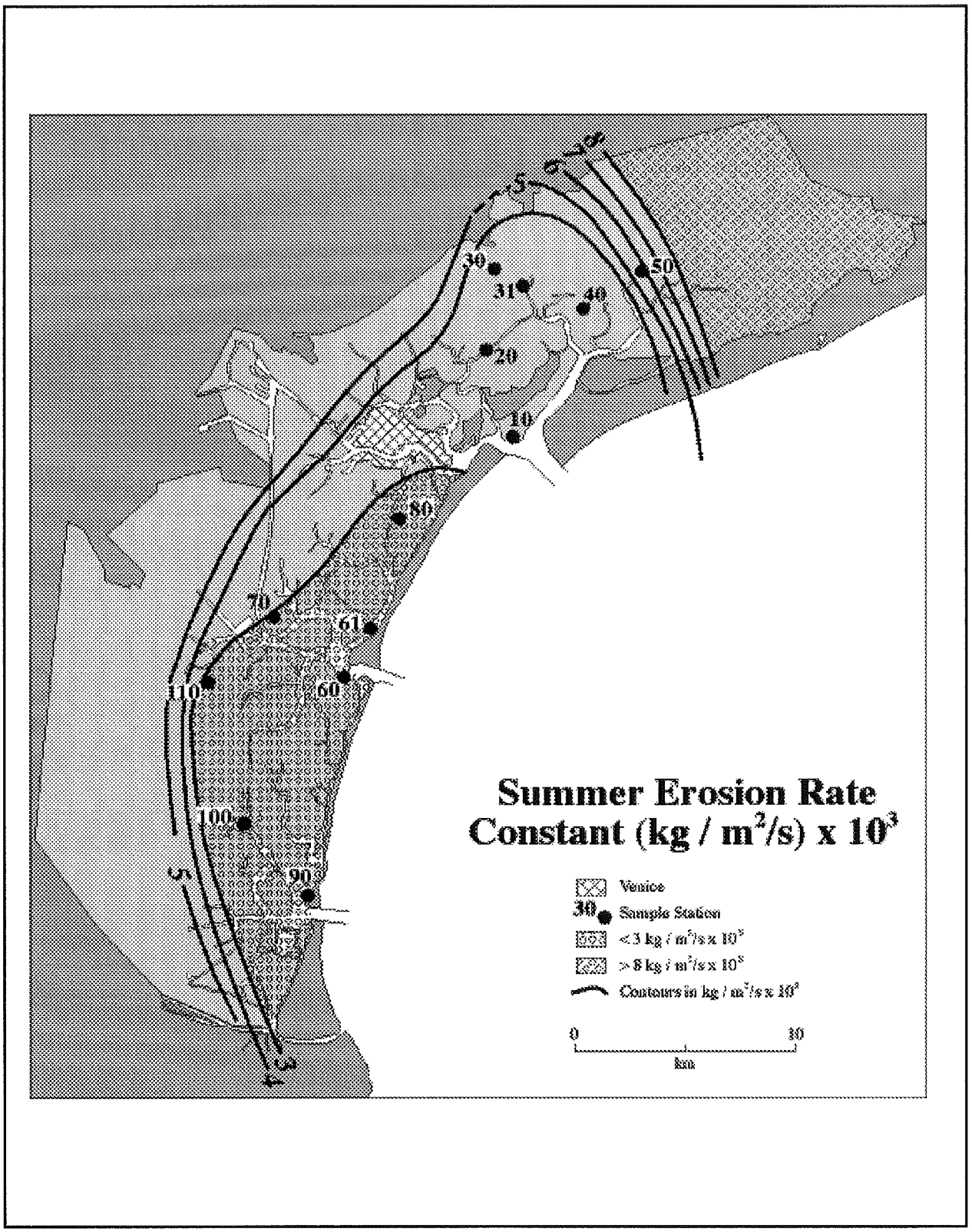

Figure 4.1.1.4: A summary of the erosion rate constant for the summer, 1999.

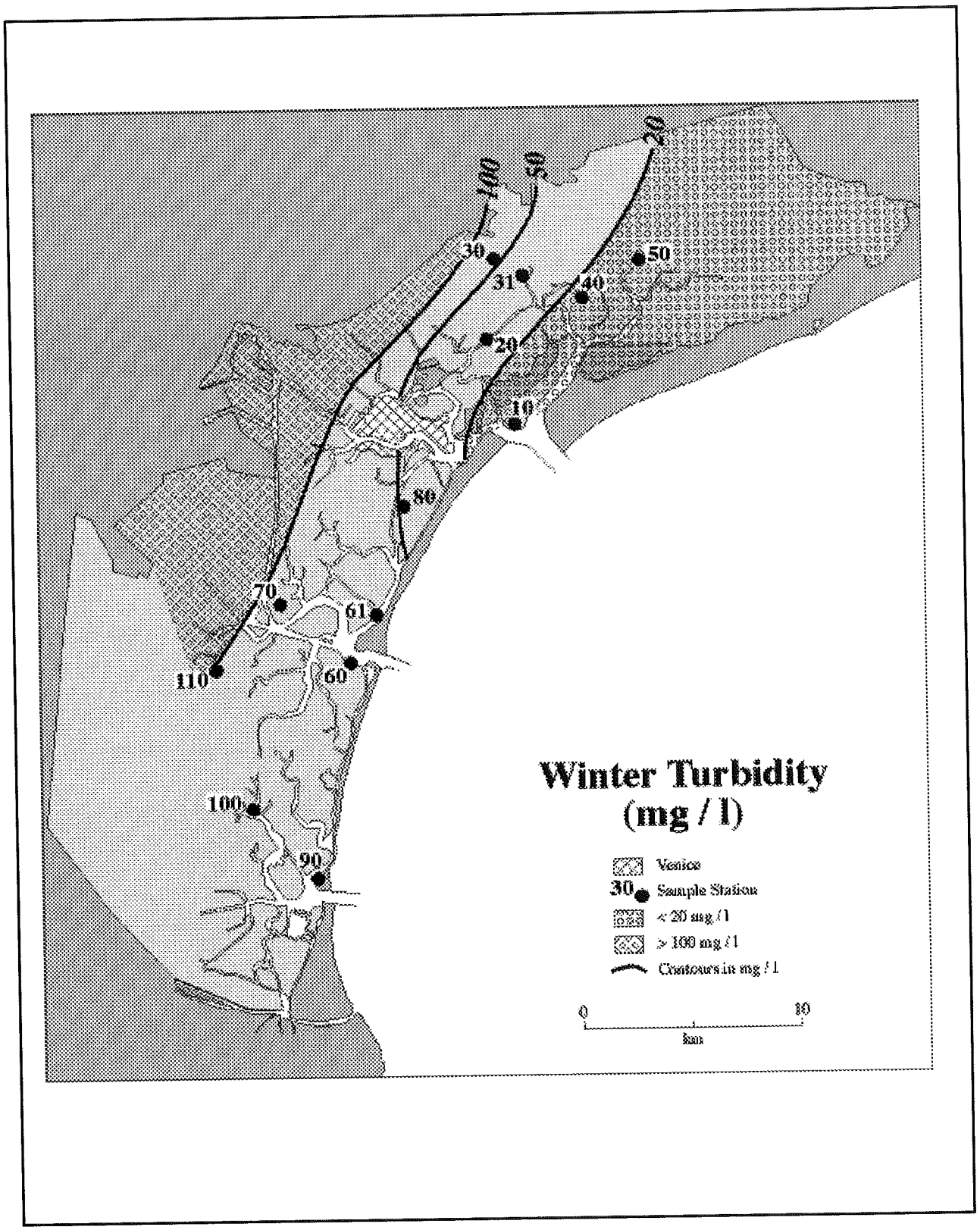

Figure 4.1.2.1: A summary of the near bed turbidity measured during February, 1999.

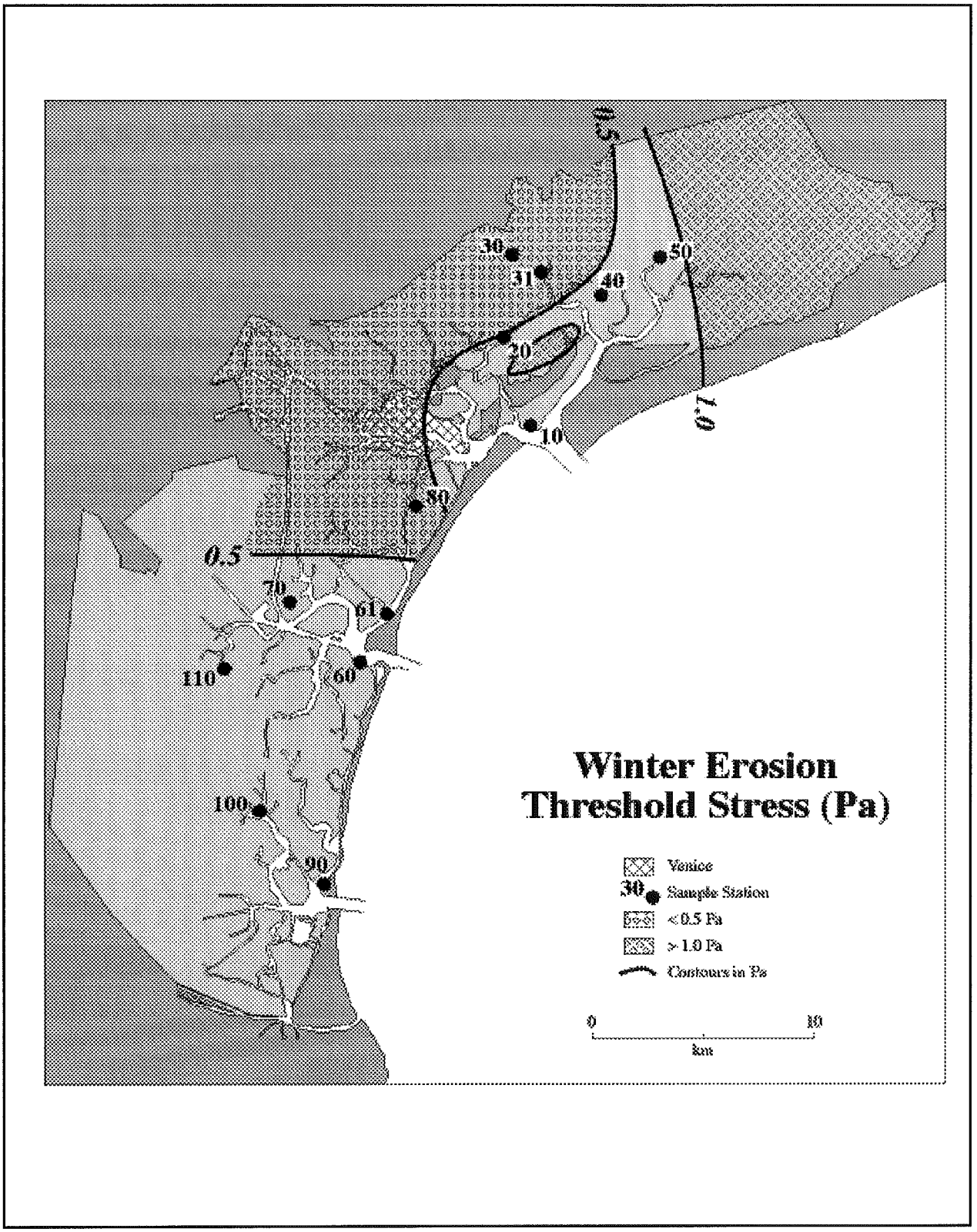

Figure 4.1.2.2: A summery of the erosion threshold measured during February, 1999.

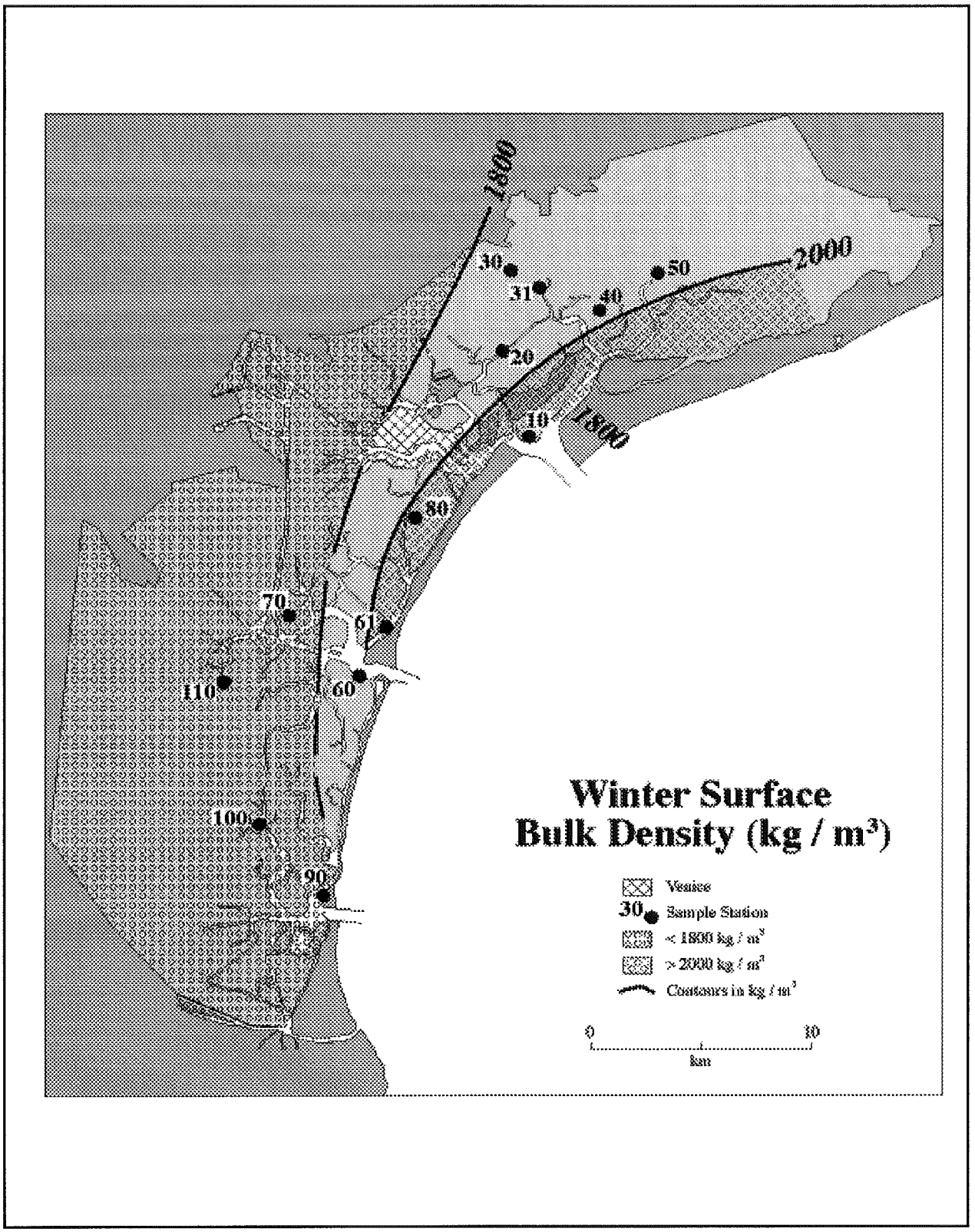

Figure 4.1.2.3: A summary of the bulk density measured during February, 1999.

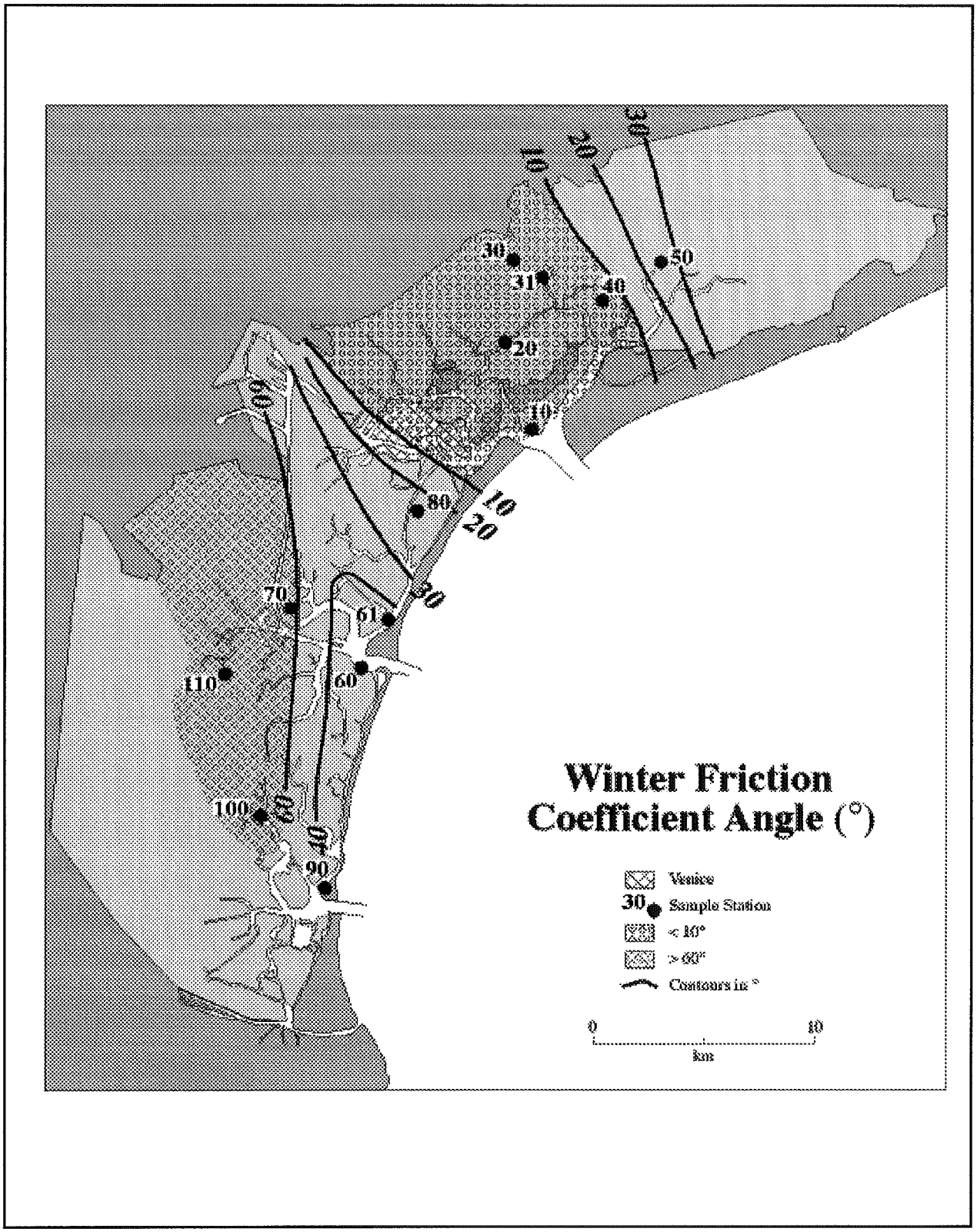

Figure 4.1.2.4: A summary of the friction coefficients measured during February, 1999.

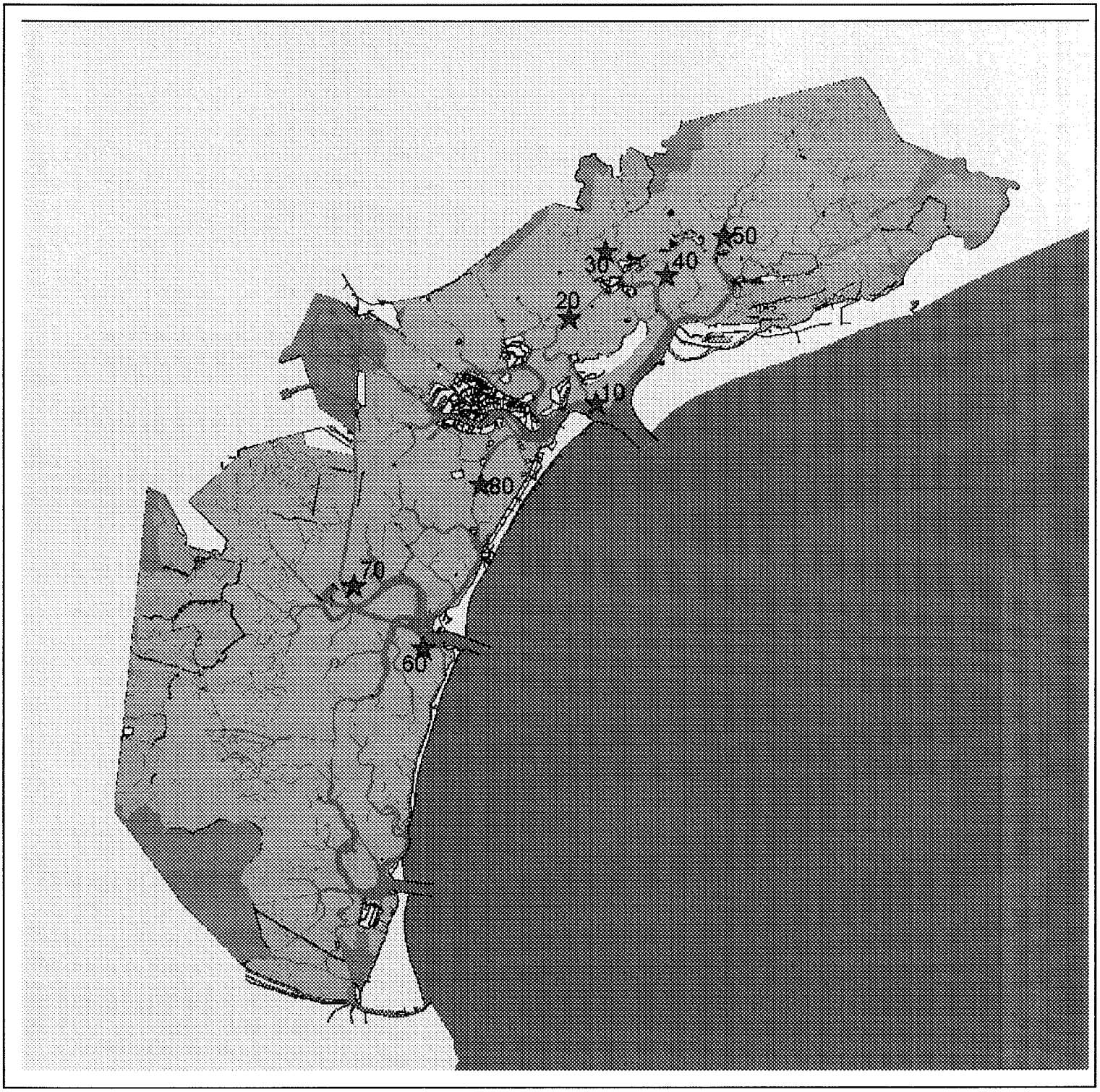

Figure 4.1.1: The site locations occupied during the winter survey. Two replicates were carried out at each site. The series of analyses were the same as those undertaken during the summer survey in order to compare results collected in mid-summer and mid-winter.

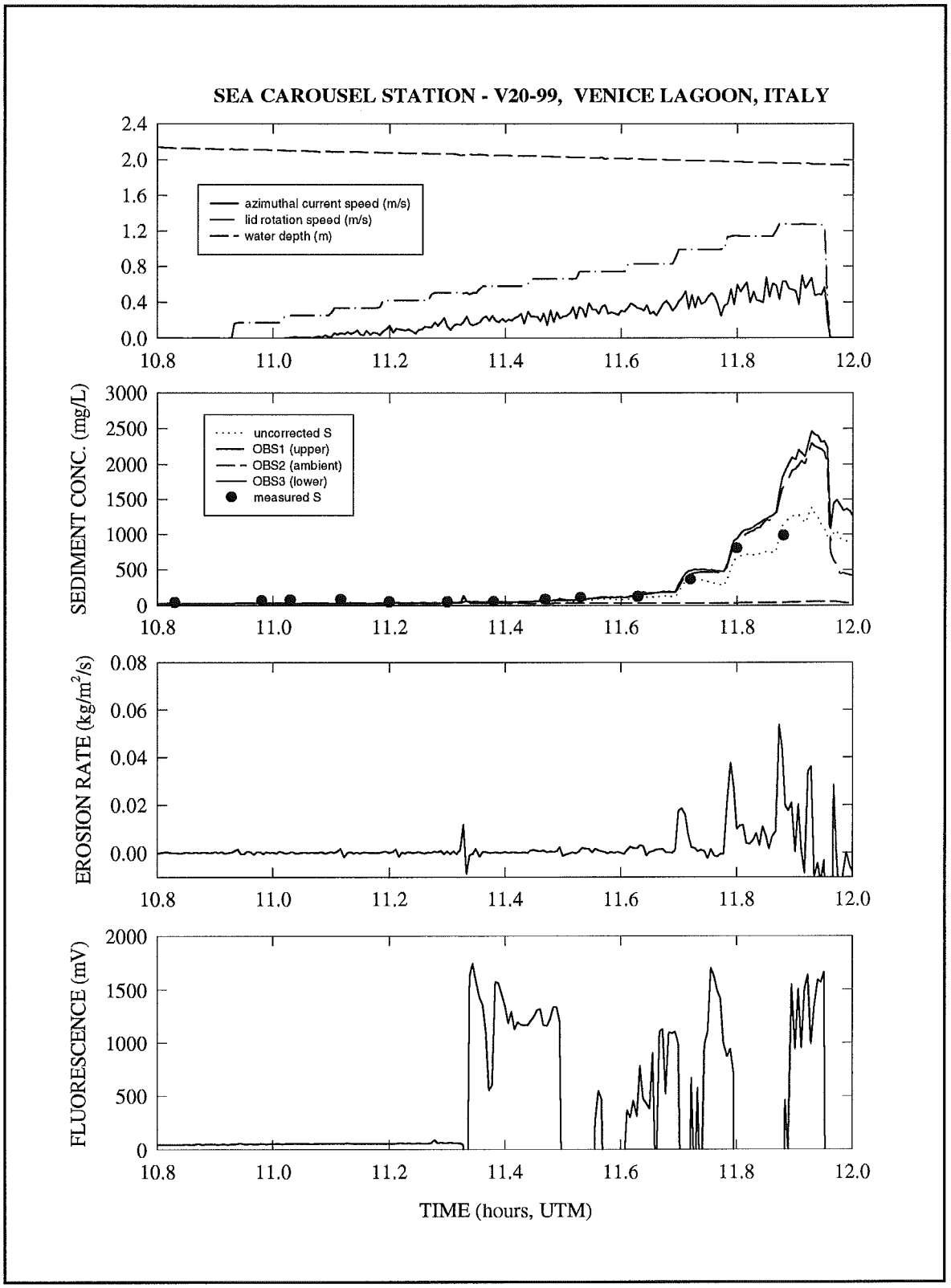

Figure 4.1.2 The Sea Carousel time-series from site V20 (S. Giacomo).

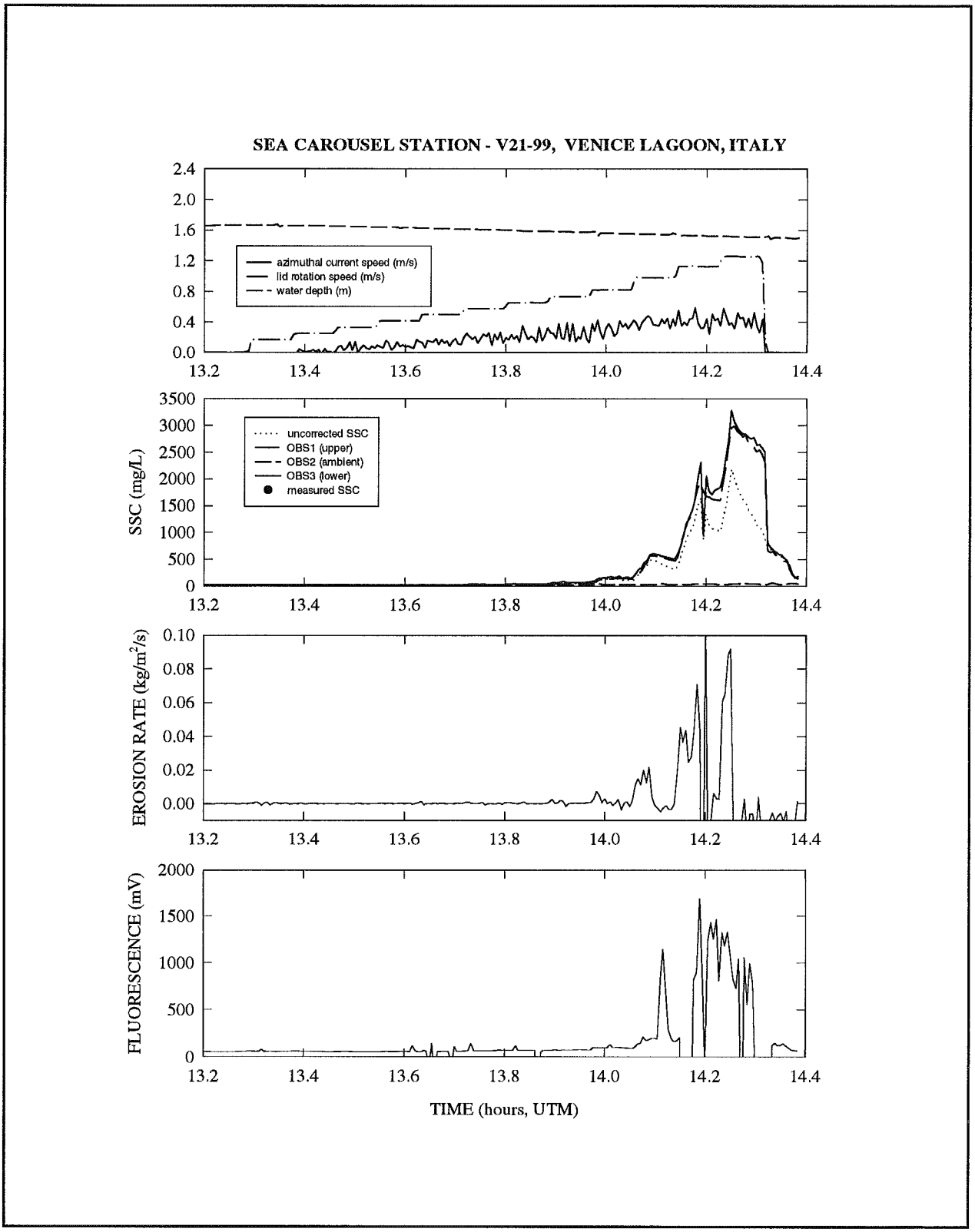

Figure 4.1.3 : The Sea Carousel time-series from site V21 (S. Giacomo)

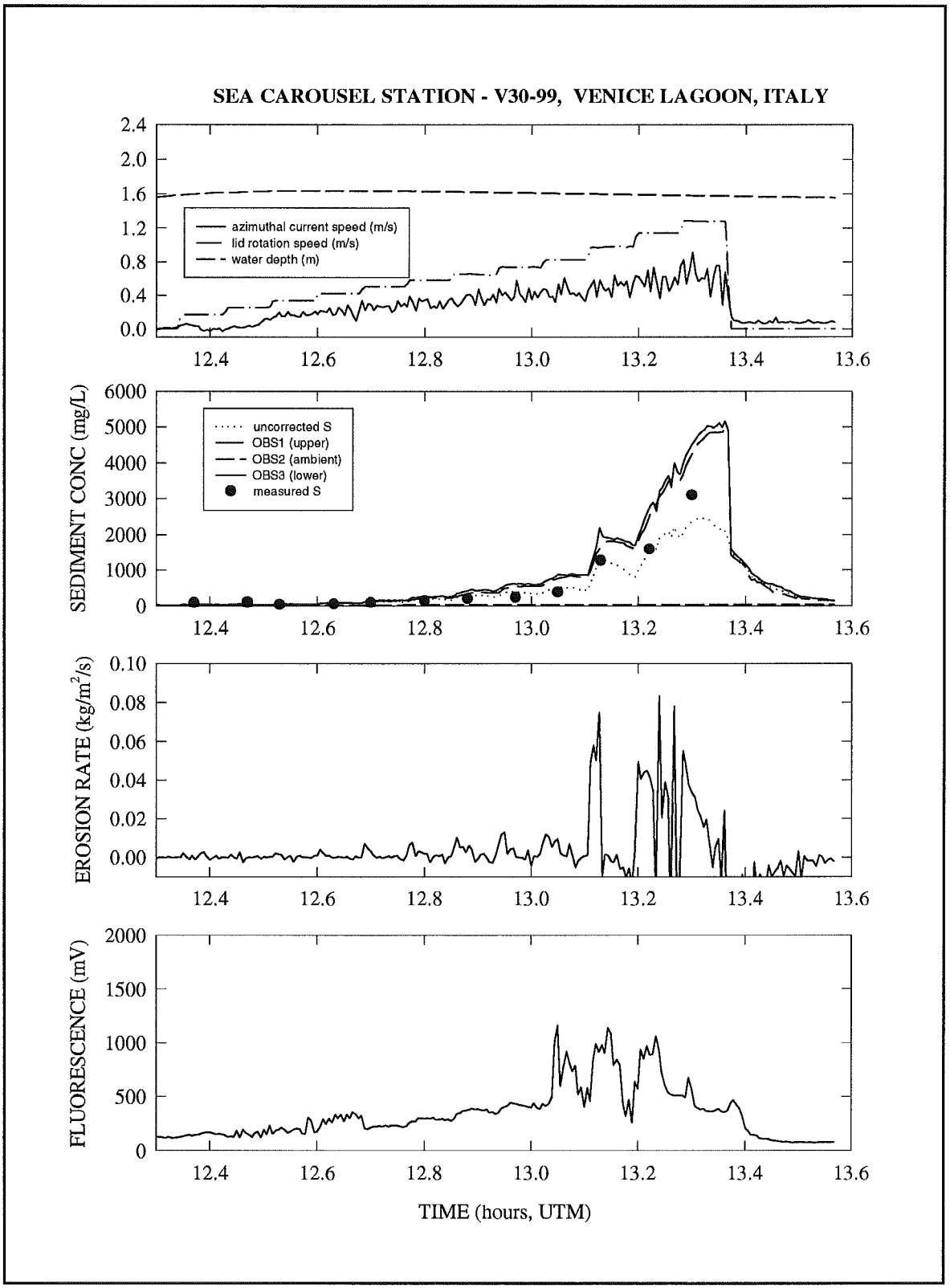

Figure 4.1.4 The Sea Carousel time-series from site V30 (Cona).

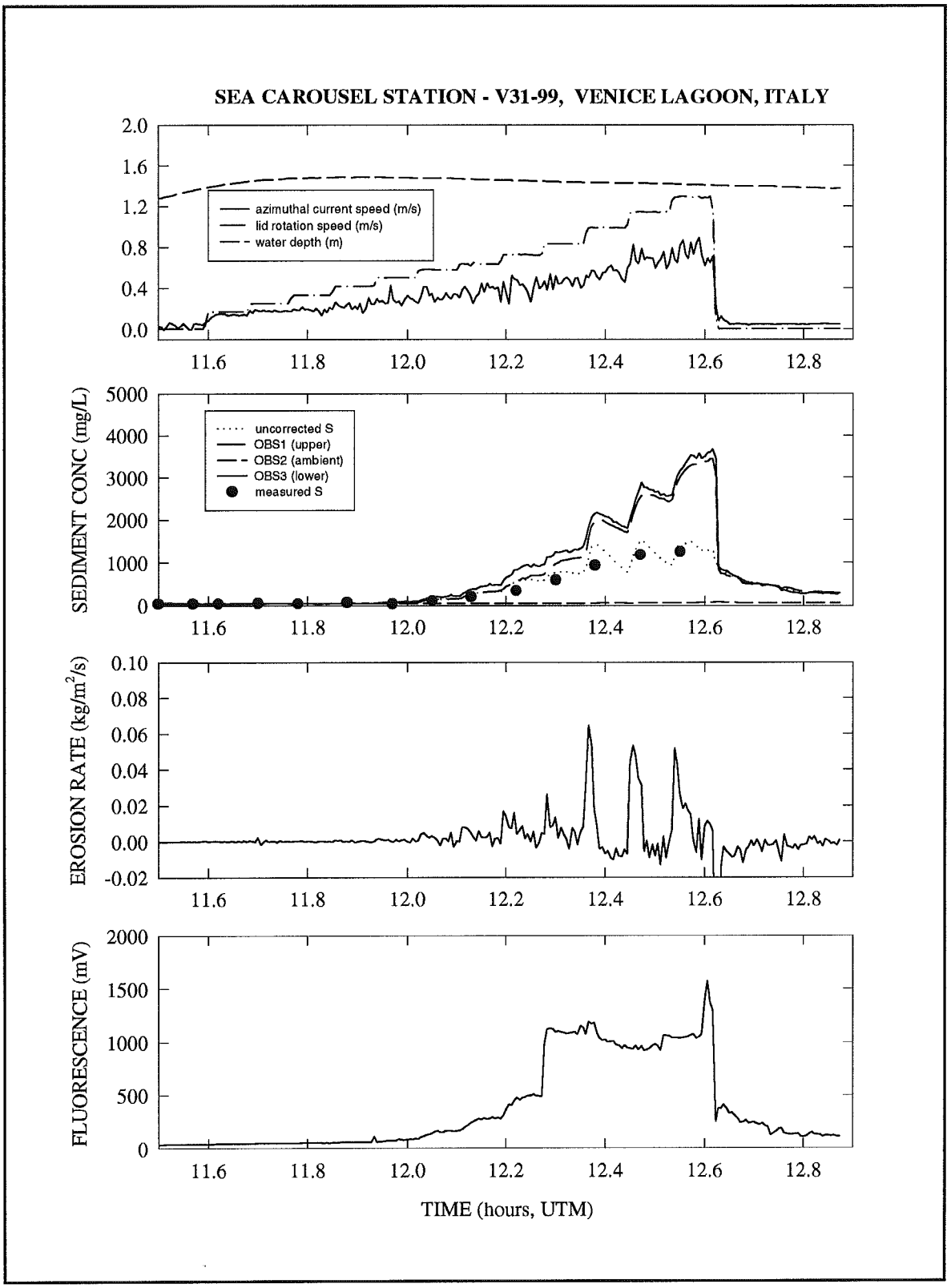

Figure 4.1.5 The Sea Carousel time-series from site V31 (Cona).

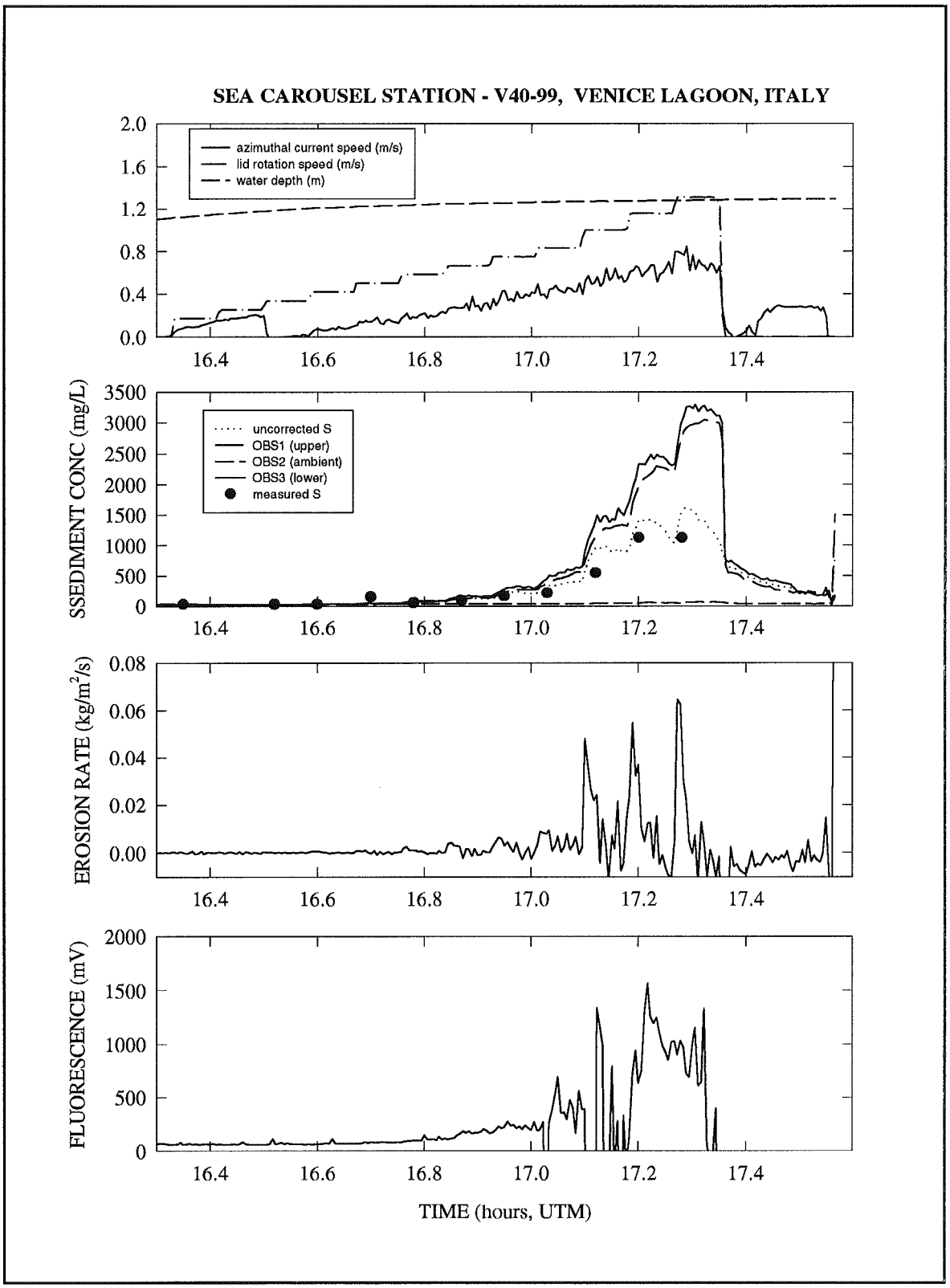

Figure 4.1.6 The Sea Carousel time-series from site V40 (Centrega).

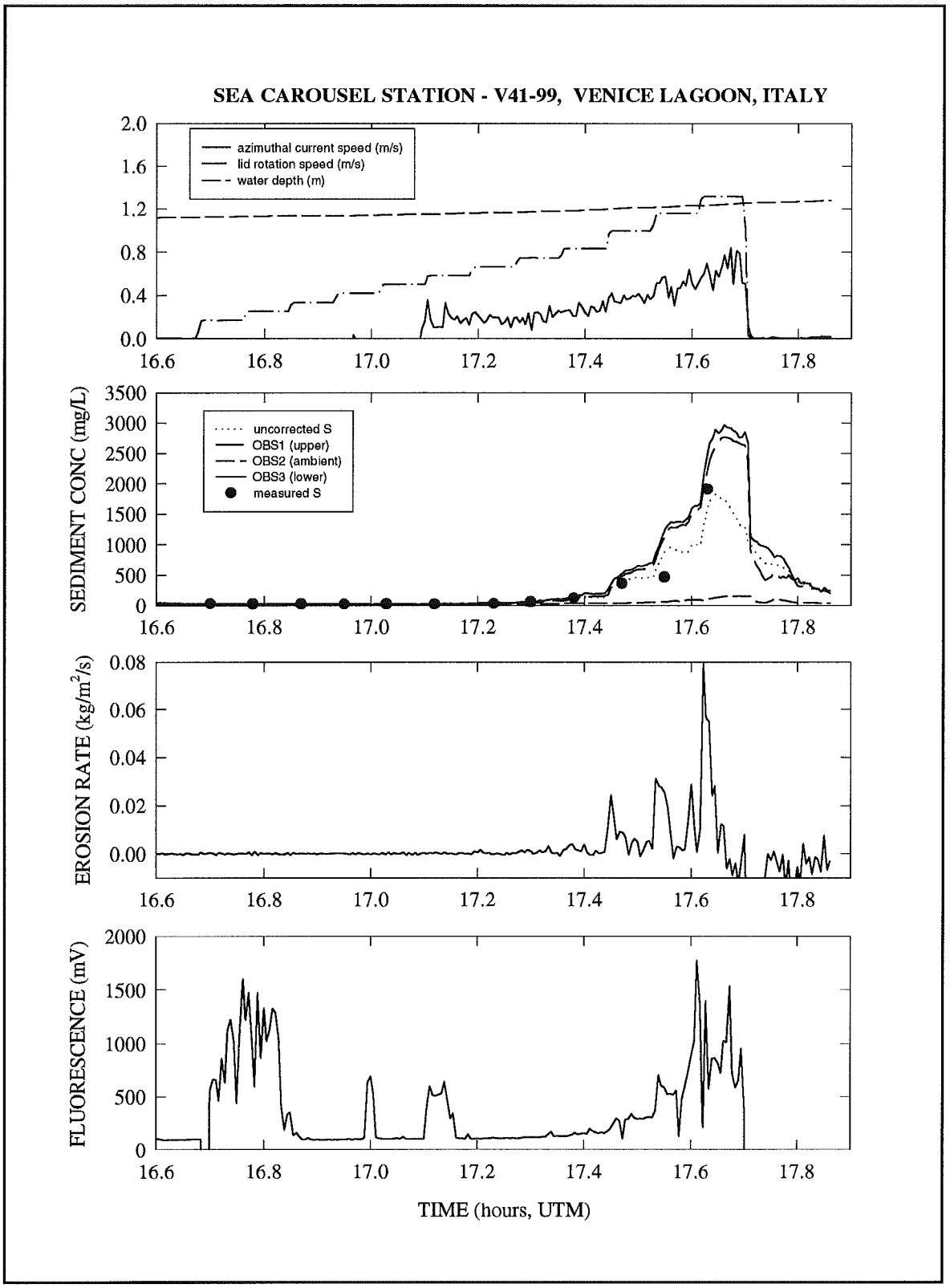

Figure 4.1.7 The Sea Carousel time-series from site V41 (Centrega)

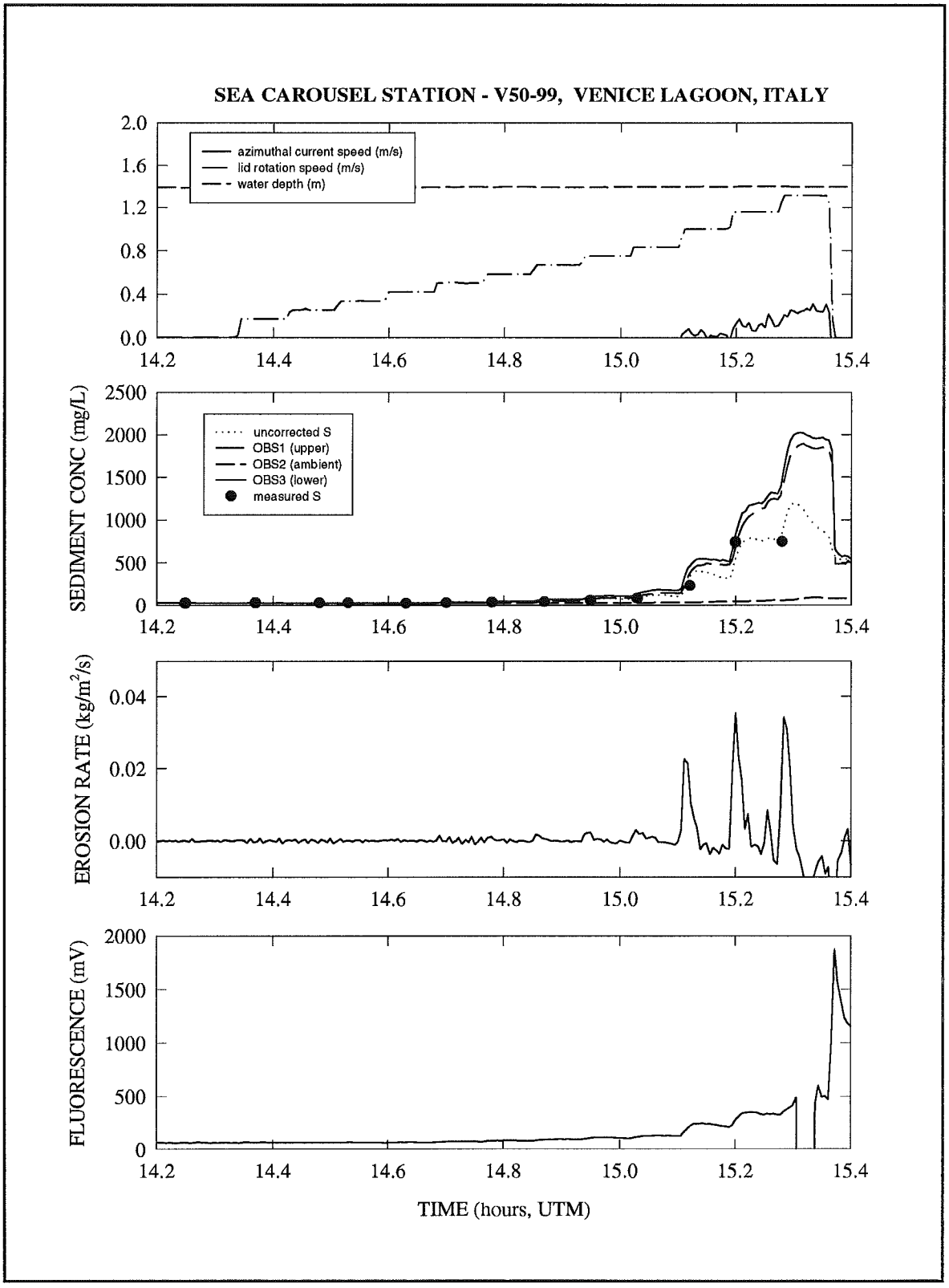

Figure 4.1.8 The Sea Carousel time-series from site V50 (Saline).

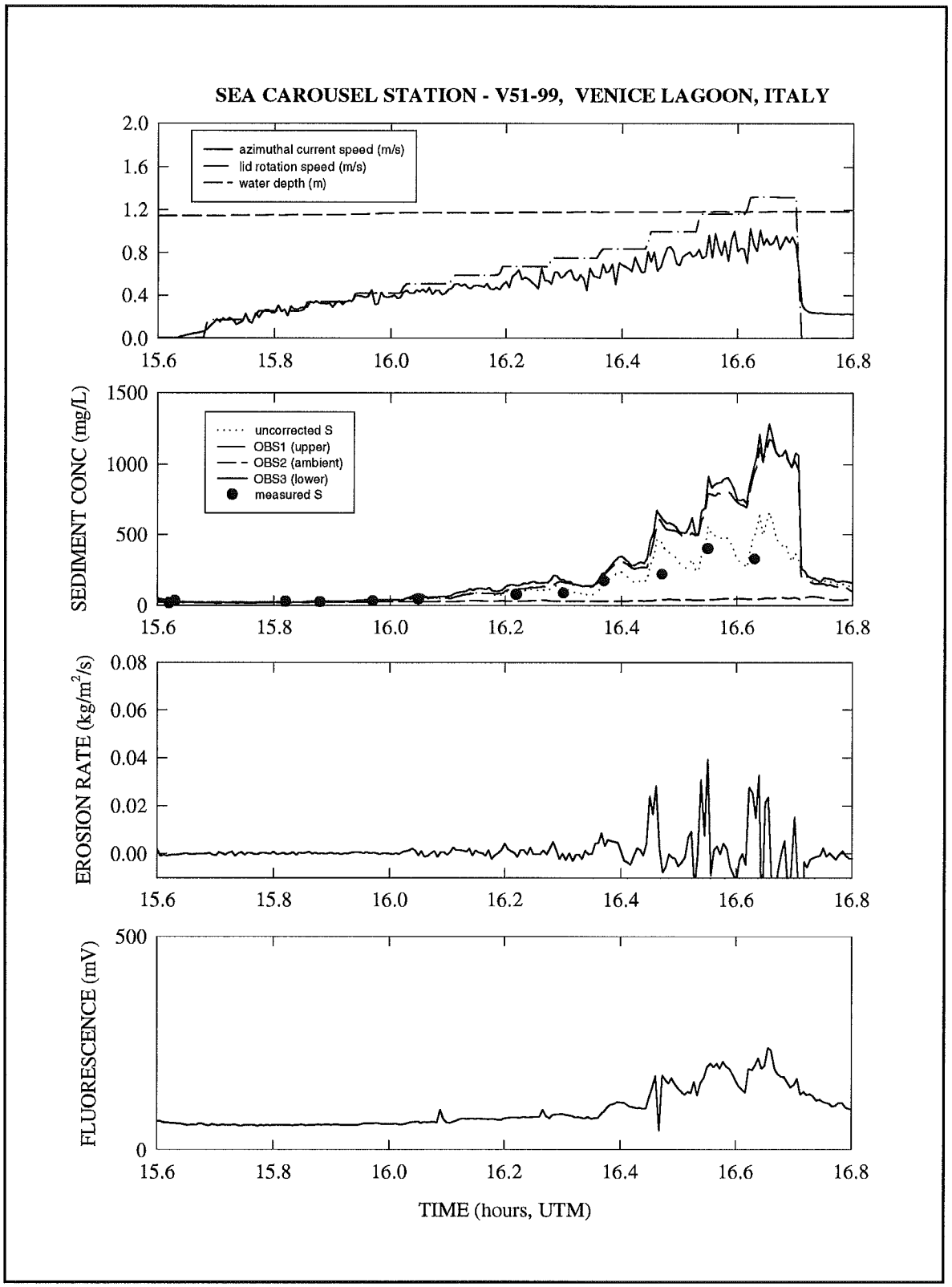

Figure 4.1.9 The Sea Carousel time-series from site V51 (Saline).

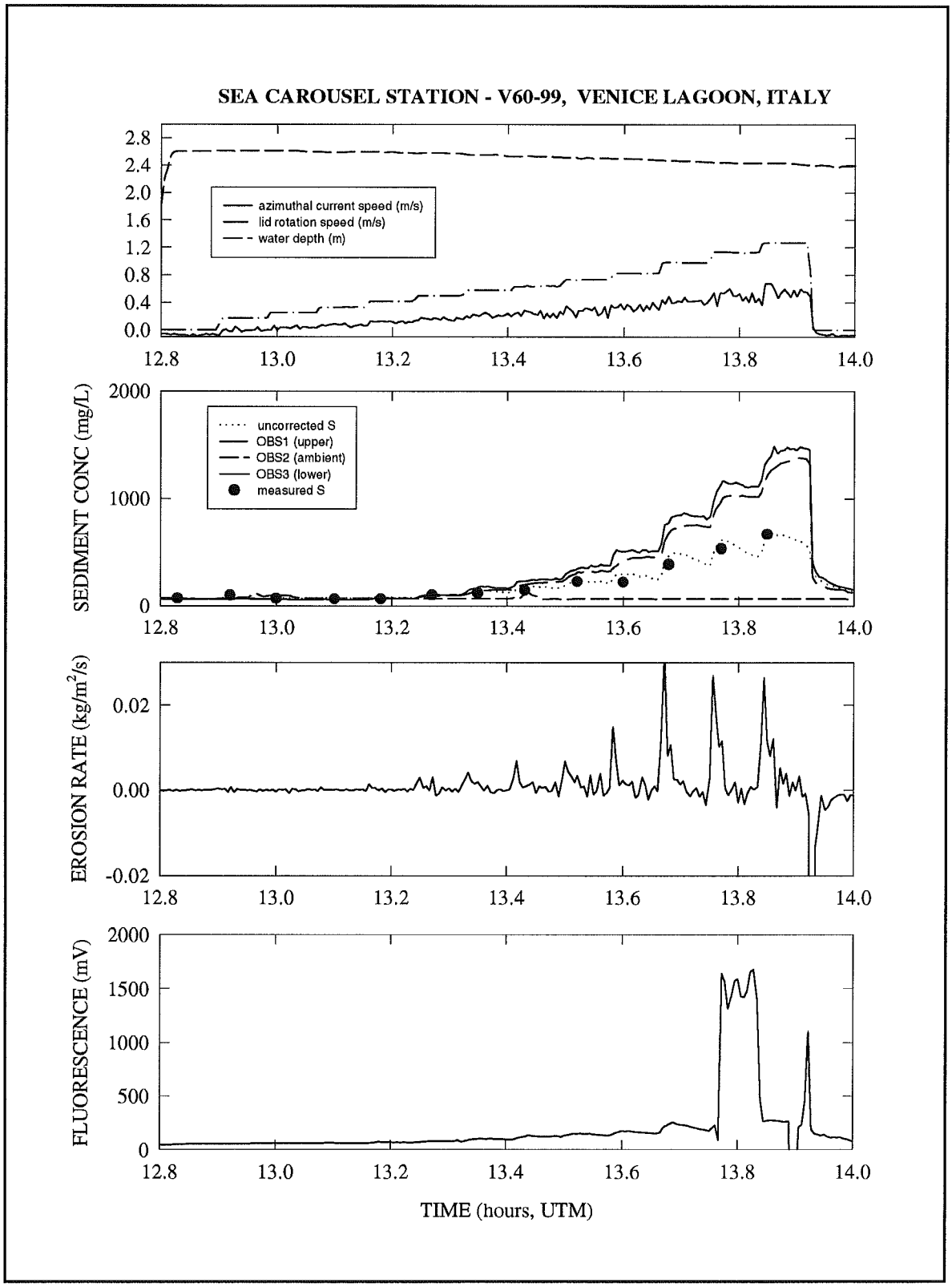

Figure 4.1.10 The Sea Carousel time-series from site V60 (S. Maria del Mare).

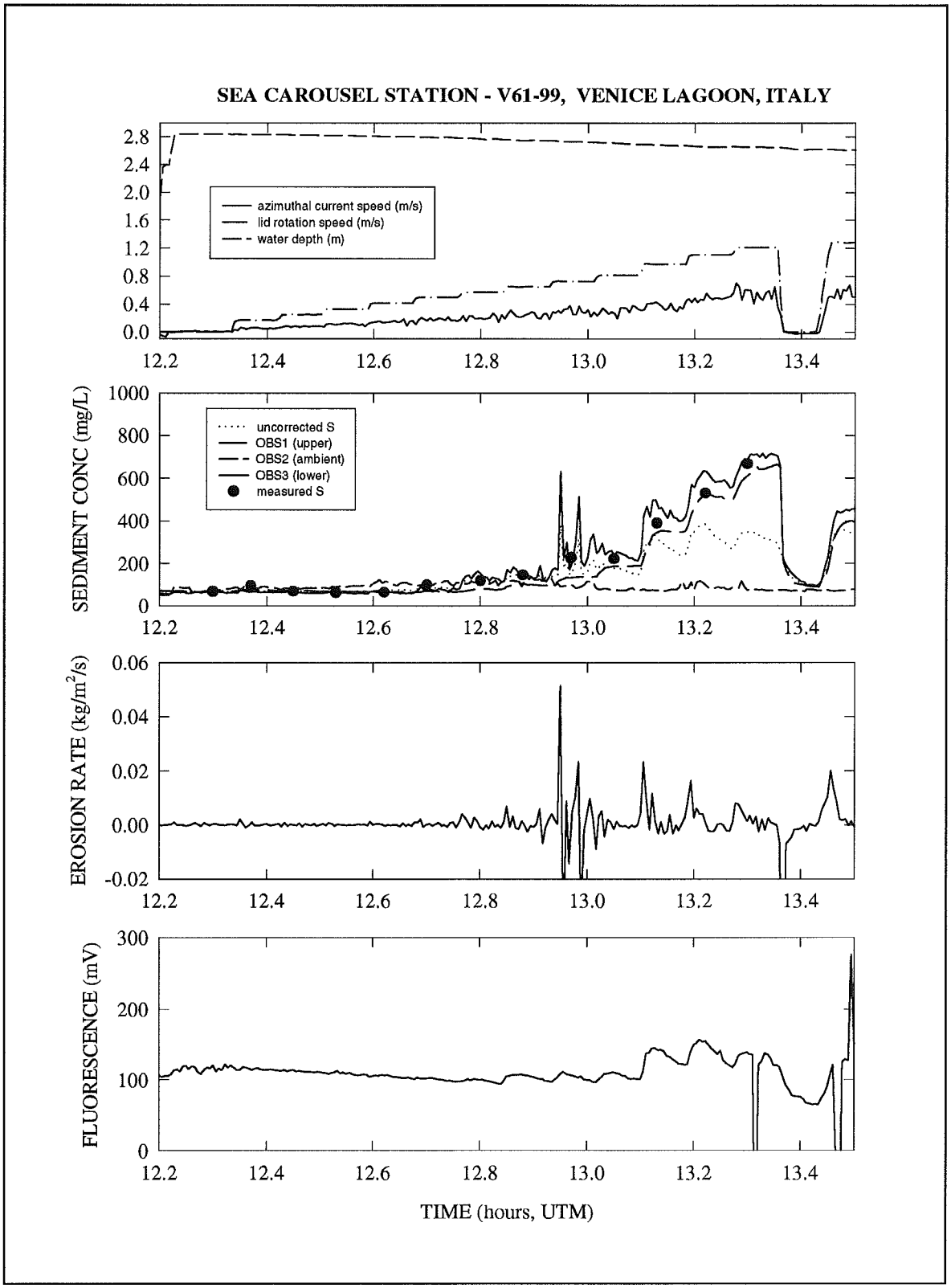

Figure 4.1.11 The Sea Carousel time-series from site V61 (S. Maria del Mare).

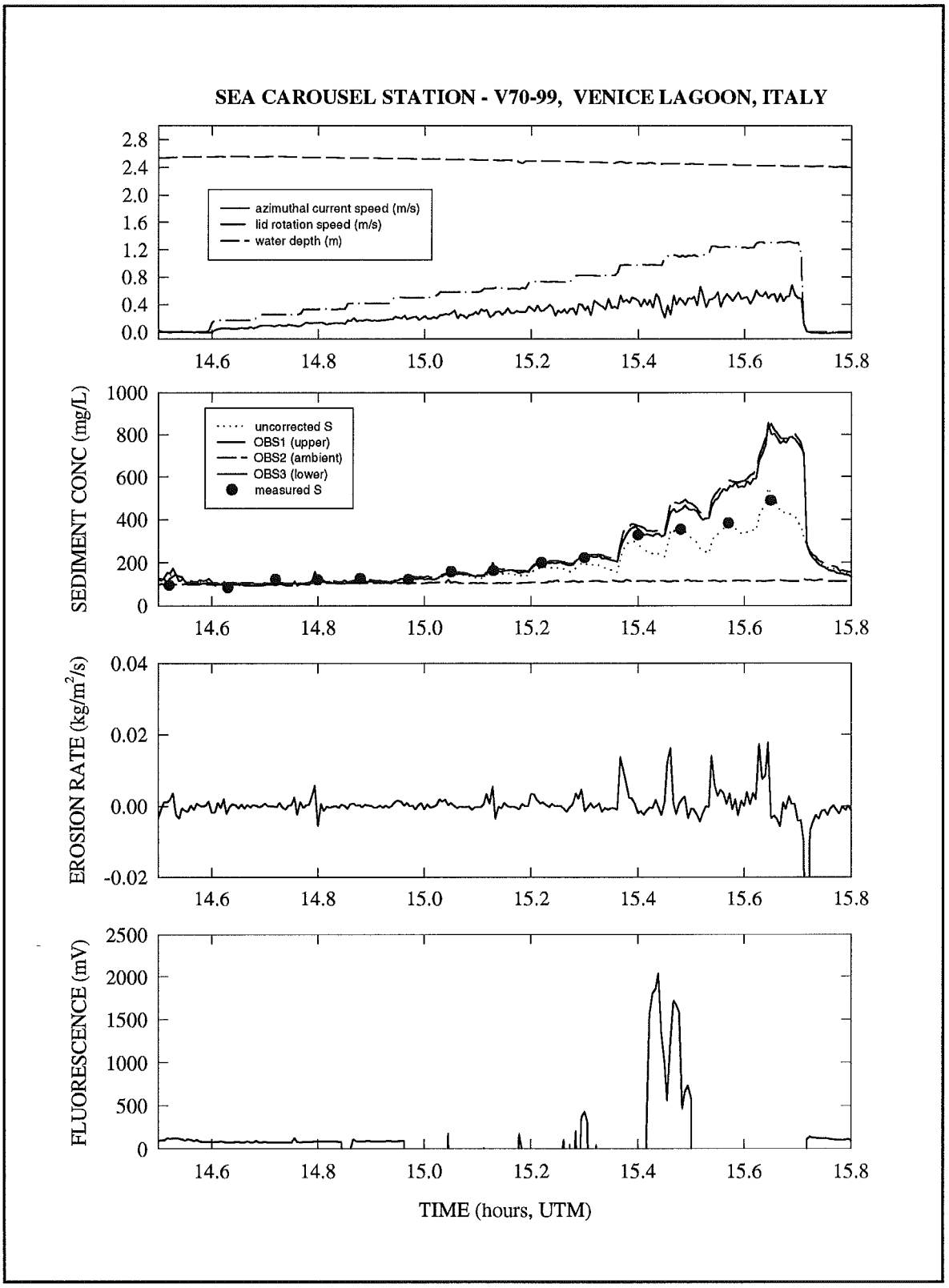

Figure 4.1.12 The Sea Carousel time-series from site V70 (S. Leonardo).

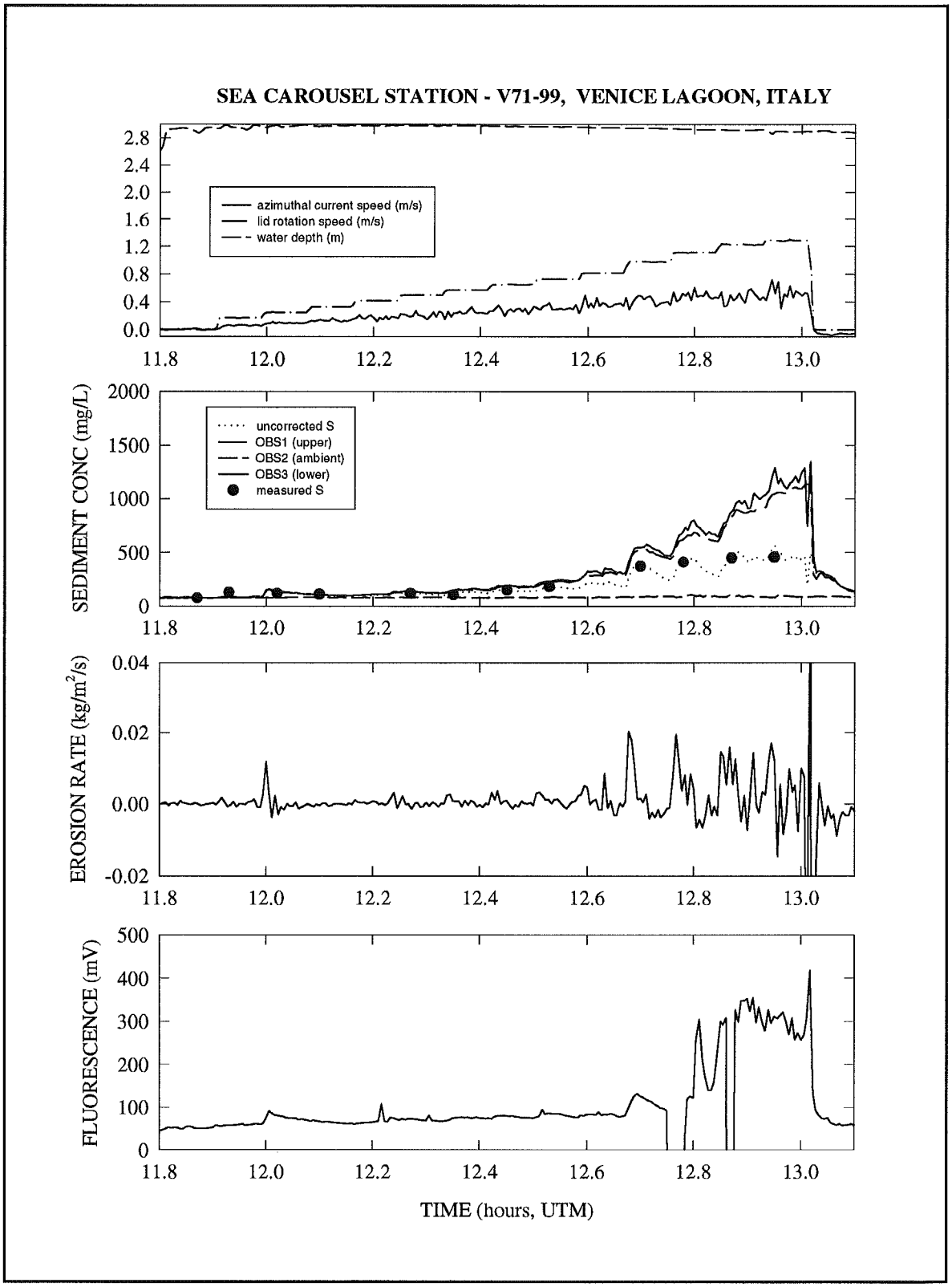

Figure 4.1.13 : The Sea Carousel time-series from site V71 (S. Leonardo).

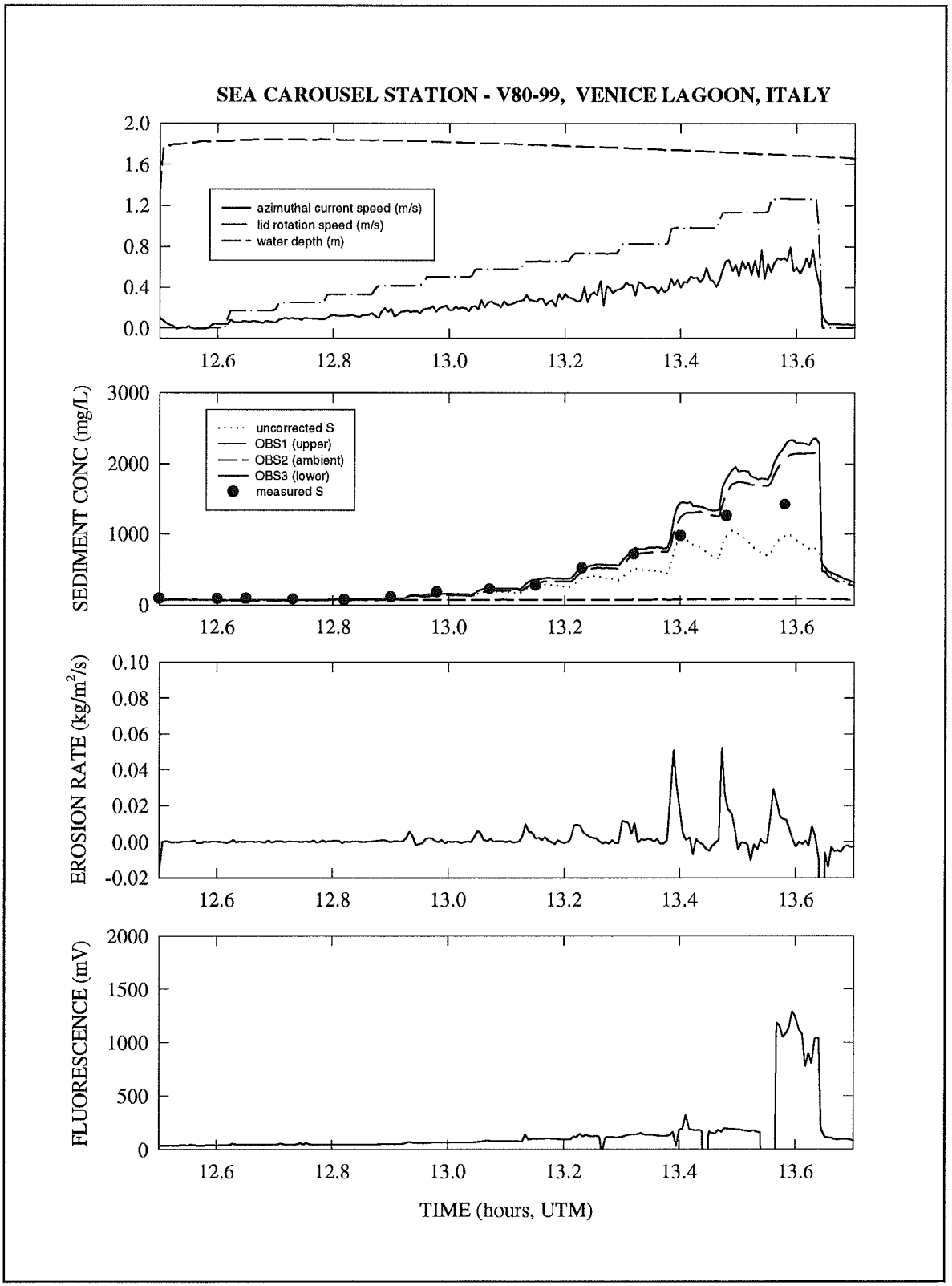

Figure 4.1.14 The Sea Carousel time-series from site V80 (Santo Spirito).

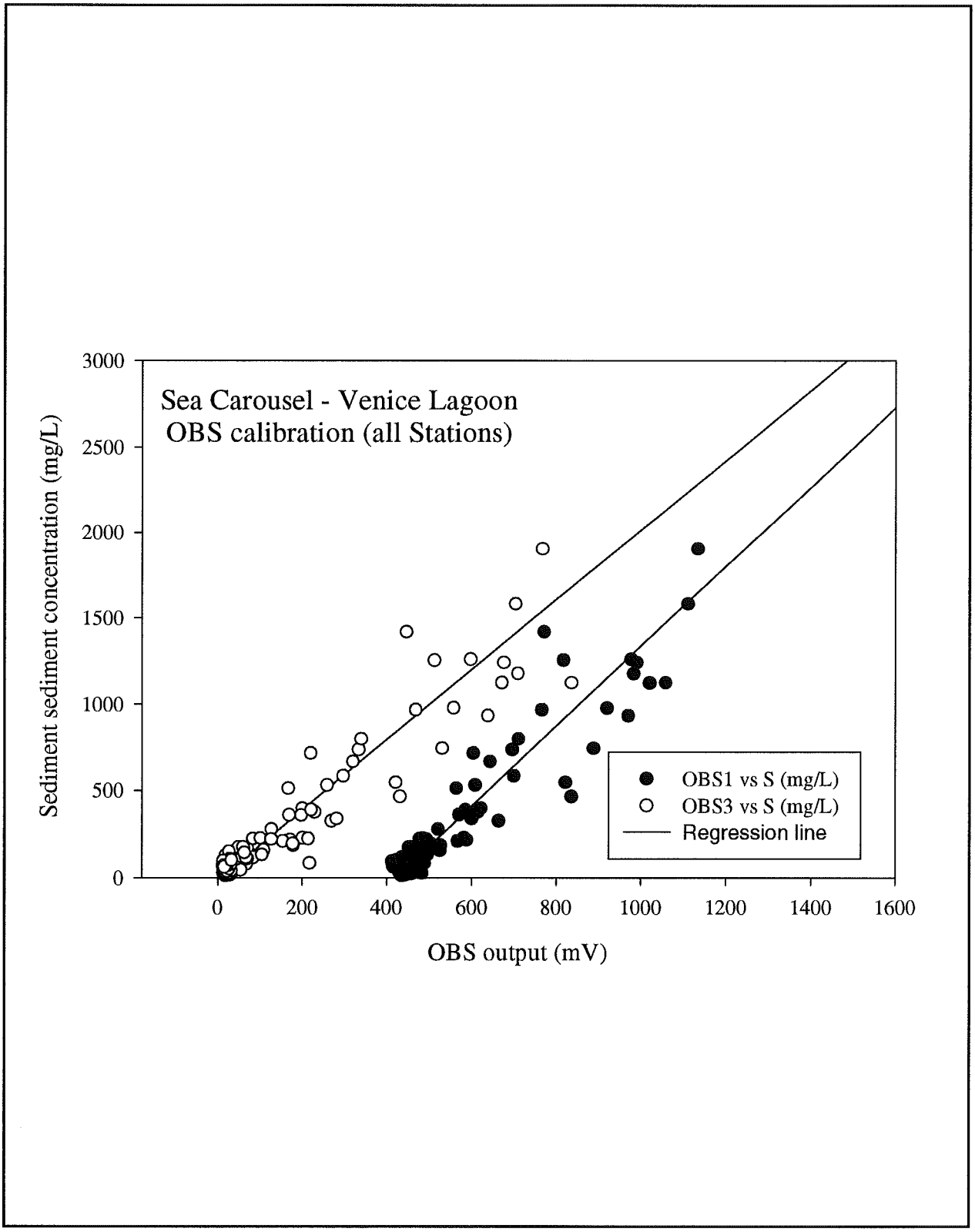

Figure 4.1.15 : The calibrations of OBS1 and OBS3 to suspended sediment concentration (S) derived from samples pumped from the Sea Carousel at each lid speed.

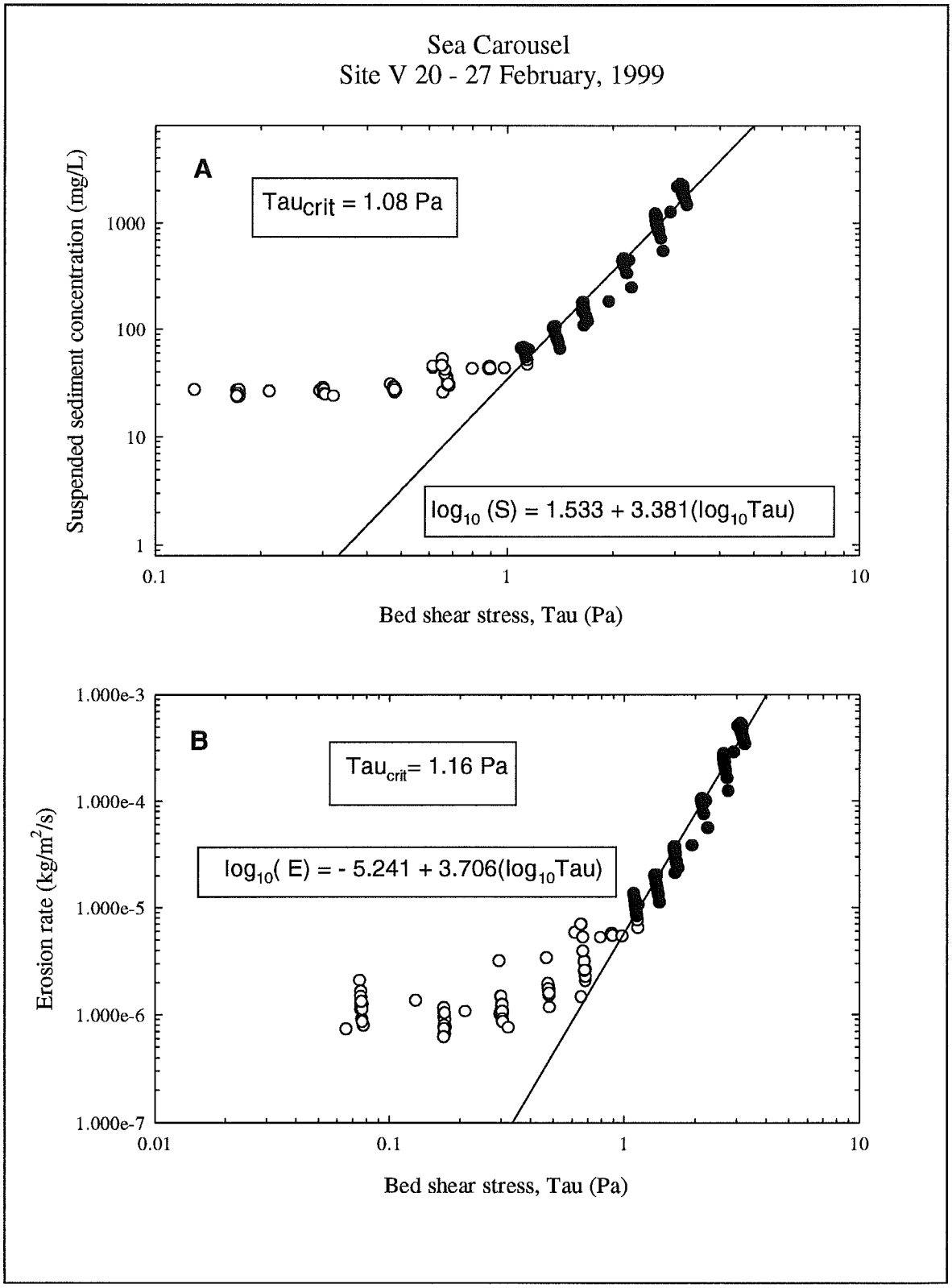

Figure 4.1.16 : (A) Suspended sediment concentrations for site V20 plotted versus bed shear stress. The intercept of the regression line at ambient S is defined as the erosion threshold. (B) Erosion rate plotted against bed shear stress. It varies linearly with the log of excess stress.

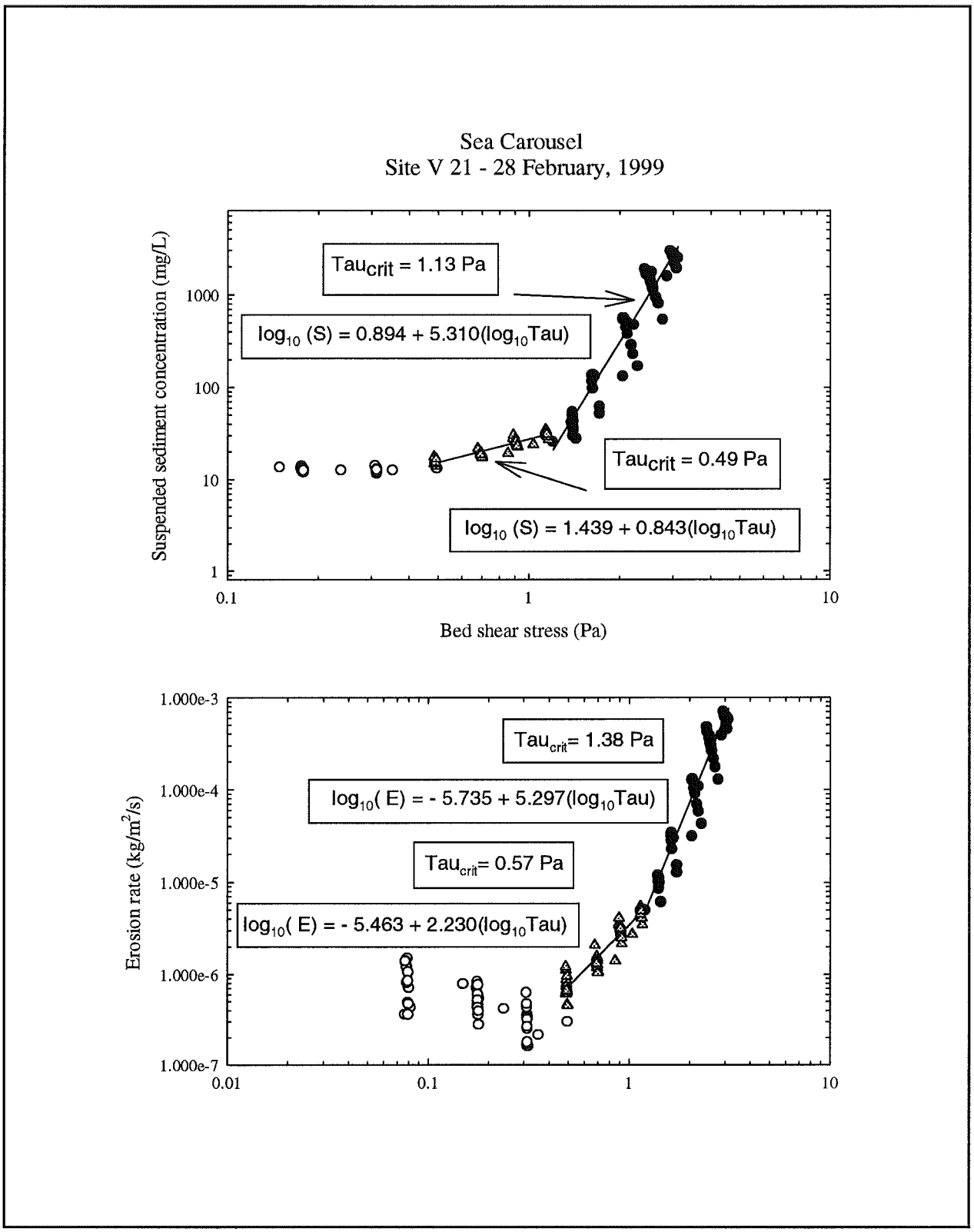

Figure 4.1.17: (A) Suspended sediment concentrations for site V21 plotted versus bed shear stress. The intercept of the regression line at ambient S is defined as the erosion threshold. (B) Erosion rate against bed shear stress. It varies linearly with the log of excess stress.

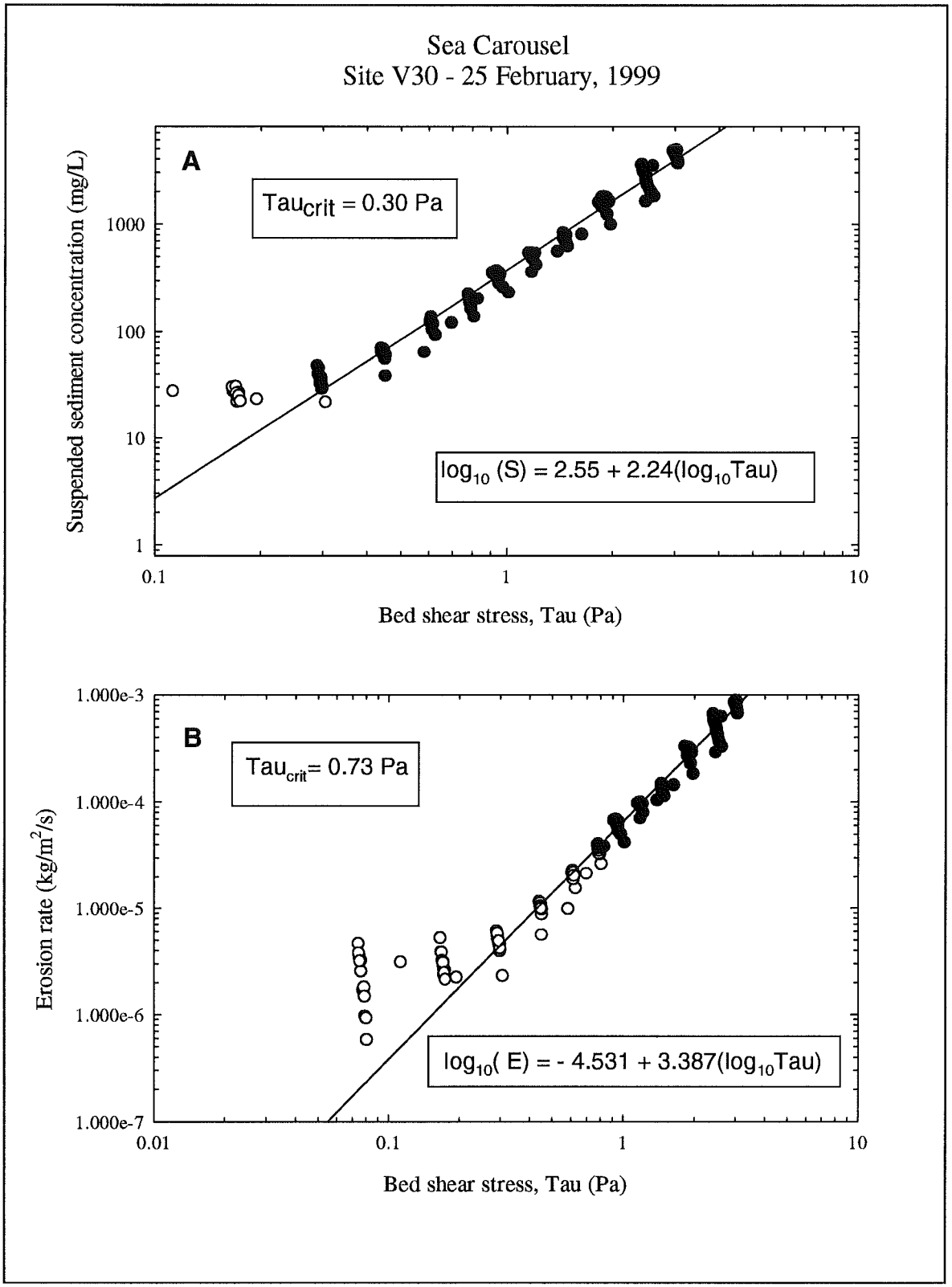

Figure 4.1.18 : (A) Suspended sediment concentrations for site V30 plotted versus bed shear stress. The intercept of the regression line at ambient S is defined as the erosion threshold. (B) Erosion rate plotted against bed shear stress. It varies linearly with the log of excess stress.

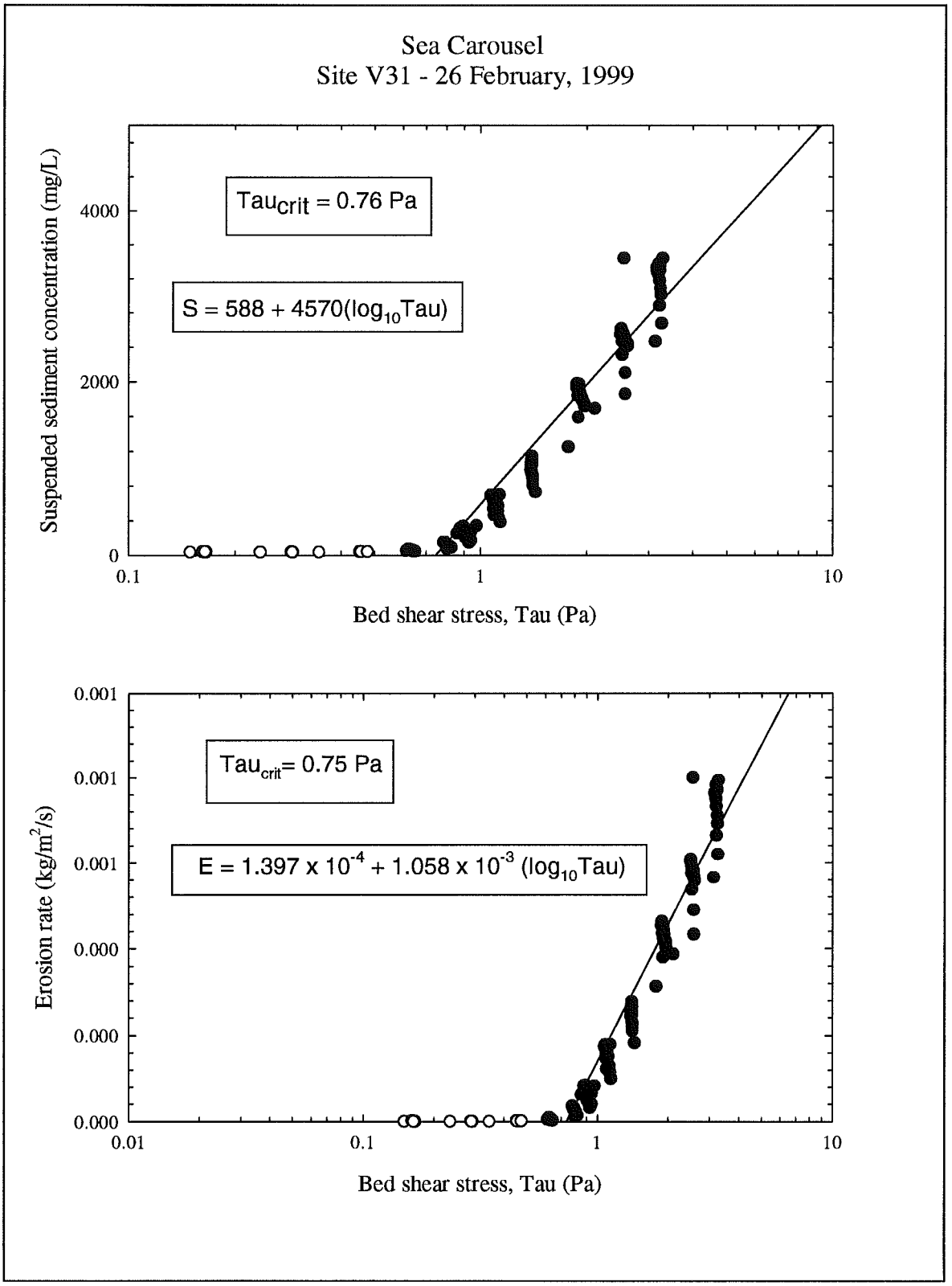

Figure 4.1.19 : (A) Suspended sediment concentrations for site V31 plotted versus bed shear stress. The intercept of the regression line at ambient S is defined as the erosion threshold. (B) Erosion rate plotted against bed shear stress. It varies linearly with the log of excess stress.

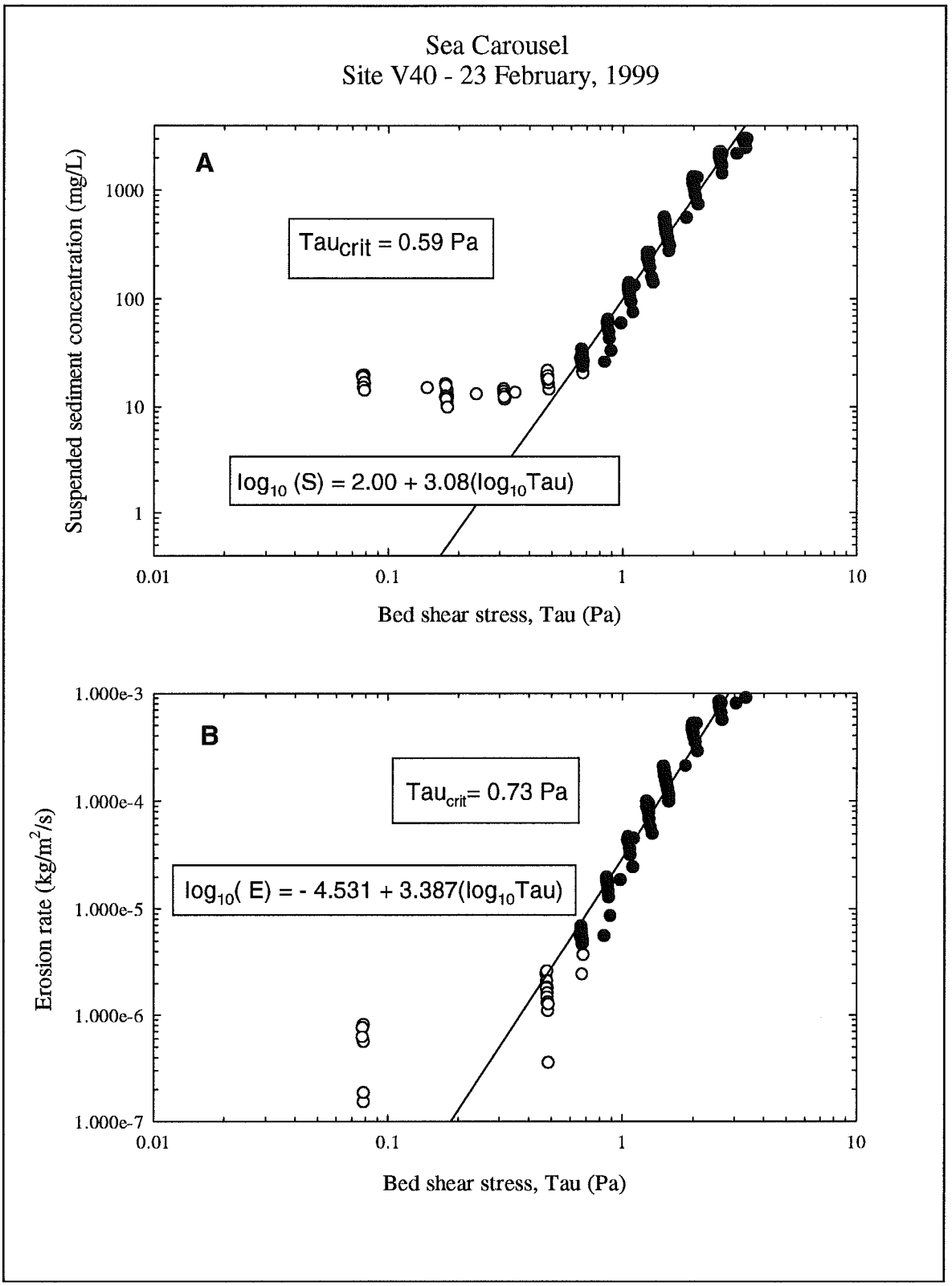

Figure 4.1.20 : (A) Suspended sediment concentrations for site V40 plotted versus bed shear stress. The intercept of the regression line at ambient S is defined as the erosion threshold. (B) Erosion rate plotted against bed shear stress. It varies linearly with the log of excess stress.

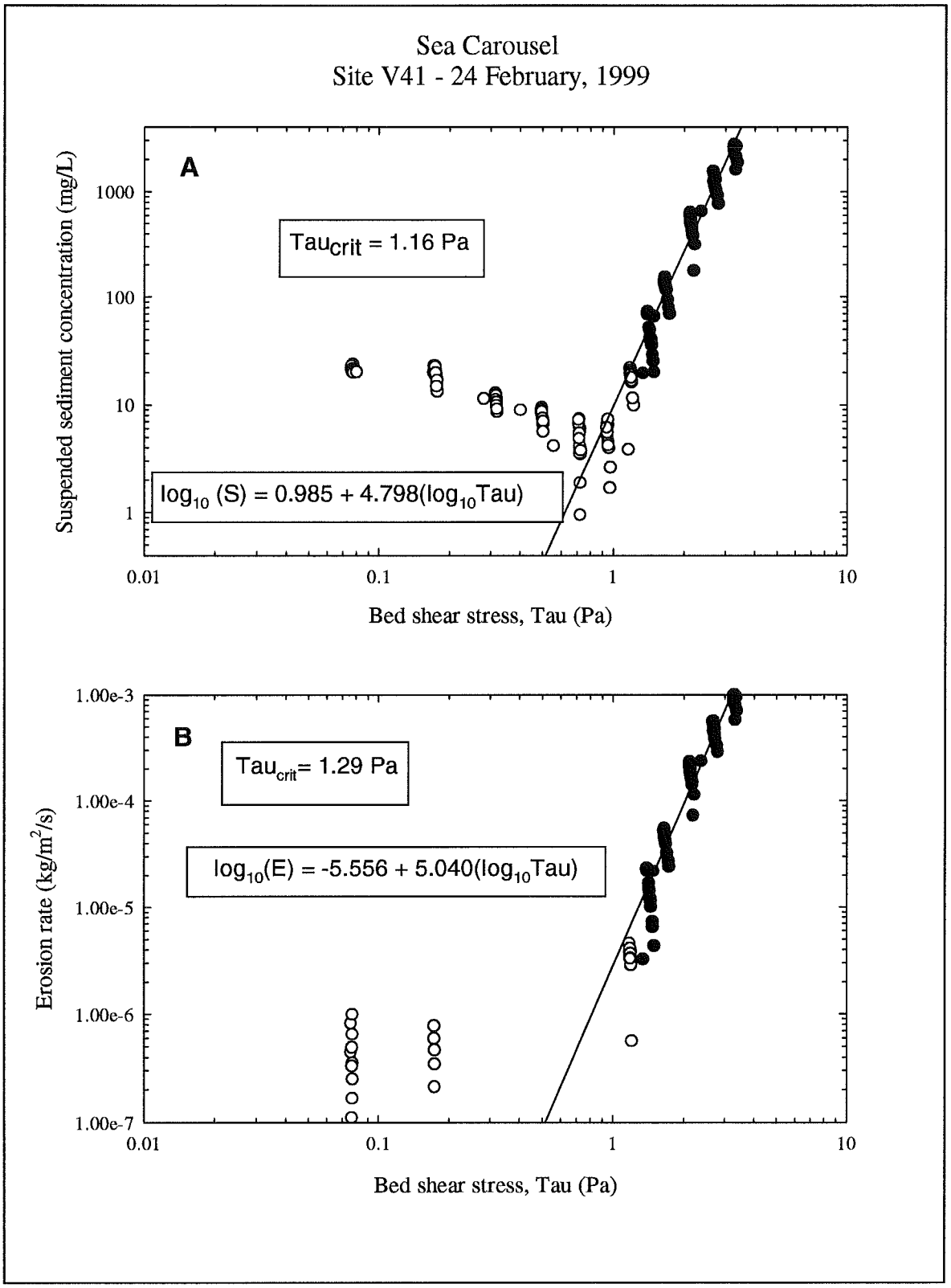

Figure 4.1.21 : (A) Suspended sediment concentrations for site V41 plotted versus bed shear stress. The intercept of the regression line at ambient S is defined as the erosion threshold. (B) Erosion rate plotted against bed shear stress. It varies linearly with the log of excess stress.

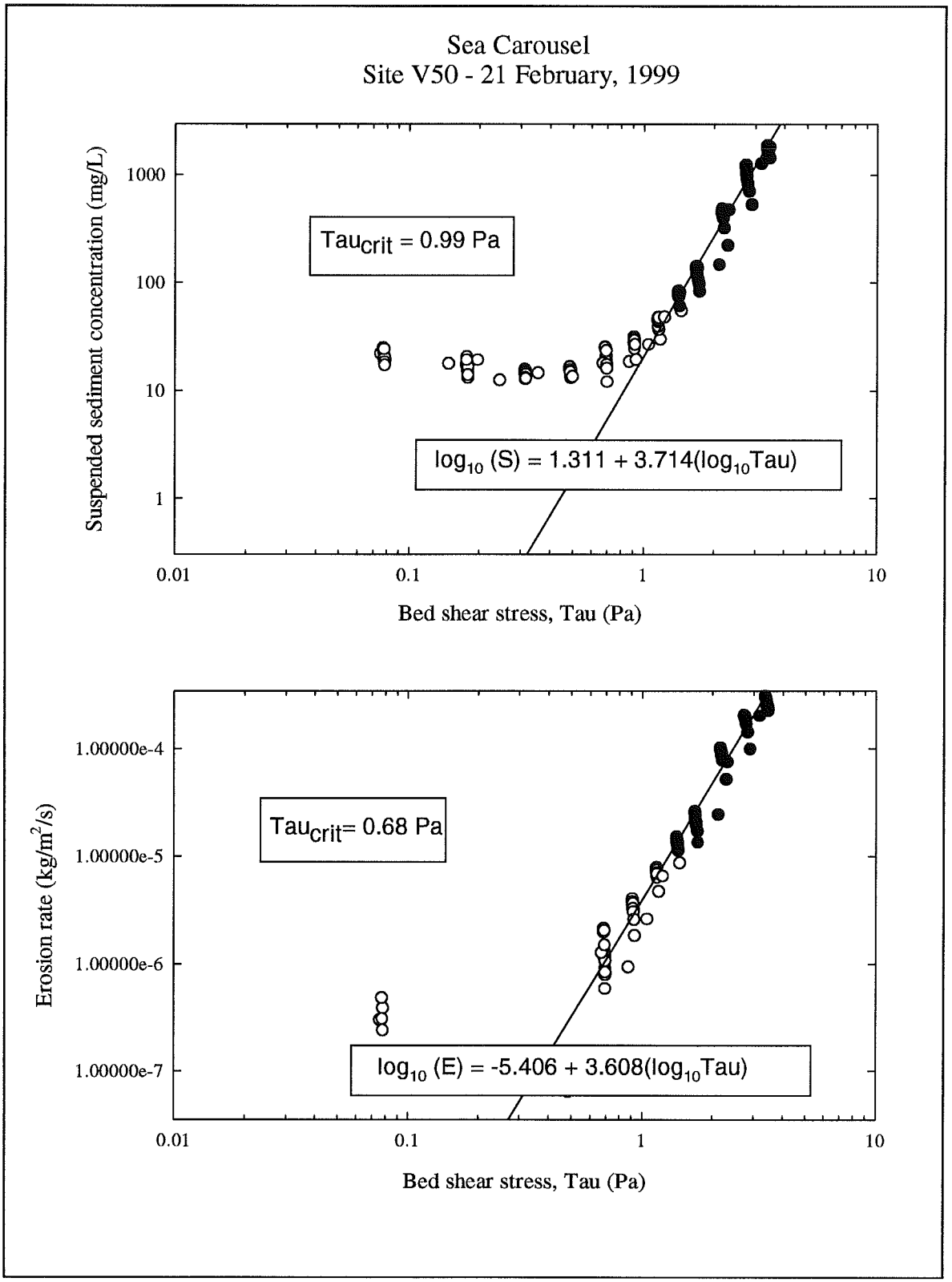

Figure 4.1.22 : (A) Suspended sediment concentrations for site V50 plotted versus bed shear stress. The intercept of the regression line at ambient S is defined as the erosion threshold. (B) Erosion rate plotted against bed shear stress. It varies linearly with the log of excess stress.

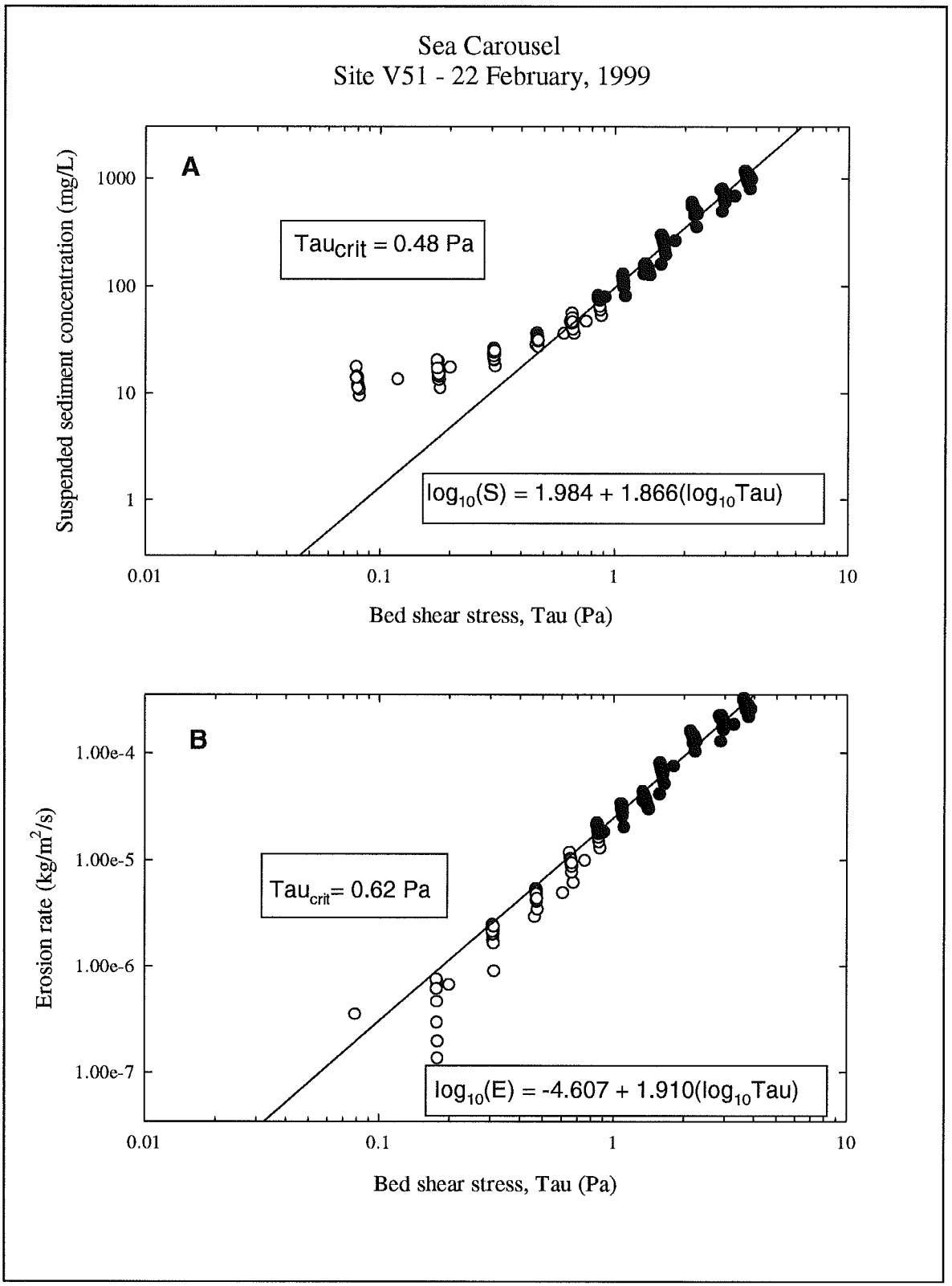

Figure 4.1.23 : (A) Suspended sediment concentrations for site V51 plotted versus bed shear stress. The intercept of the regression line at ambient S is defined as the erosion threshold. (B) Erosion rate plotted against bed shear stress. It varies linearly with the log of excess stress.

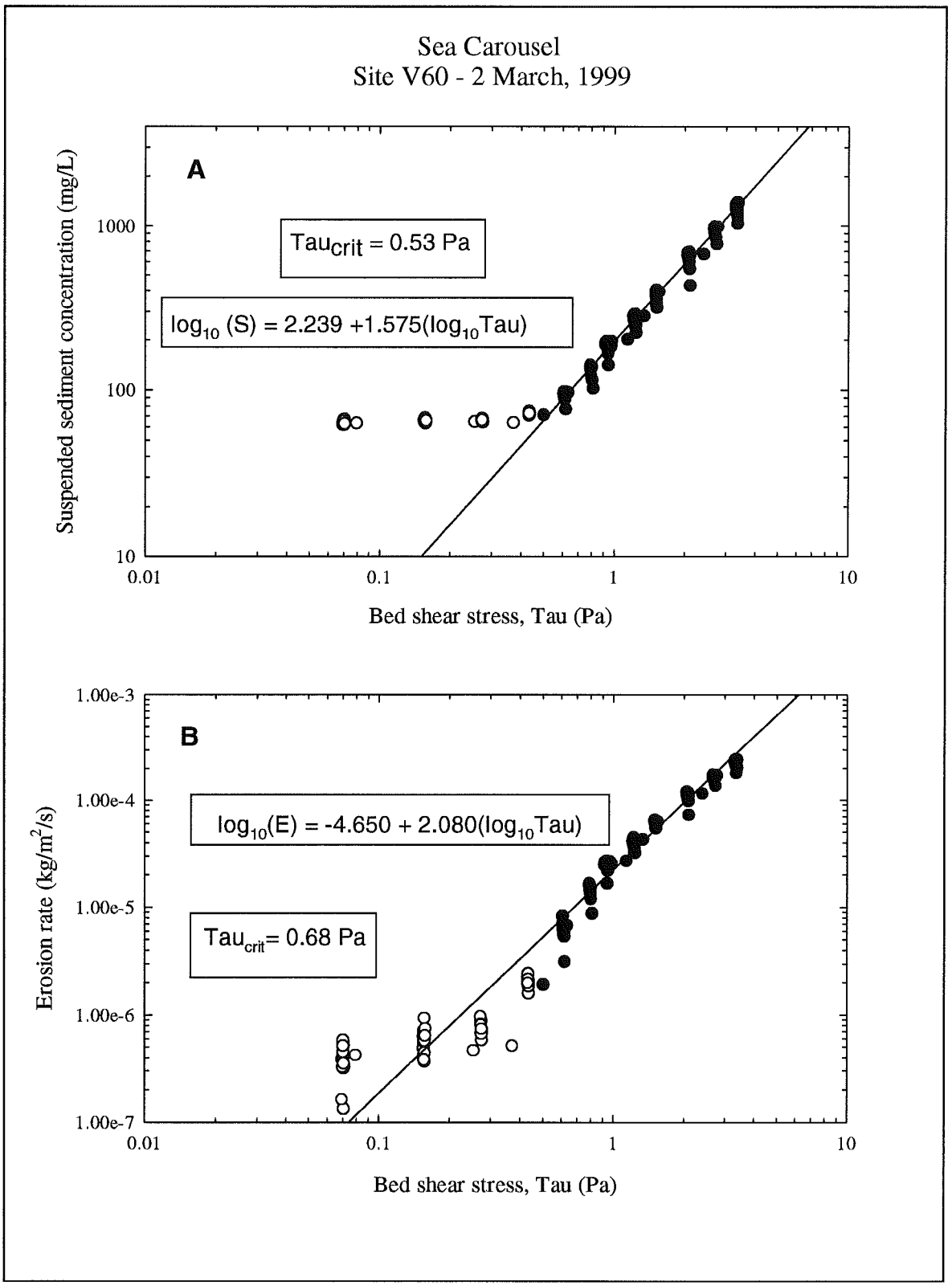

Figure 4.1.24 : (A) Suspended sediment concentrations for site V60 plotted versus bed shear stress. The intercept of the regression line at ambient S is defined as the erosion threshold. (B) Erosion rate plotted against bed shear stress. It varies linearly with the log of excess stress.

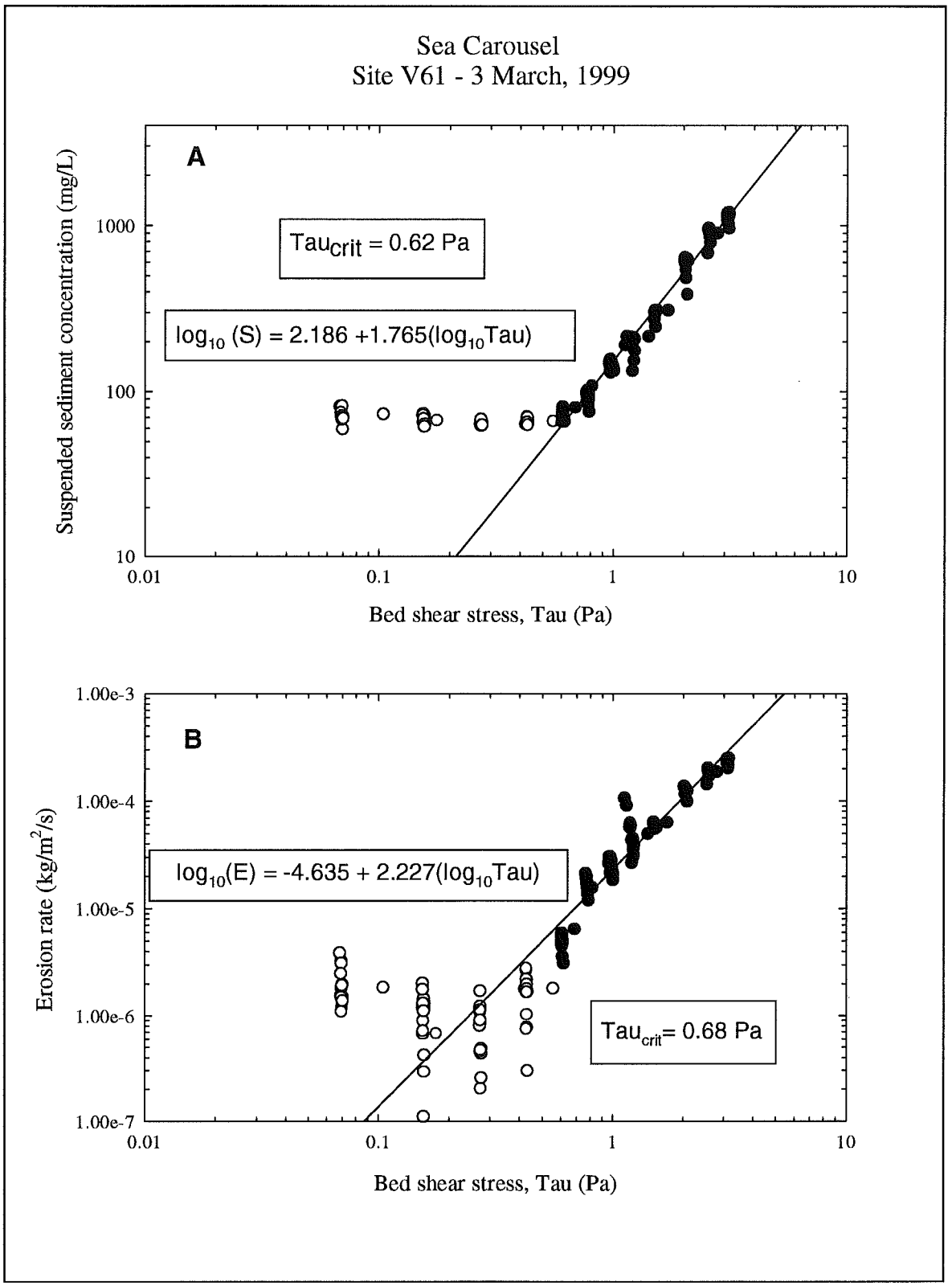

Figure 4.1.25 : (A) Suspended sediment concentrations for site V61 plotted versus bed shear stress. The intercept of the regression line at ambient S is defined as the erosion threshold. (B) Erosion rate plotted against bed shear stress. It varies linearly with the log of excess stress.

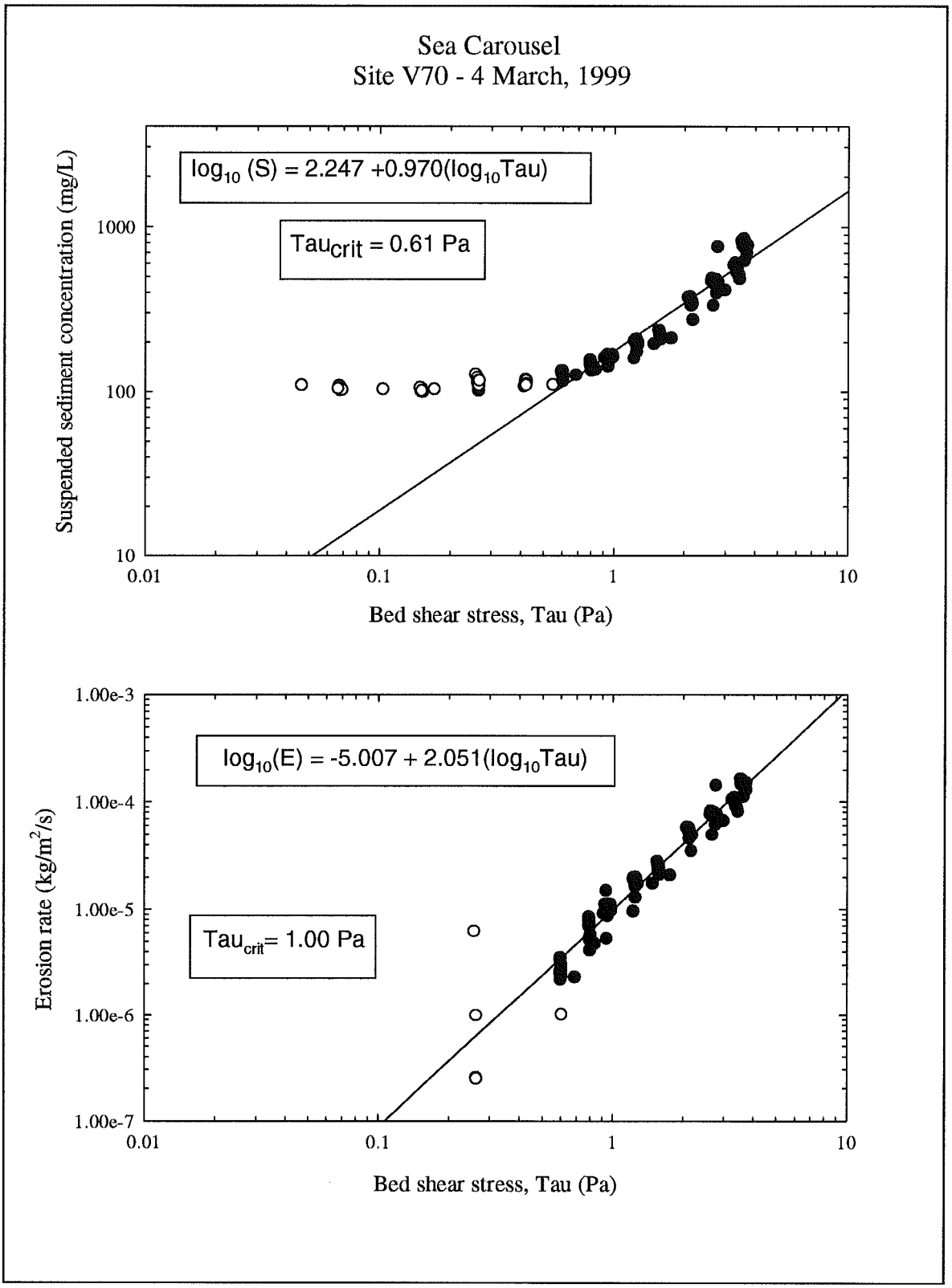

Figure 4.1.26 : (A) Suspended sediment concentrations for site V70 plotted versus bed shear stress. The intercept of the regression line at ambient S is defined as the erosion threshold. (B) Erosion rate plotted against bed shear stress. It varies linearly with the log of excess stress.

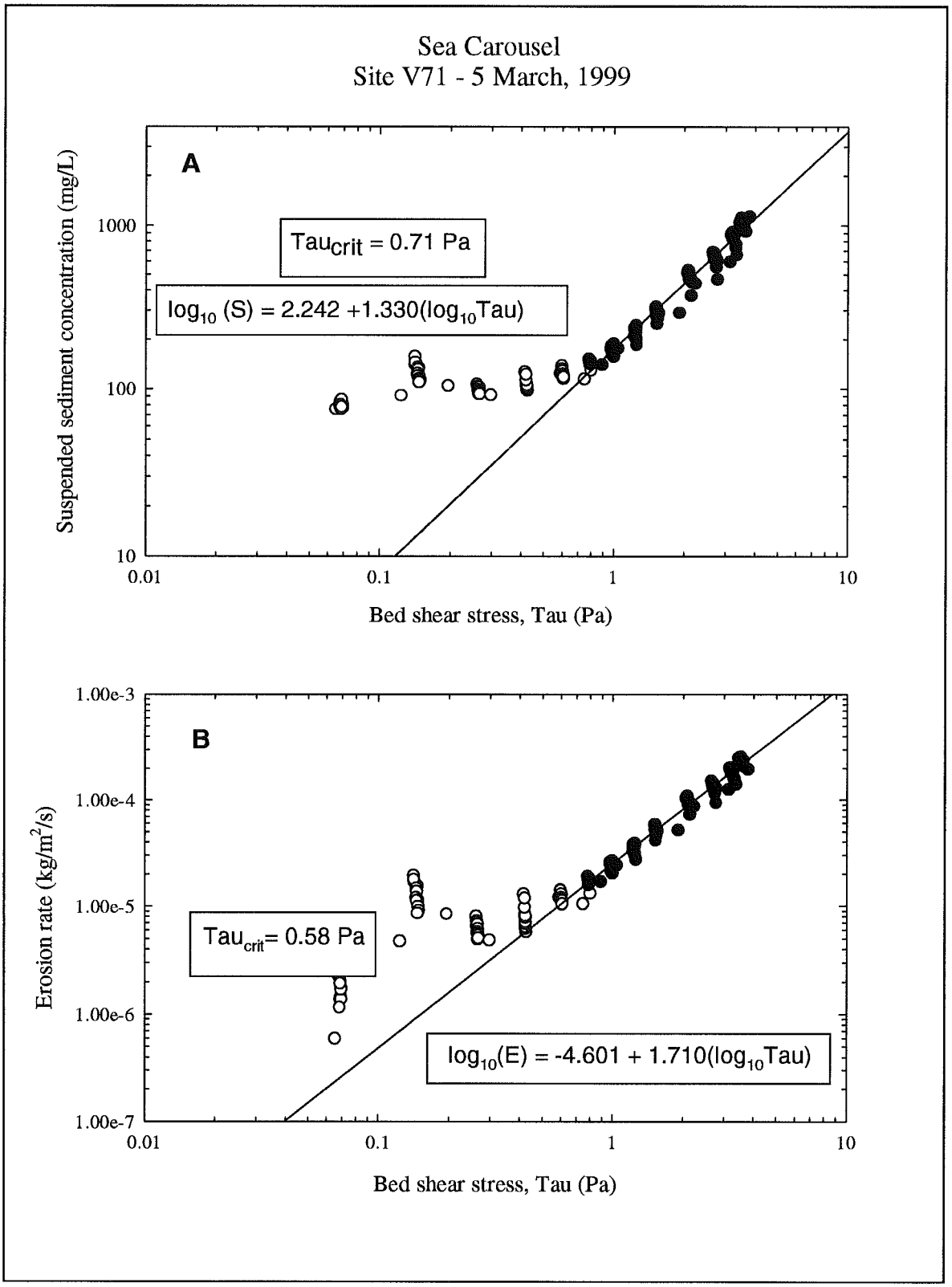

Figure 4.1.27 : (A) Suspended sediment concentrations for site V71 plotted versus bed shear stress. The intercept of the regression line at ambient S is defined as the erosion threshold. (B) Erosion rate plotted against bed shear stress. It varies linearly with the log of excess stress.

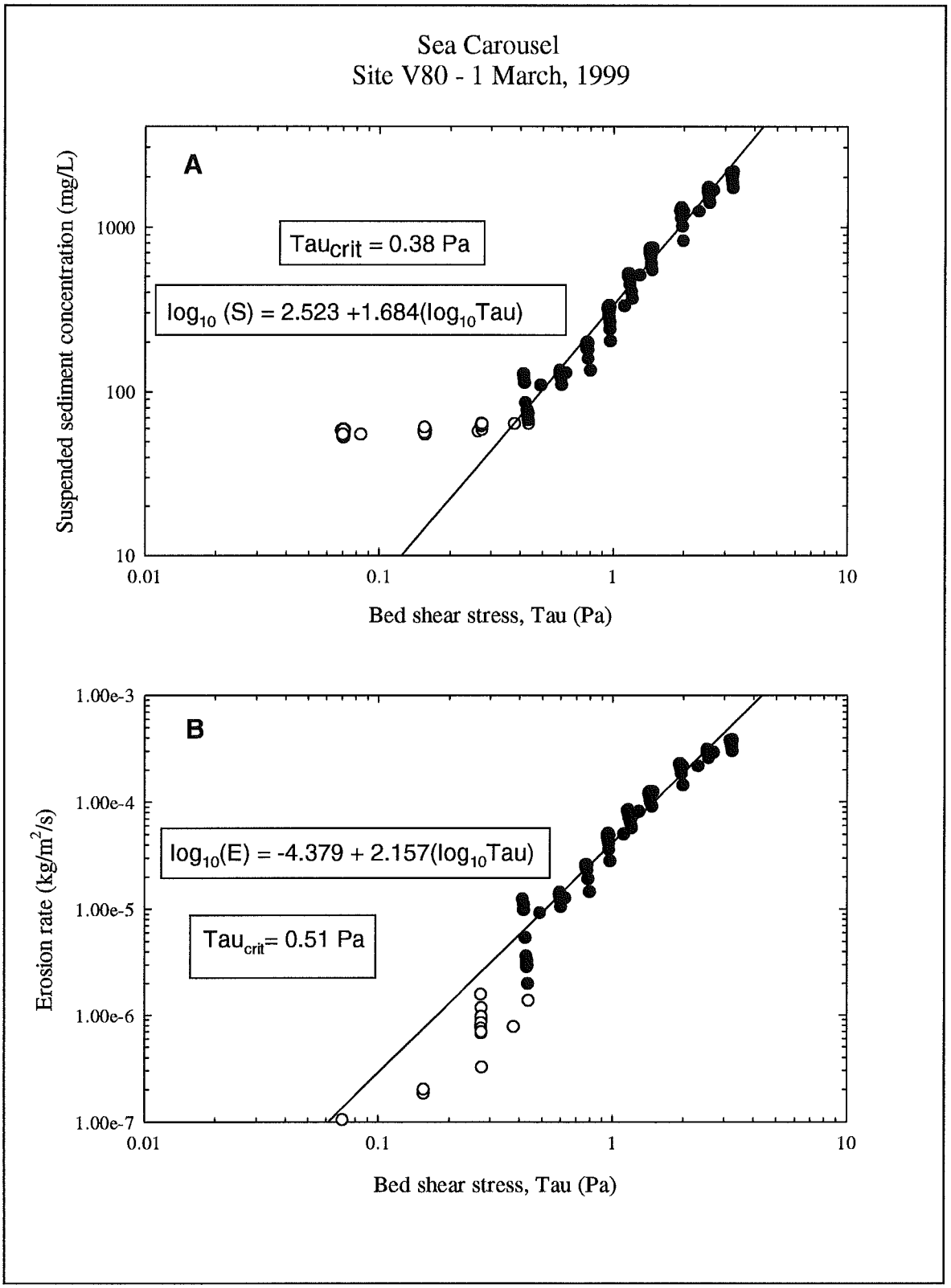

Figure 4.1.28 : (A) Suspended sediment concentrations for site V80 plotted versus bed shear stress. The intercept of the regression line at ambient S is defined as the erosion threshold. (B) Erosion rate plotted against bed shear stress. It varies linearly with the log of excess stress.

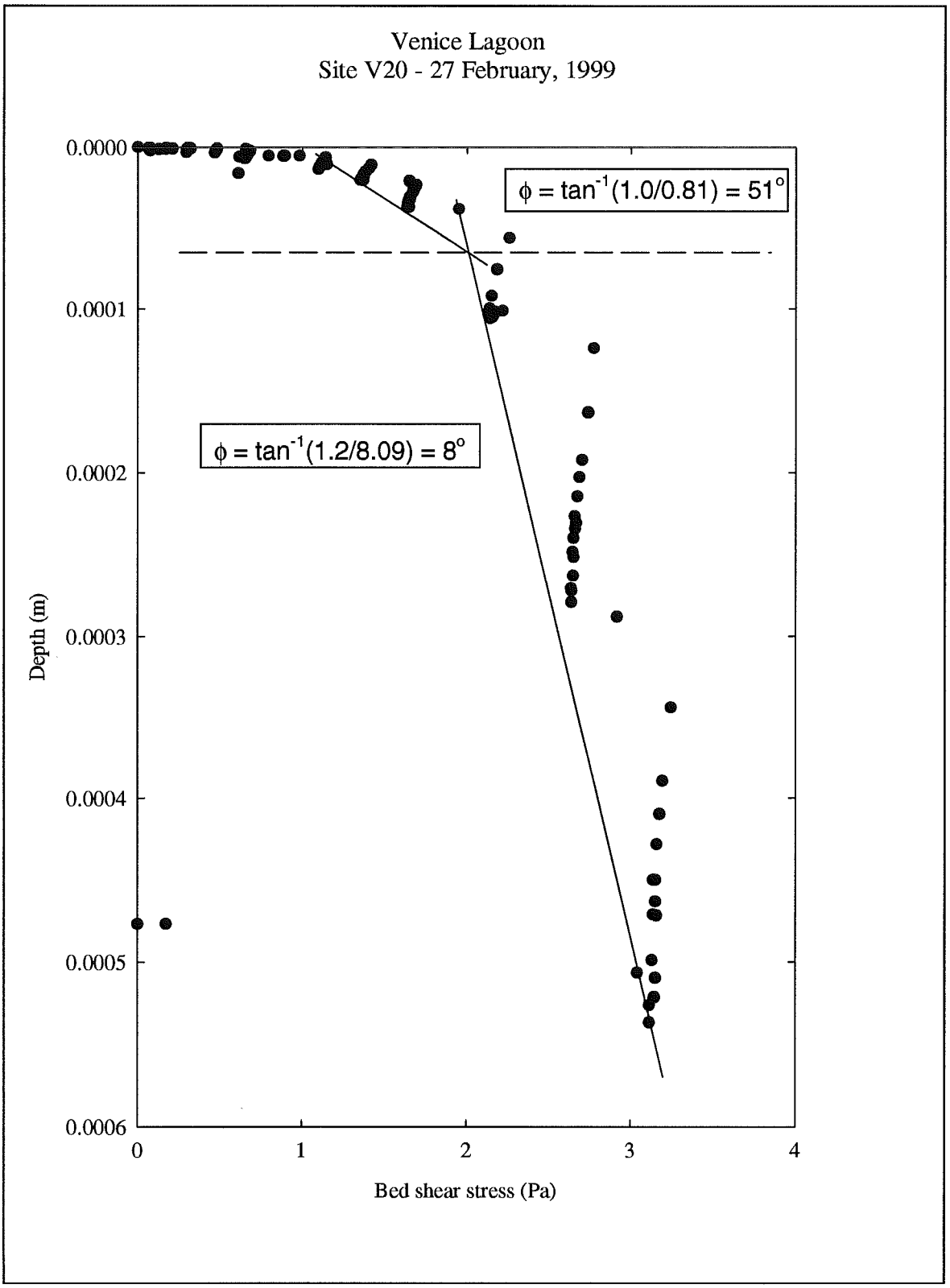

Figure 4.2.1 : A synthetic core of site V20 derived from the Sea Carousel time series. Note the high friction coefficient (bed strenghening) near the surface and the lower (8°) value beneath. This profile may be interpreted as of low stability.

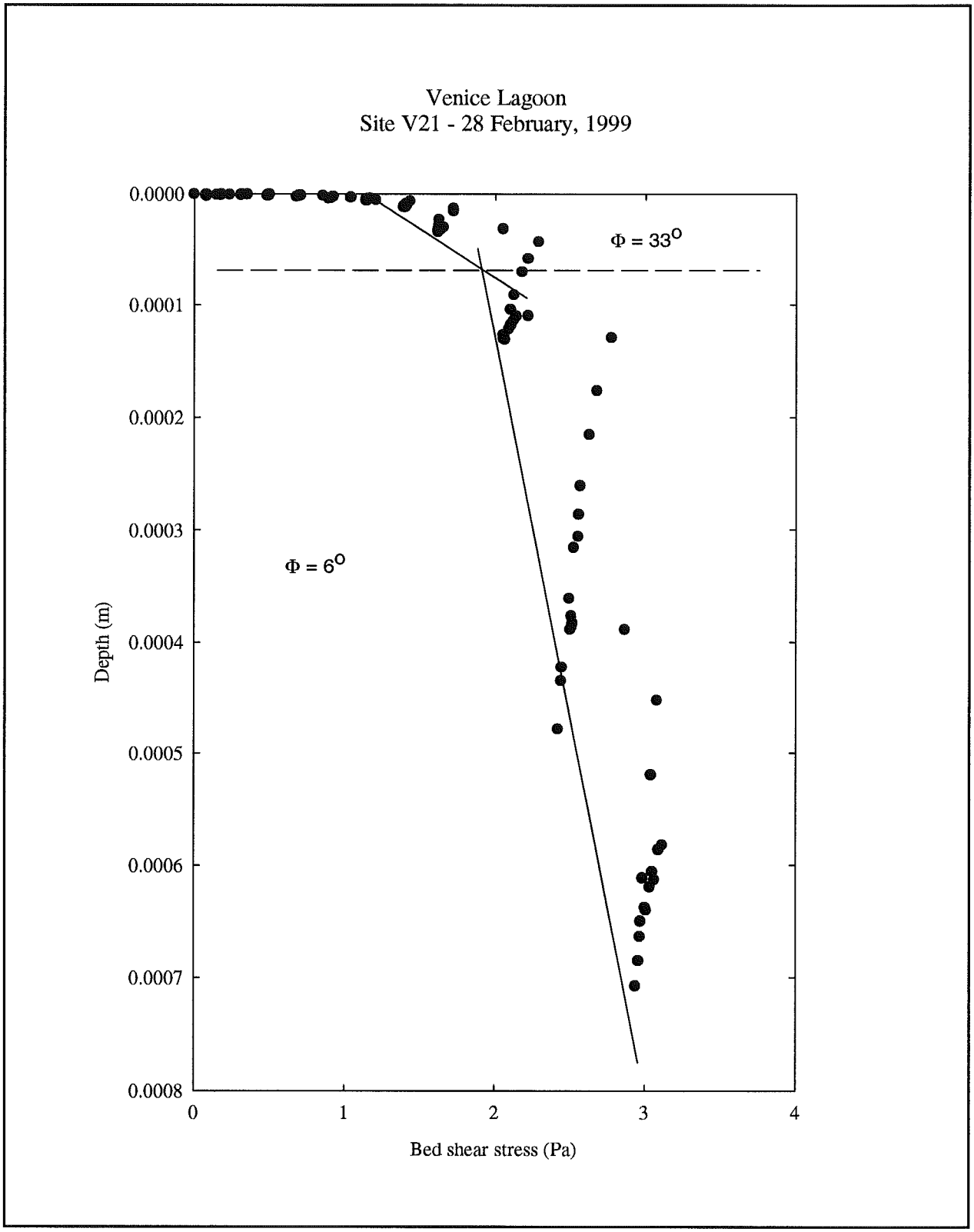

Figure 4.2.2 : A synthetic core of site V21 derived from the Sea Carousel time series.

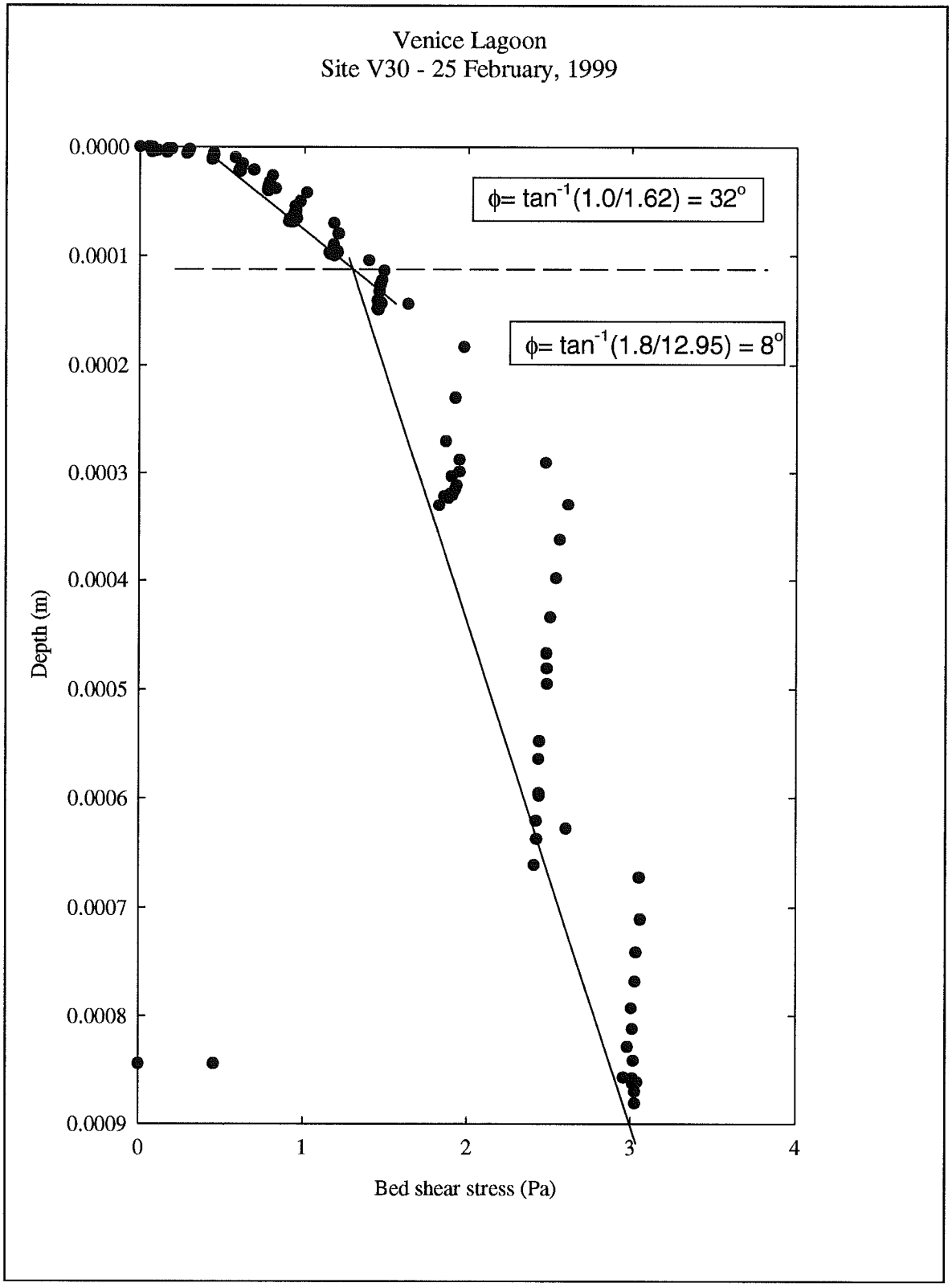

Figure 4.2.3 : A synthetic core of site V30 derived from the Sea Carousel time series.

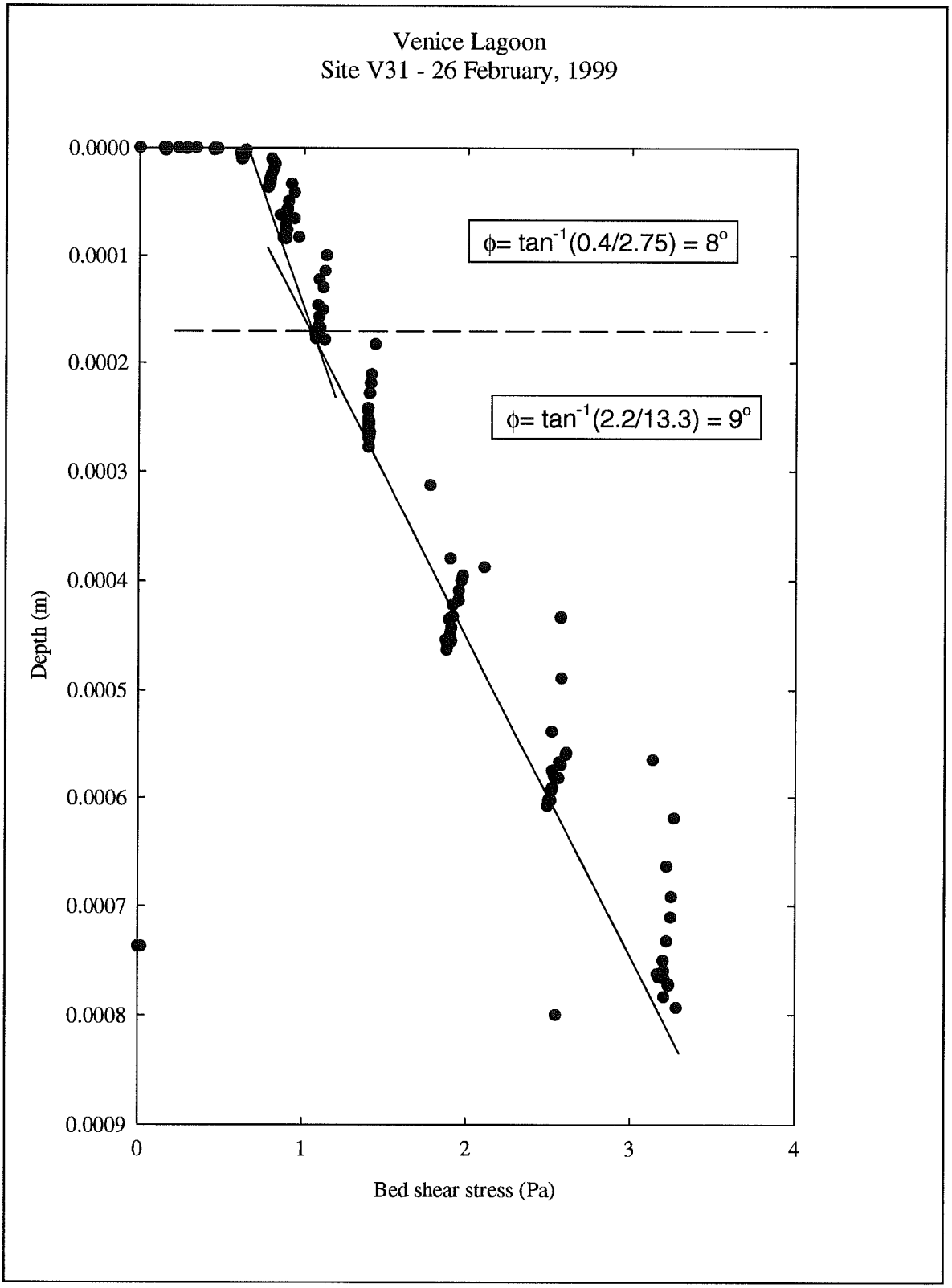

Figure 4.2.4 : A synthetic core of site V31 derived from the Sea Carousel time series.

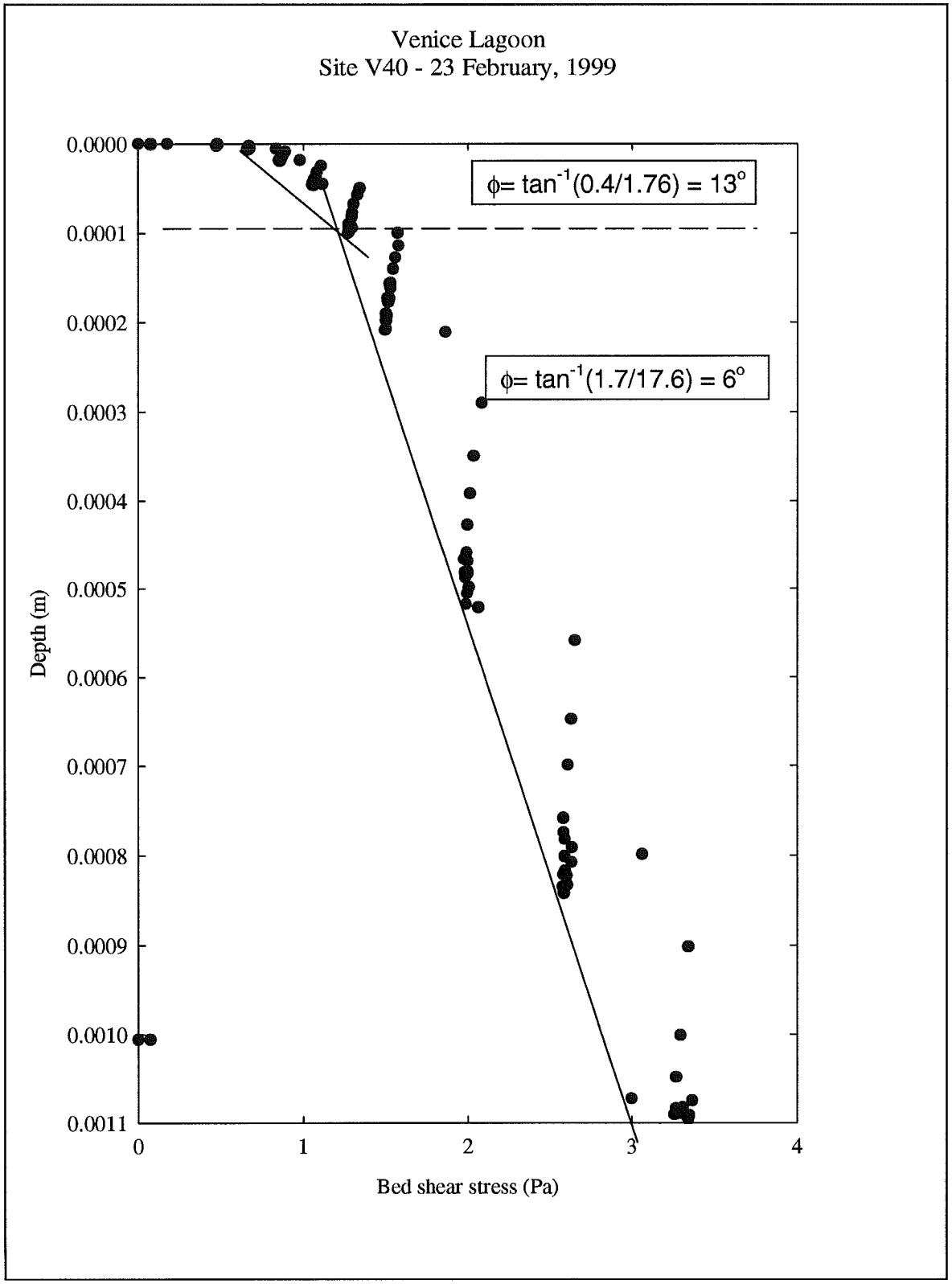

Figure 4.2.5 : A synthetic core of site V40 derived from the Sea Carousel time series.

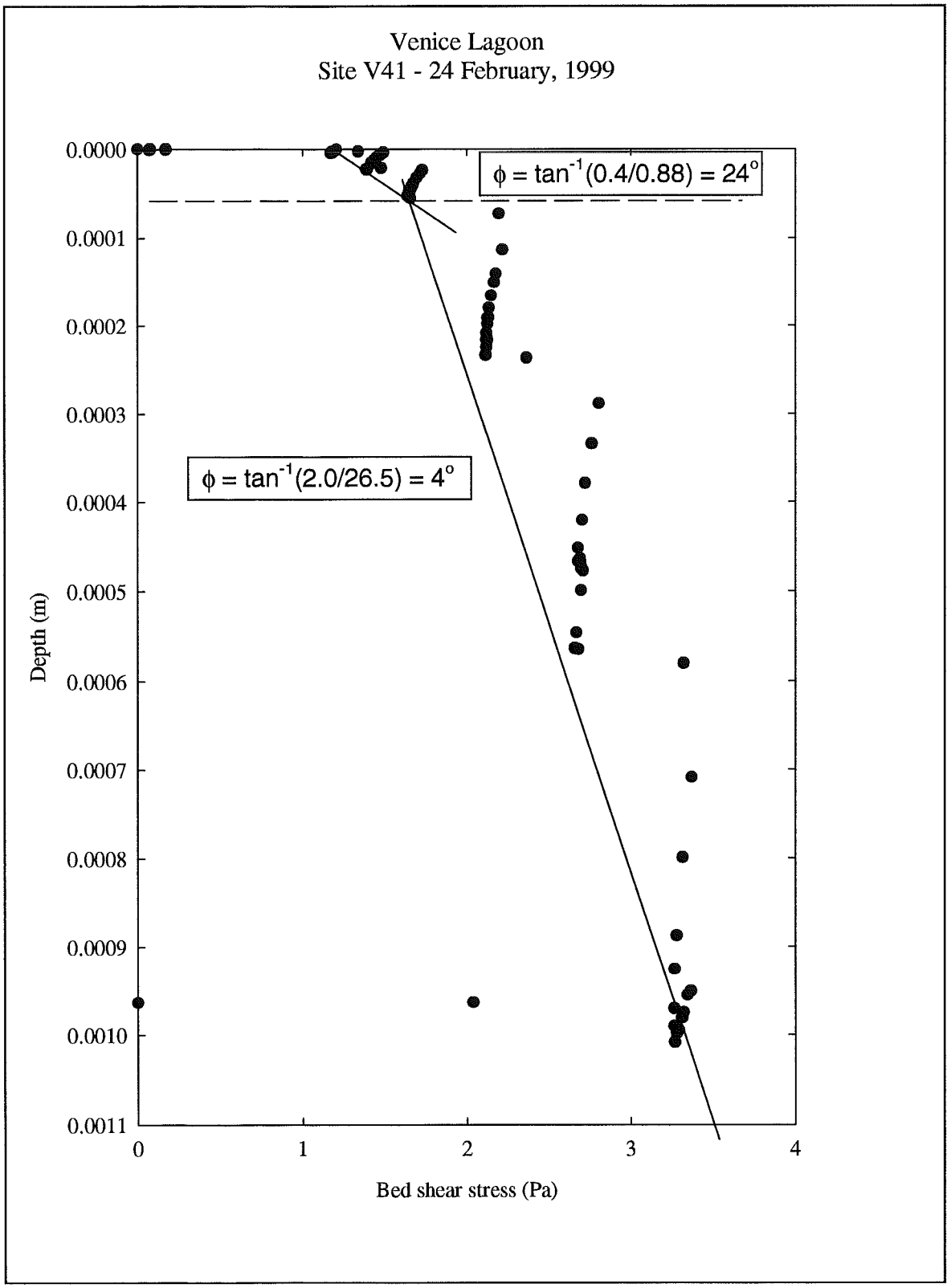

Figure 4.2.6 : A synthetic core of site V41 derived from the Sea Carousel time series.

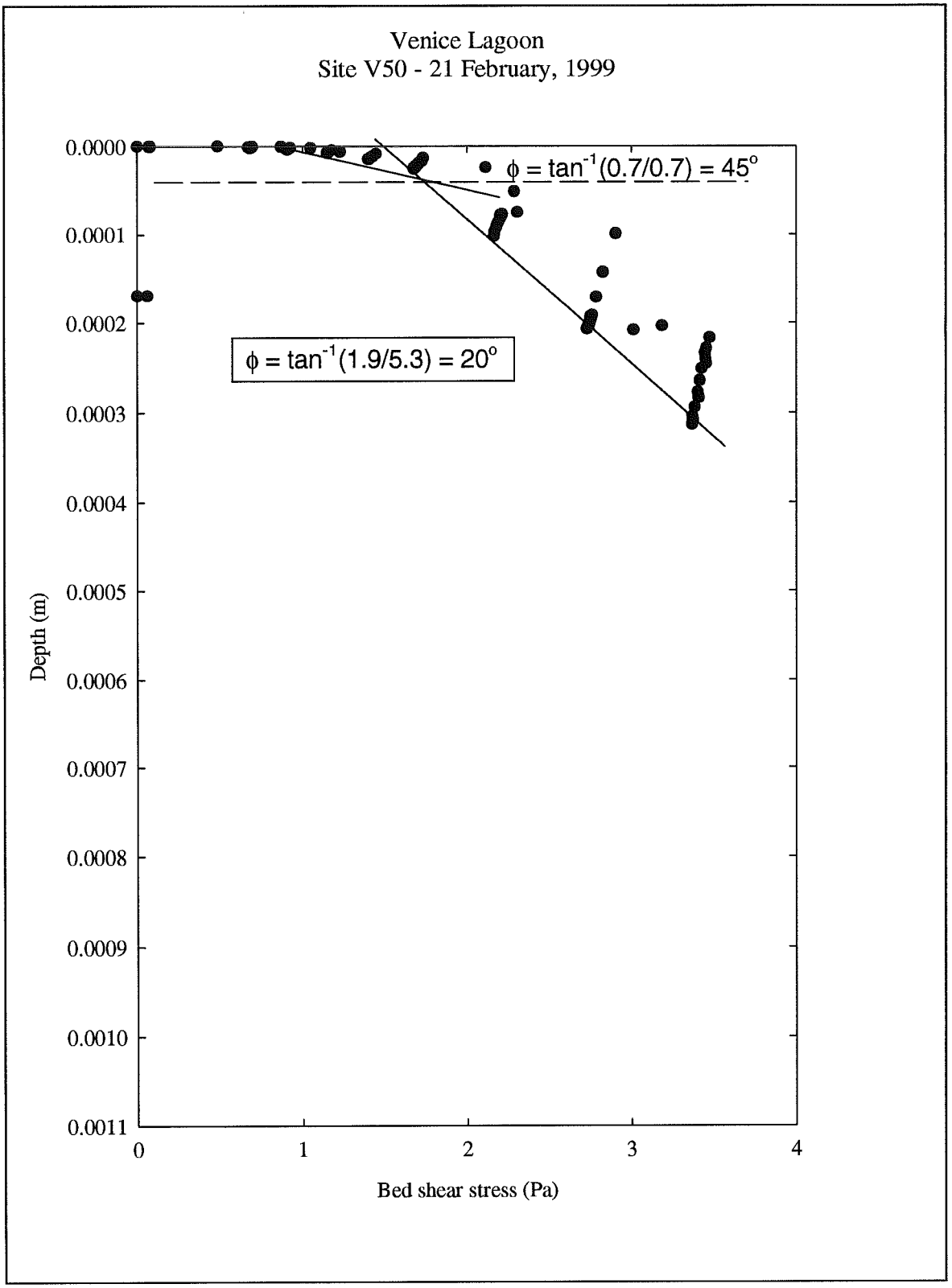

Figure 4.2.7 : A synthetic core of site V50 derived from the Sea Carousel time series

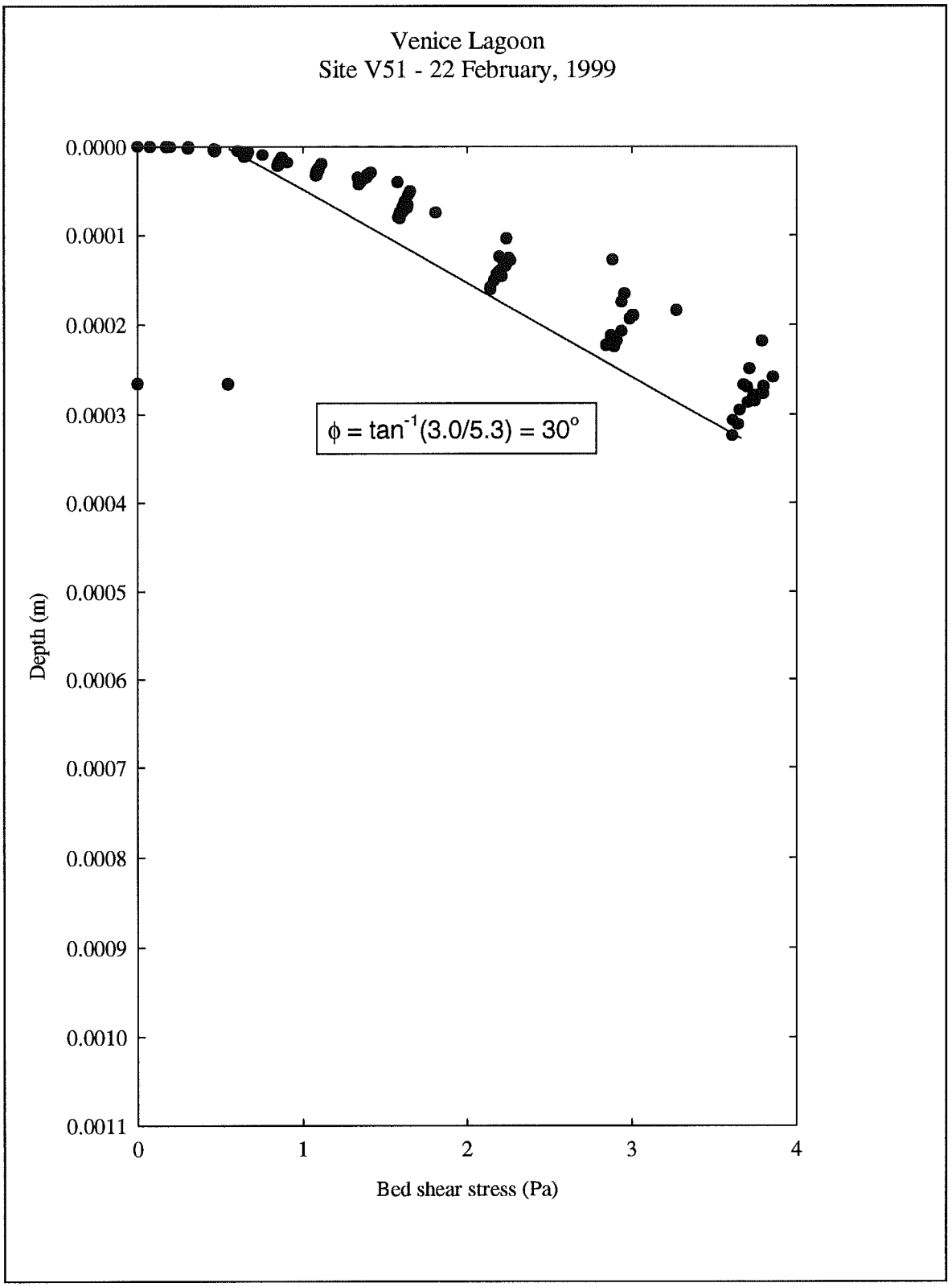

Figure 4.2.8 : A synthetic core of site V51 derived from the Sea Carousel time series.

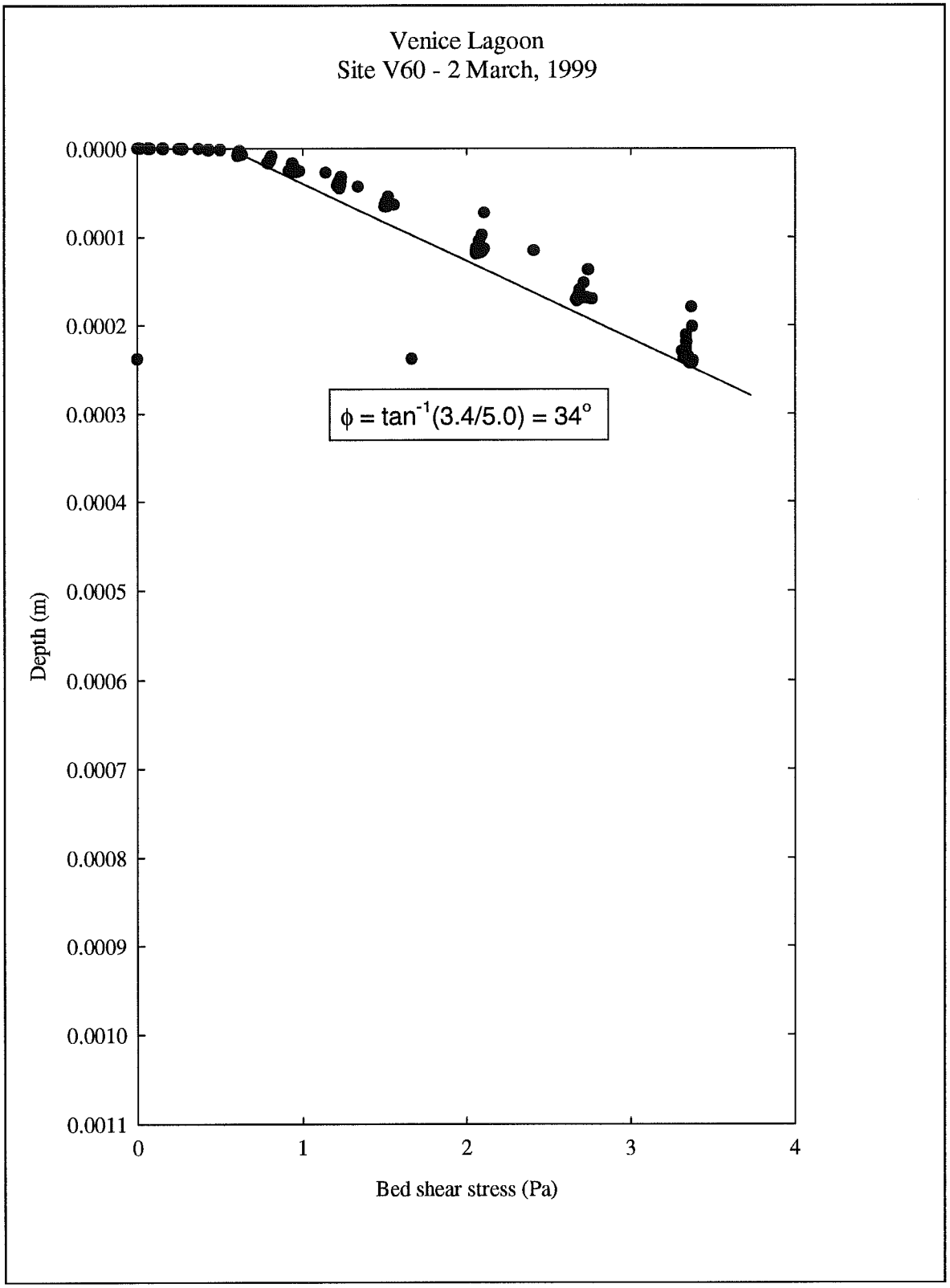

Figure 4.2.9 : A synthetic core of site V60 derived from the Sea Carousel time series.

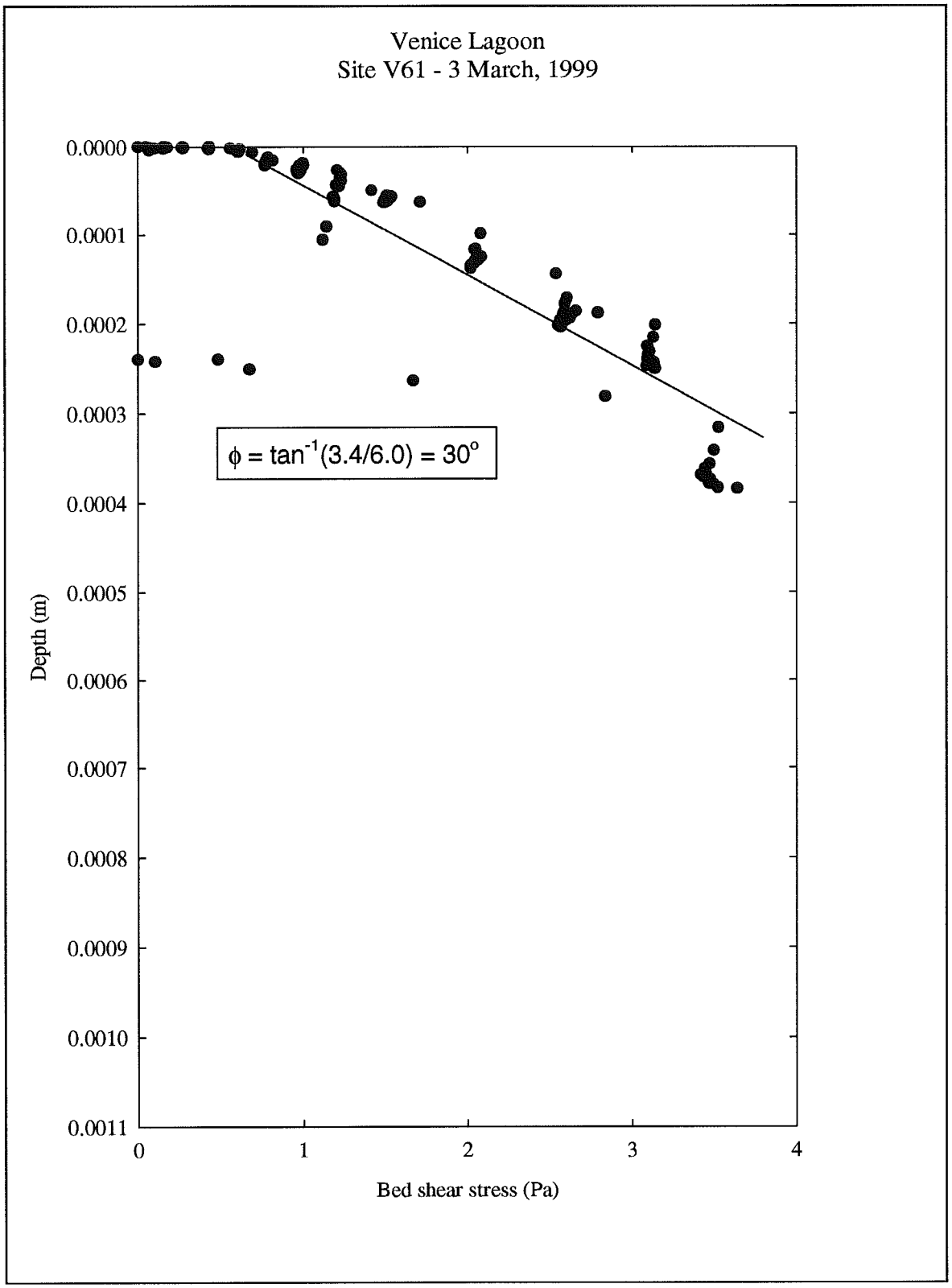

Figure 4.2.10 : A synthetic core of site V61 derived from the Sea Carousel time series.

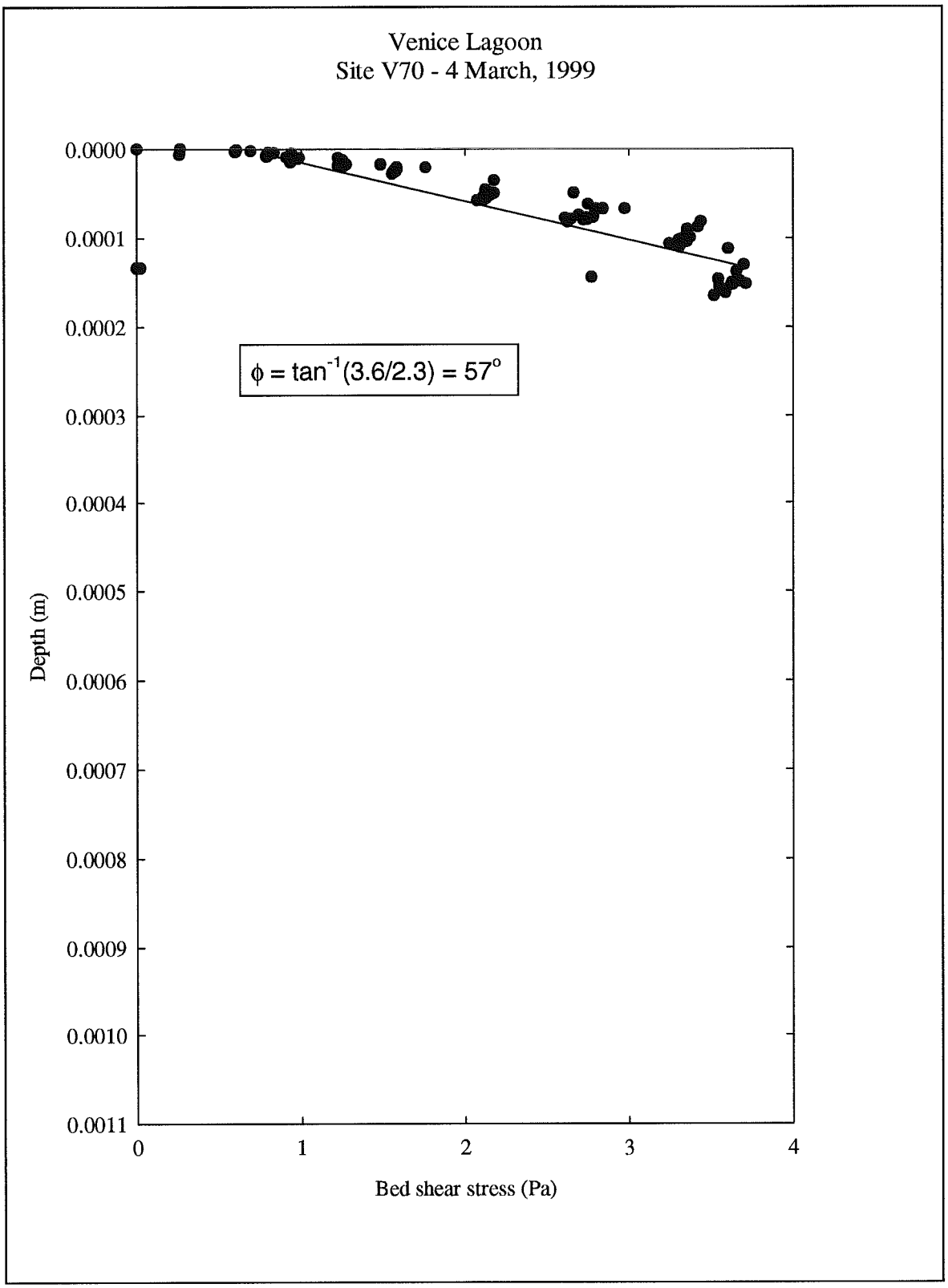

Figure 4.2.11 : A synthetic core of site V70 derived from the Sea Carousel time series.

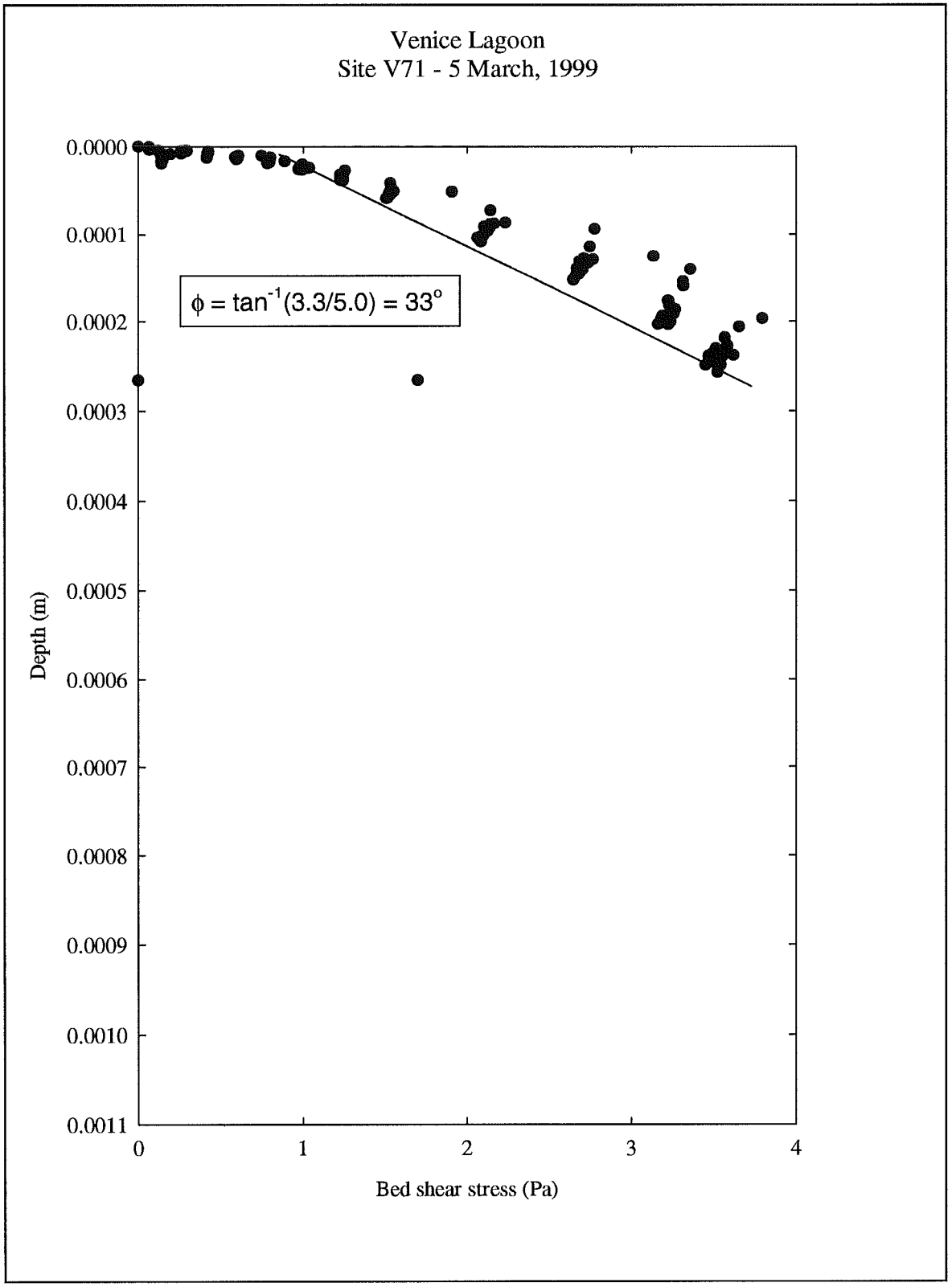

Figure 4.2.12 : A synthetic core of site V71 derived from the Sea Carousel time series

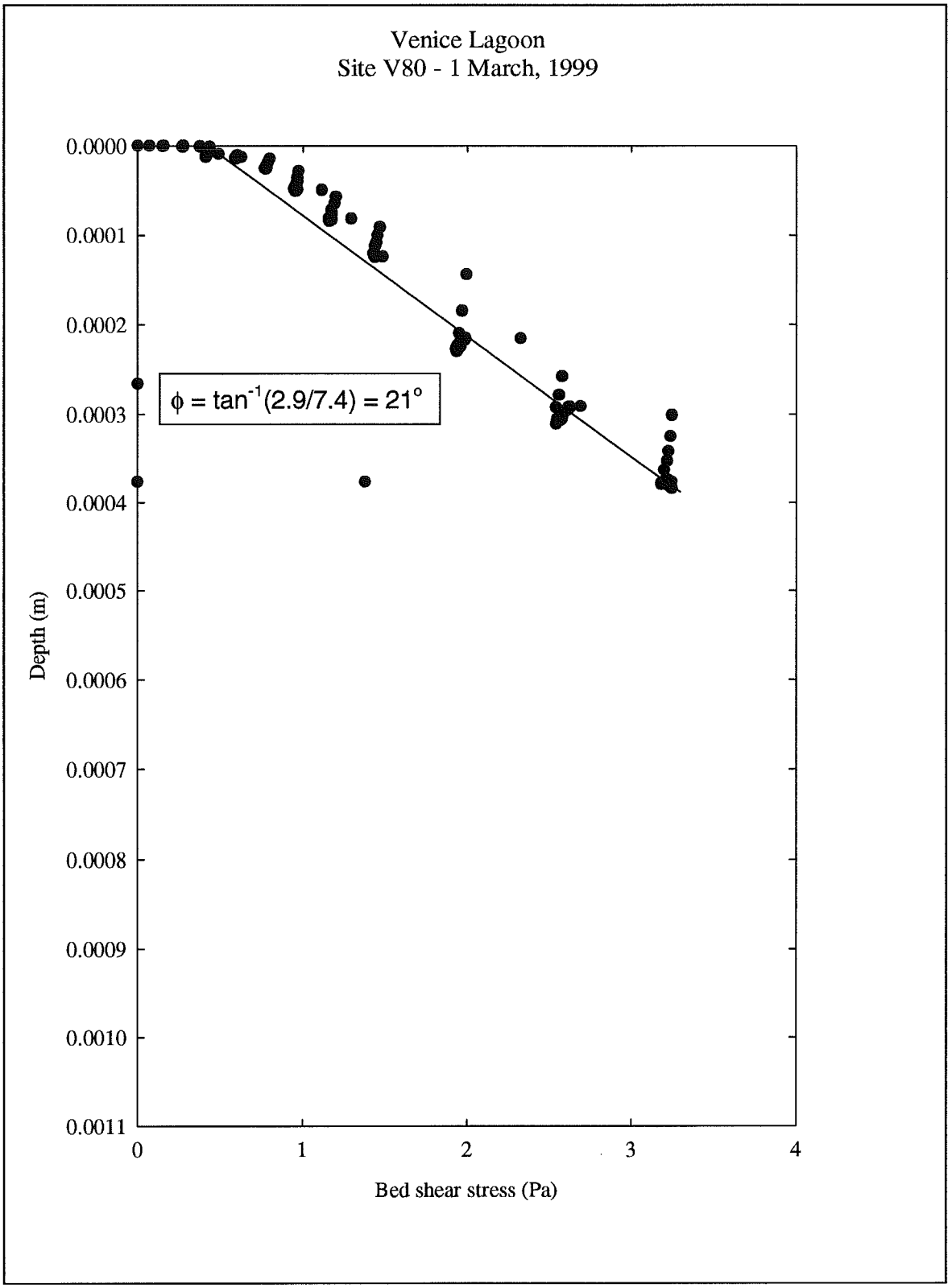

Figure 4.2.13 : A synthetic core of site V80 derived from the Sea Carousel time series

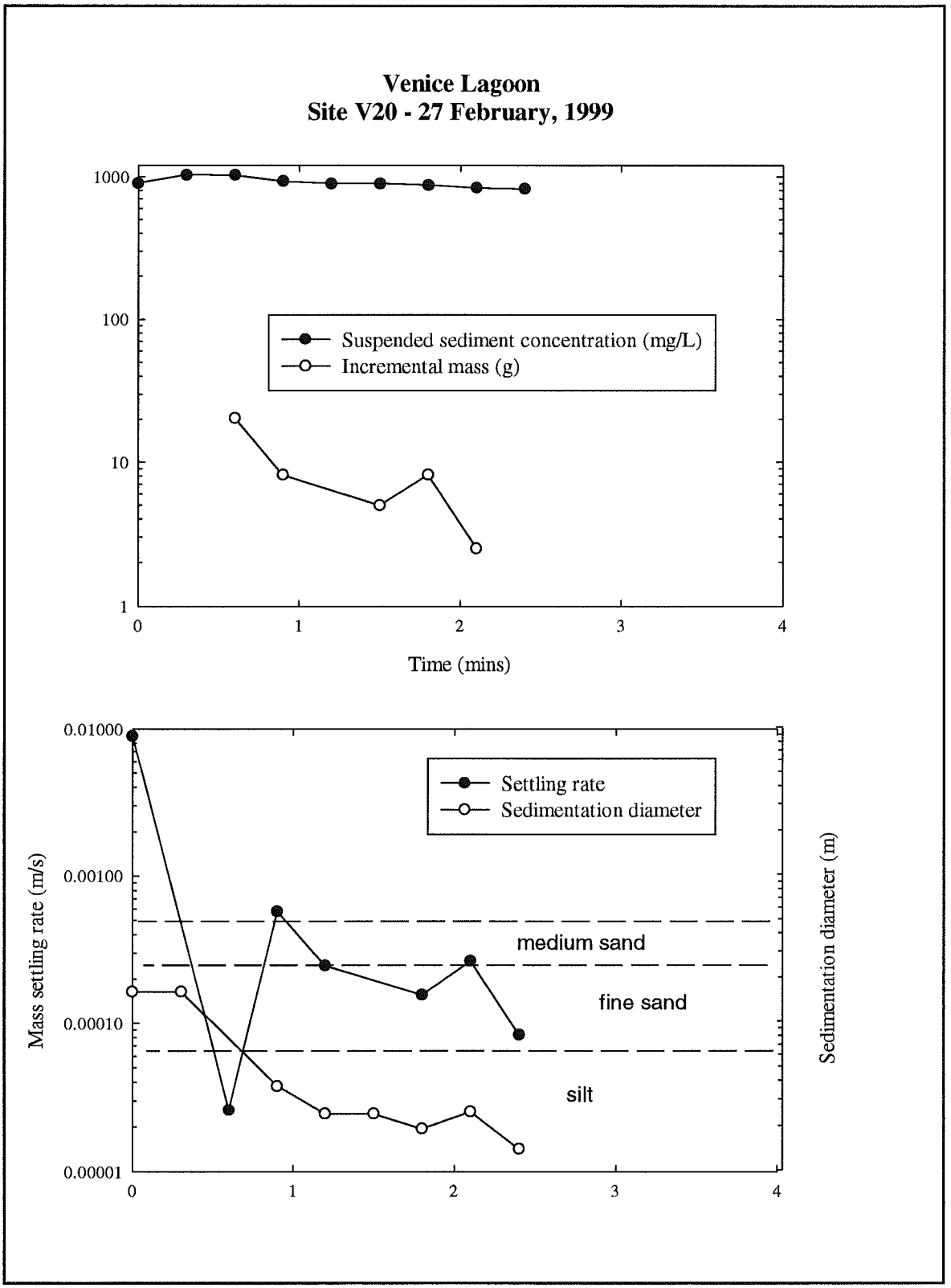

Figure 4.3.1 : The still water settling of material eroded in Sea Carousel at site V20 (A) suspended sediment concentration decay and incremental mass deposition, (B) estimated mass settling rate and equivalent sedimentation diameter. Note the decrease in size from fine sand to silt with time.

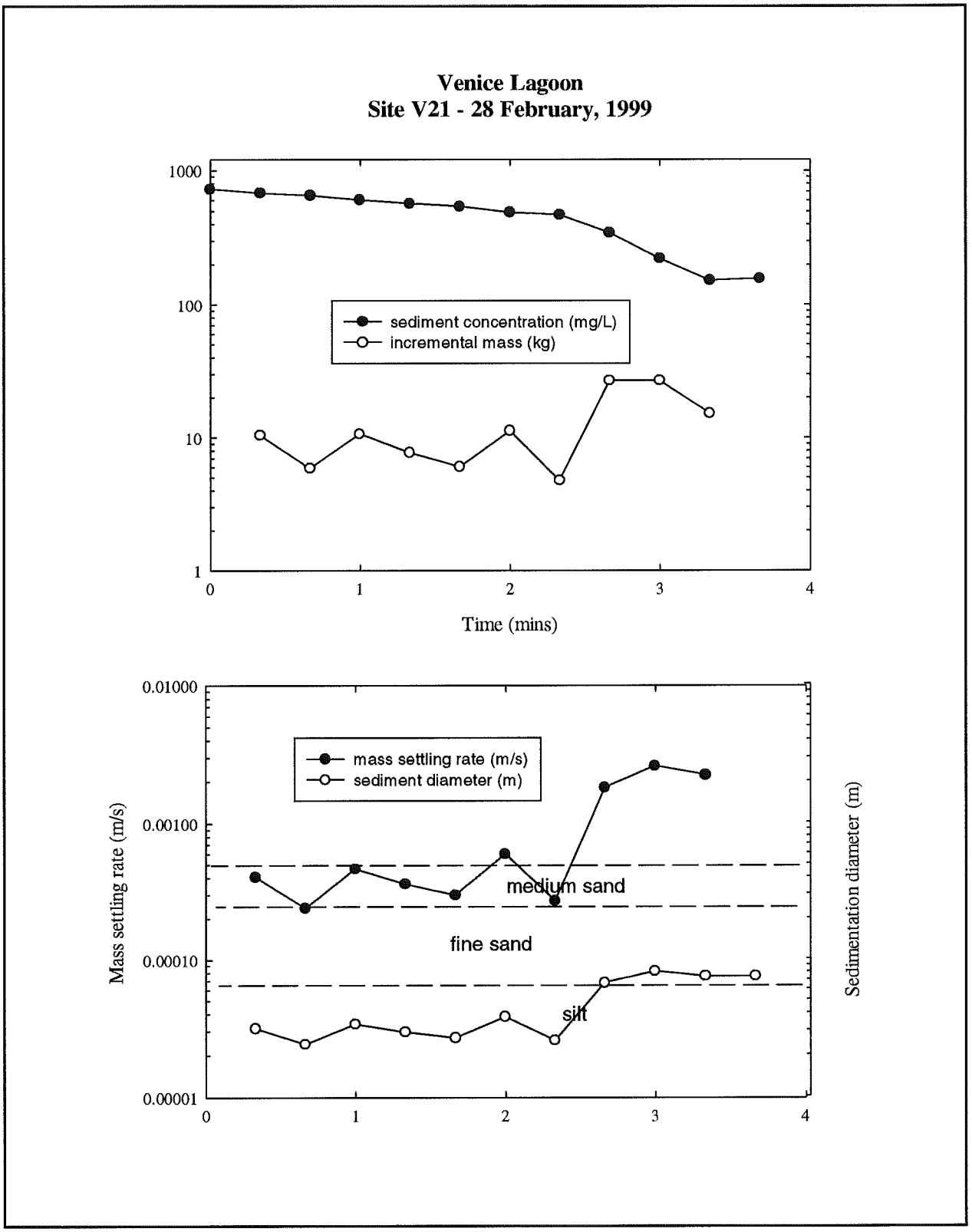

Figure 4.3.2 : The still water settling of material eroded in Sea Carousel at site V21 (A) suspended sediment concentration decay and incremental mass deposition, (B) estimated mass settling rate and equivalent sedimentation diameter

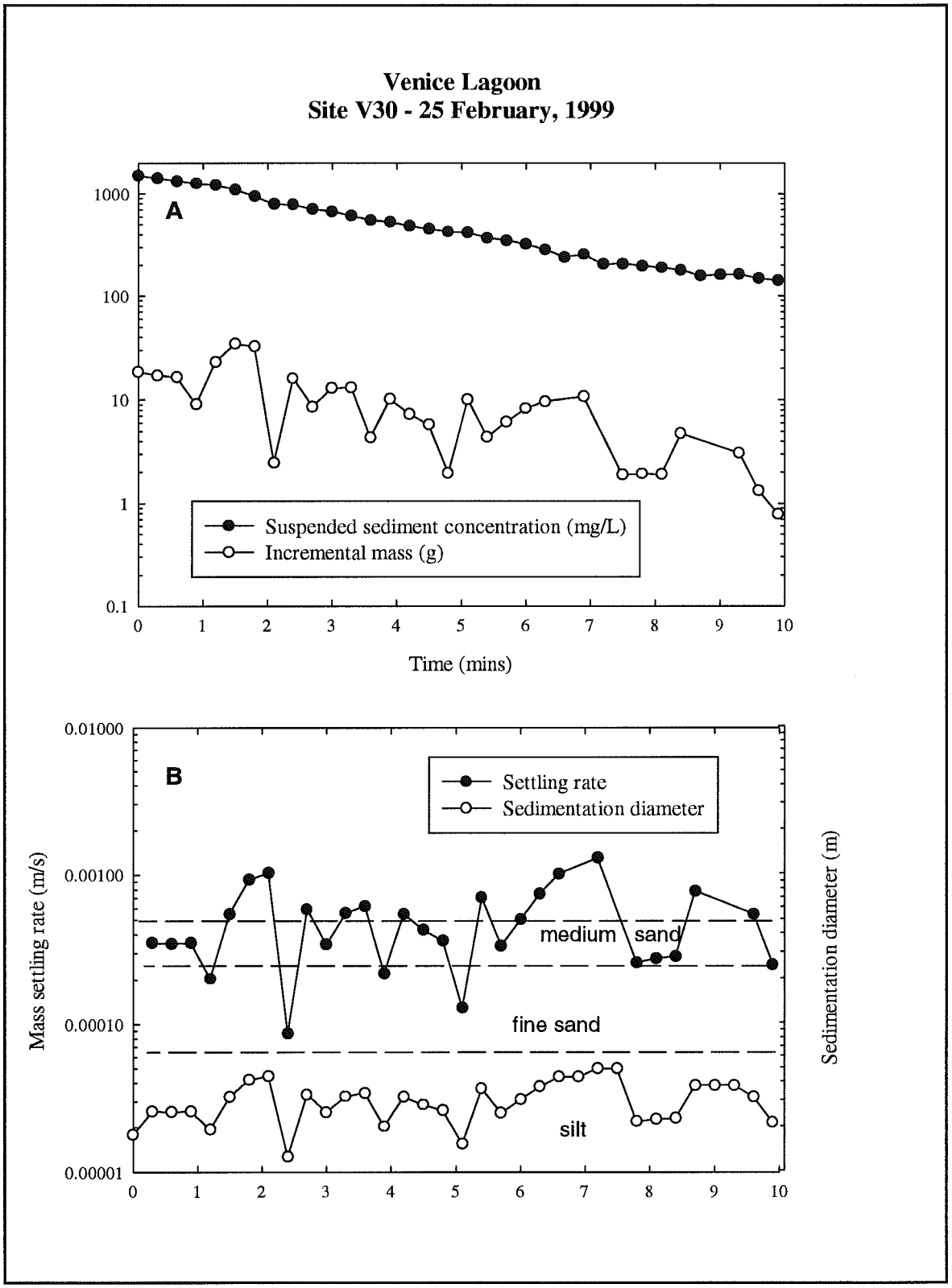

Figure 4.3.3 : The still water settling of material eroded in Sea Carousel at site V30 (A) suspended sediment concentration decay and incremental mass deposition, (B) estimated mass settling rate and equivalent sedimentation diameter. Note the constant size of material in the coarse silt range.

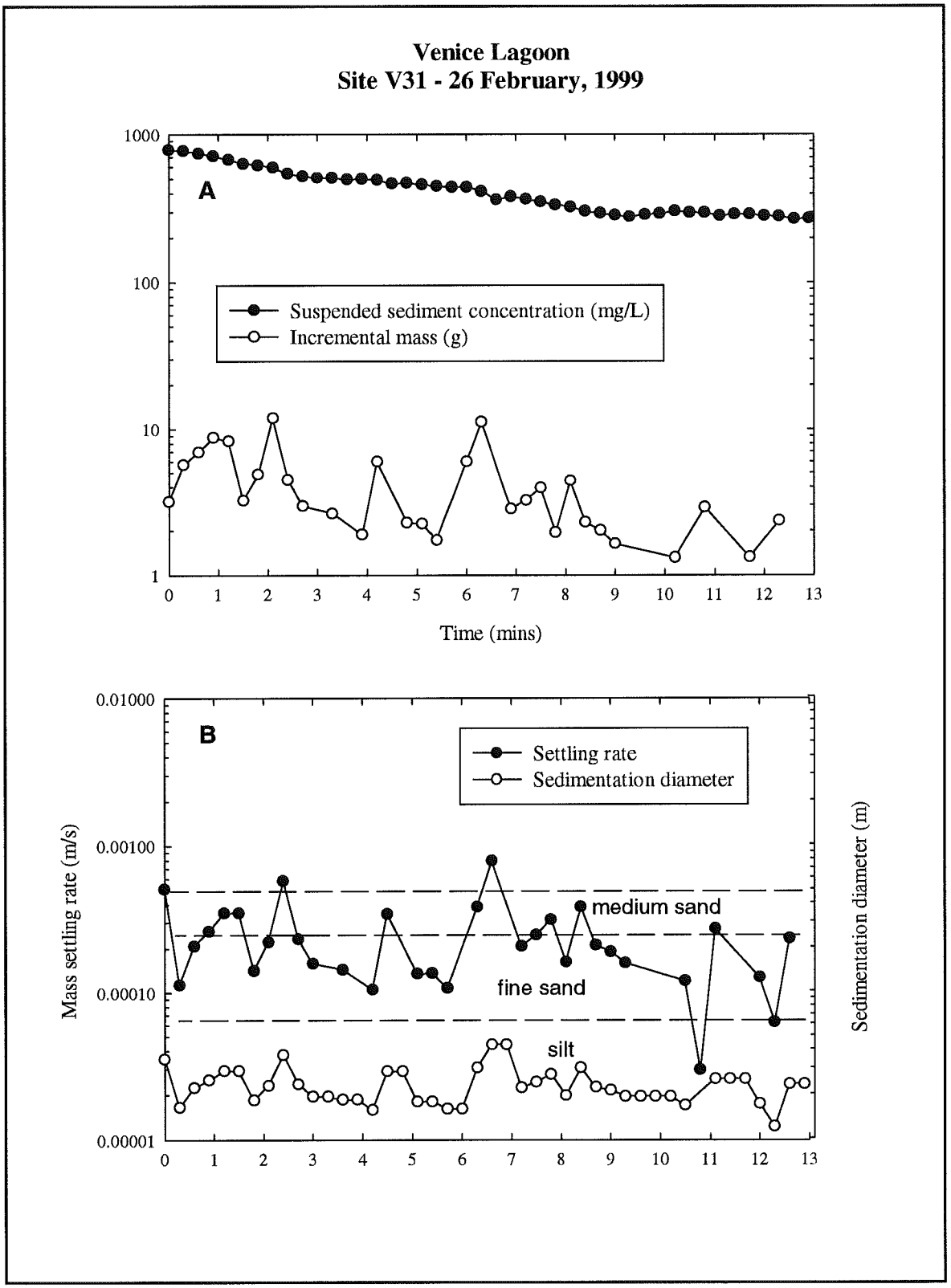

Figure 4.3.4 : The still water settling of material eroded in Sea Carousel at site V31 (A) suspended sediment concentration decay and incremental mass deposition, (B) estimated mass settling rate and equivalent sedimentation diameter. The material in suspension appears consistent in the coarse silt range.

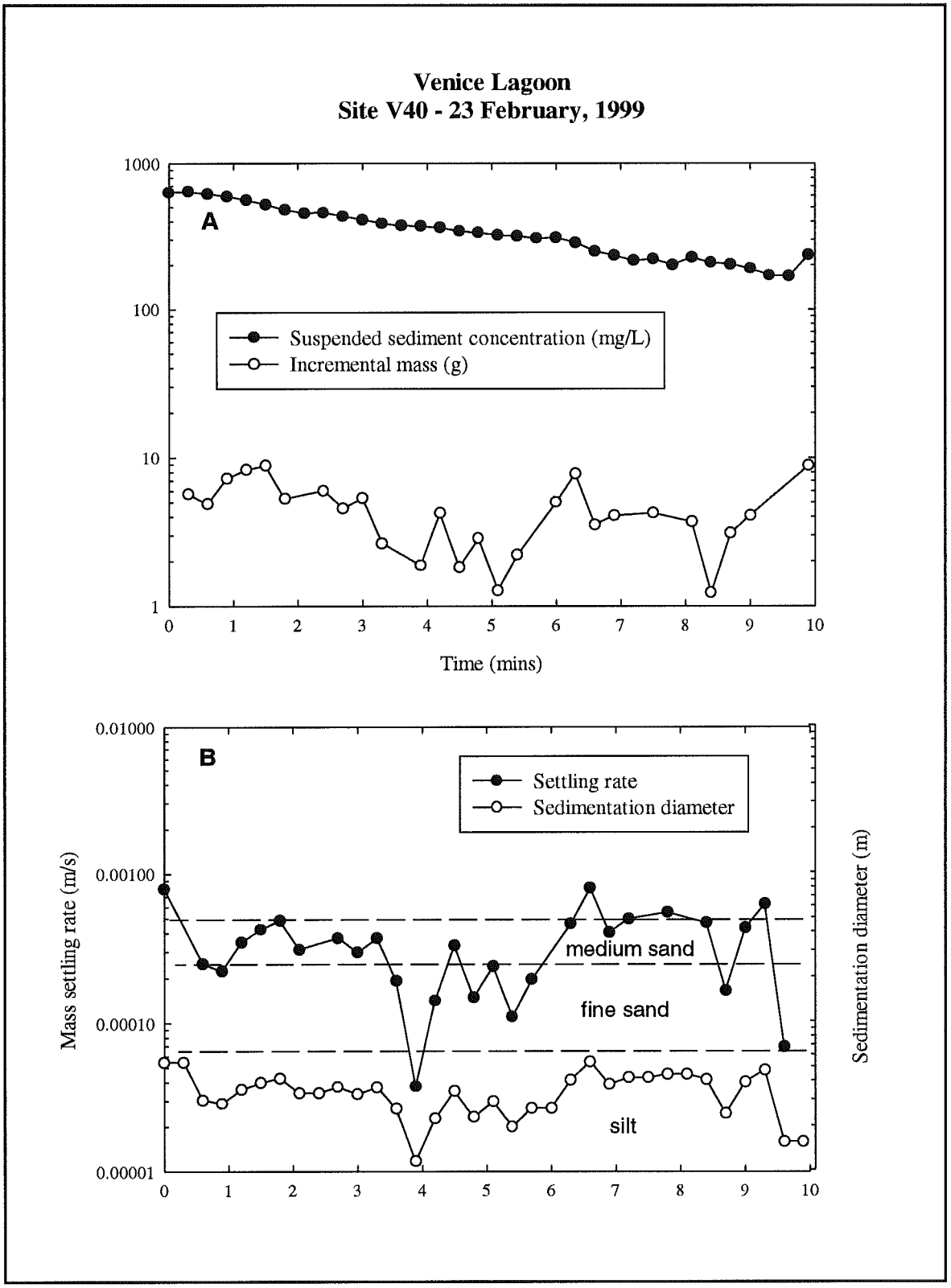

Figure 4.3.5 : The still water settling of material eroded in Sea Carousel at site V40 (A) suspended sediment concentration decay and incremental mass deposition, (B) estimated mass settling rate and equivalent sedimentation diameter.

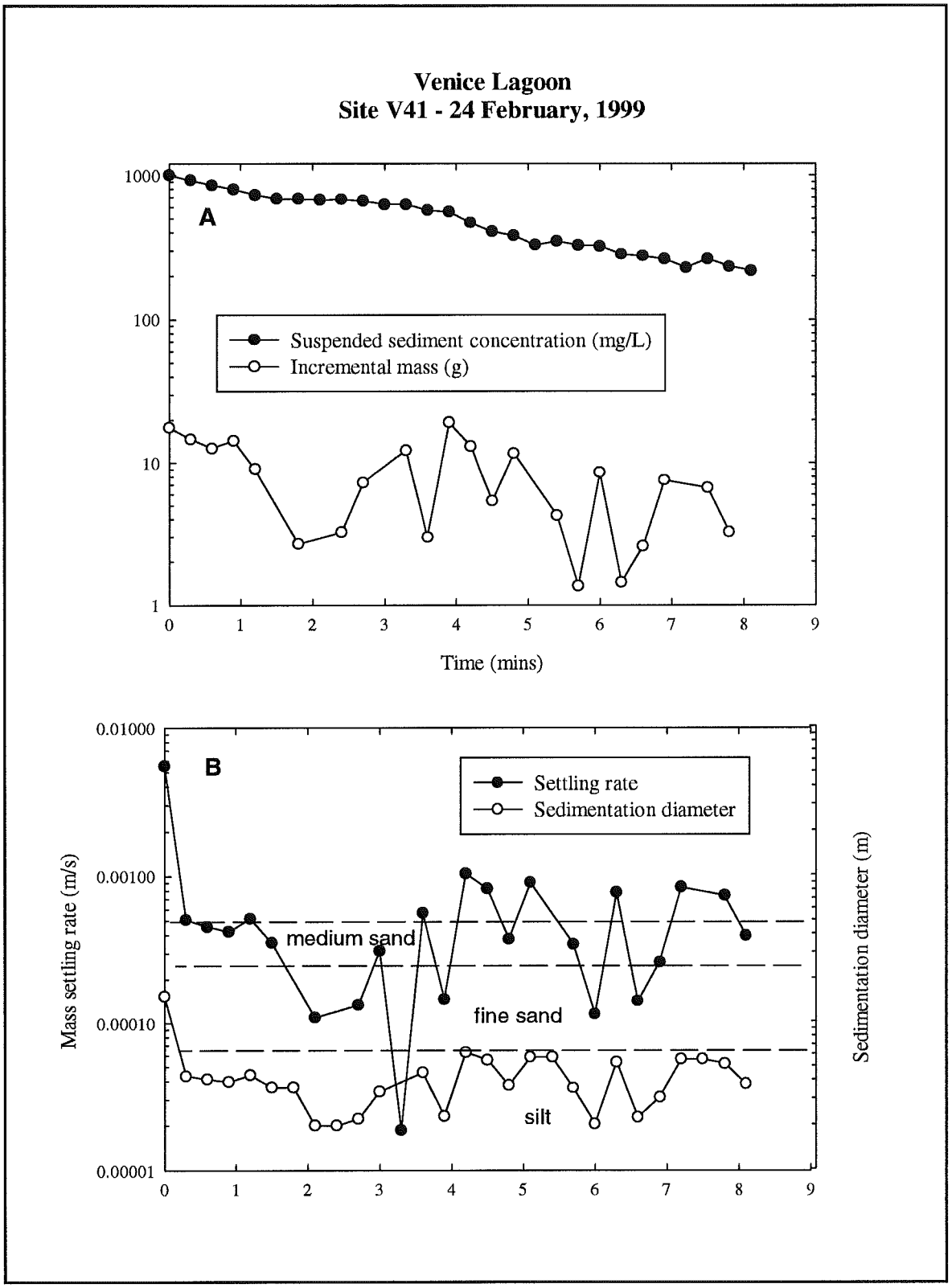

Figure 4.3.6 : The still water settling of material eroded in Sea Carousel at site V41 (A) suspended sediment concentration decay and incremental mass deposition, (B) estimated mass settling rate and equivalent sedimentation diameter.

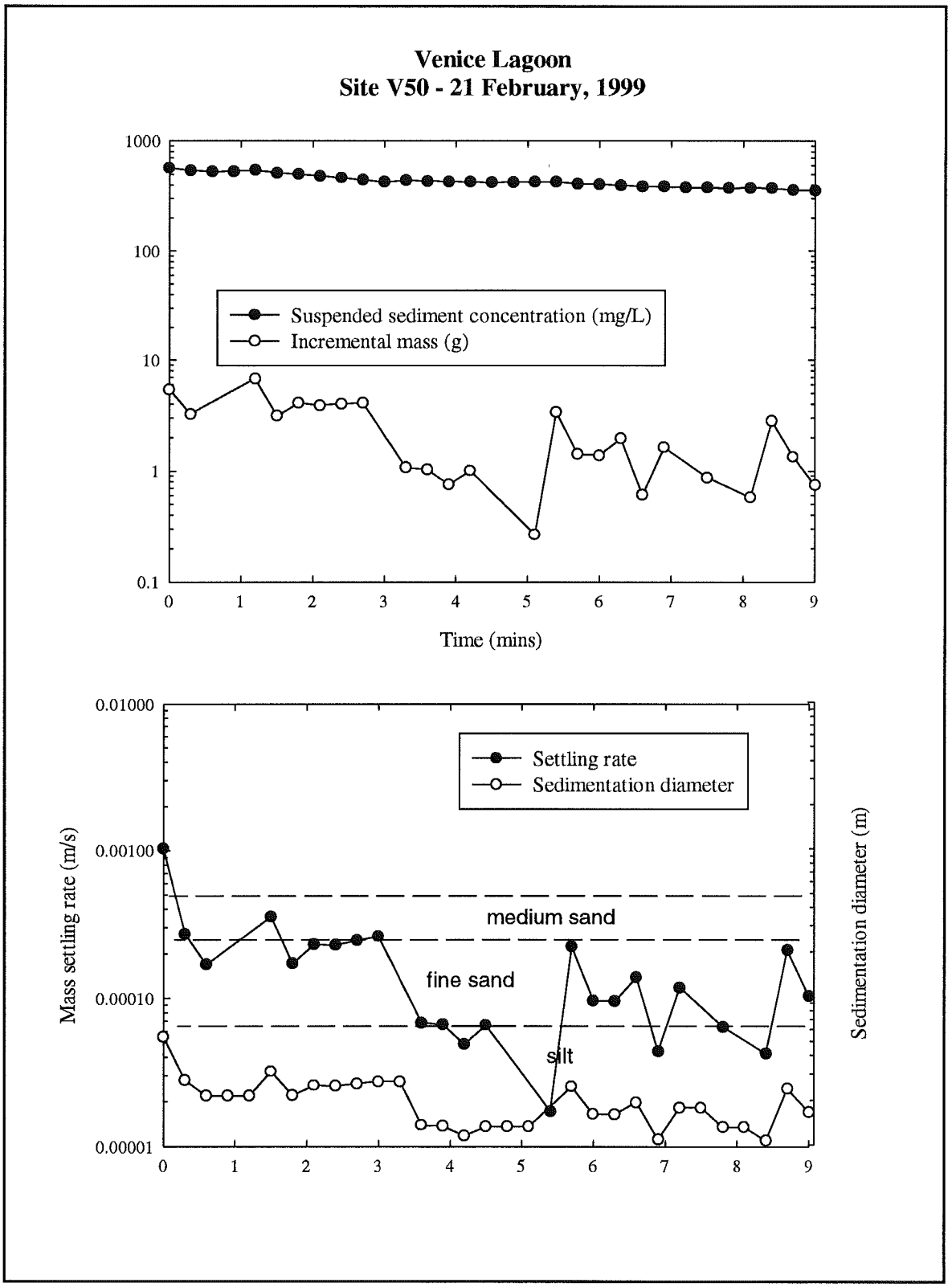

Figure 4.3.7 : The still water settling of material eroded in Sea Carousel at site V50 (A) suspended sediment concentration decay and incremental mass deposition, (B) estimated mass settling rate and equivalent sedimentation diameter. Note the decrease in size from coarse to medium silt with time.

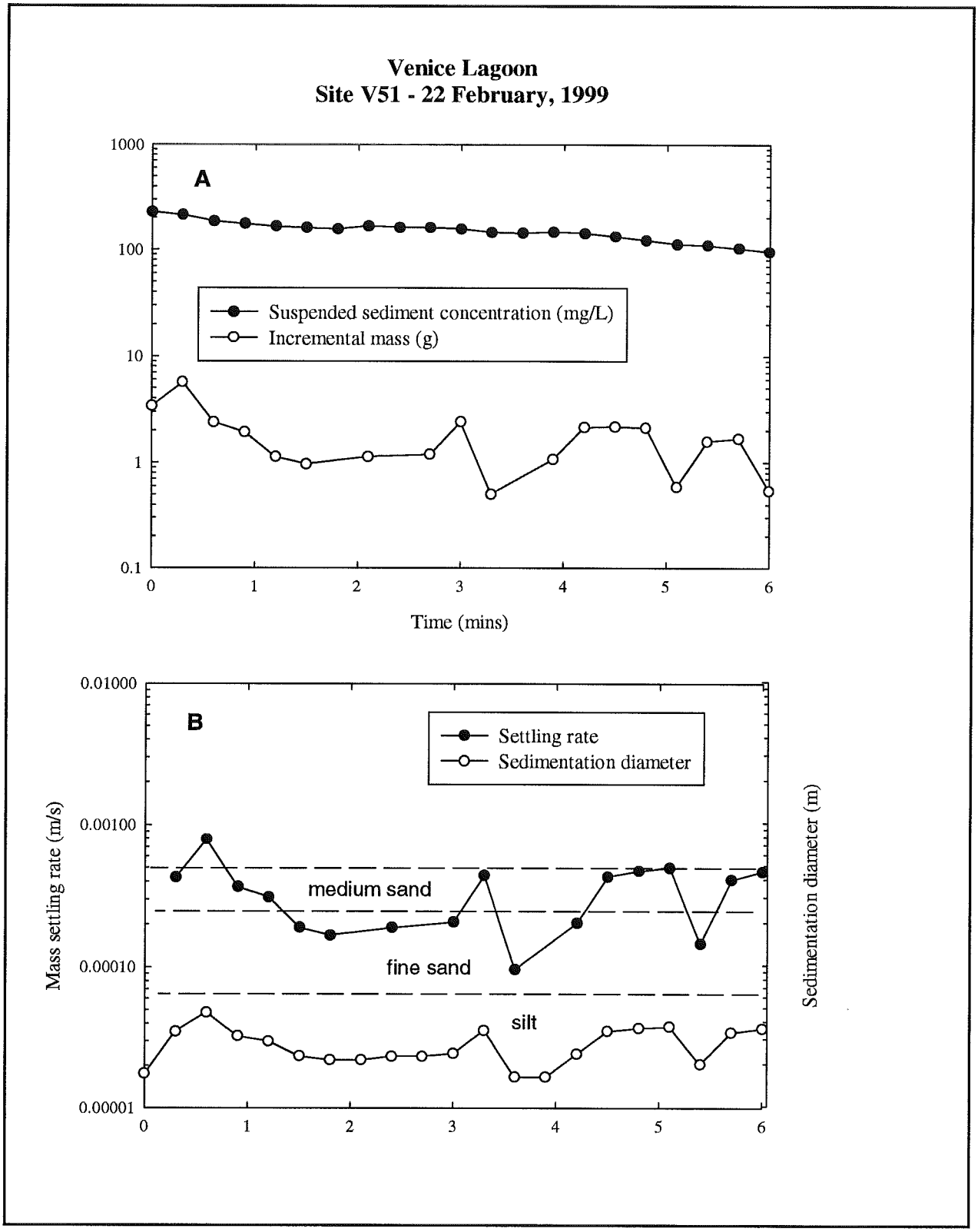

Figure 4.3.8 : The still water settling of material eroded in Sea Carousel at site V51 (A) suspended sediment concentration decay and incremental mass deposition, (B) estimated mass settling rate and equivalent sedimentation diameter.

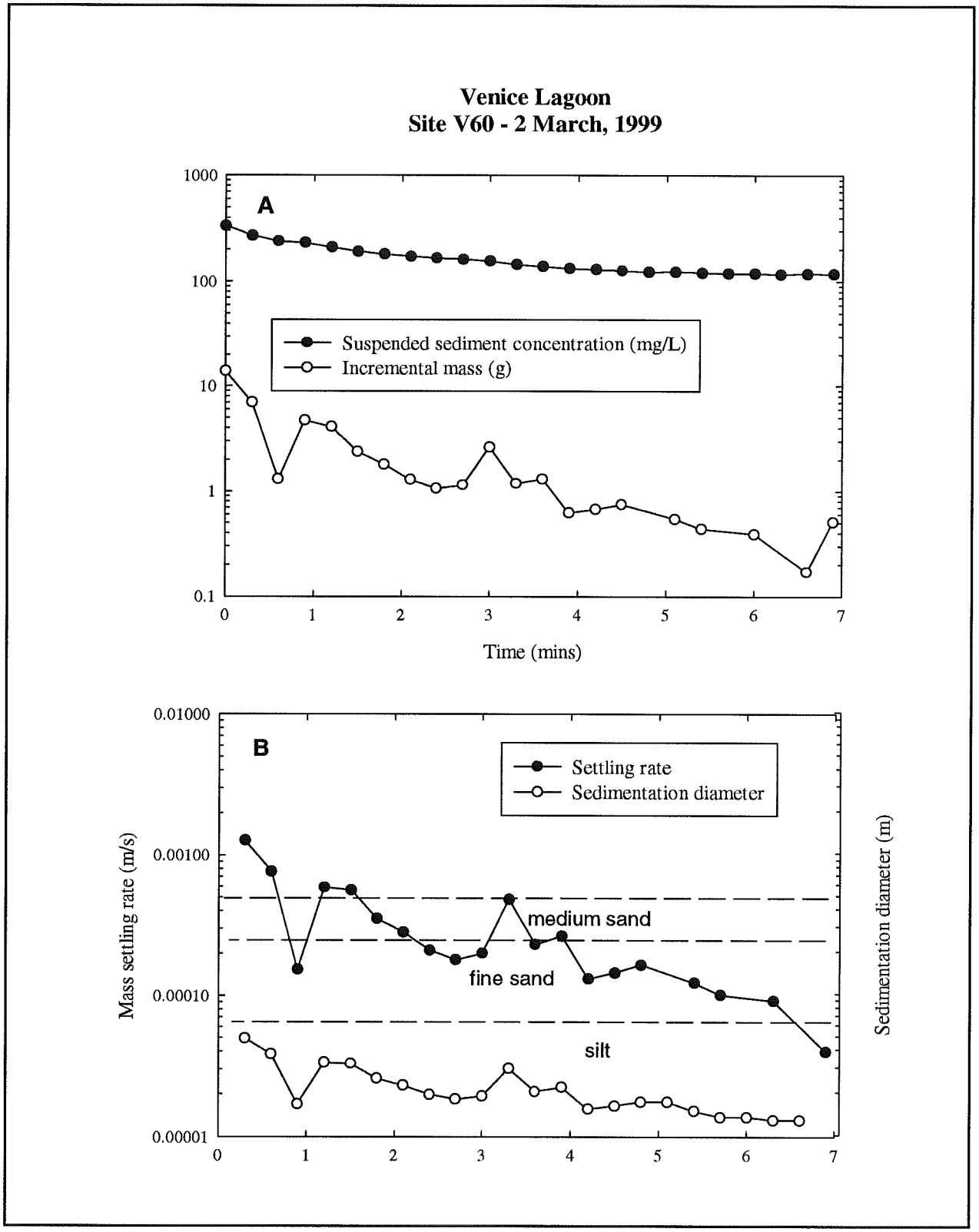

Figure 4.3.9 : The still water settling of material eroded in Sea Carousel at site V60 (A) suspended sediment concentration decay and incremental mass deposition, (B) estimated mass settling rate and equivalent sedimentation diameter. Note the steady decrease in size from coarse to medium silt with time.

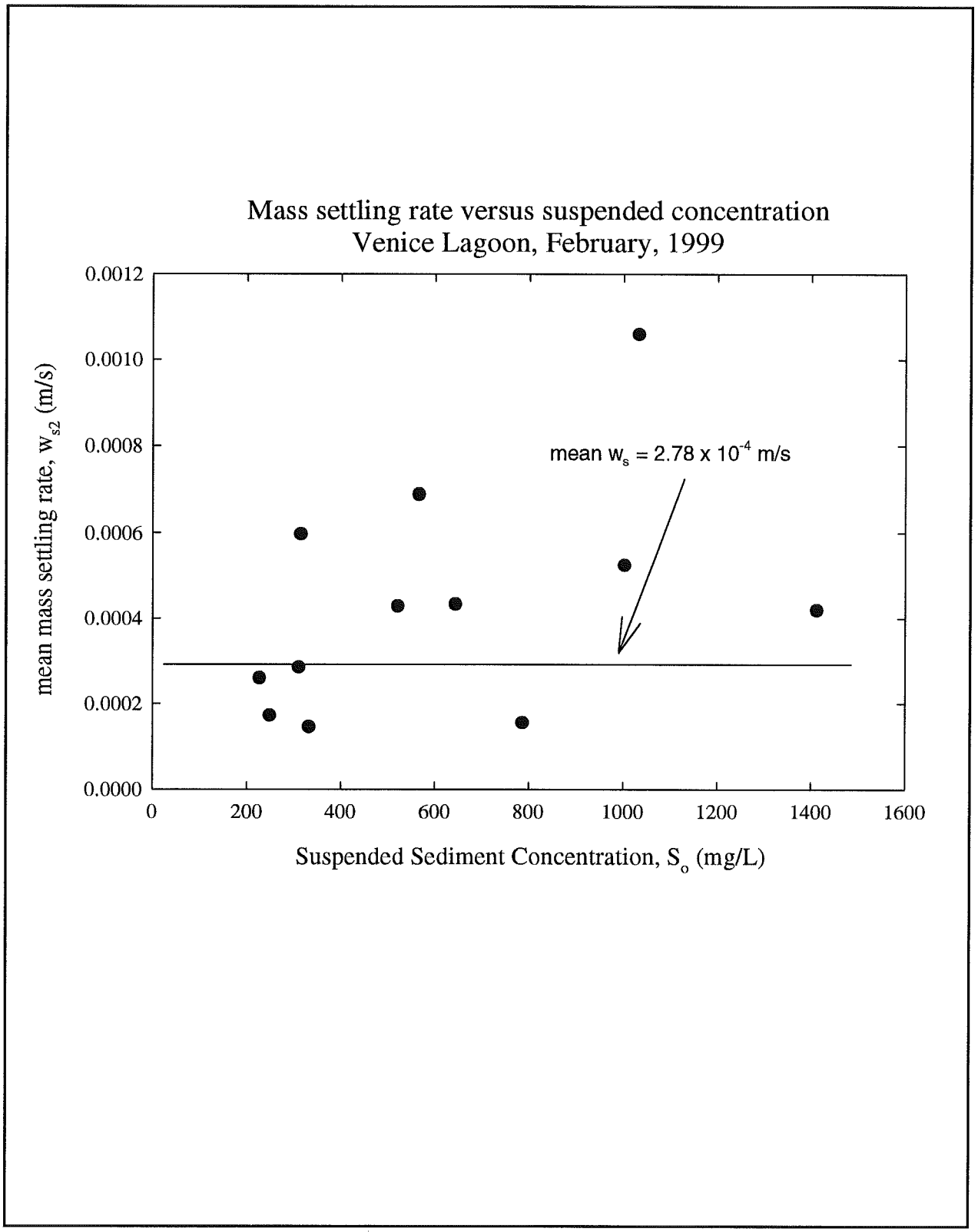

Figure 4.3.10 : Mean mass settling rate plotted versus starting suspended sediment concentration (S_0). There appears to be no relationship between the two variables, which supports the summer trends. The mean W_s value is about 50% that found during the summer indicating a longer setting time during winter.

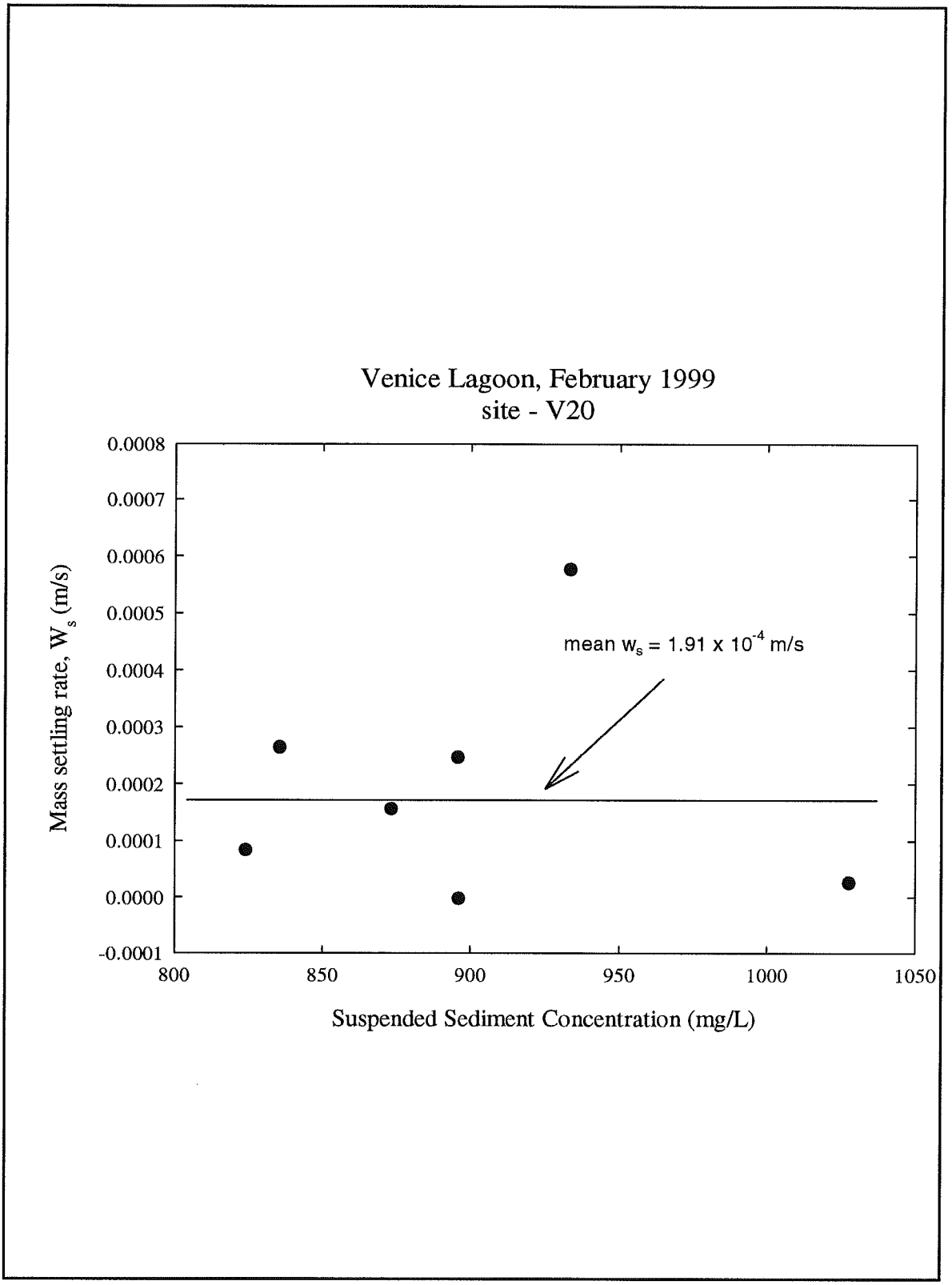

Figure 4.3.11 : Mass settling velocity of the initial plume suspended in Sea Carousel at site V20 during deployment. Notice there is no relationships between mass settling rate (Ws) and S.

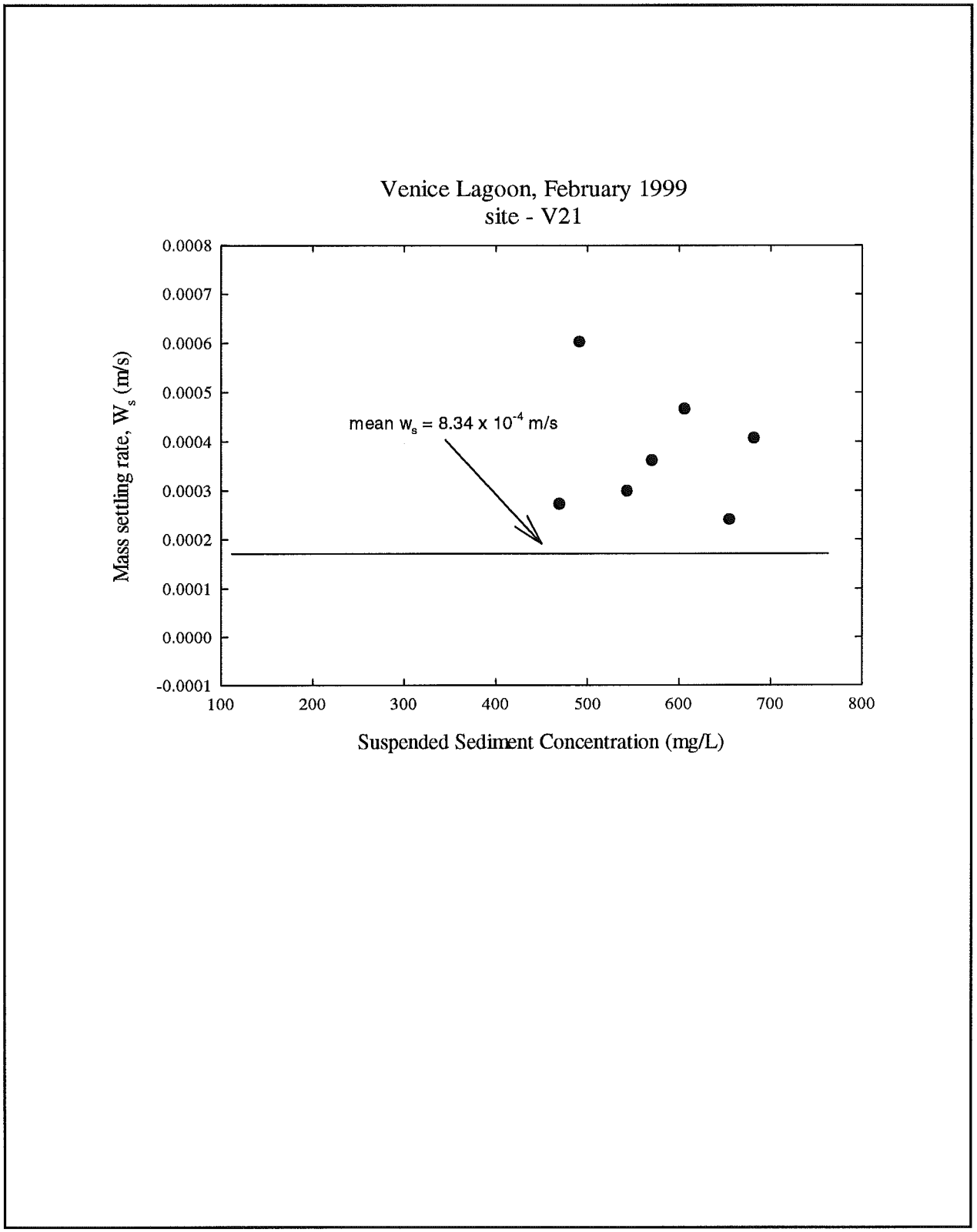

Figure 4.3.12: The mass settling velocity of material eroded into suspension in Sea Carousel at site V21 during late deployment.

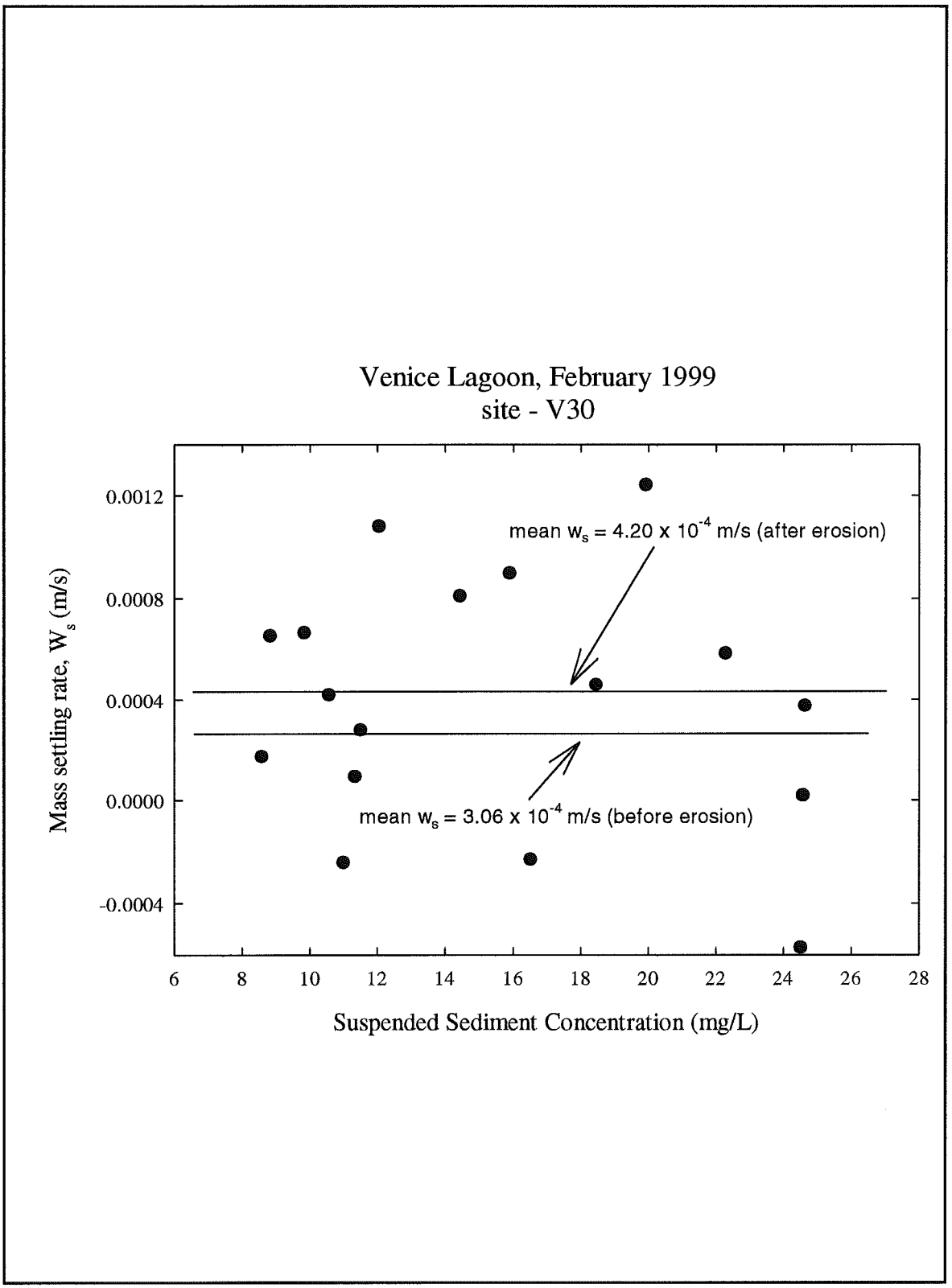

Figure 4.3.13 : Mass settling velocity of the initial plume suspended in Sea Carousel at site V30 during deployment. The settling rate before erosion was evaluated from settling of a plume suspended during initial deployment (we call this 'before erosion'). The value of Ws derived 'after erosion' was made during the end of the deployment and reflects the effects of the maximum bed shear stress.

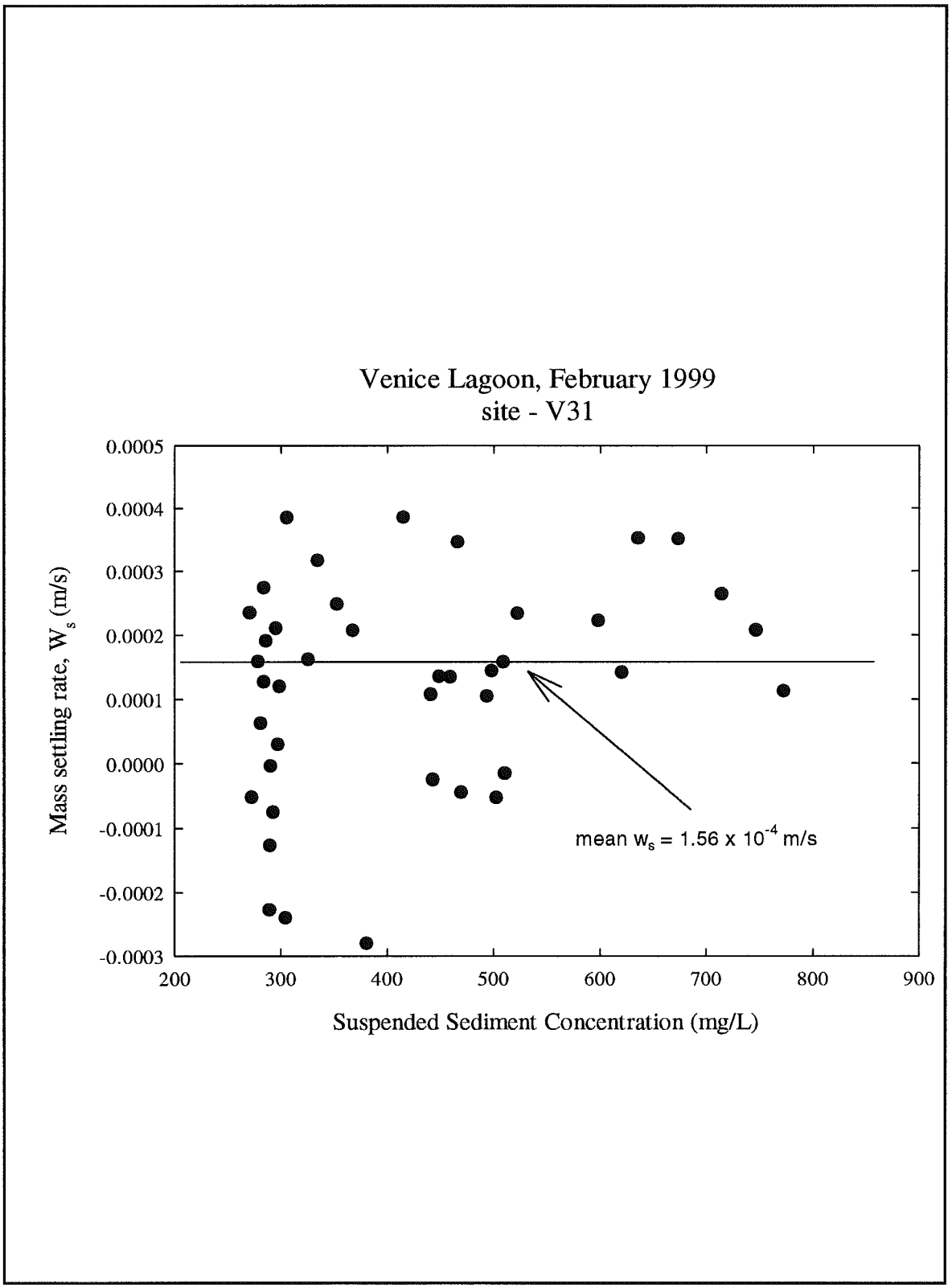

Figure 4.3.14 : Mass settling velocity of the initial plume suspended in Sea Carousel at site V31 during deployment.

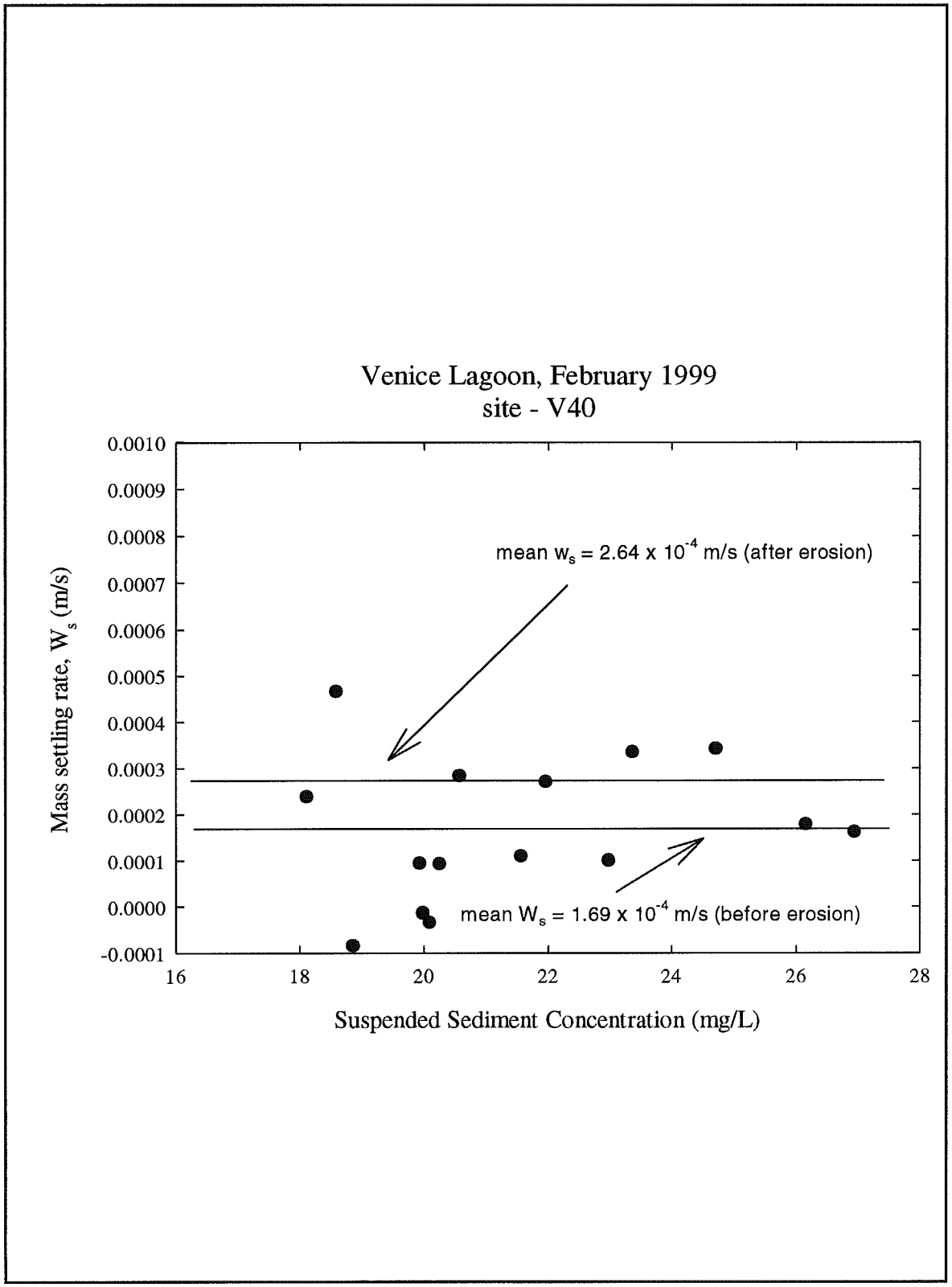

Figure 4.3.15 : Mass settling velocity of the initial plume suspended in Sea Carousel at site V40 during deployment.

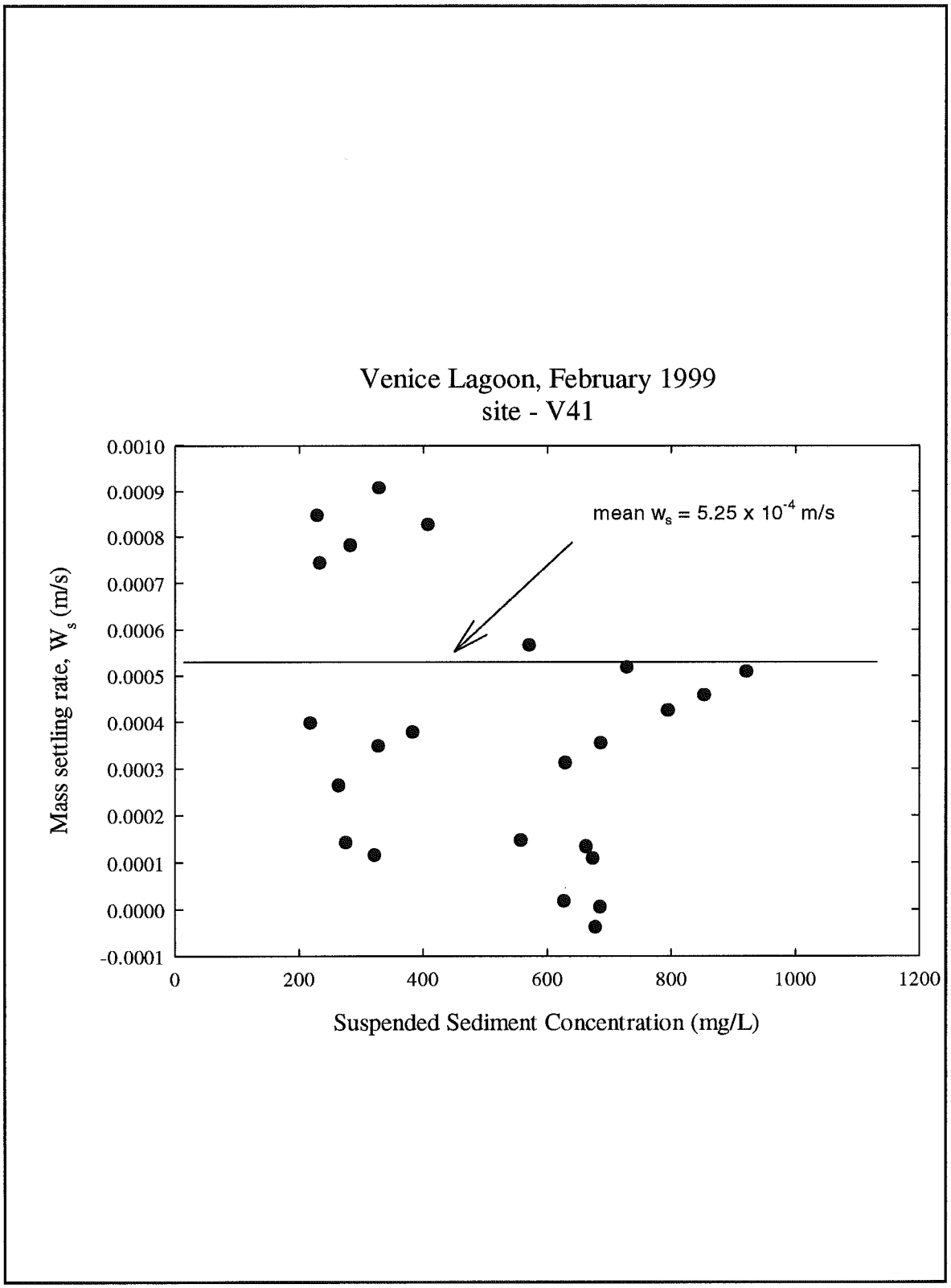

Figure 4.3.16 : Mass settling velocity of the initial plume suspended in Sea Carousel at site V41 during deployment.

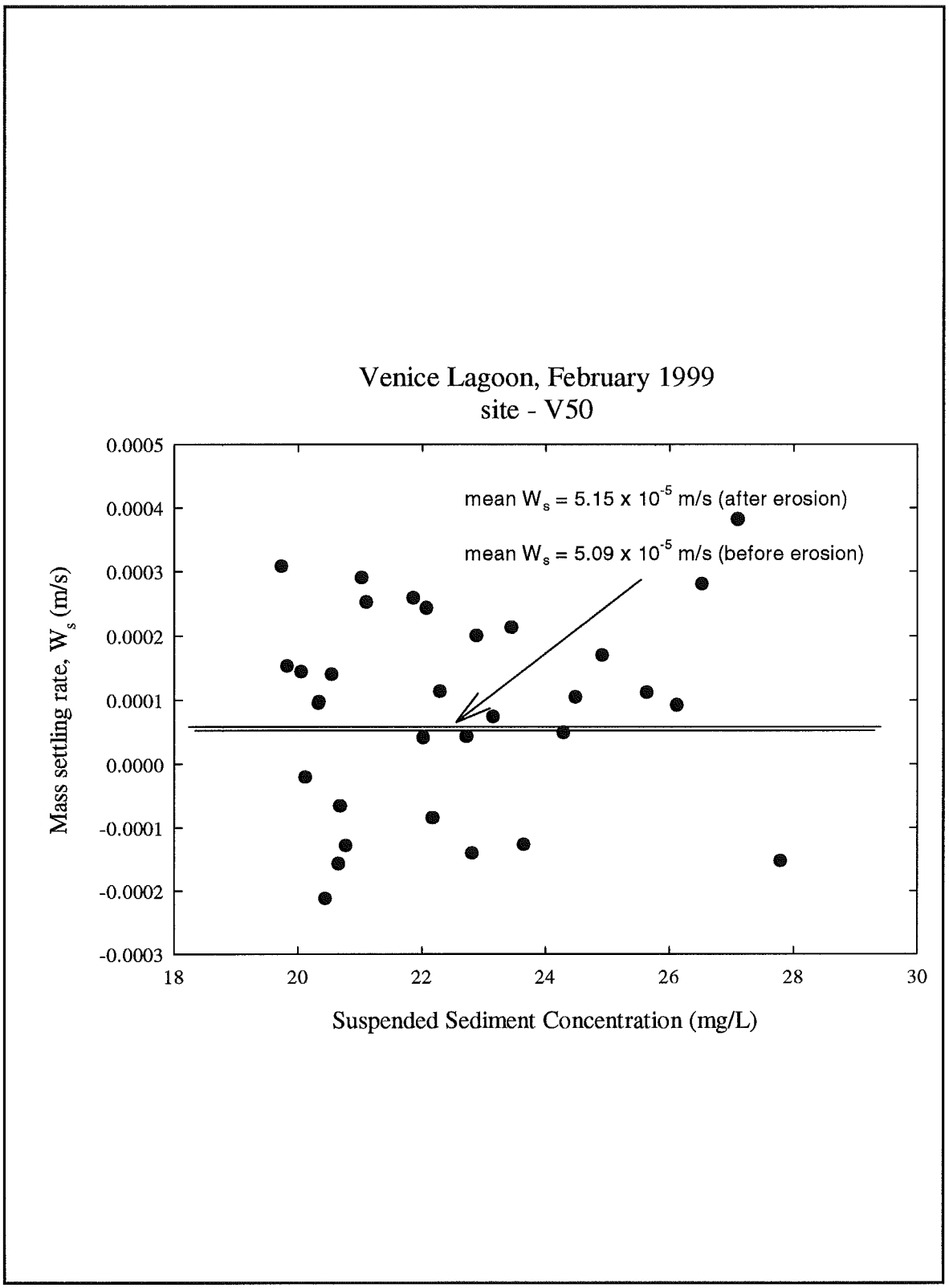

Figure 4.3.17 : Mass settling velocity of the initial plume suspended in Sea Carousel at site V50 during deployment.

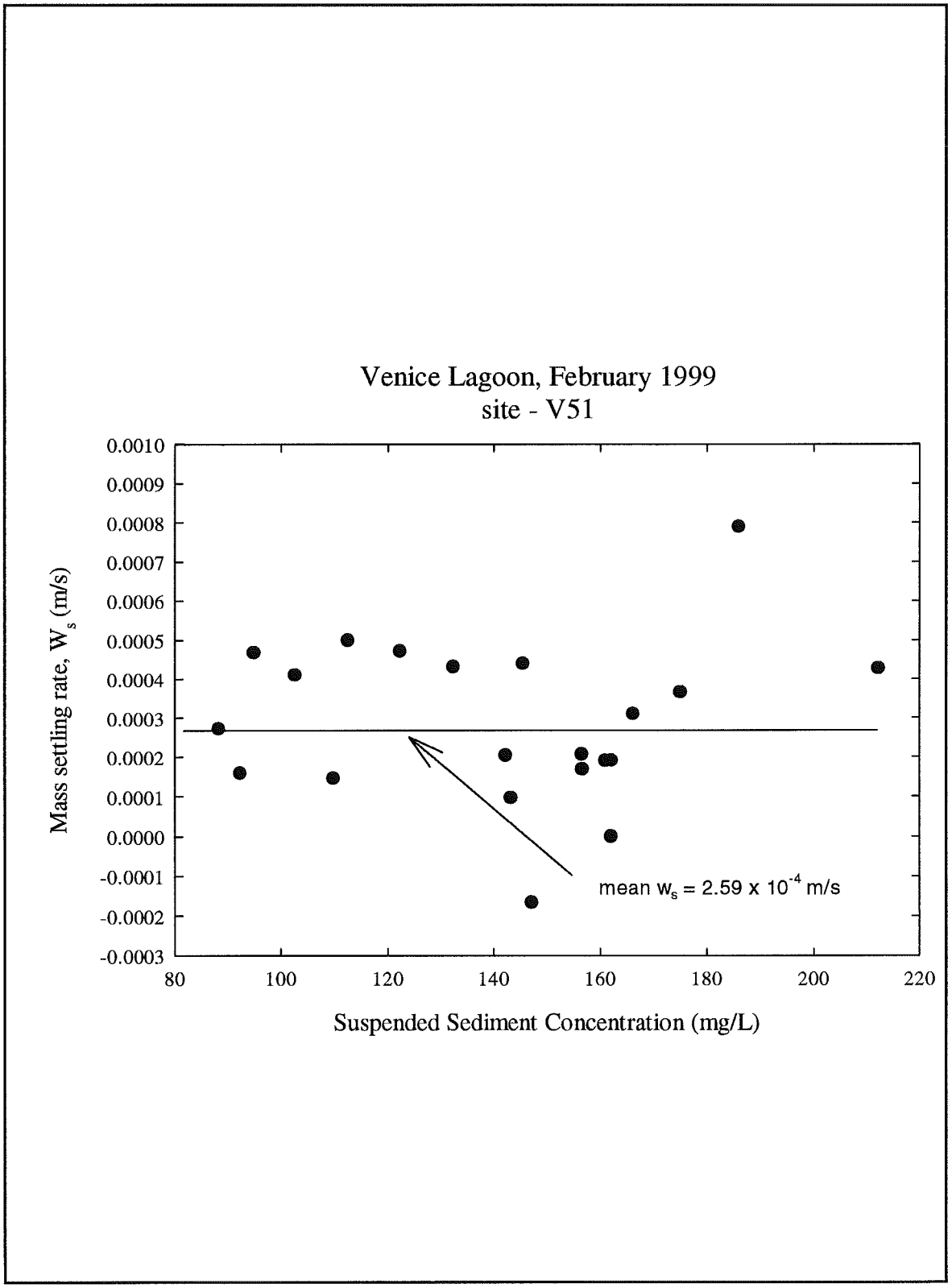

Figure 4.3.18 : Mass settling velocity of the initial plume suspended in Sea Carousel at site V51 during deployment during deployment.

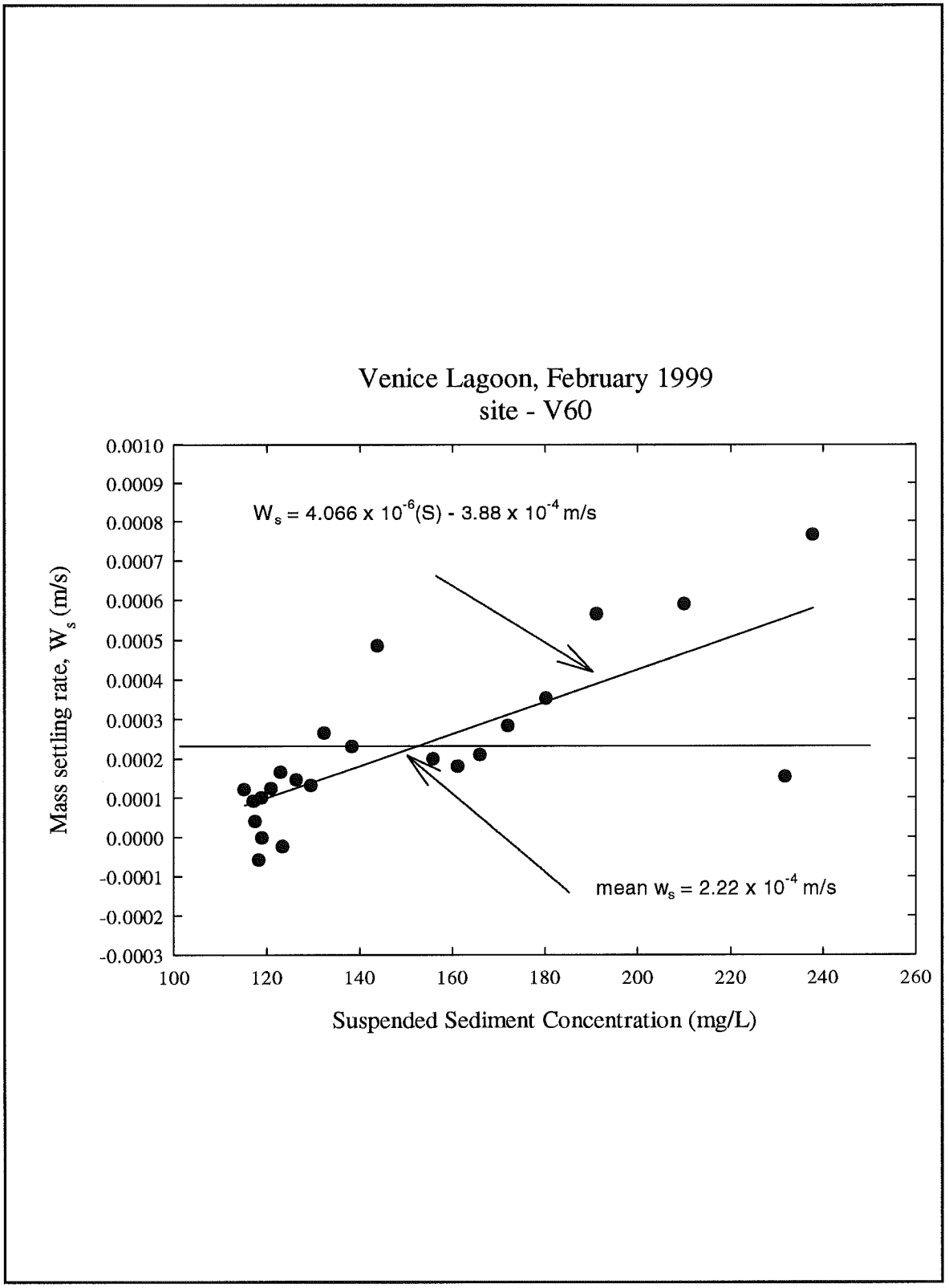

Figure 4.3.19 : Mass settling velocity of the initial plume suspended in Sea Carousel at site V60 during deployment.

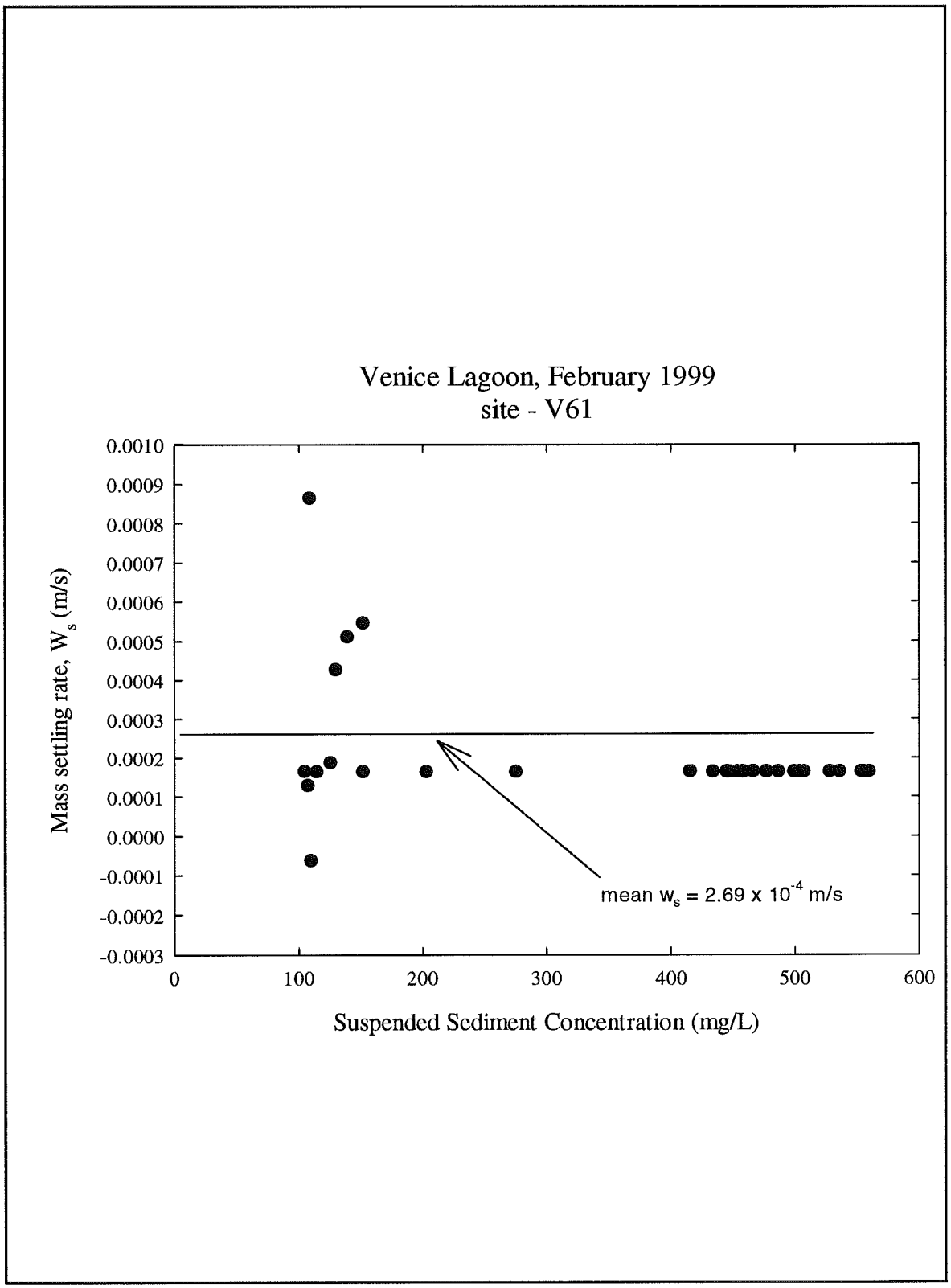

Figure 4.3.20 : Mass settling velocity of the initial plume suspended in Sea Carousel at site V61 during deployment.

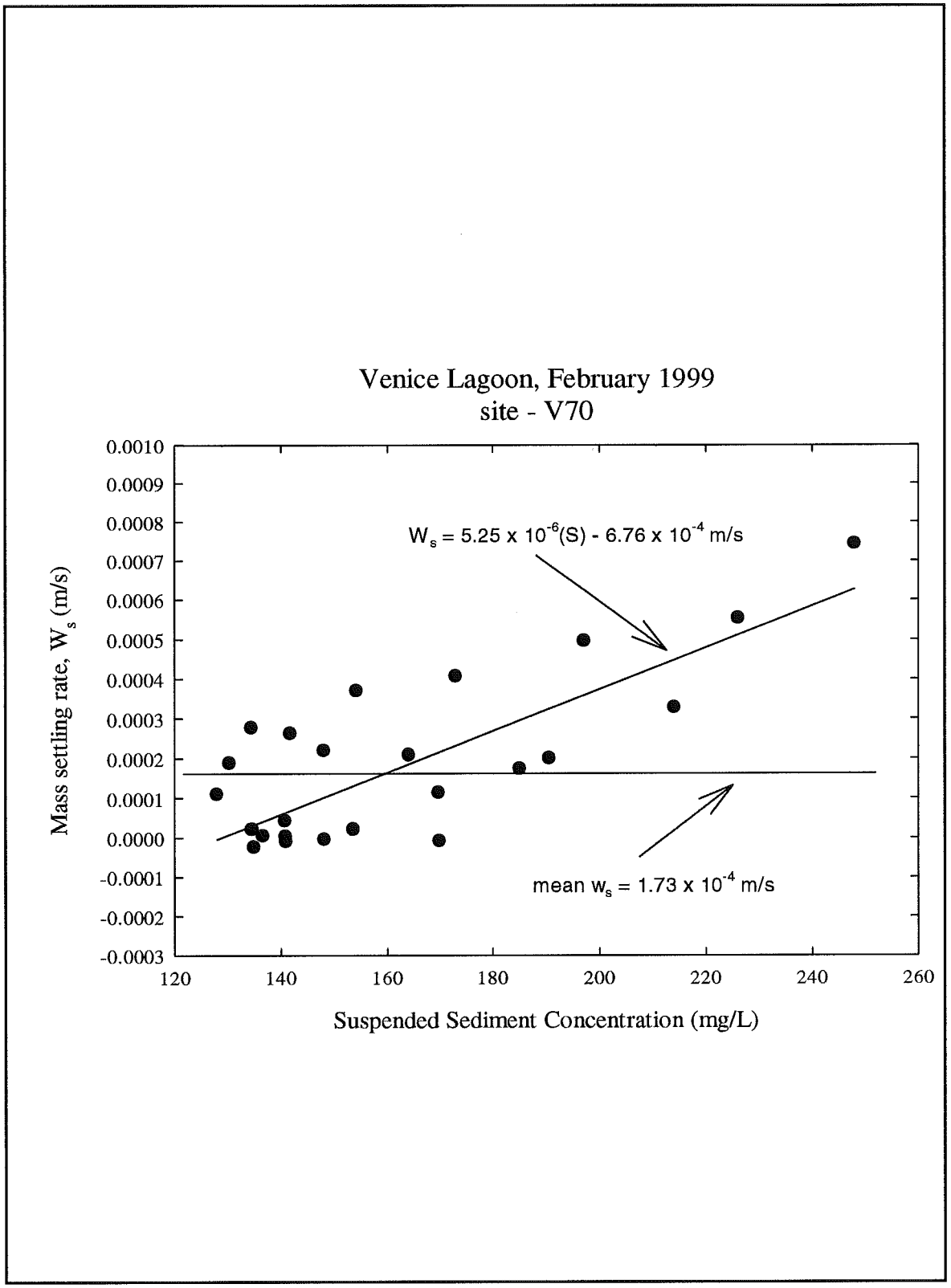

Figure 4.3.21 : Mass settling velocity of the initial plume suspended in Sea Carousel at site V70 during deployment.

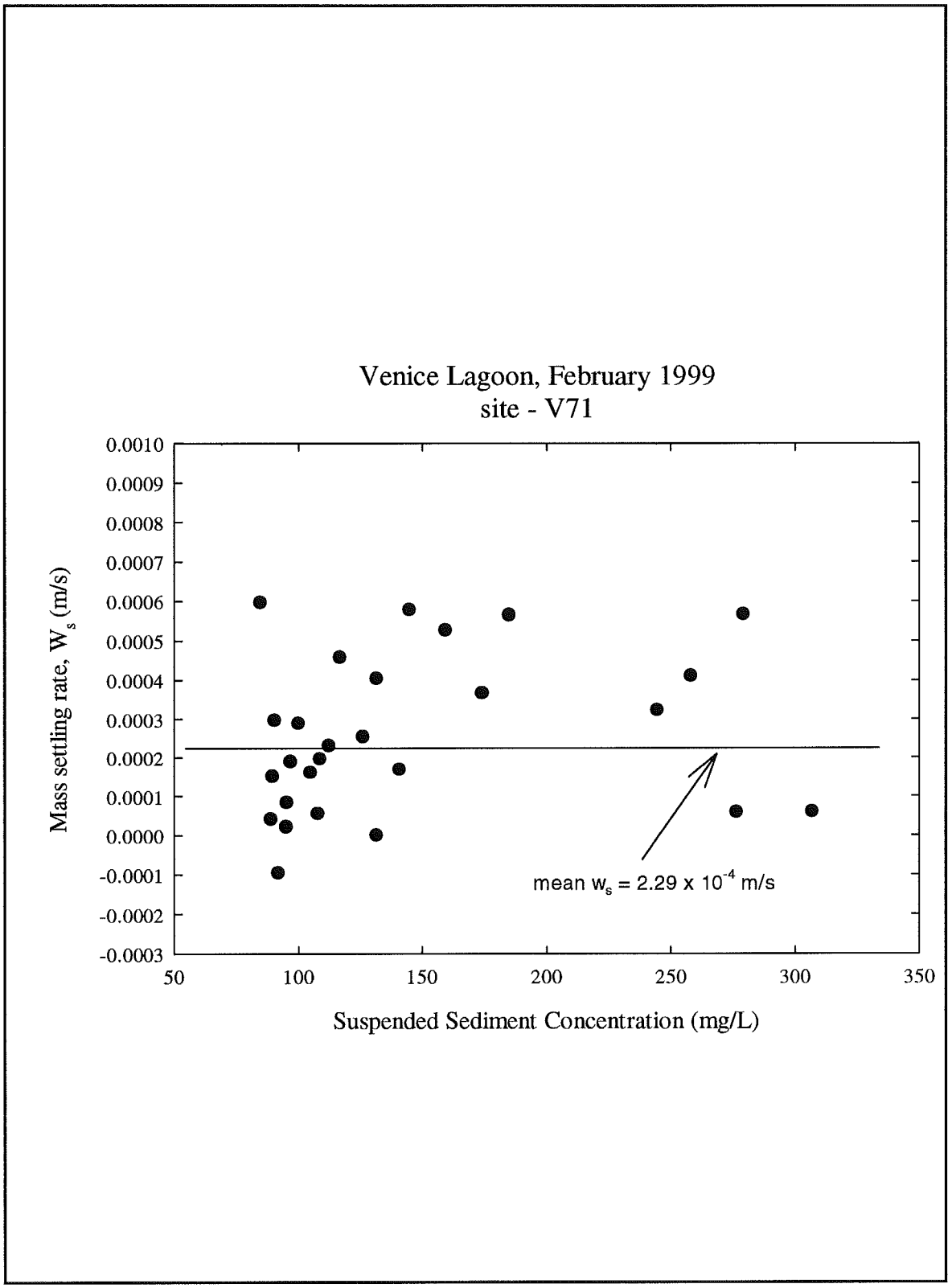

Figure 4.3.22 : Mass settling velocity of the initial plume suspended in Sea Carousel at site V71 during deployment.

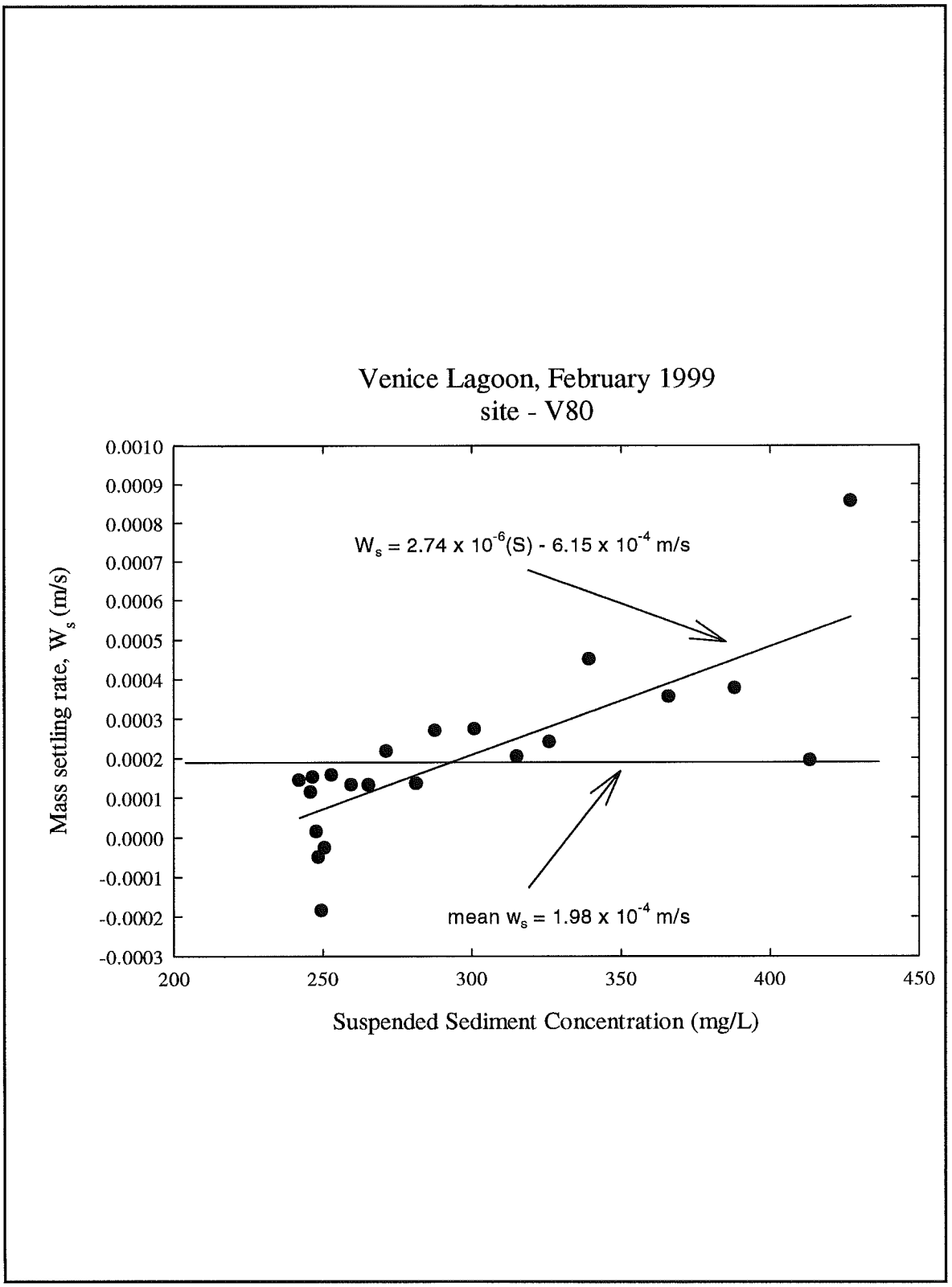

Figure 4.3.23 : Mass settling velocity of the initial plume suspended in Sea Carousel at site V80 during deployment.

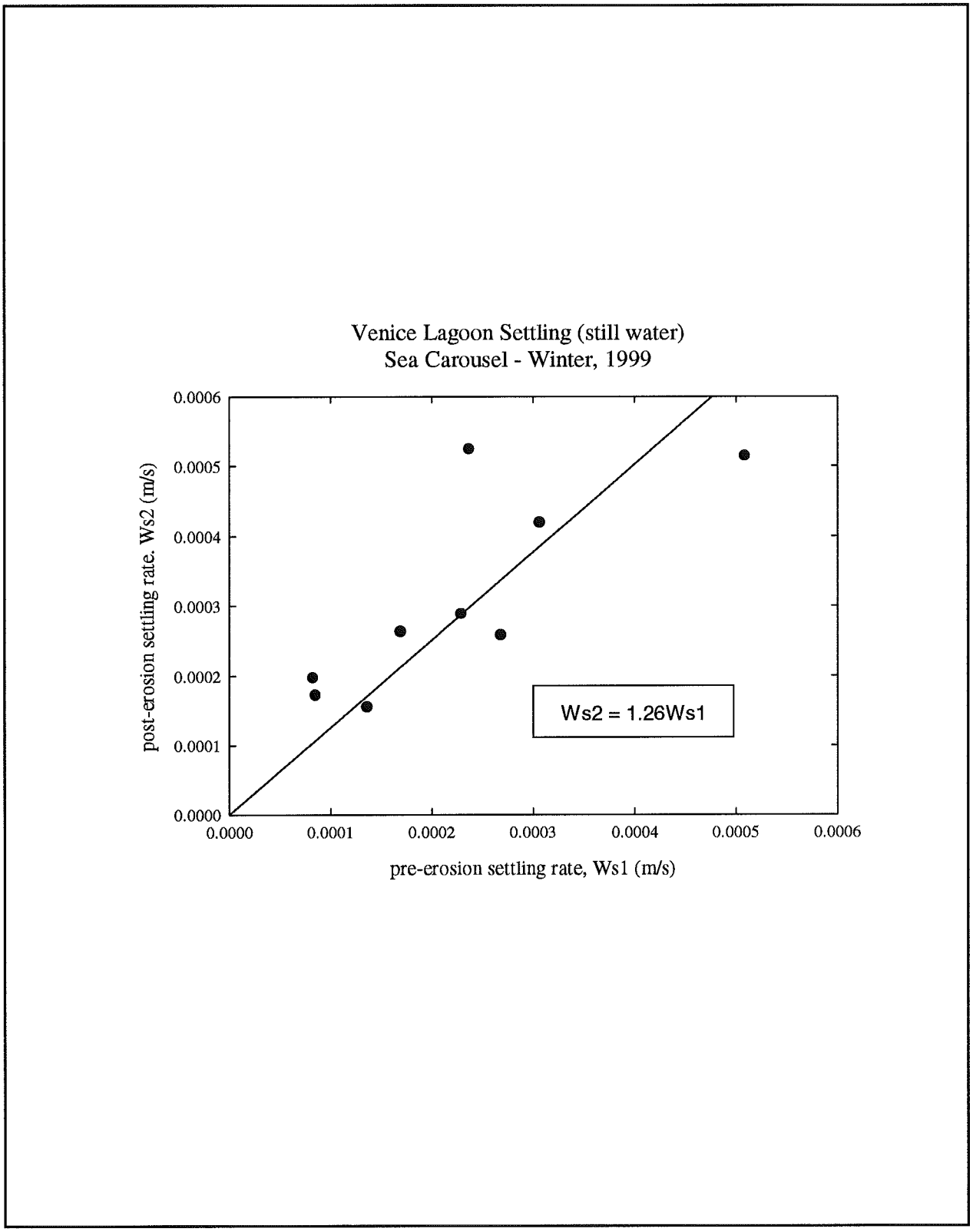

Figure 4.3.24: A comparison between settling velocities of pre-erosional (Ws1) and post-erosional (Ws2) material.

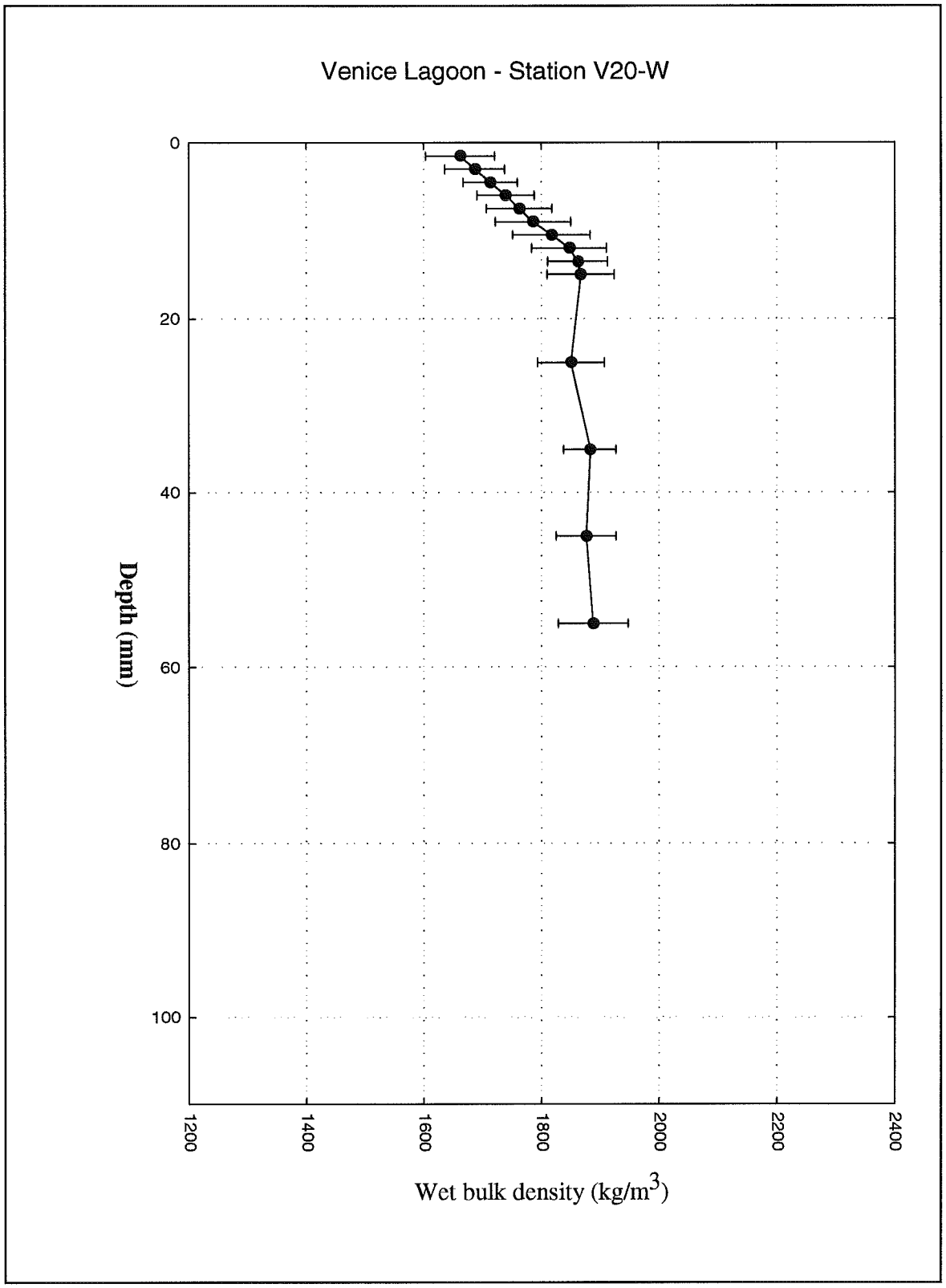

Figure 4.4.1 : A bulk density profile derived from Catscan analysis of a syringe core collected at site V20. Notice the surface layer of rapidly increasing density and the relatively constant values beneath.

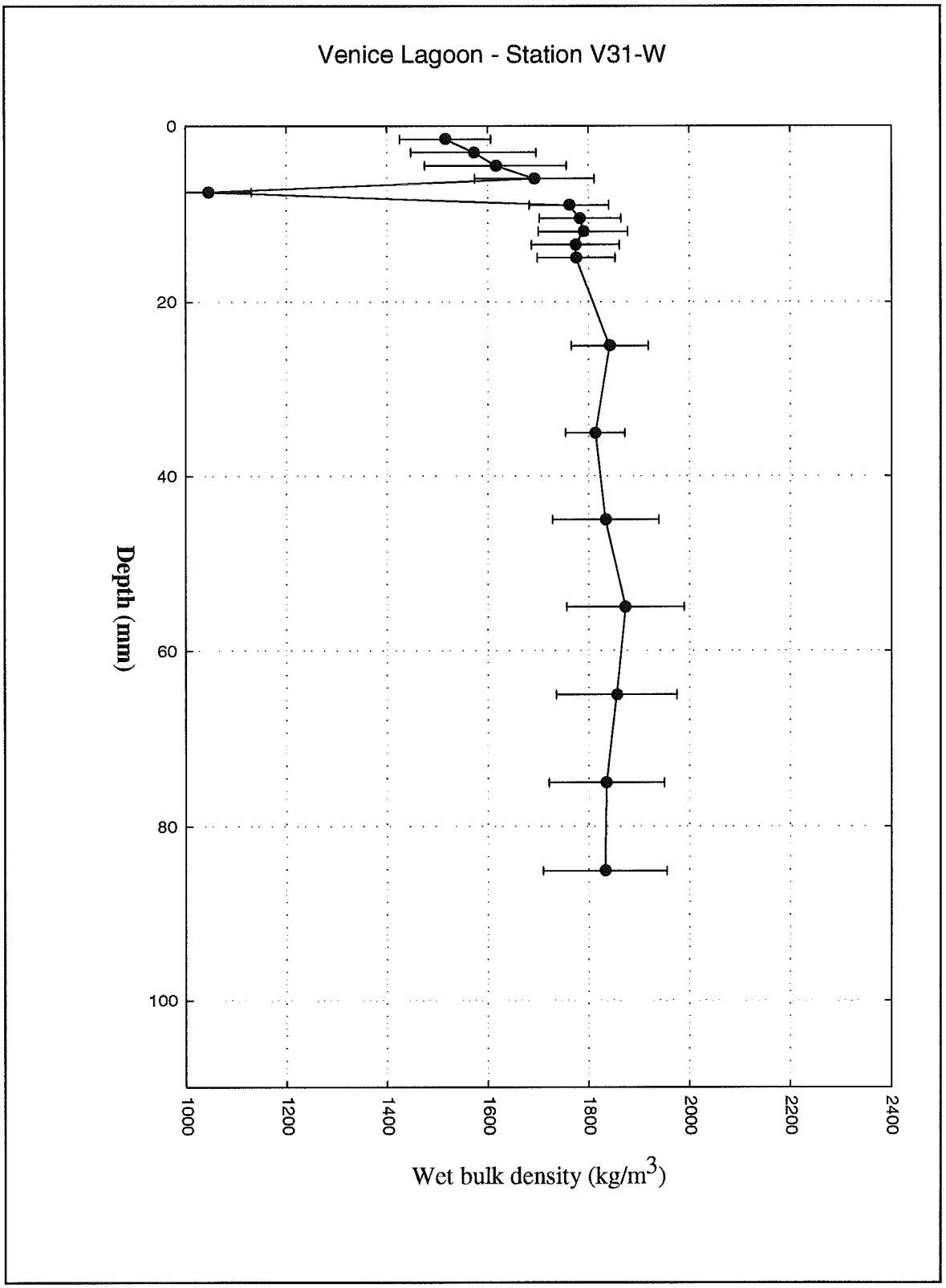

Figure 4.4.2 : A bulk density profile derived from Catscan analysis of a syringe core collected at site V31.

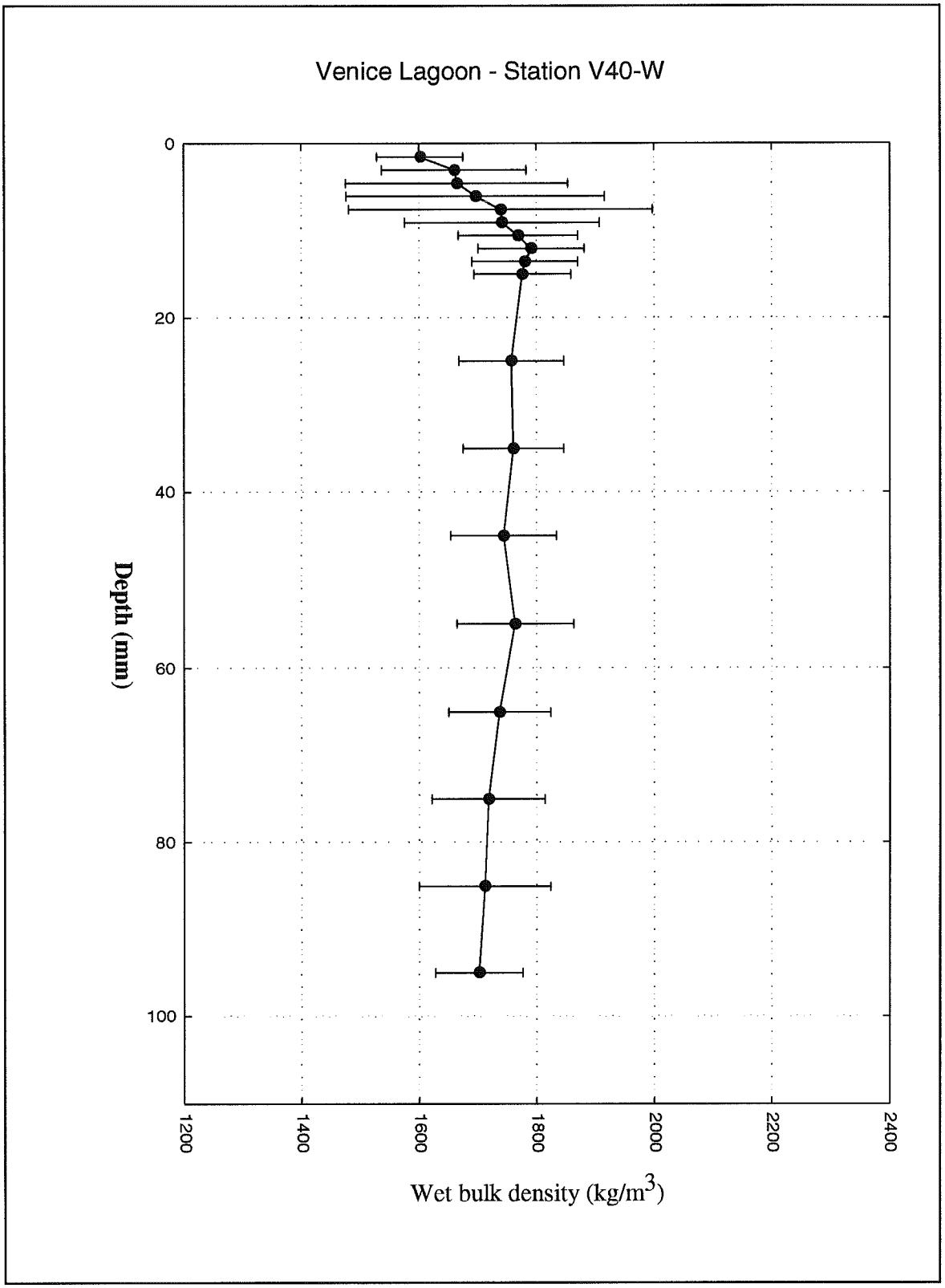

Figure 4.4.3 : A bulk density profile derived from Catscan analysis of a syringe core collected at site V40.

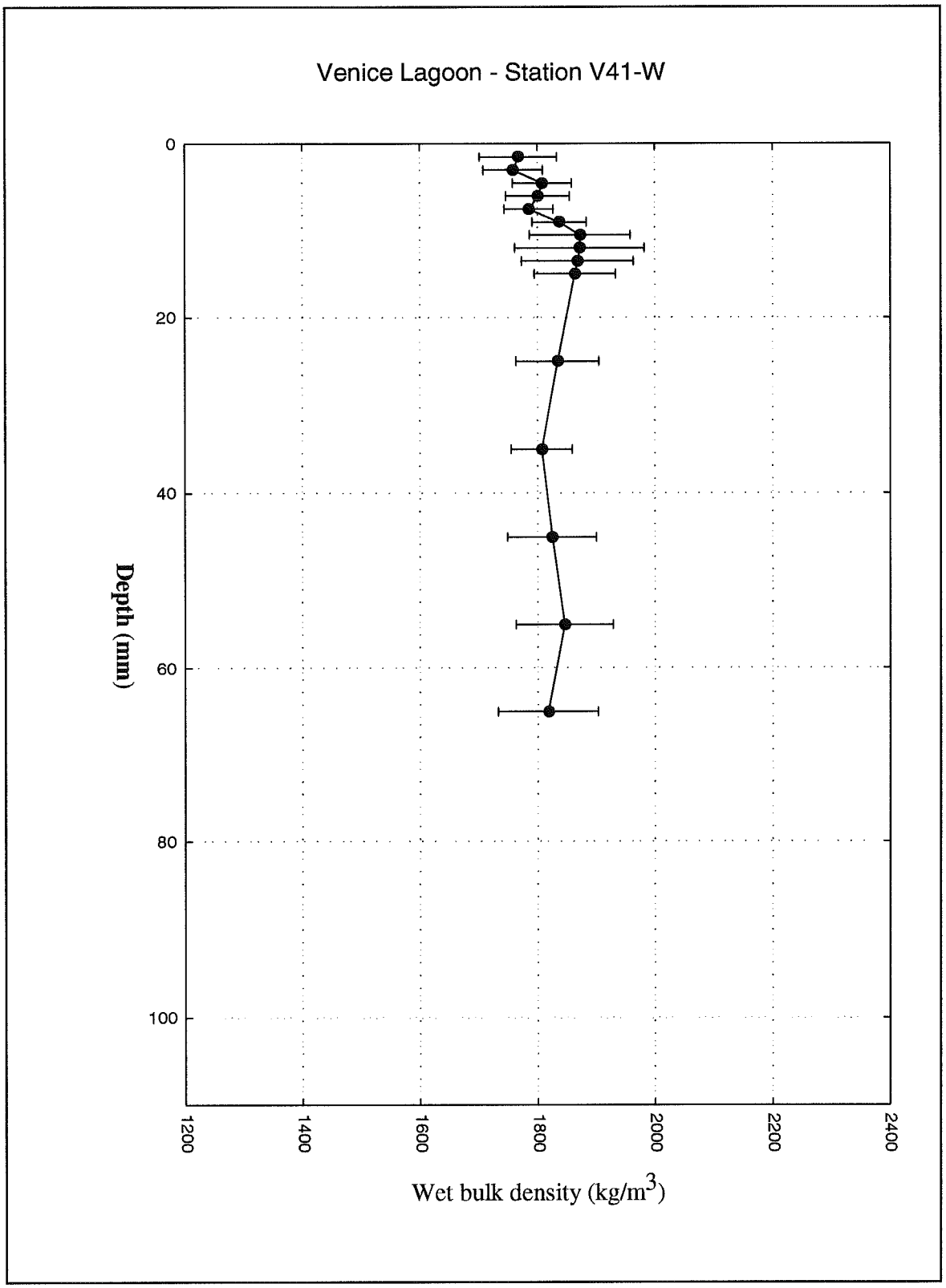

Figure 4.4.4 : A bulk density profile derived from Catscan analysis of a syringe core collected at site V41.

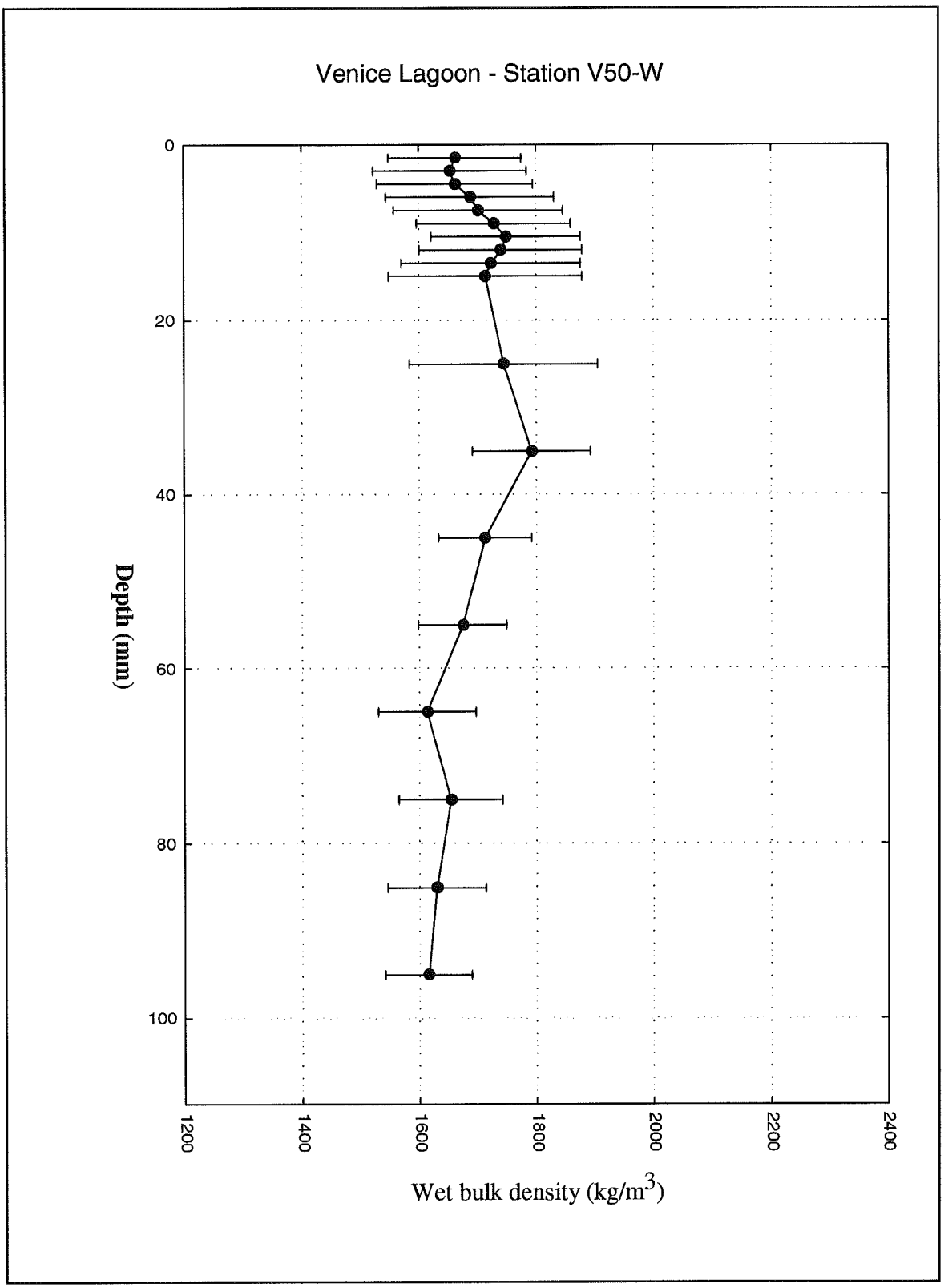

Figure 4.4.5 : A bulk density profile derived from Catscan analysis of a syringe core collected at site V50.

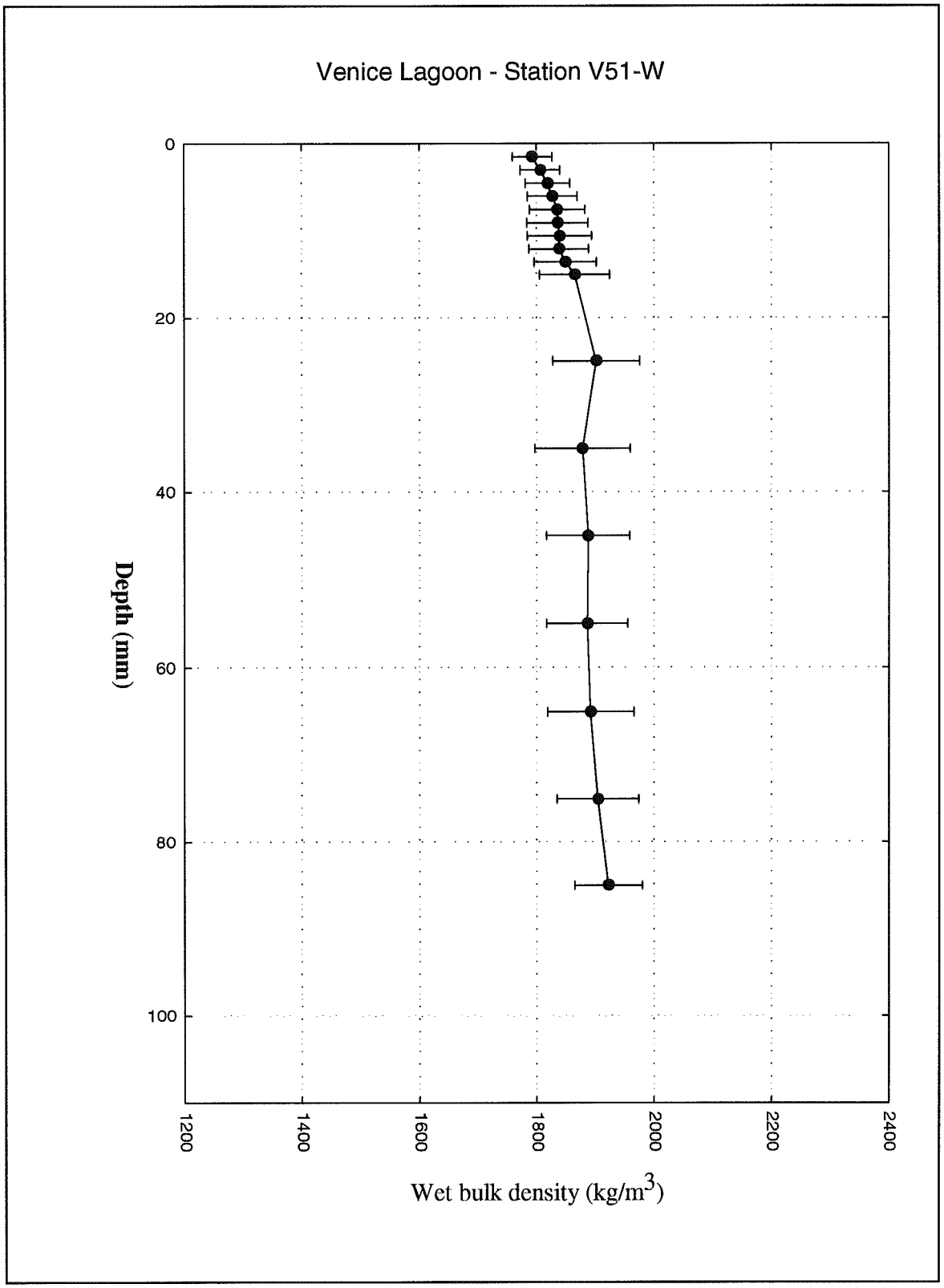

Figure 4.4.6 : A bulk density profile derived from Catscan analysis of a syringe core collected at site V51.

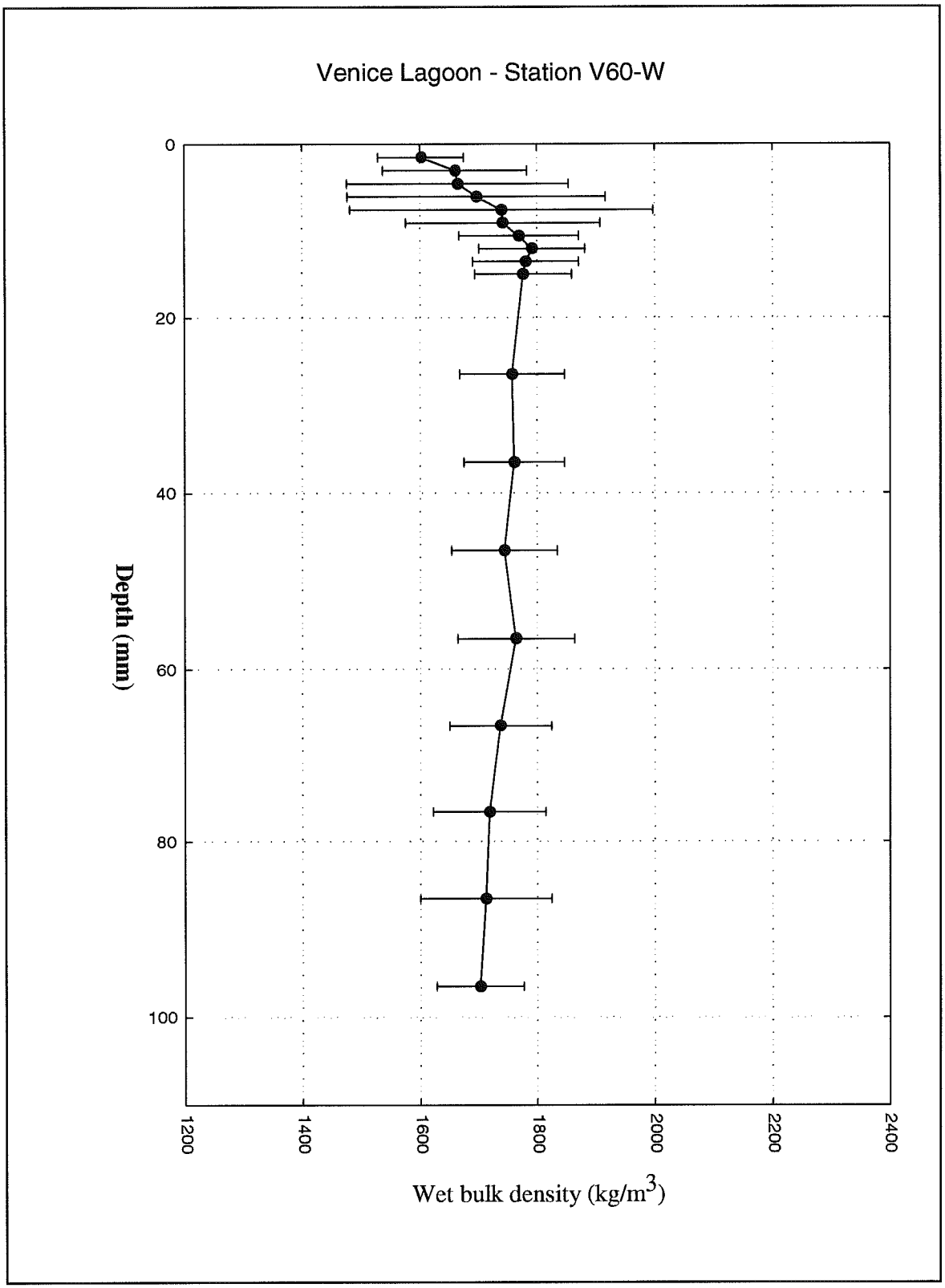

Figure 4.4.7 : A bulk density profile derived from Catscan analysis of a syringe core collected at site V60

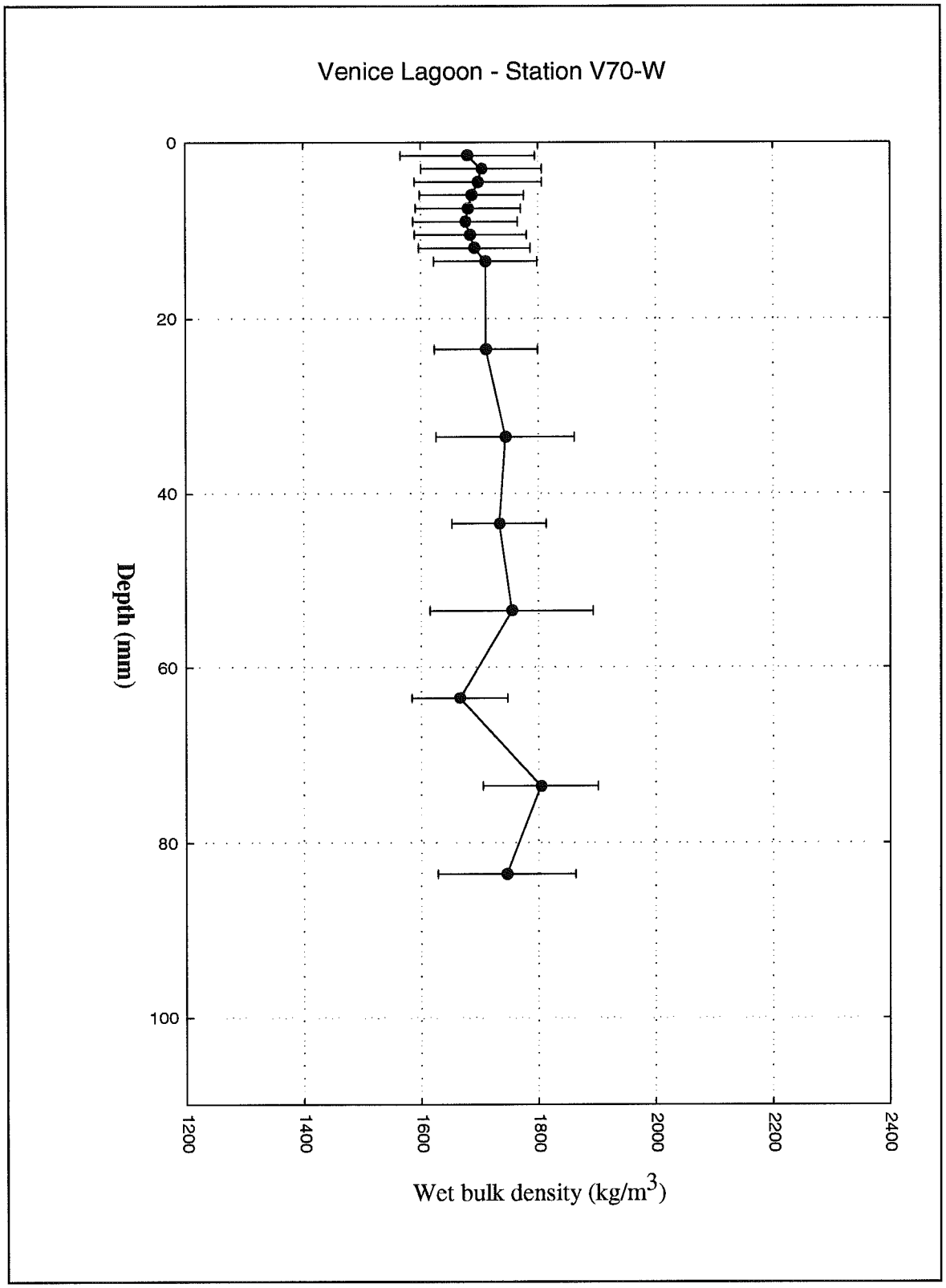

Figure 4.4.8 : A bulk density profile derived from Catscan analysis of a syringe core collected at site V70.

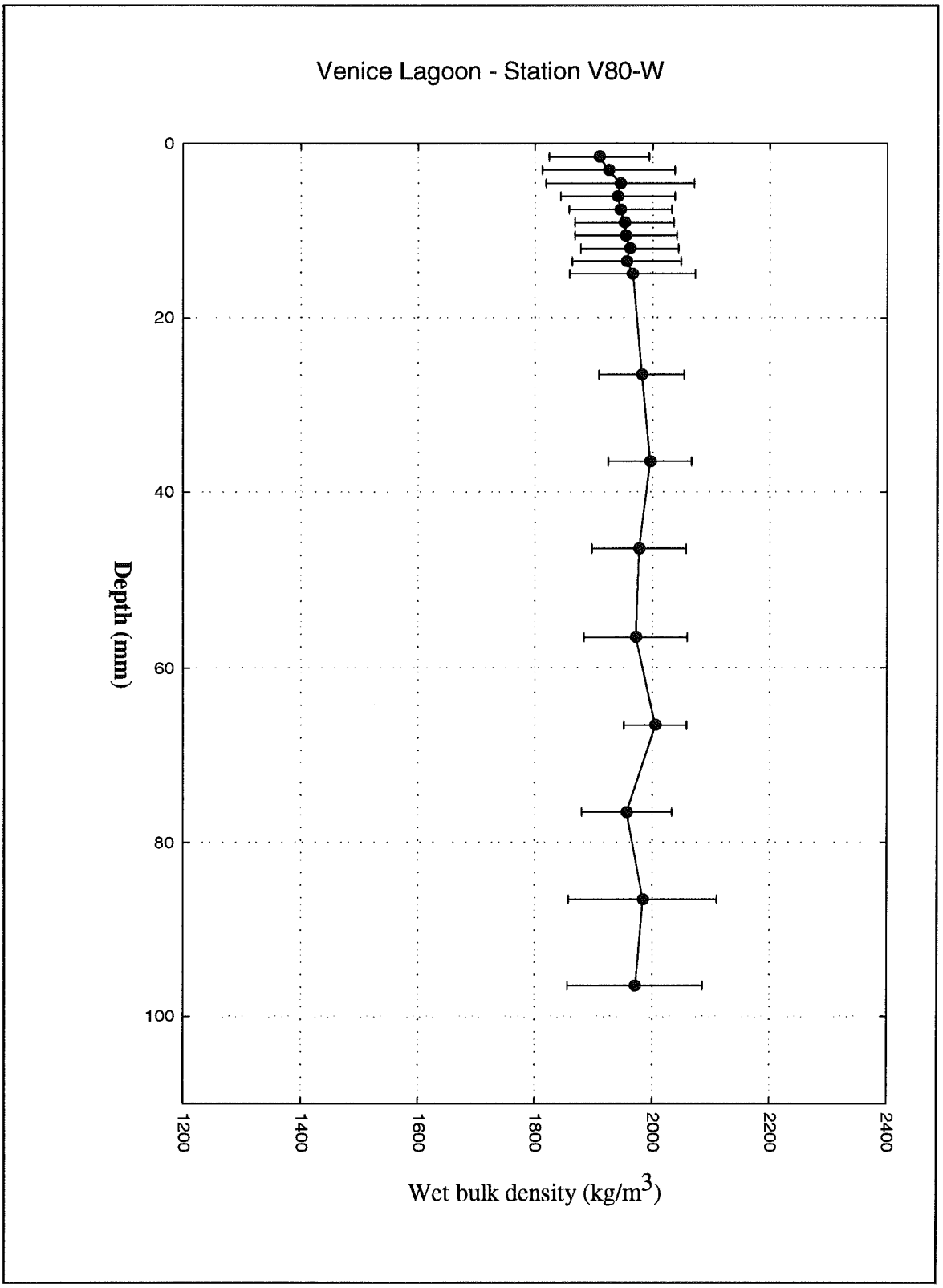

Figure 4.4.9 : A bulk density profile derived from Catscan analysis of a syringe core collected at site V80.

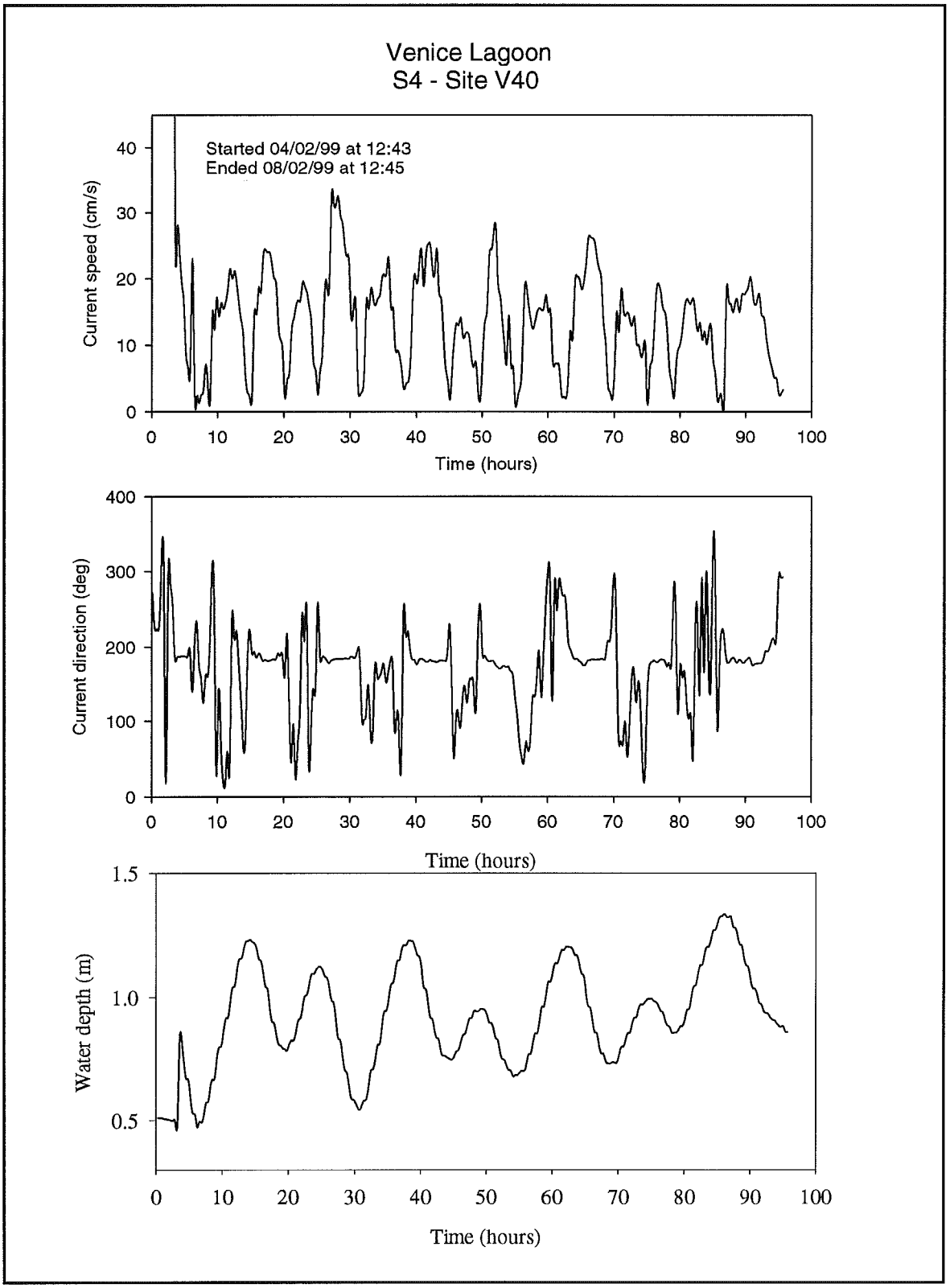

Figure 4.5.1 : The InterOcean S4 current meter time-series from Site V40.

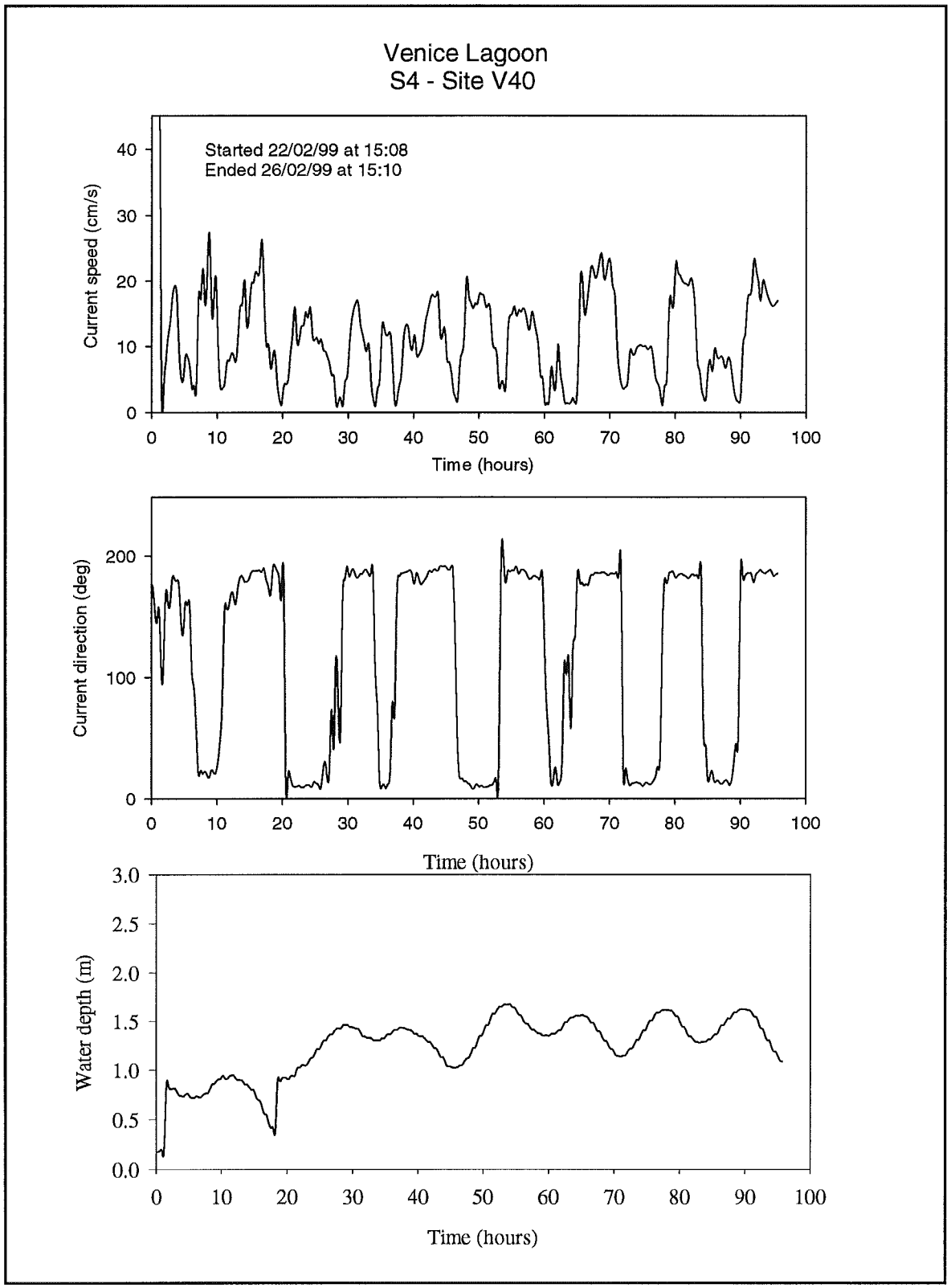

Figure 4.5.2: The InterOcean S4 current meter time-series from Site V40.

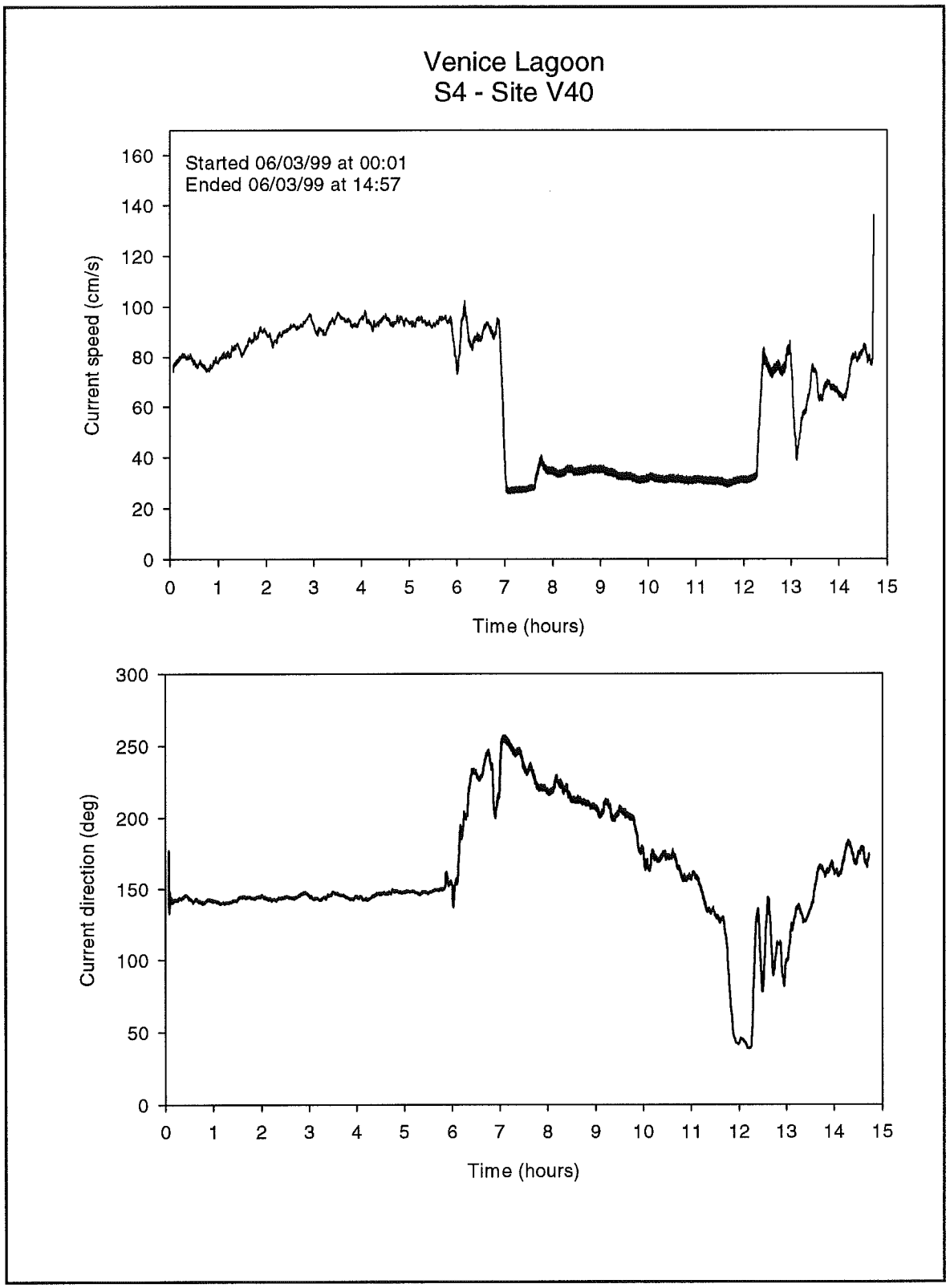

Figure 4.5.3 : The InterOcean S4 current meter time-series from Site V40.

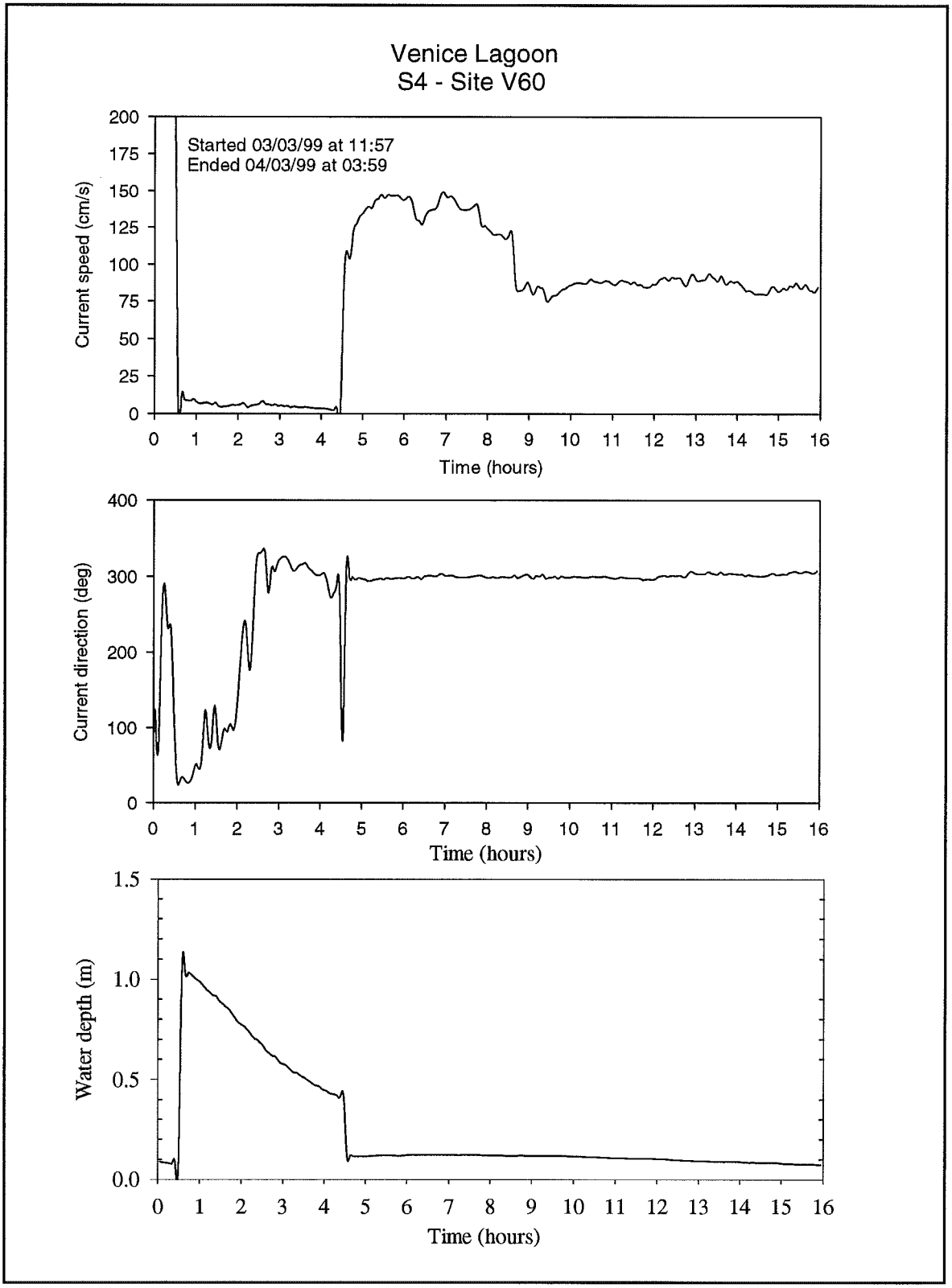

Figure 4.5.4 : The InterOcean S4 current meter time-series from Site V60.

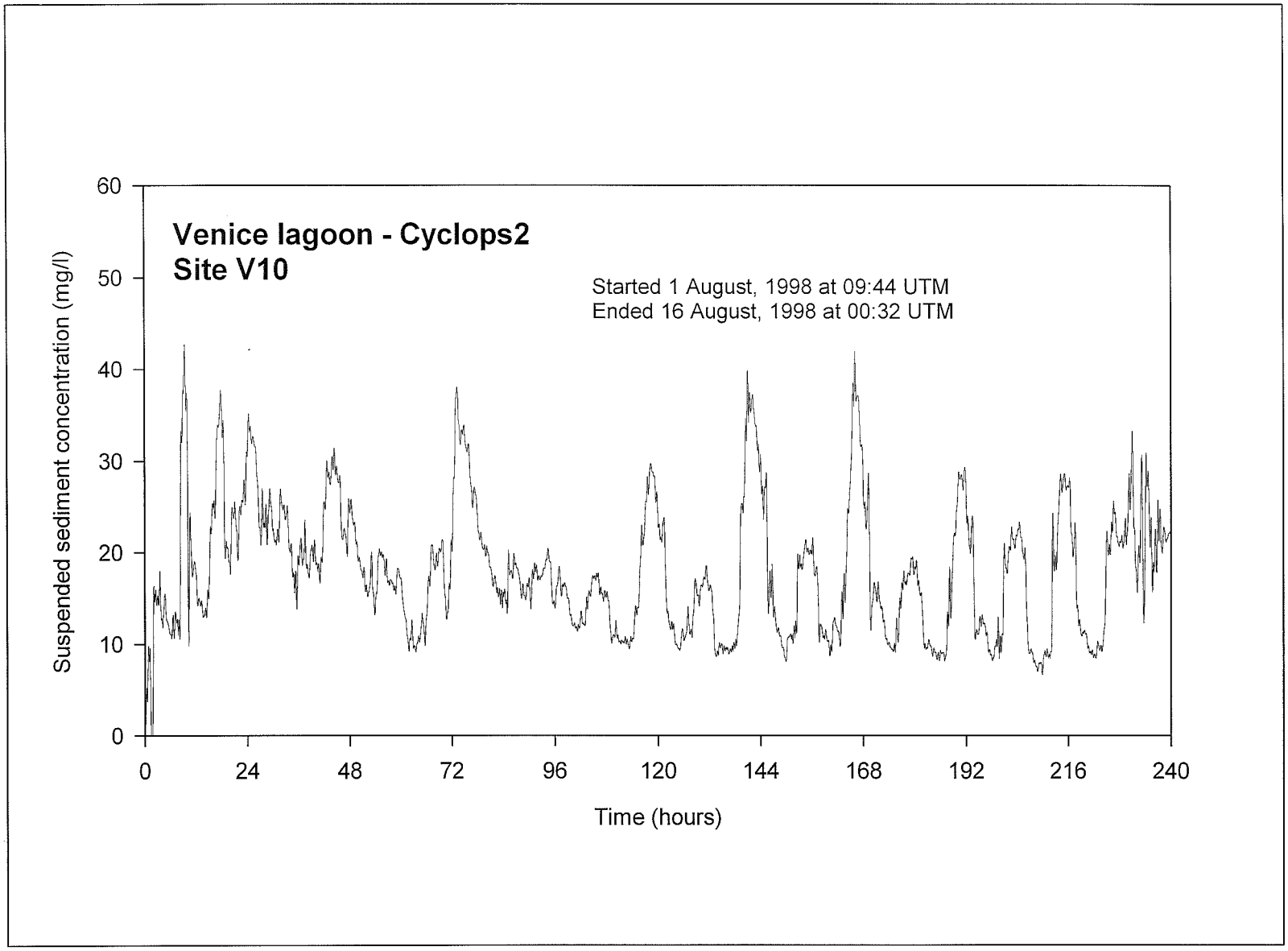

Figure 4.6.1.1 : Cyclops turbidity measures from site V10. Note the changing offset, probably the result of biofouling.

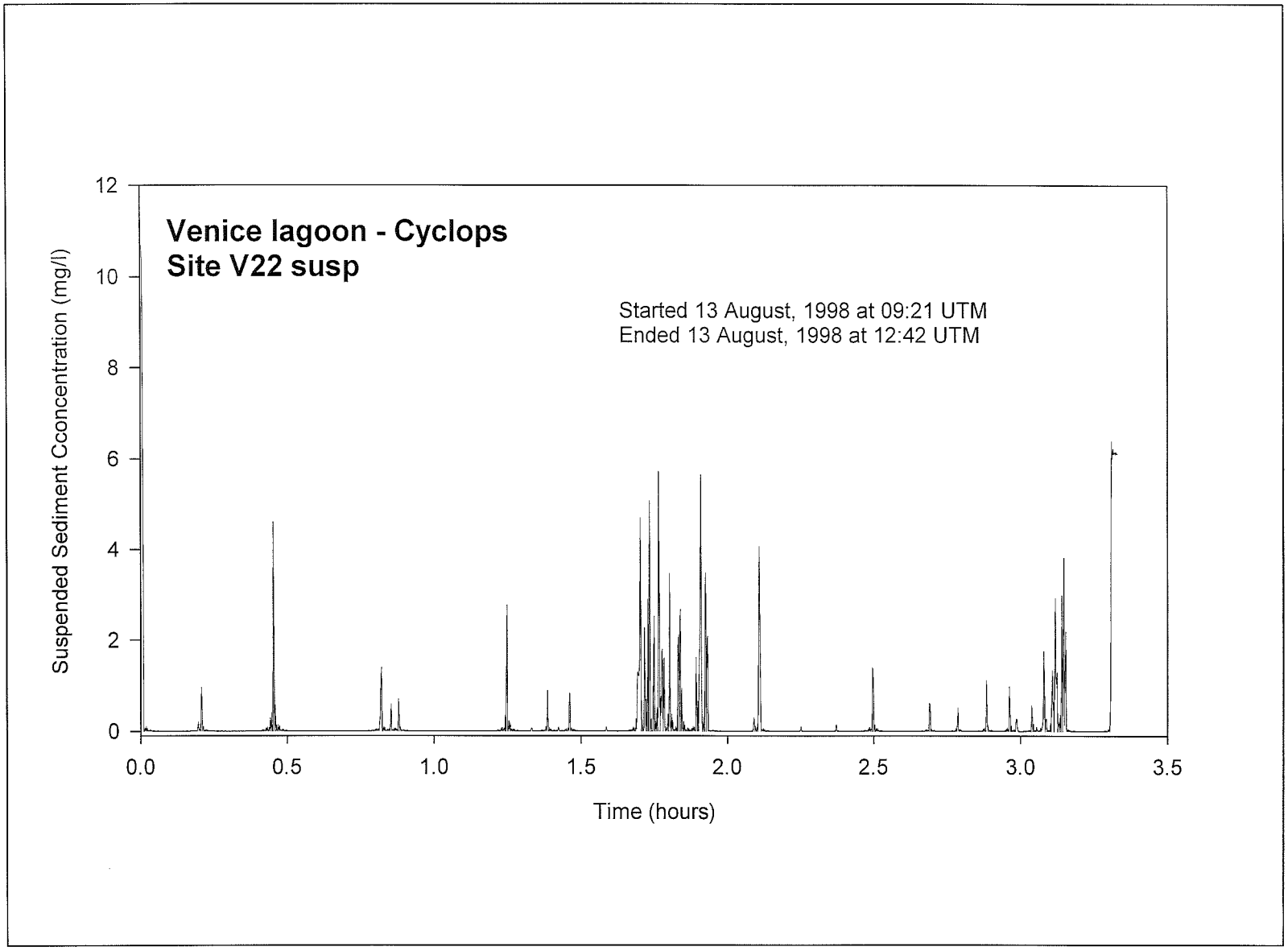

Figure 4.6.1.2 : Cyclops turbidity measures from site V22 (ship resuspension study). Note the short-lived peaks which suggest resuspension due to passage of the Torcello ferry.

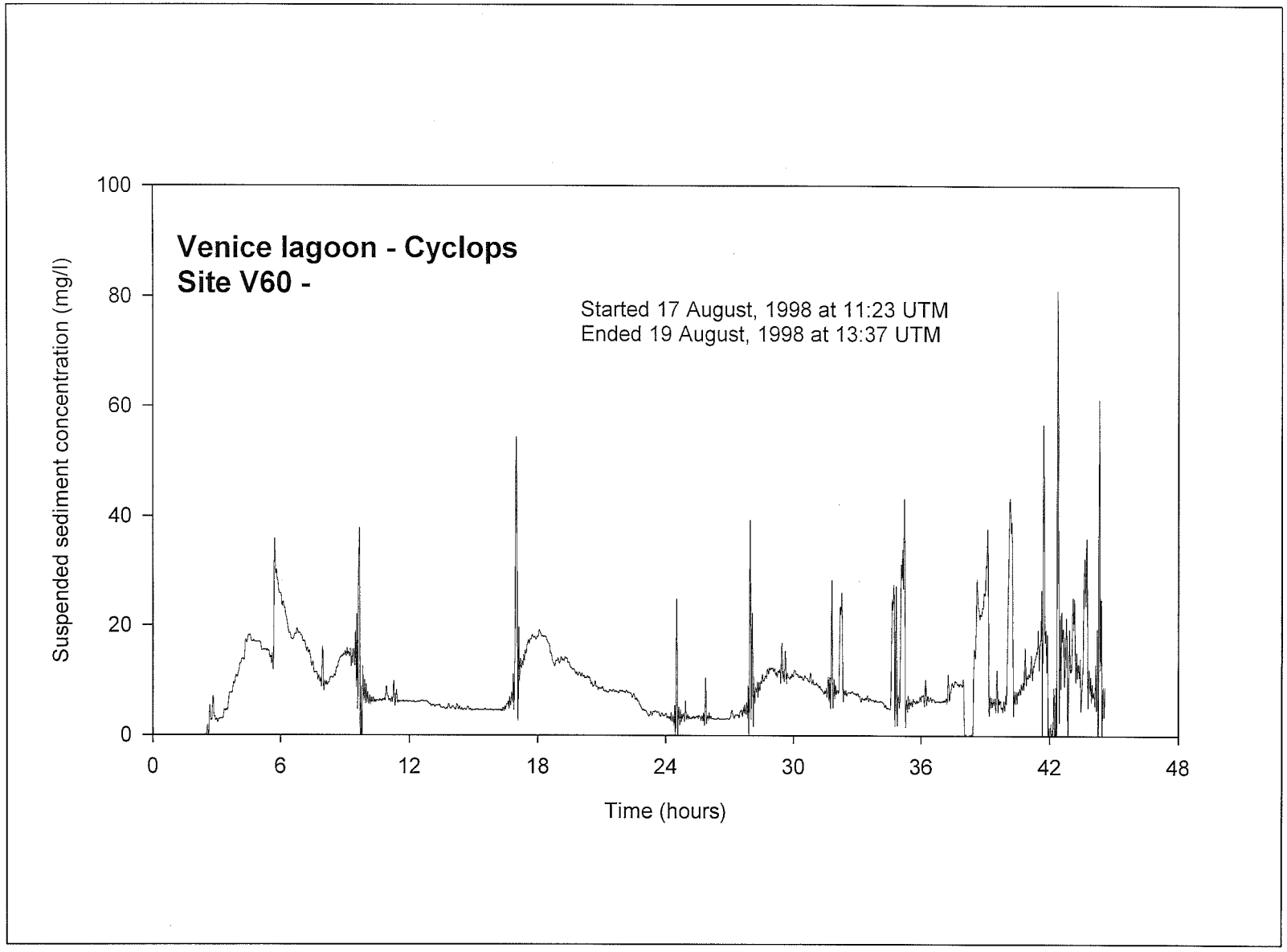

Figure 4.6.1.3: Cyclops turbidity measures from site V60.

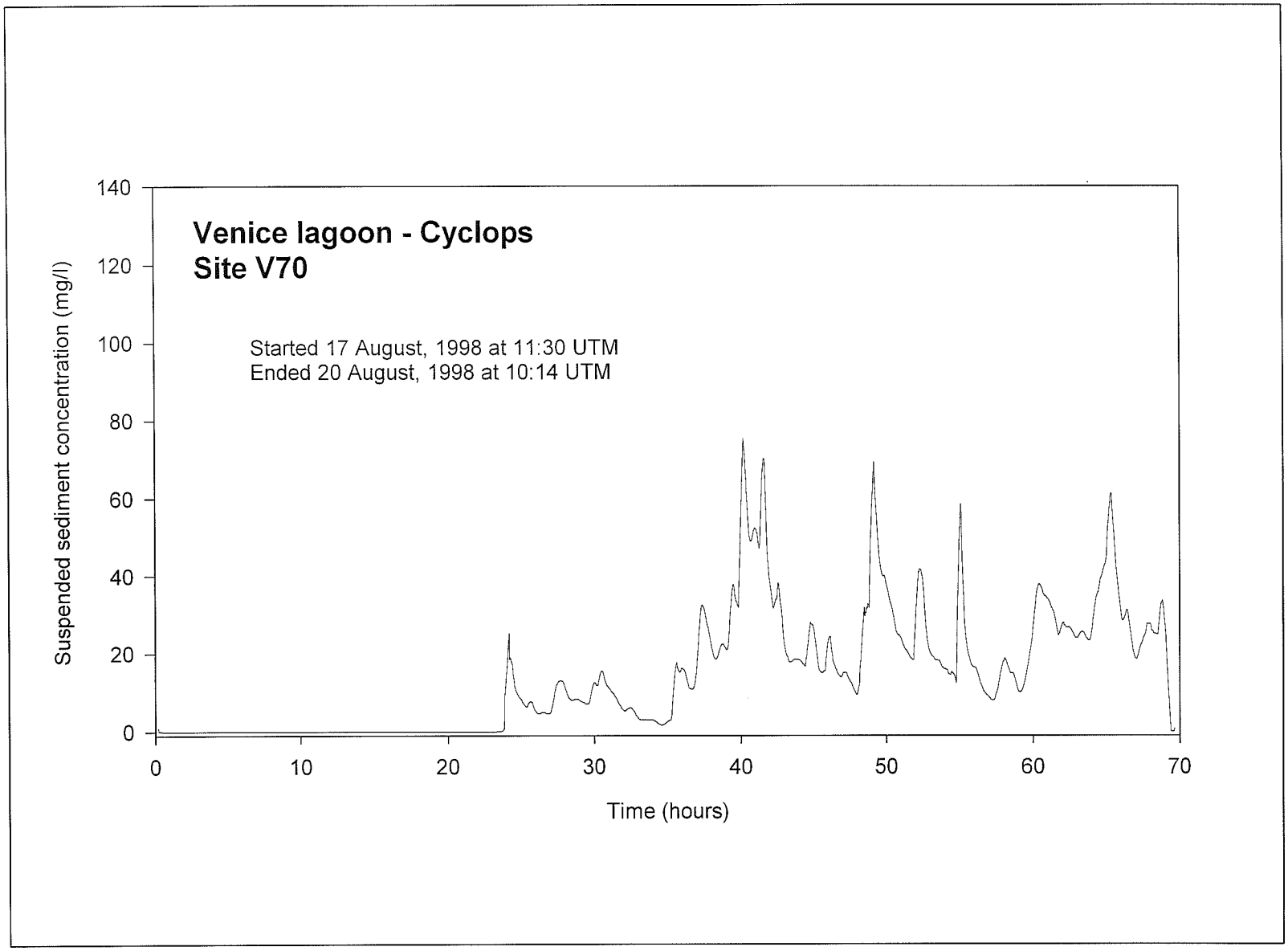

Figure 4.6.1.4 : Cyclops turbidity measures from site V70. The peaks in turbidity are probably the result of ship resuspension.

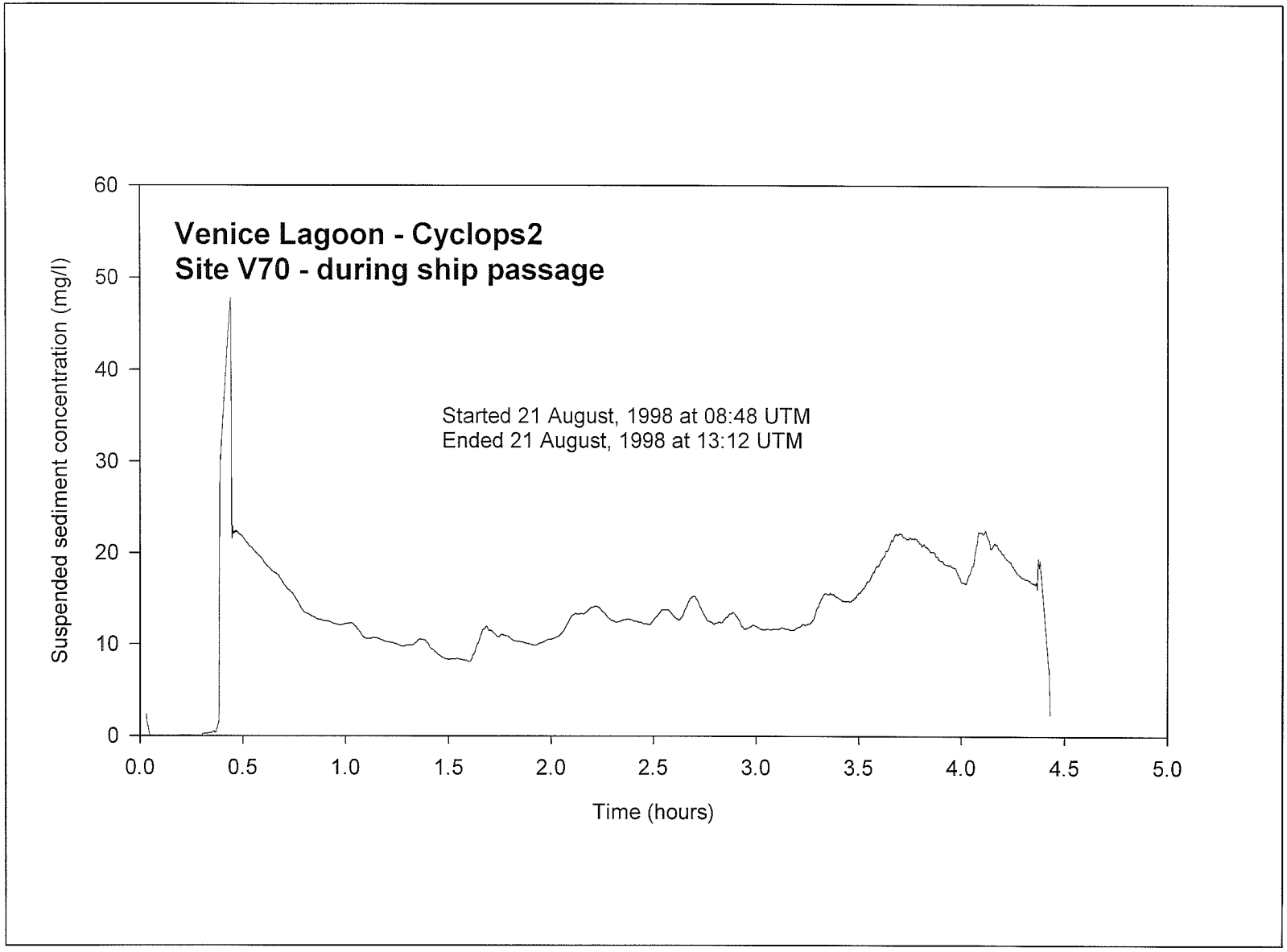

Figure 4.6.1.5: Cyclops turbidity measures from site V70 (ship channel resuspension). Note the short-lived peaks which suggest resuspension due ro ship passage in the main shipping channel.

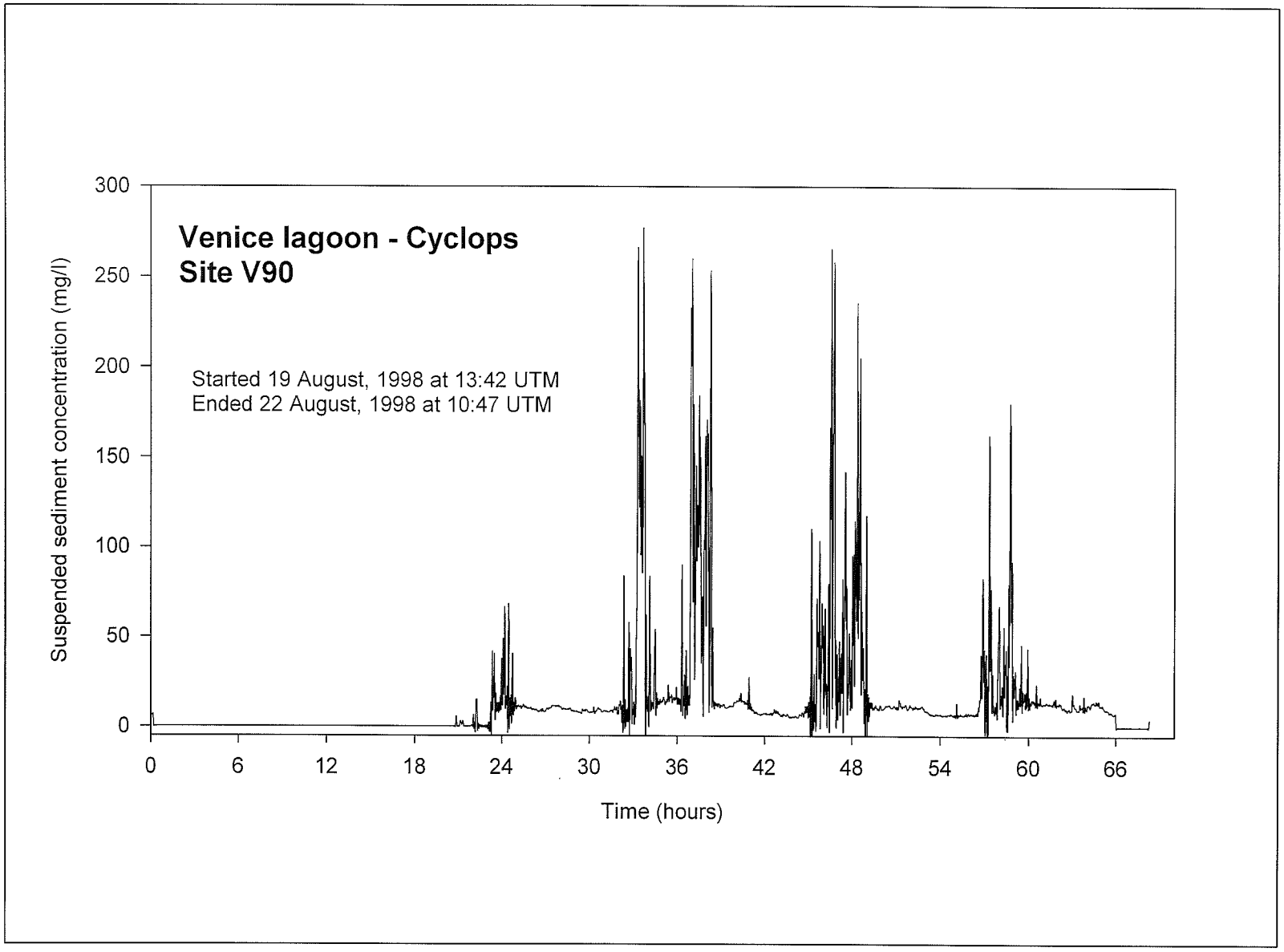

Figure 4.6.1.6 Cyclops turbidity measures from site V70. The peaks in turbidity are probably the result of ship resuspension.

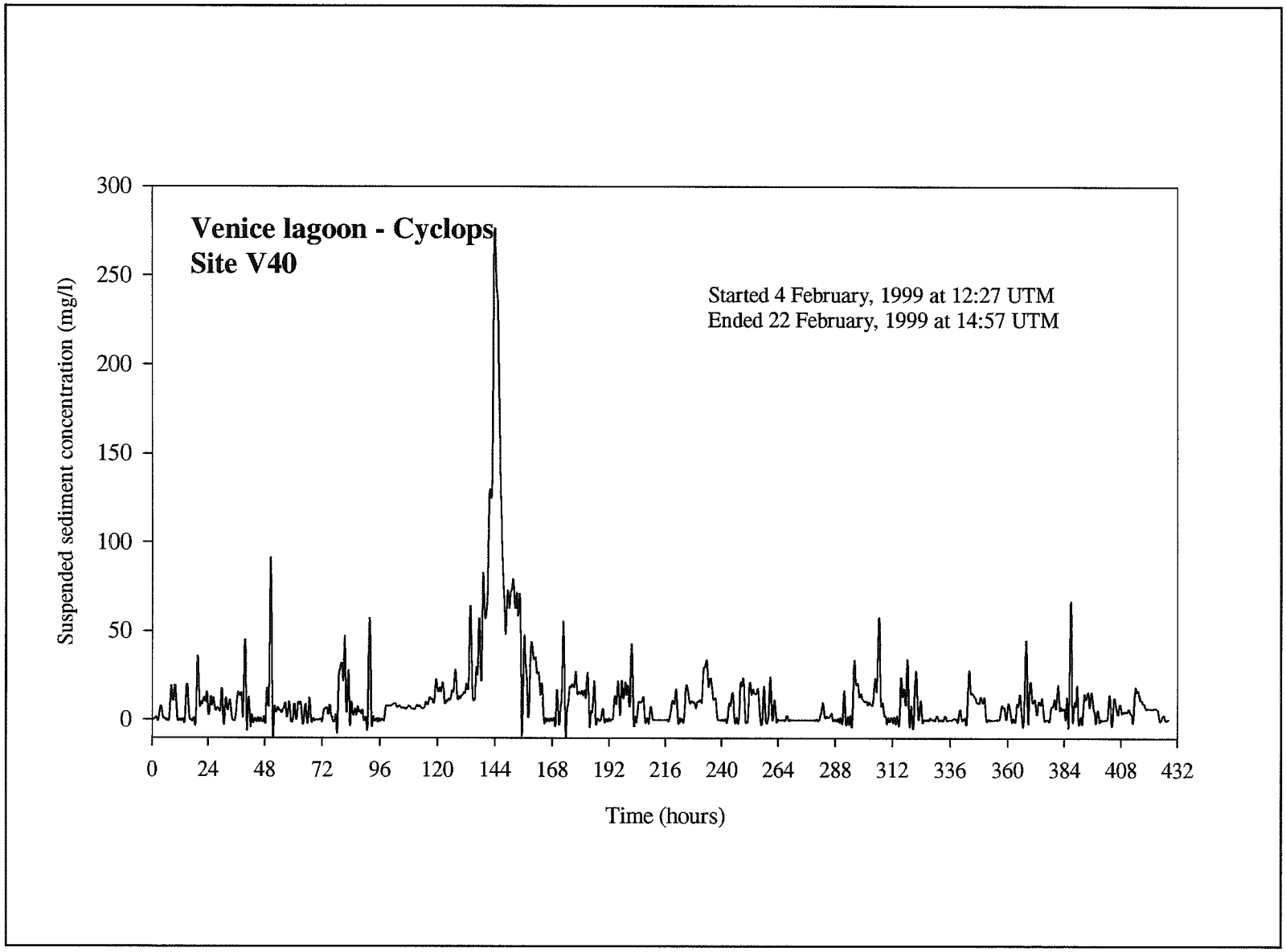

Figure 4.6.2.1 : Cyclops turbidity measures from site V40 during the winter field campaign.

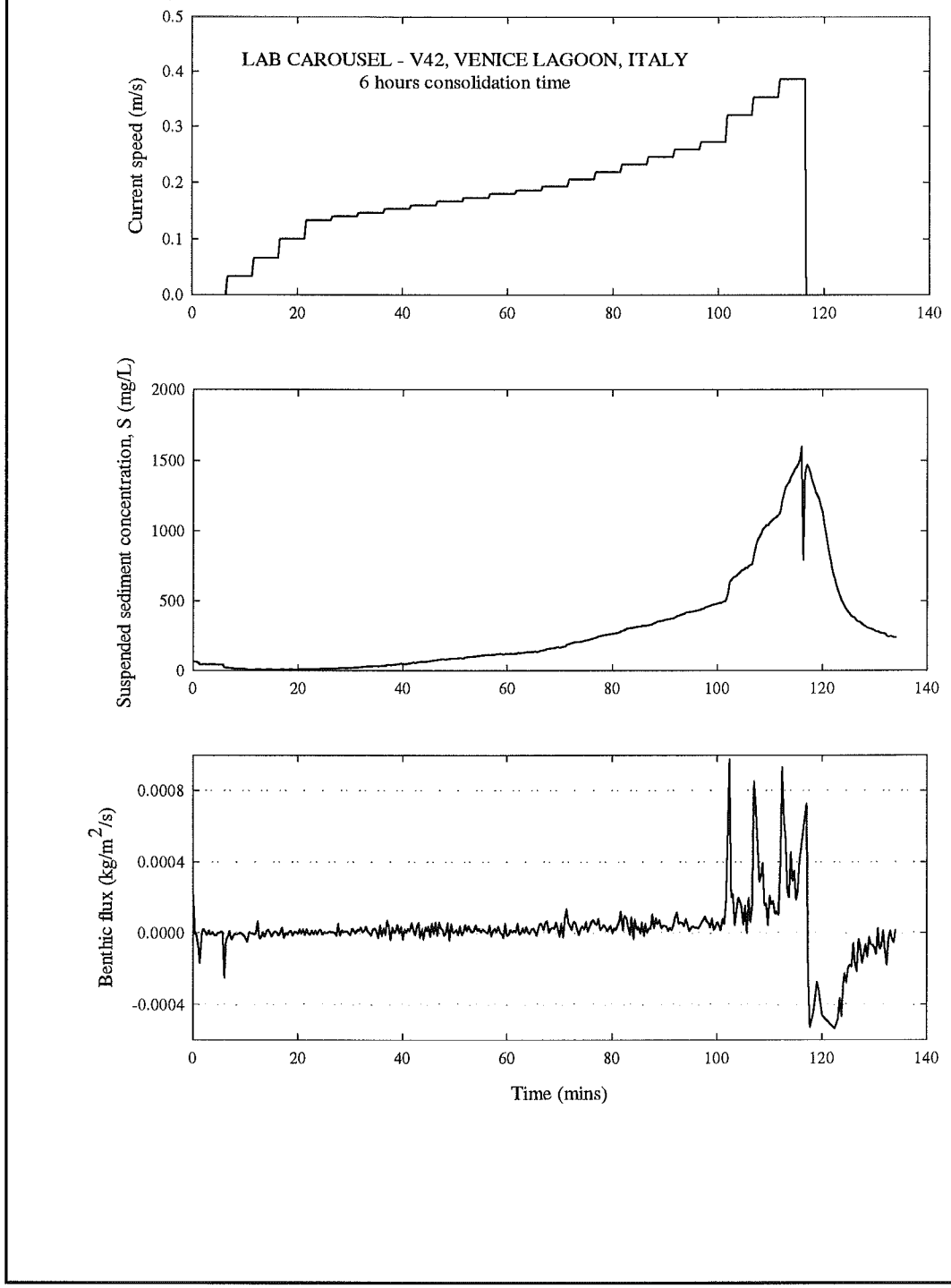

Figure 4.7.1: The time series of results from Lab Carousel experiment with 6 hours of consolidation time.

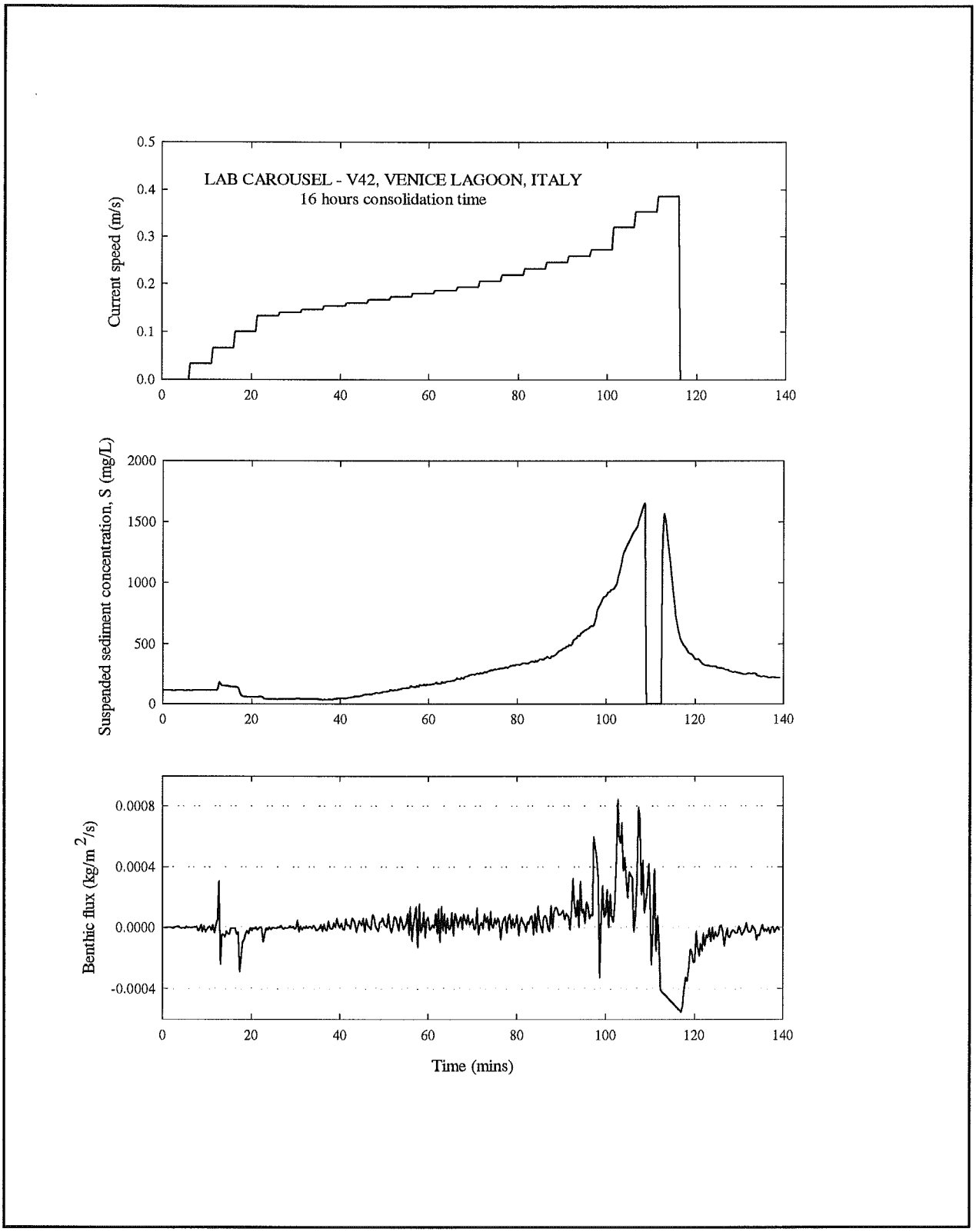

Figure 4.7.2: The time series of results from Lab Carousel experiment with 16 hours of consolidation time.

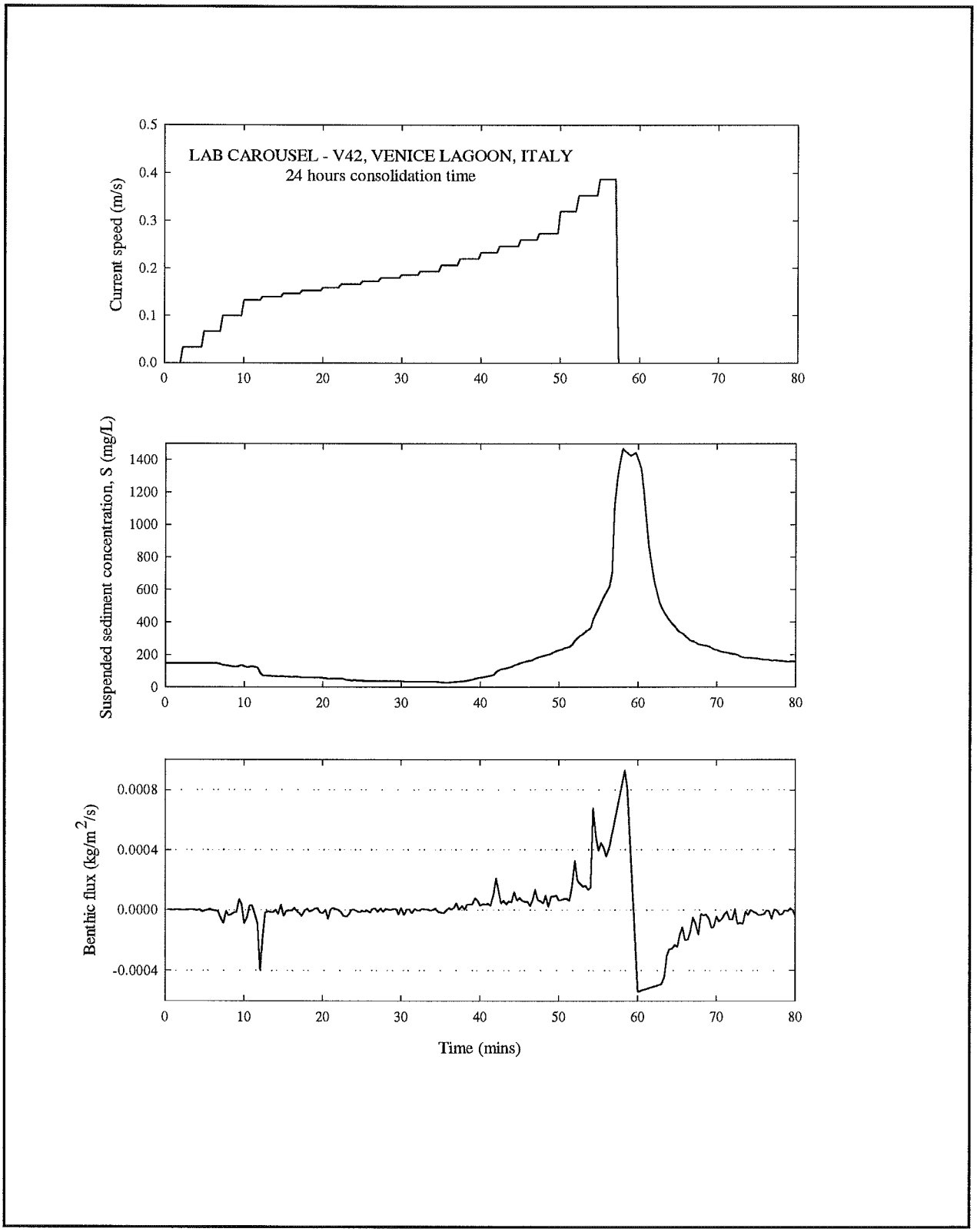

Figure 4.7.3: The time series of results from Lab Carousel experiment with 24 hours of consolidation time.

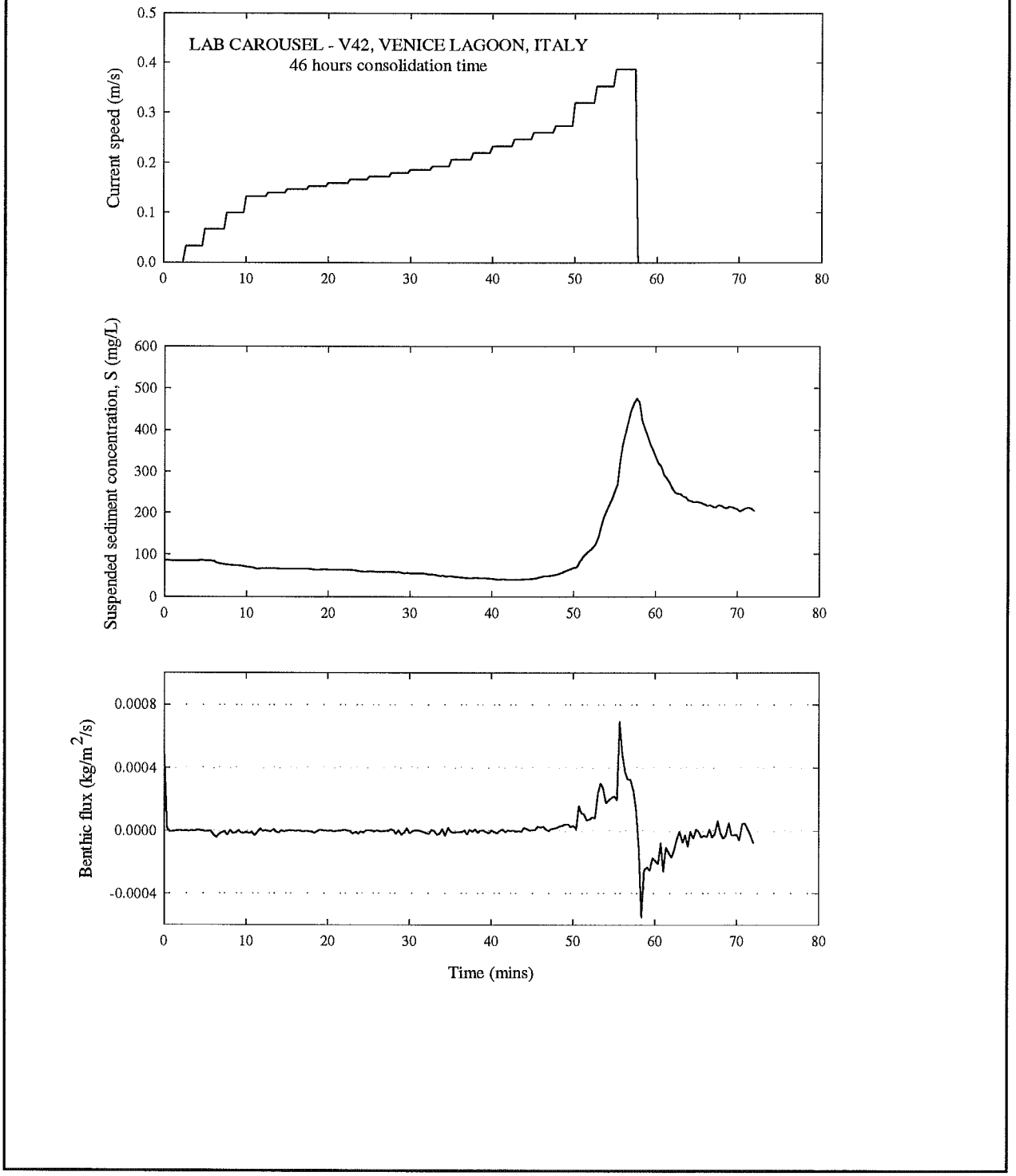

Figure 4.7.4: The time series of results from Lab Carousel experiment with 46 hours of consolidation time.

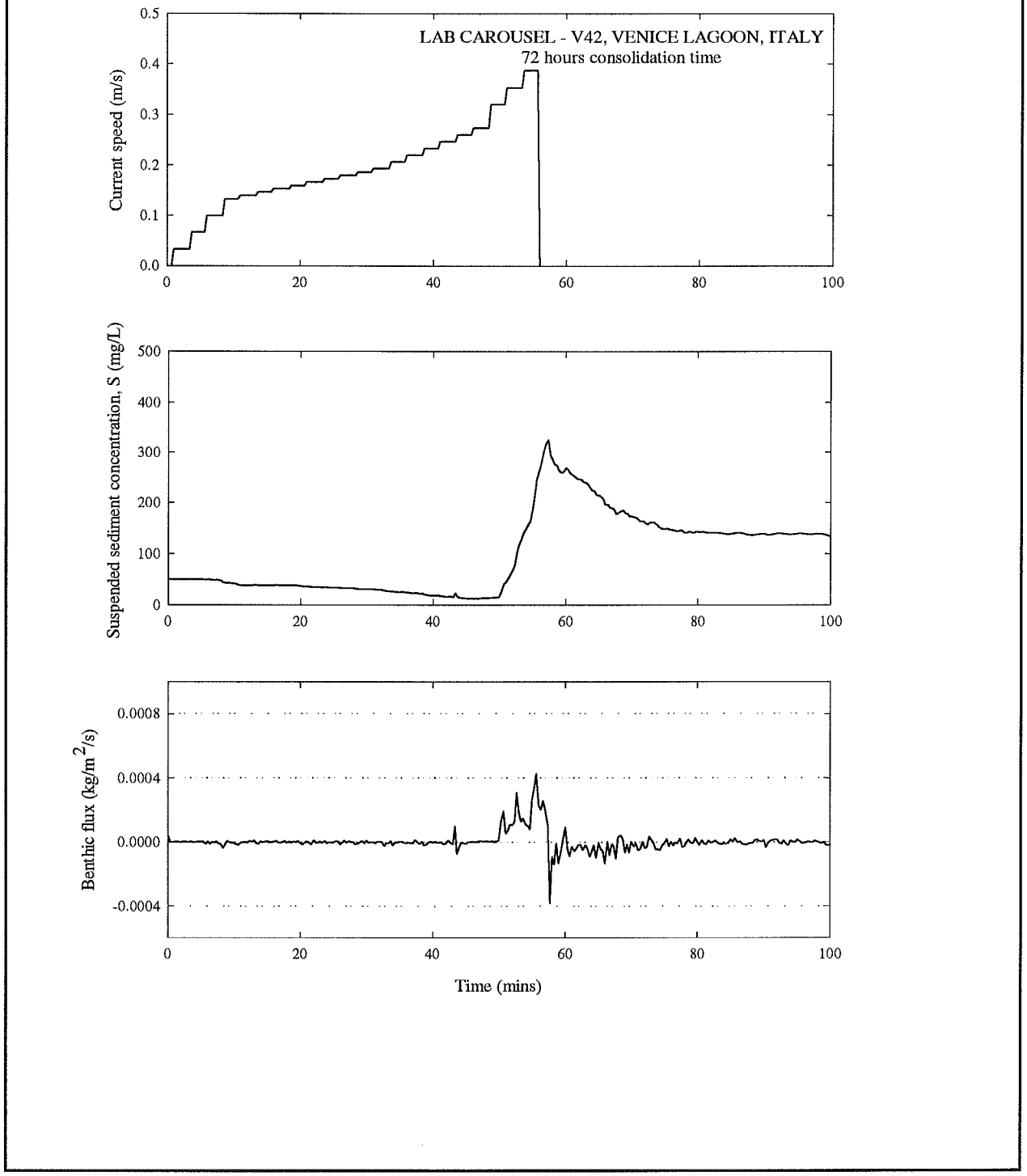

Figure 4.7.5: The time series of results from Lab Carousel experiment with 72 hours of consolidation time

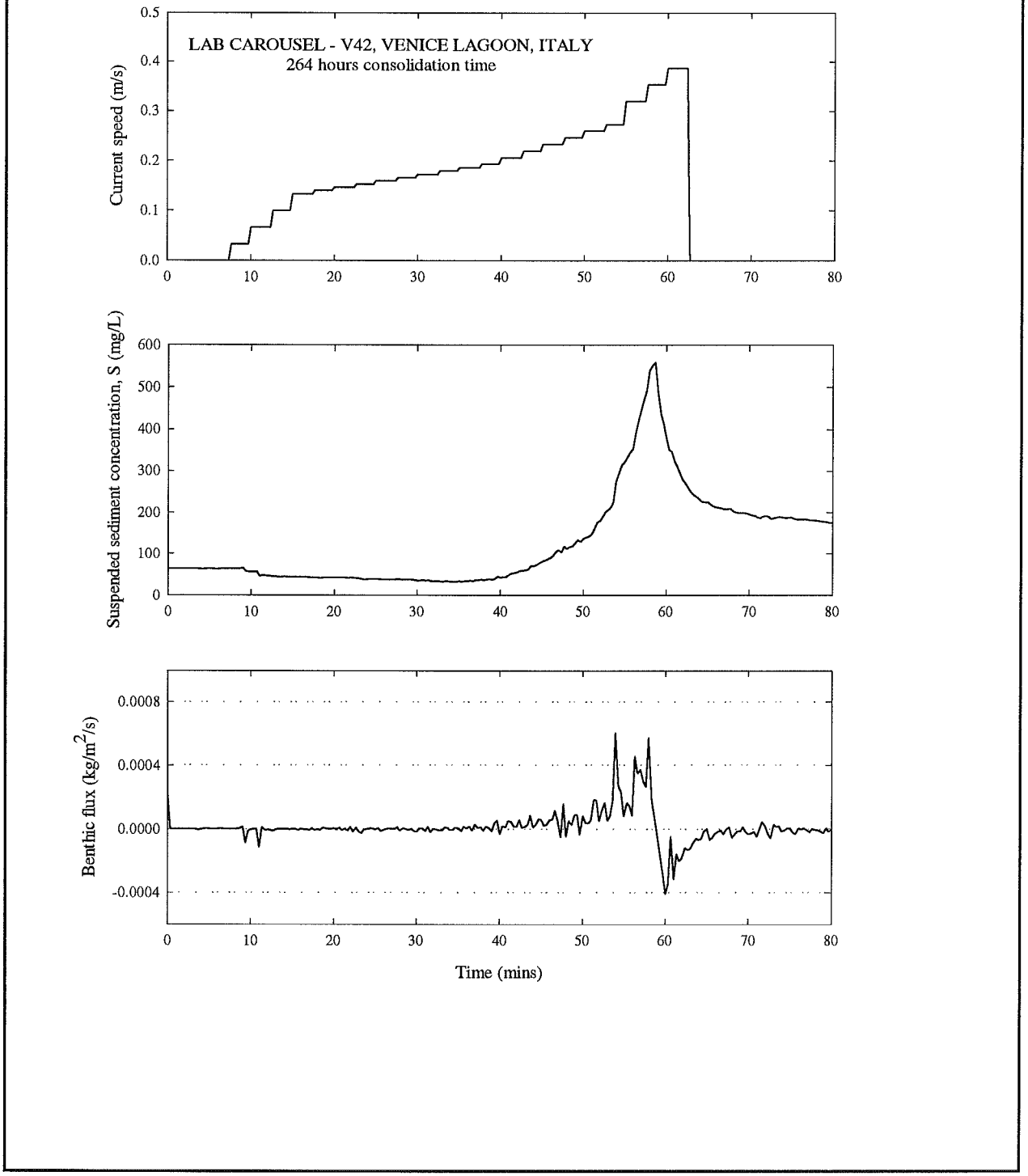

Figure 4.7.6: The time series of results from Lab Carousel experiment with 264 hours of consolidation time

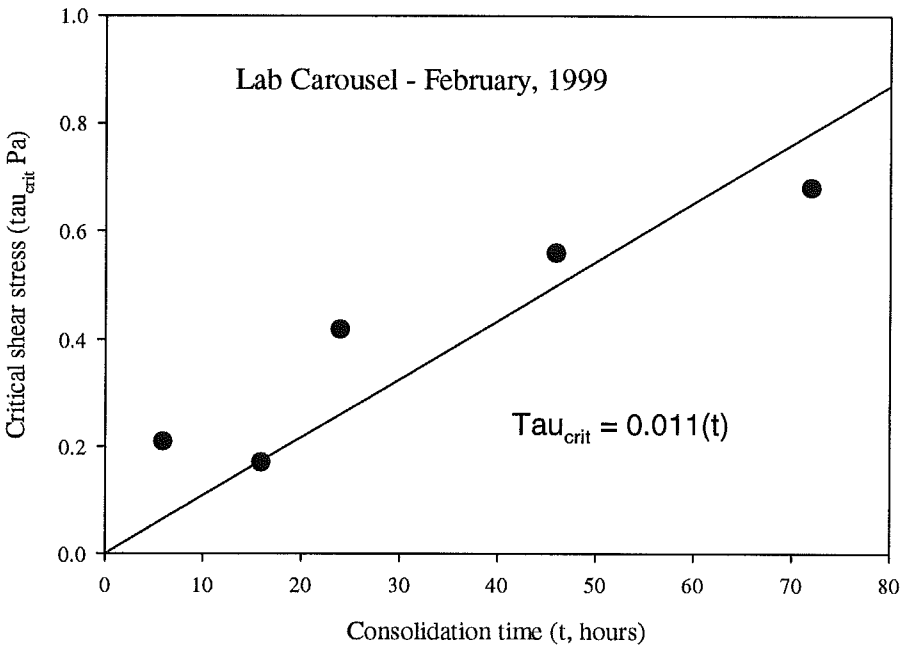

Figure 4.7.7: The threshold shear stress as a function of consolidation time for site V42 material.

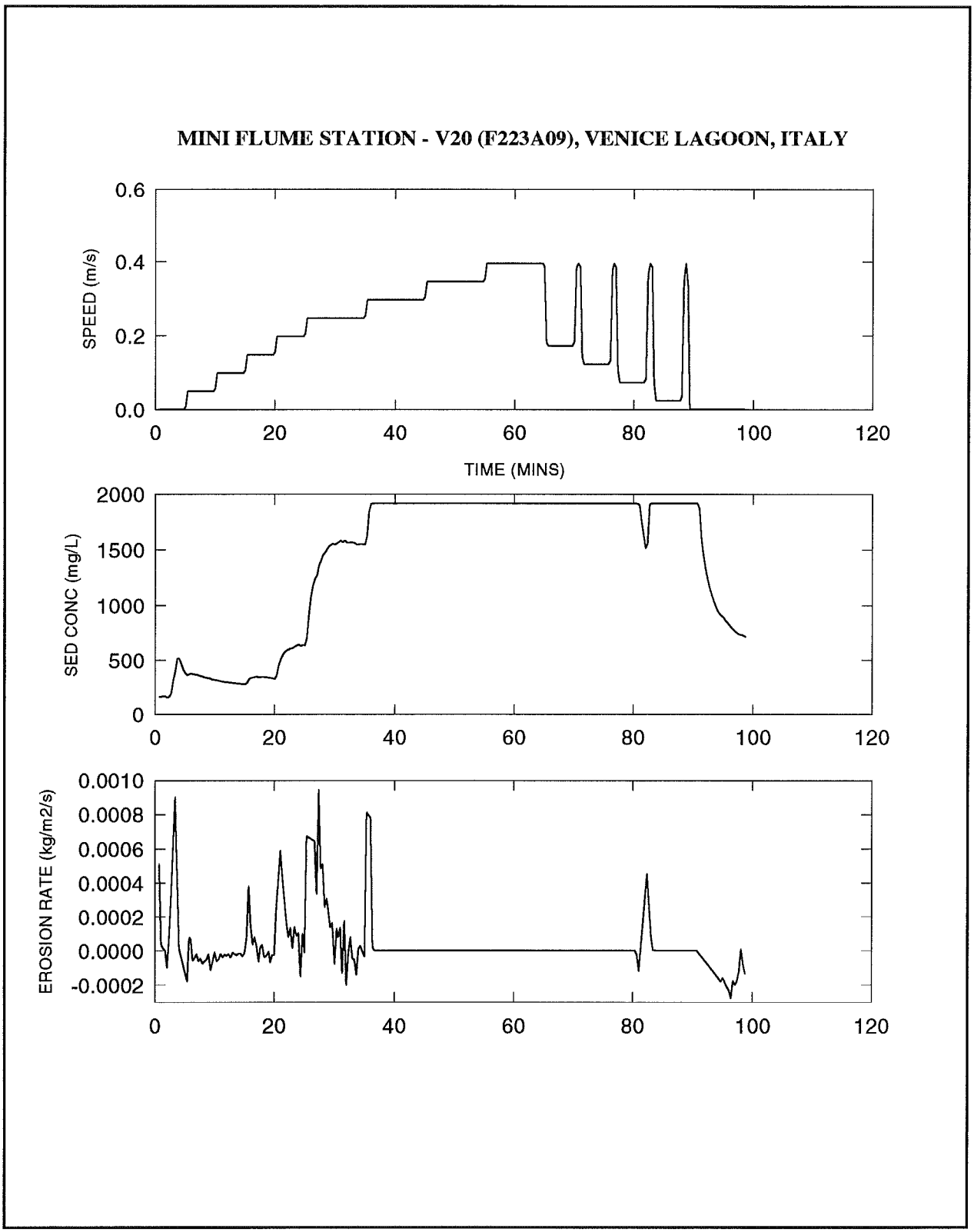

Figure 4.8.1 : Mini Flume time-series from site V20 recorded during the summer campaign.

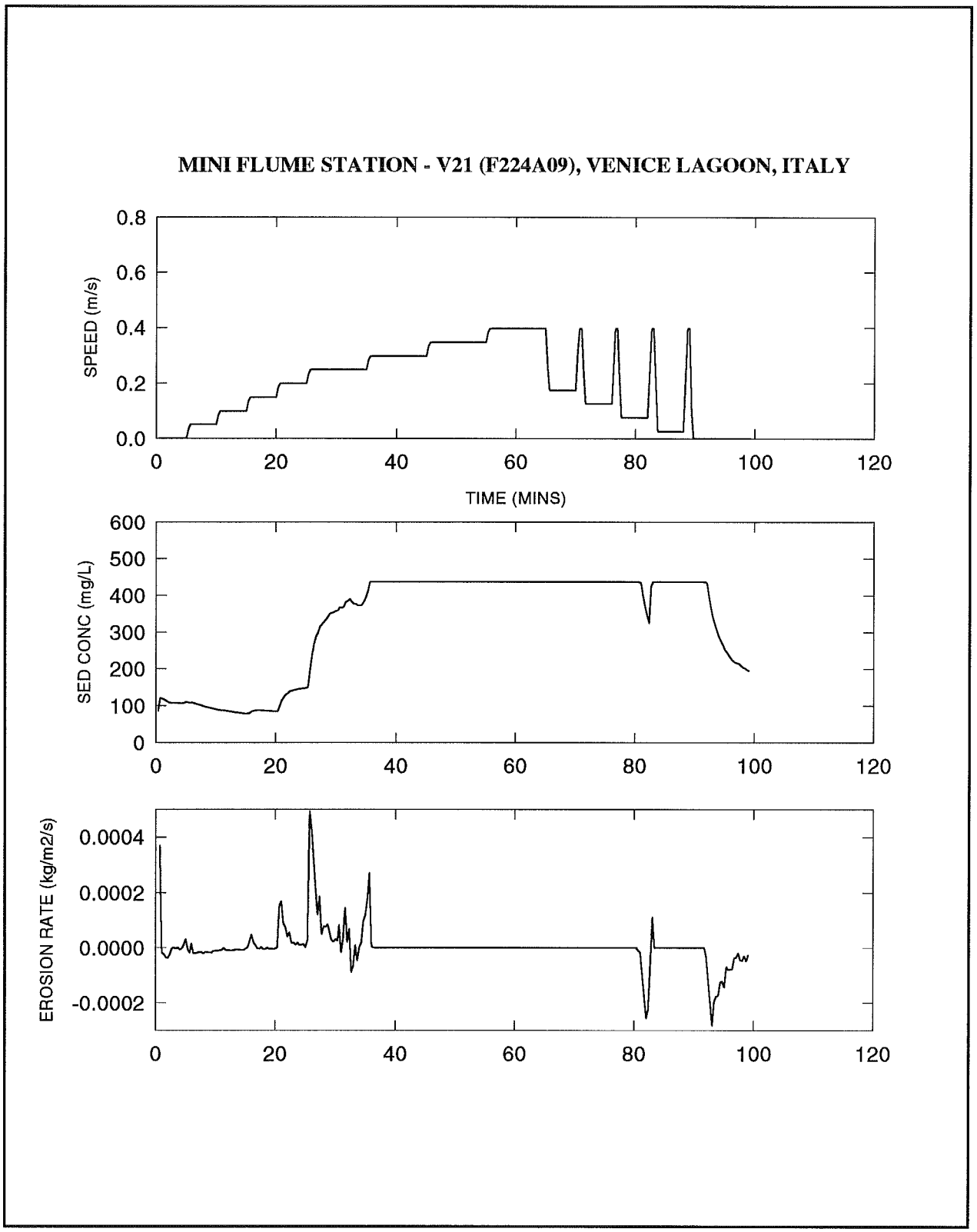

Figure 4.8.2 : Mini Flume time-series from site V21 recorded during the summer campaign.

.

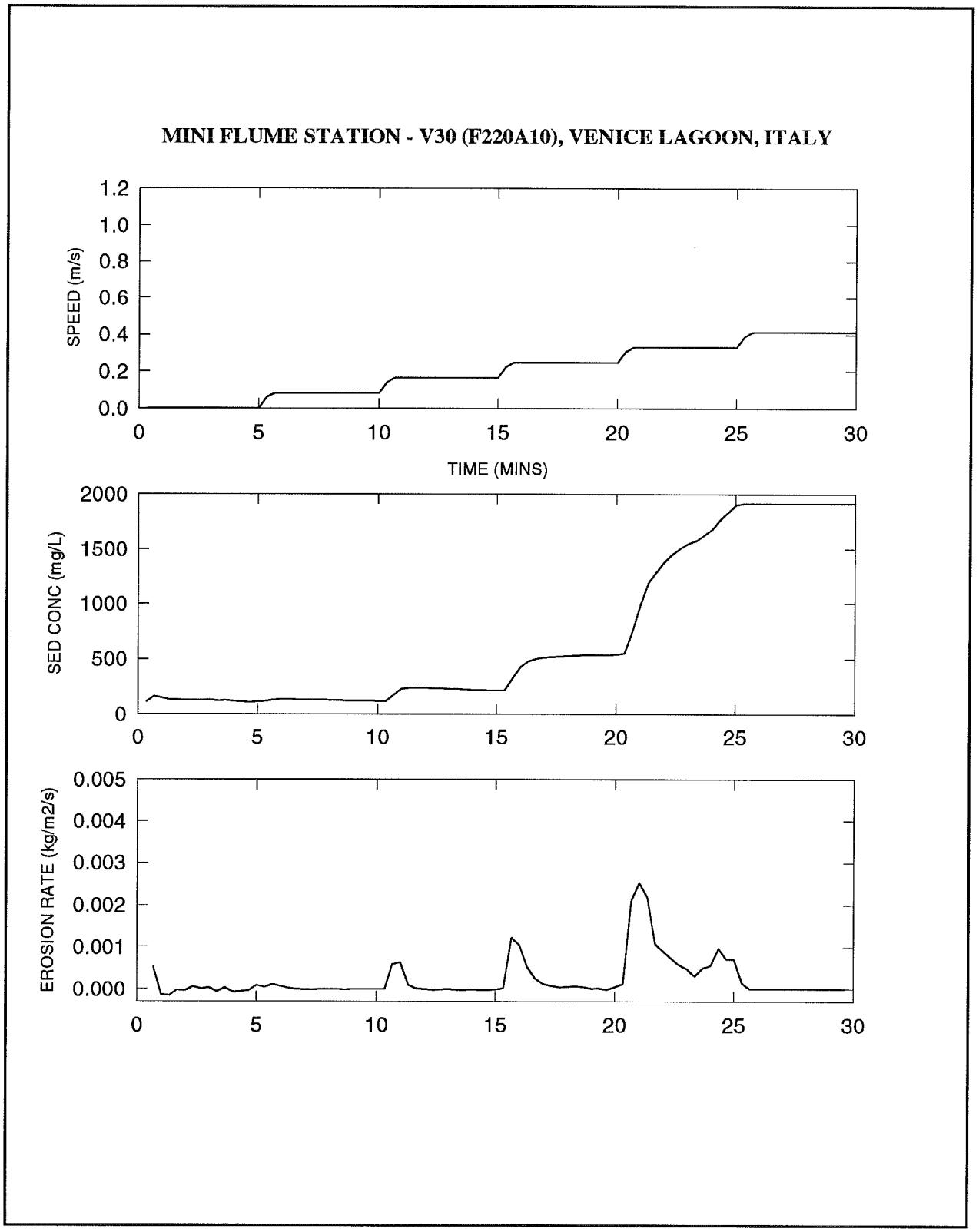

Figure 4.8.3 : Mini Flume time-series from site V30 recorded during the summer campaign.

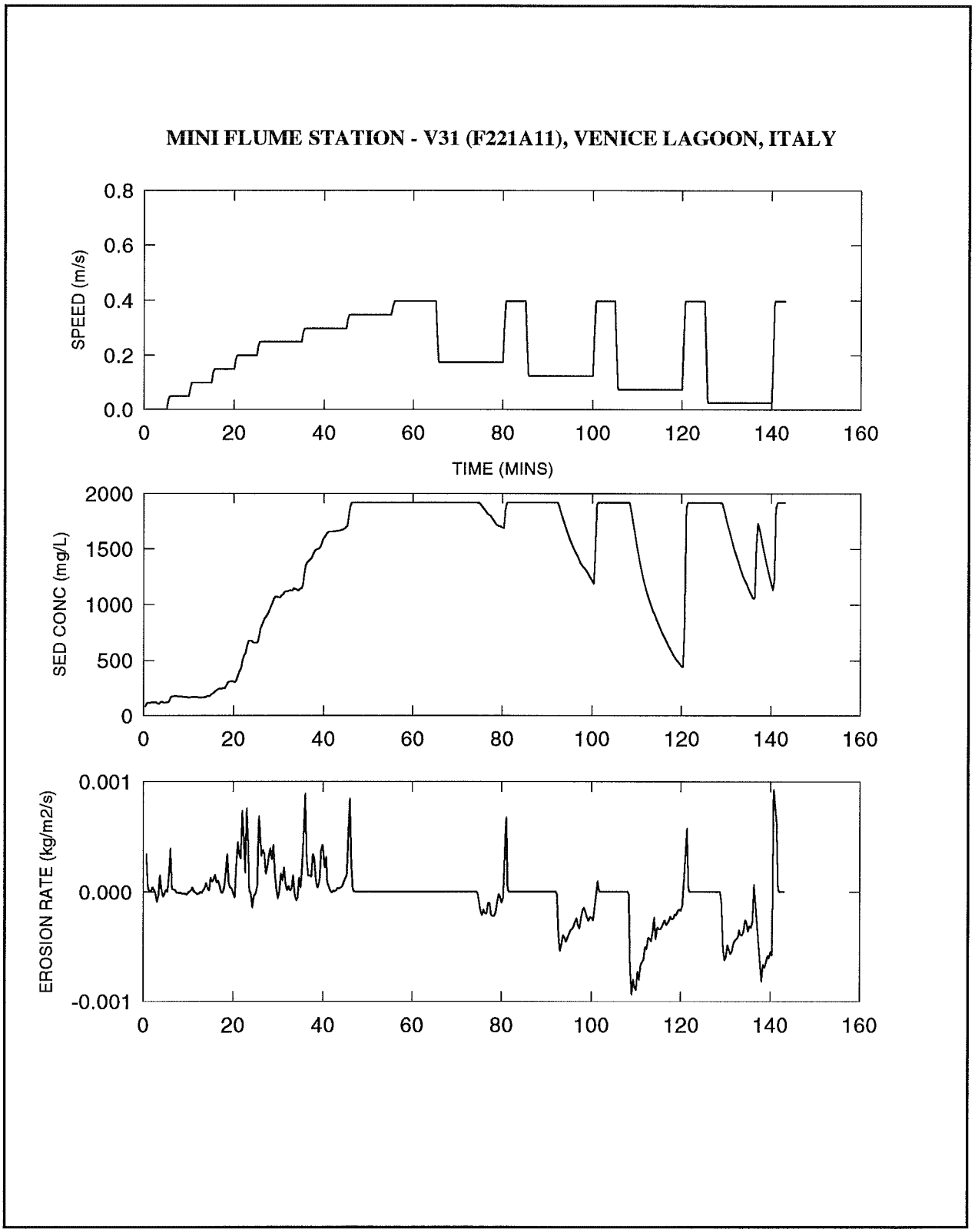

Figure 4.8.4 : Mini Flume time-series from site V31 recorded during the summer campaign.

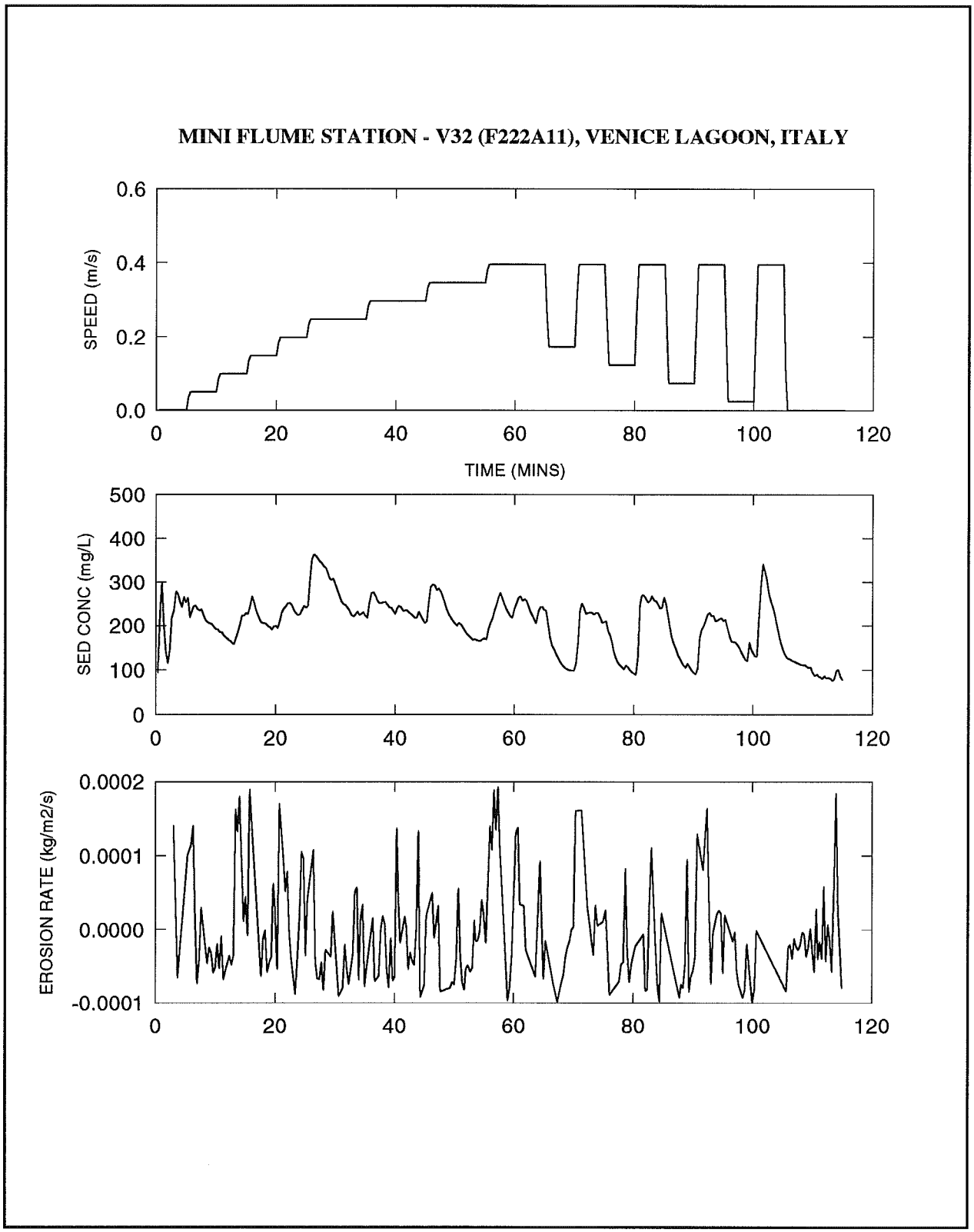

Figure 4.8.5 : Mini Flume time-series from site V32 recorded during the summer campaign.

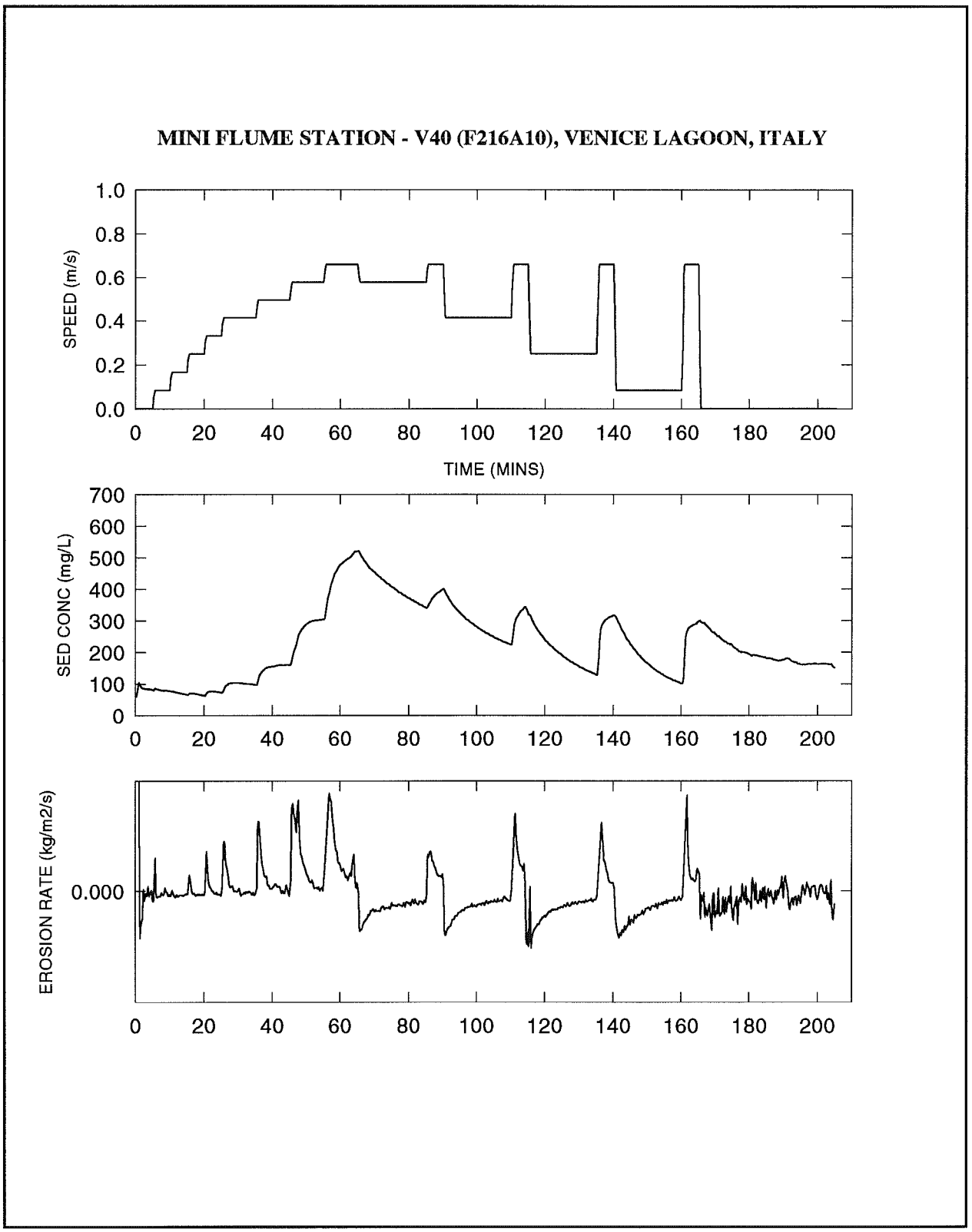

Figure 4.8.6 : Mini Flume time-series from site V40 recorded during the summer campaign.

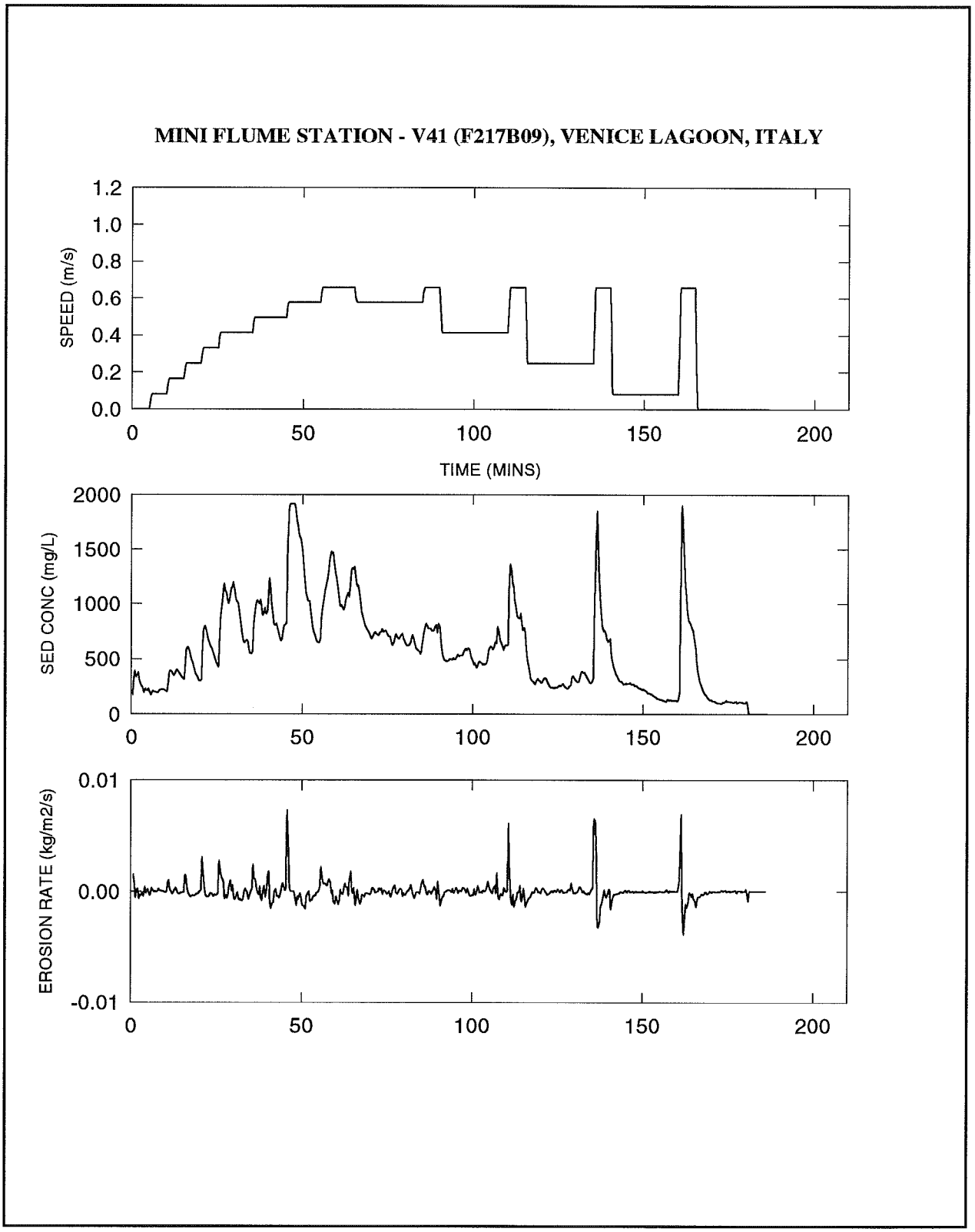

Figure 4.8.7 : Mini Flume time-series from site V41 recorded during the summer campaign.

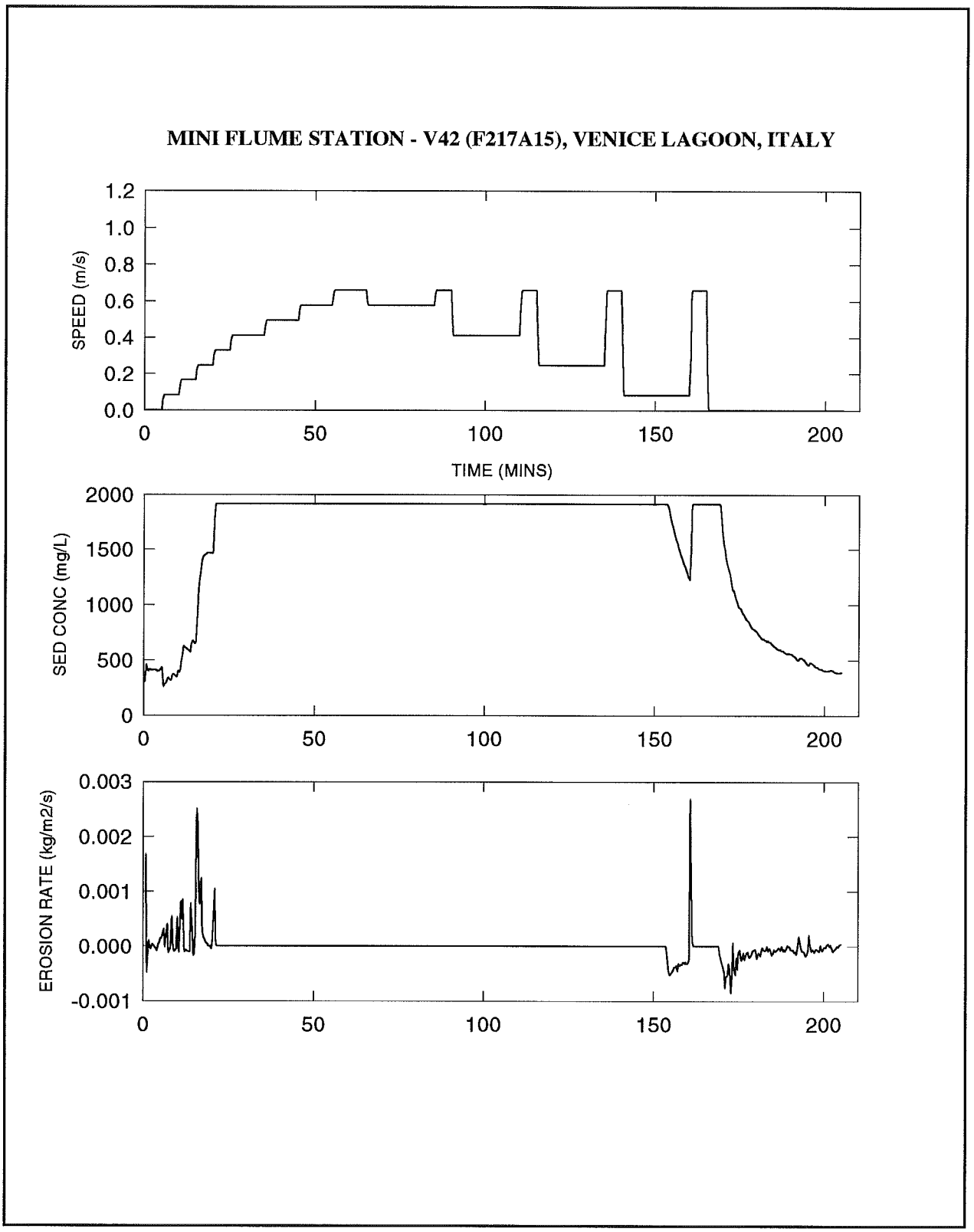

Figure 4.8.8 : Mini Flume time-series from site V42 recorded during the summer campaign.

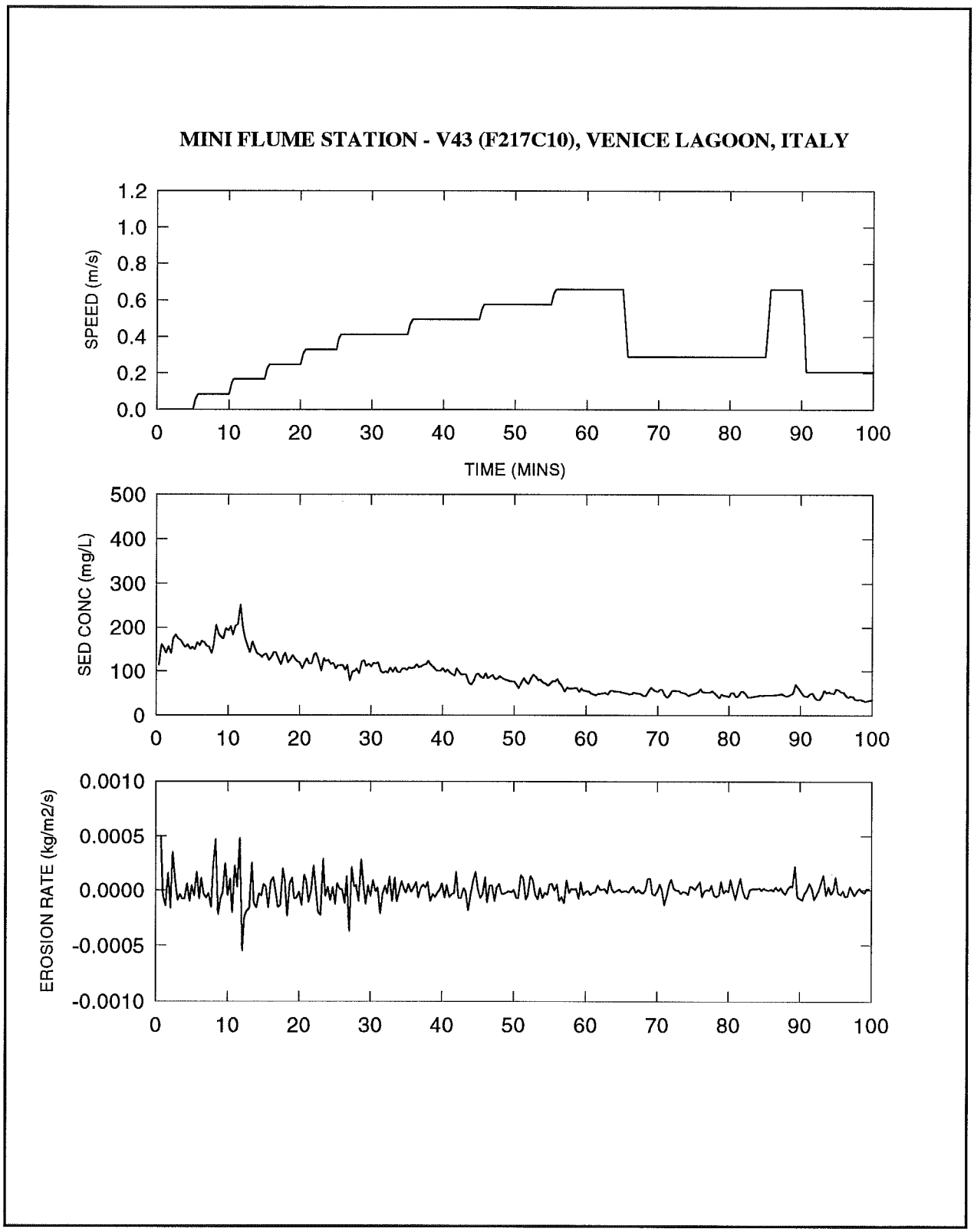

Figure 4.8.9 : Mini Flume time-series from site V43 recorded during summer campaign.

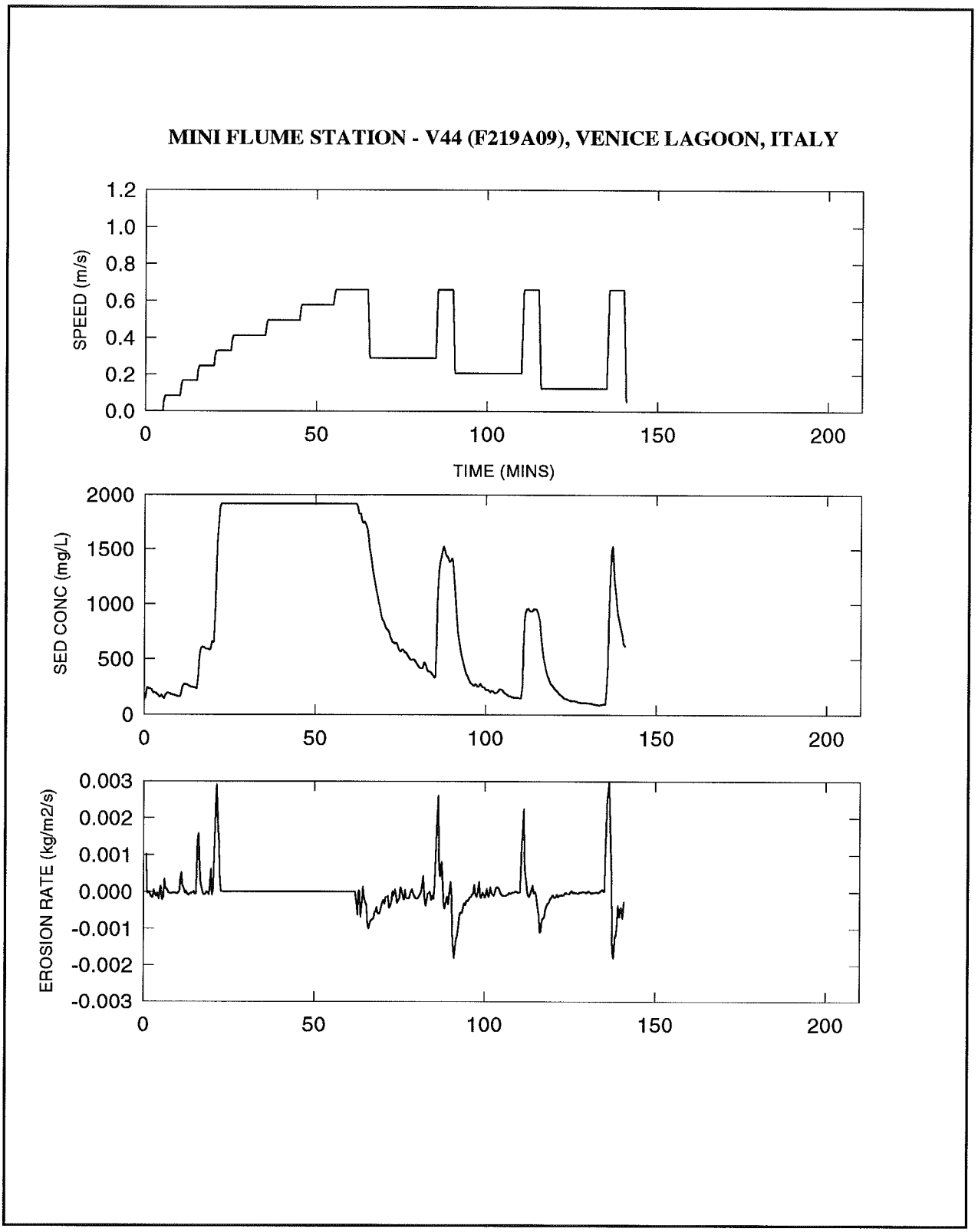

Figure 4.8.10 : Mini Flume time-series from site V44 recorded during summer campaign.

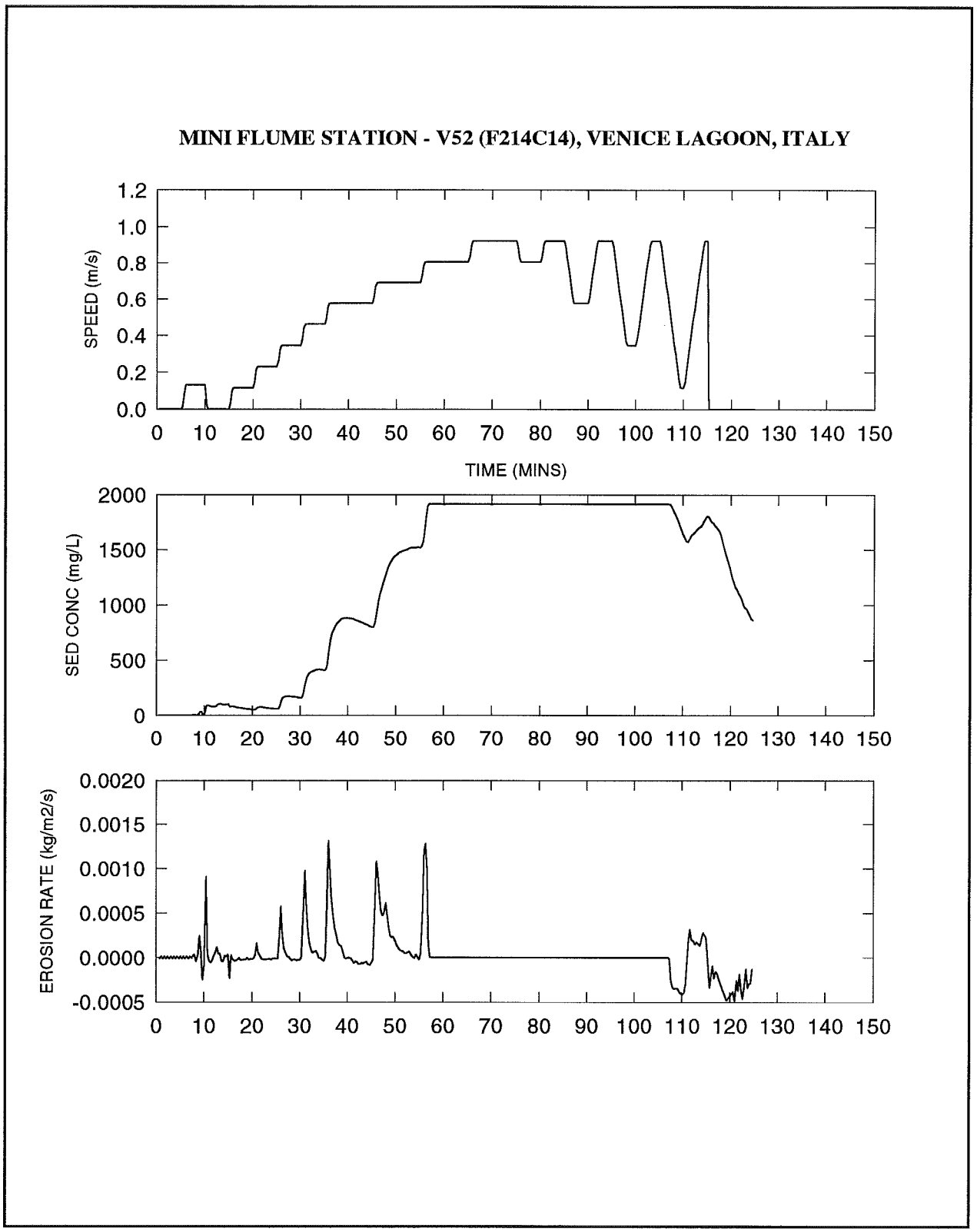

Figure 4.8.11 : Mini Flume time-series from site V52 recorded during summer campaign.

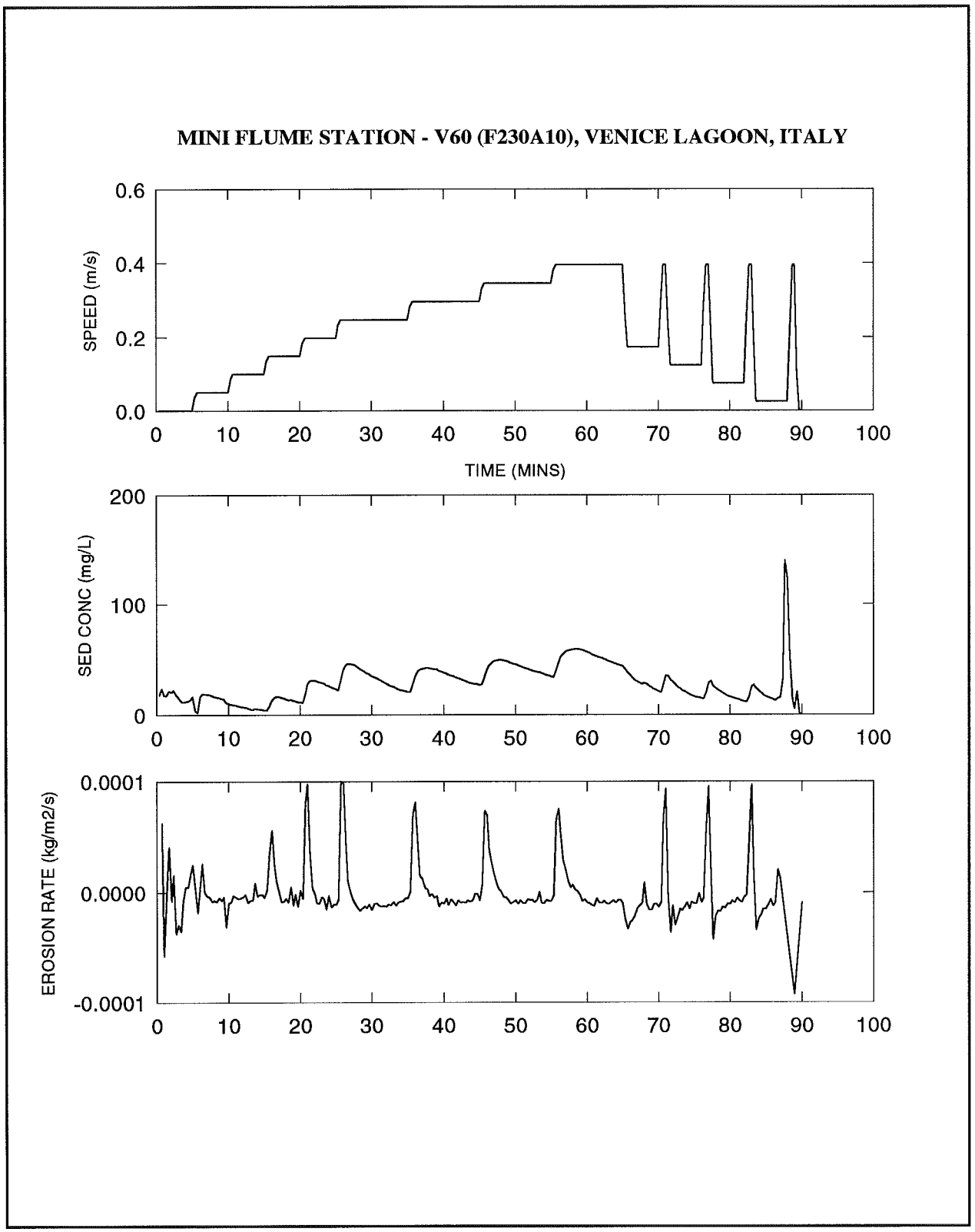

Figure 4.8.12 : Mini Flume time-series from site V60 recorded during summer campaign.

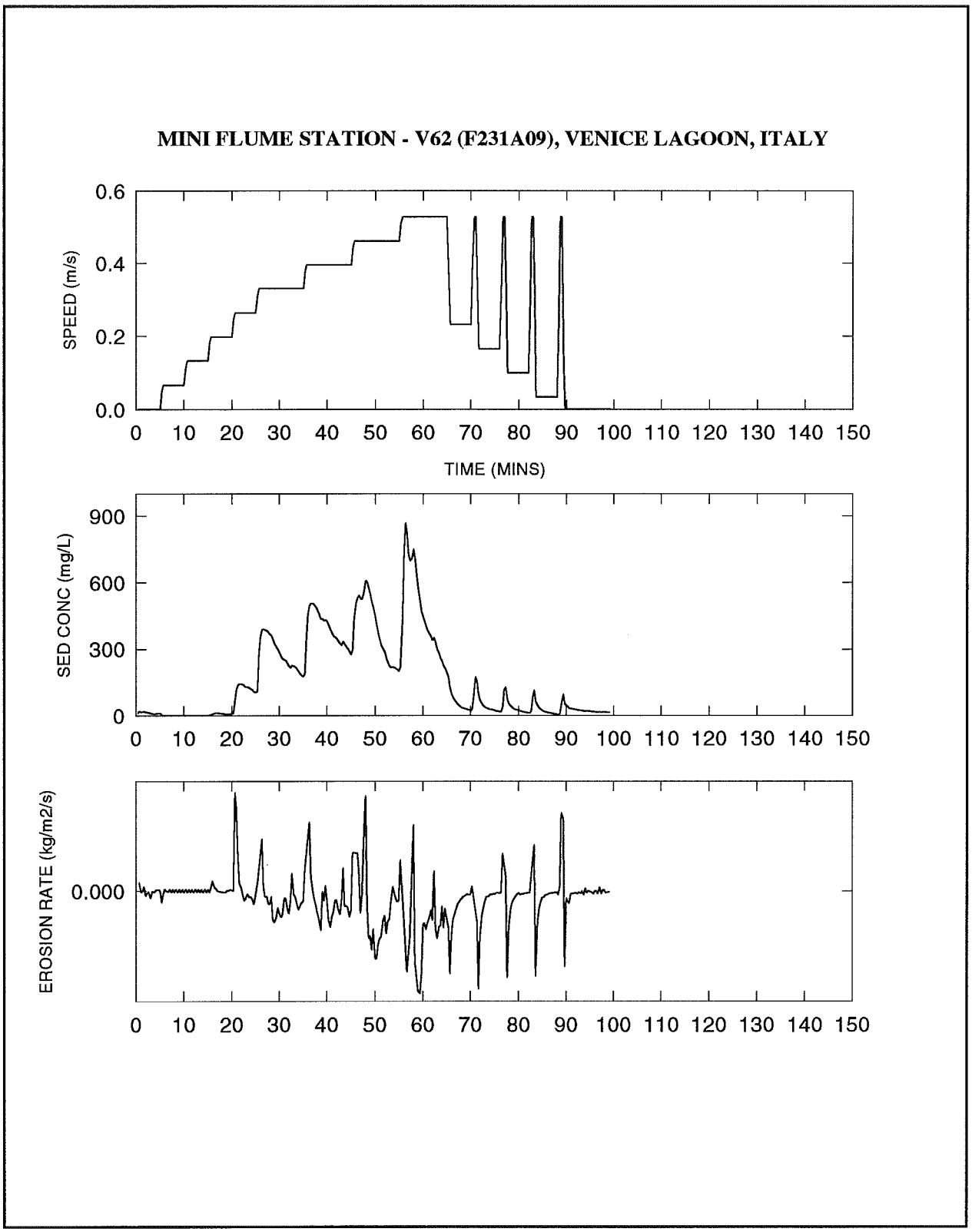

Figure 4.8.13 : Mini Flume time-series from site V62 recorded during summer campaign.

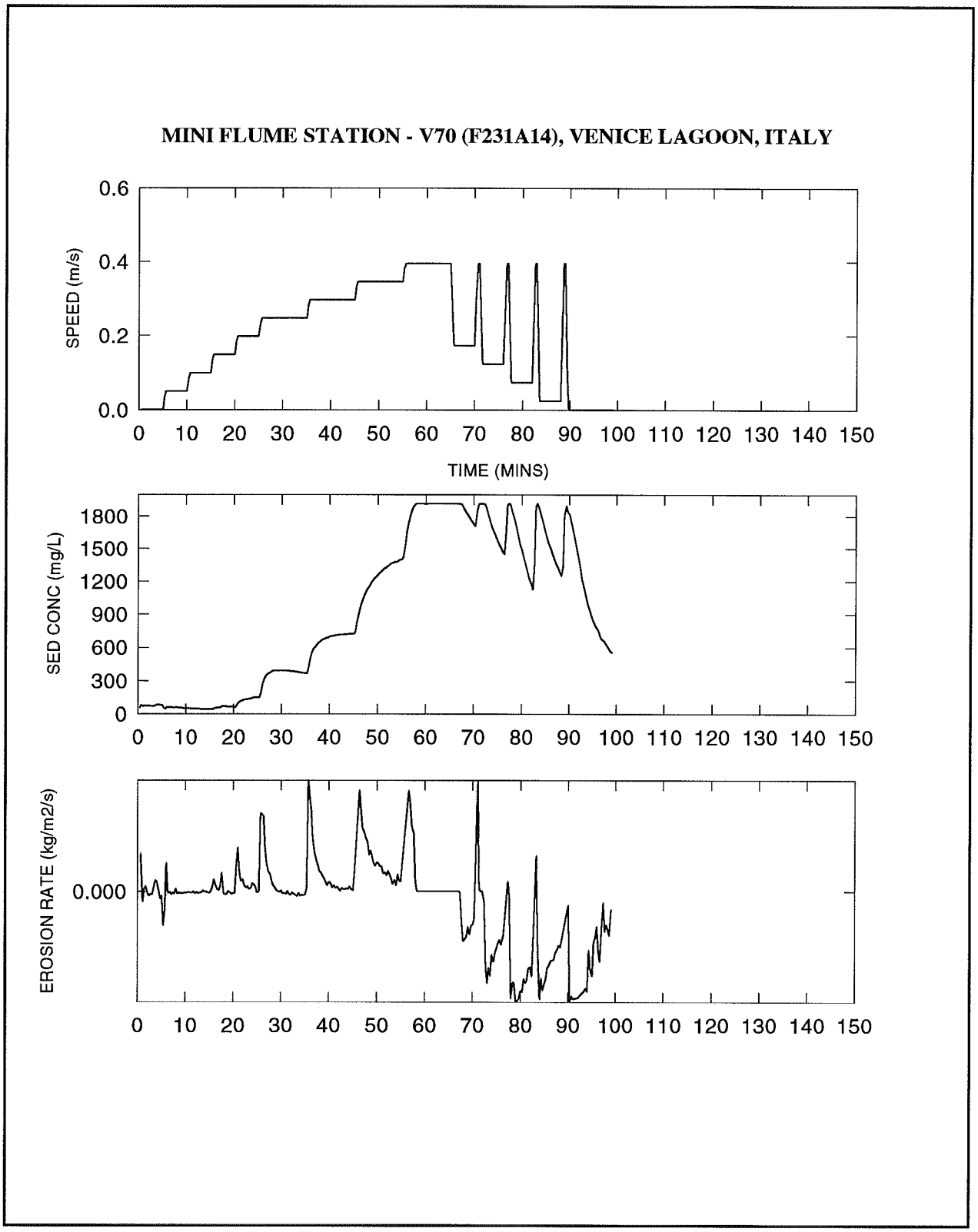

Figure 4.8.14 : Mini Flume time-series from site V70 recorded during summer campaign.

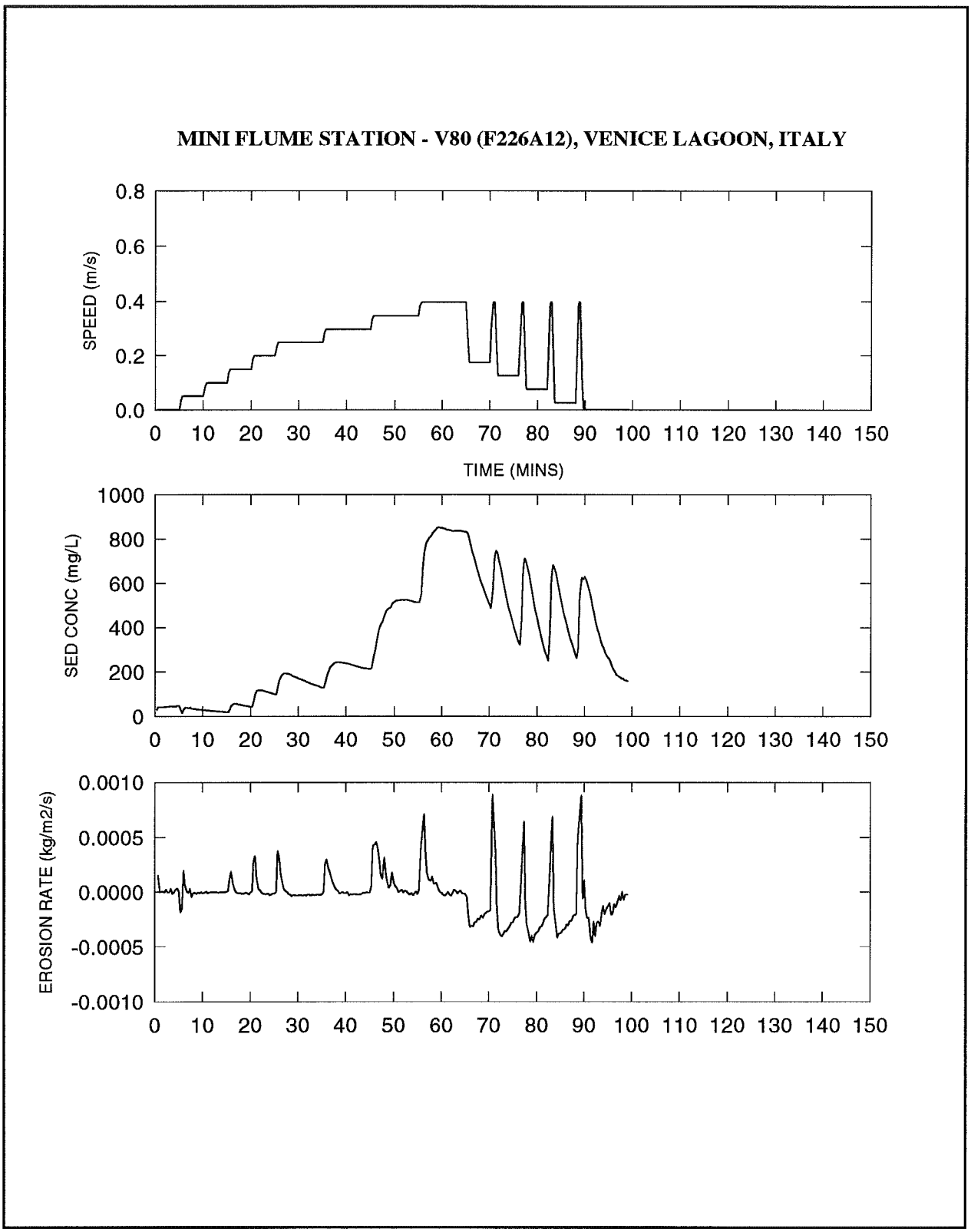

Figure 4.8.15 : Mini Flume time-series from site V80 recorded during summer campaign.

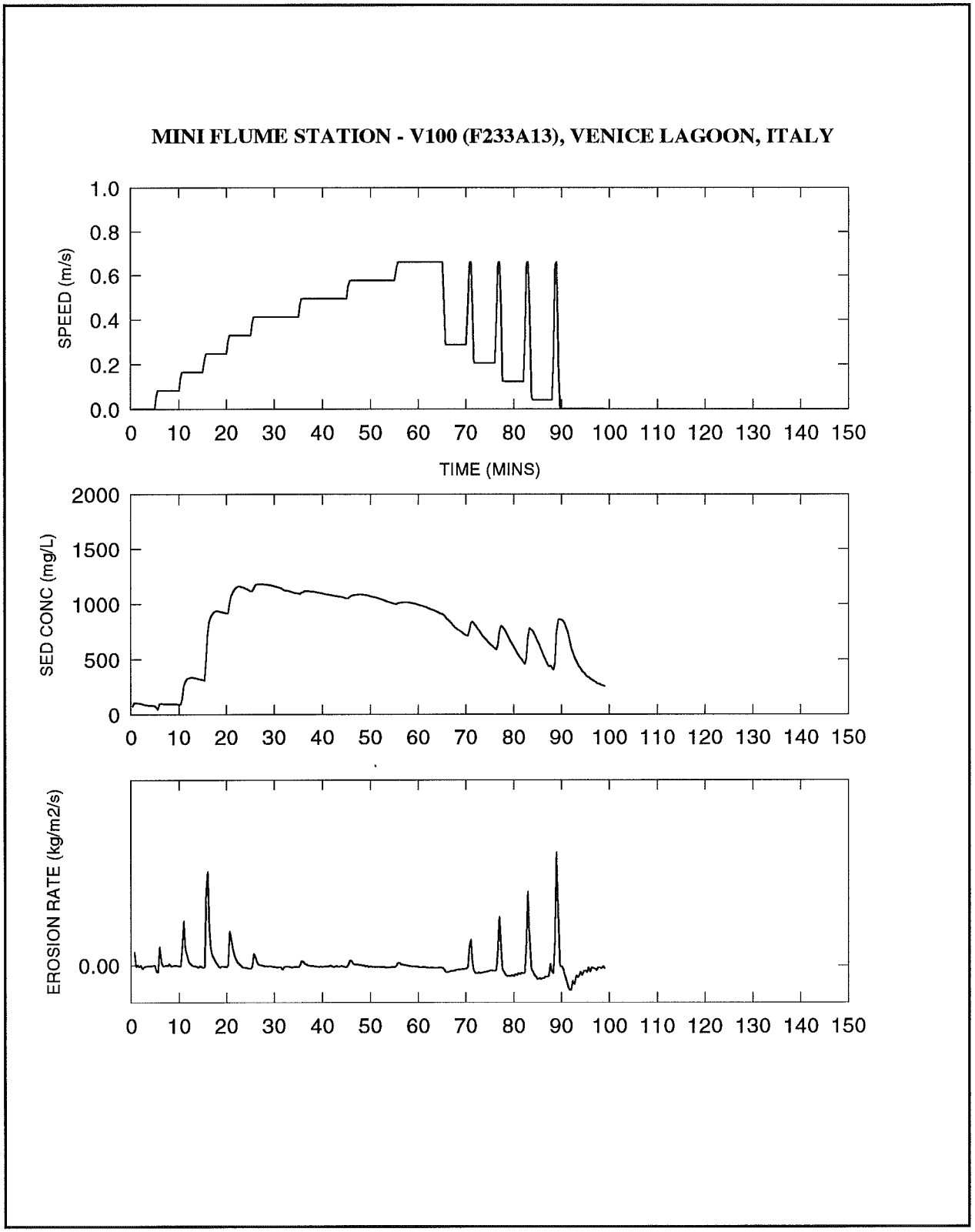

Figure 4.8.16 : Mini Flume time-series from site V100 recorded during summer campaign.

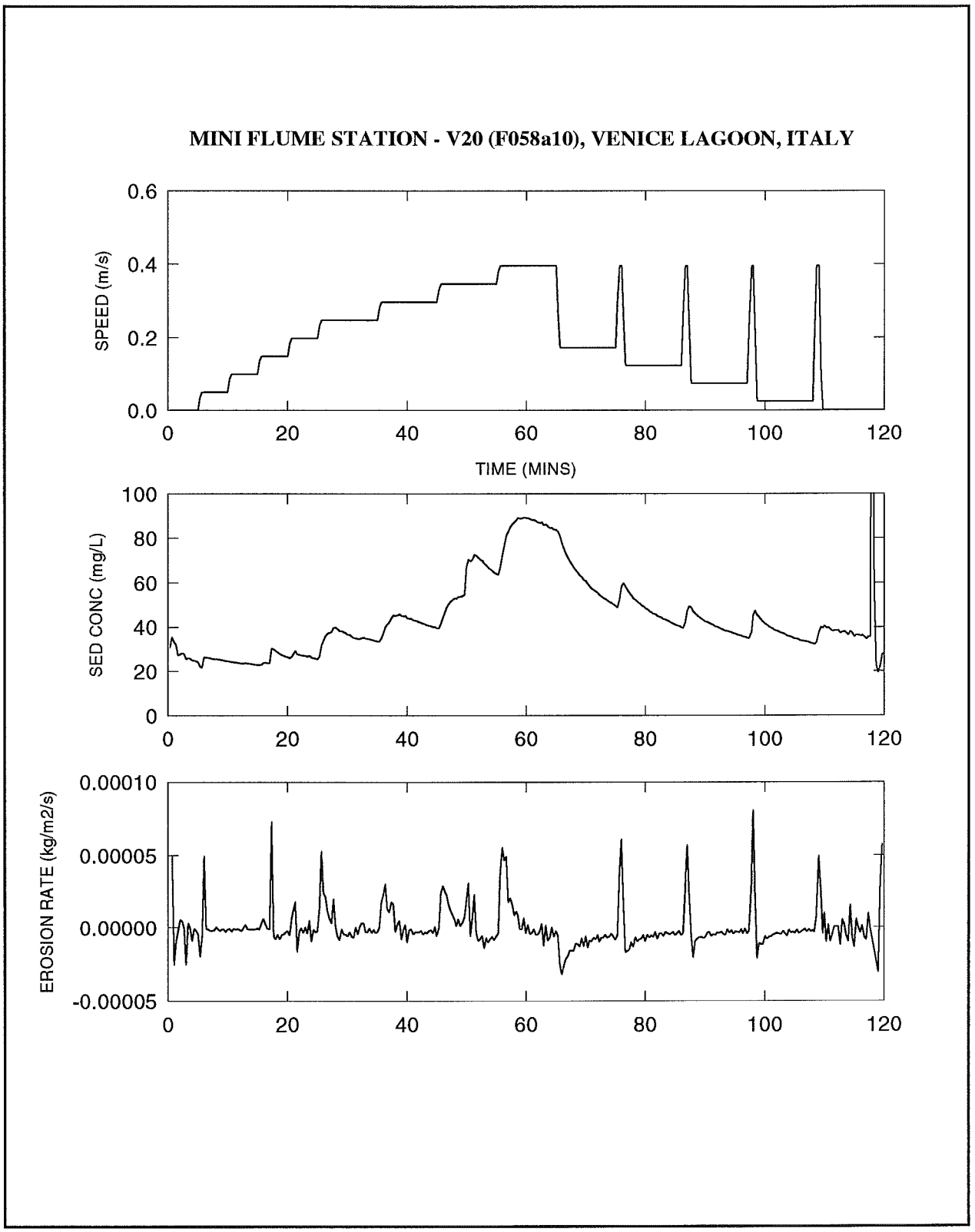

Figure 4..9.1 : Mini Flume time-series from site V20 recorded during the winter campaign.

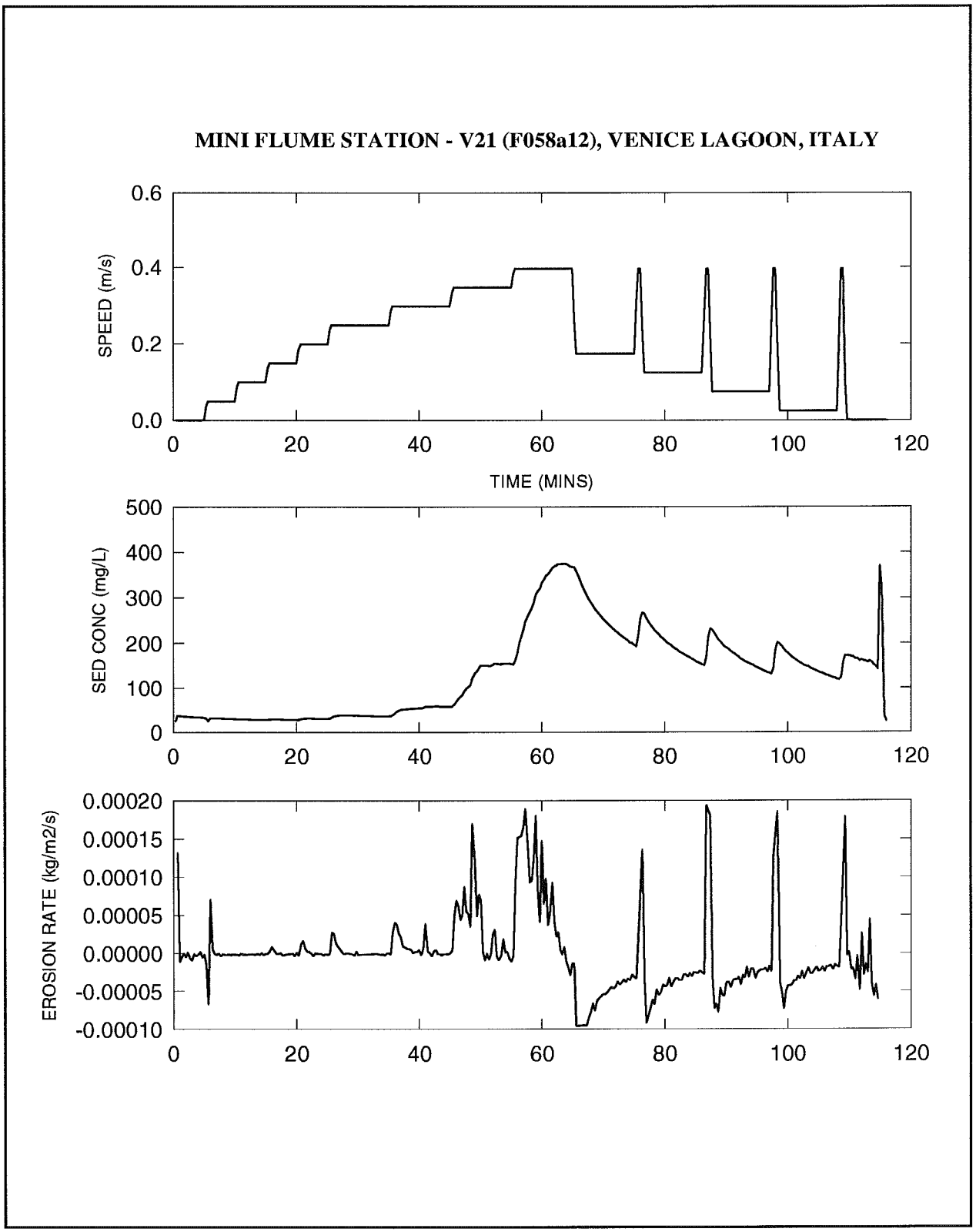

Figure 4.9.2 : Mini Flume time-series from site V21.

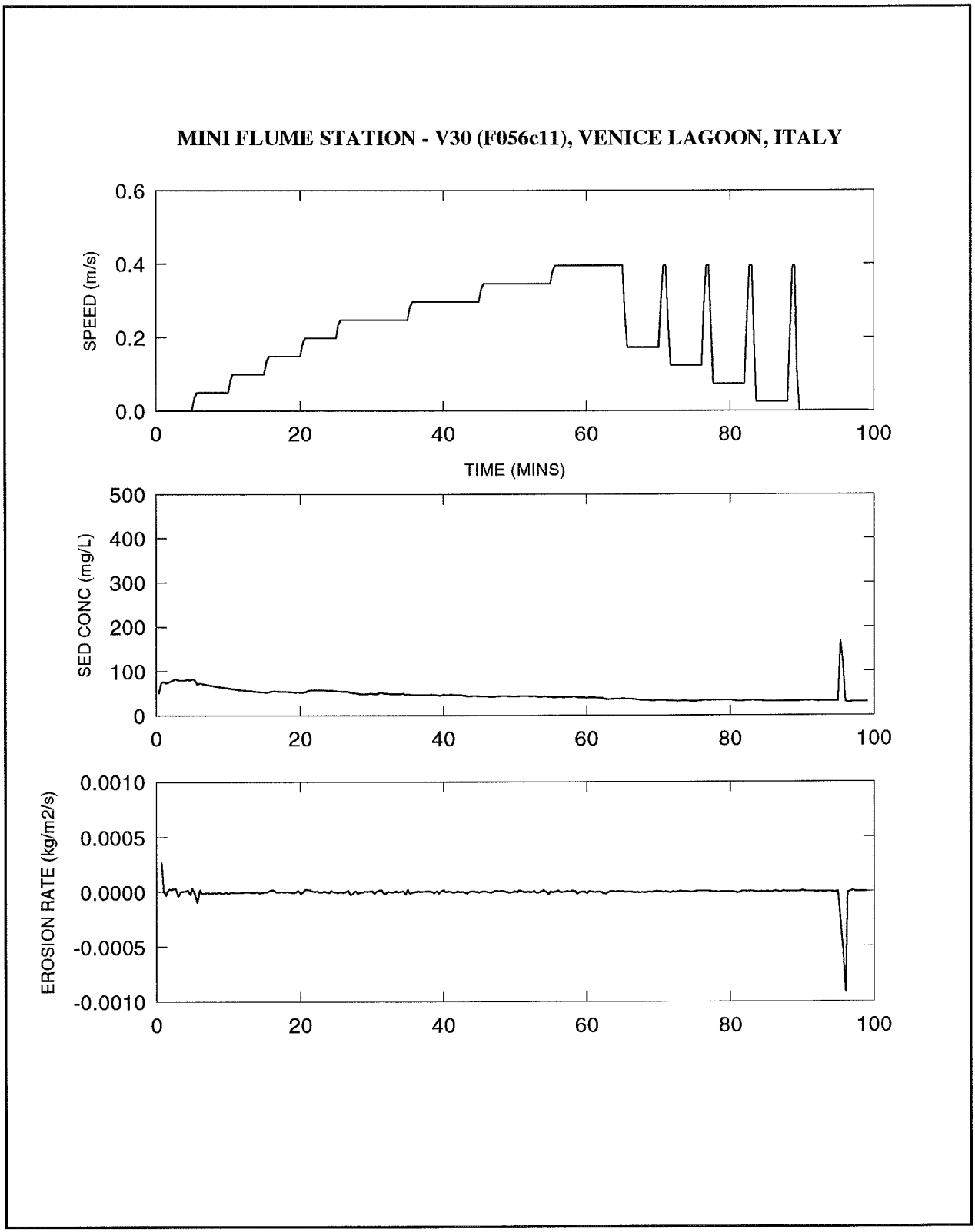

Figure 4.9.3 : Mini Flume time-series from site V30.

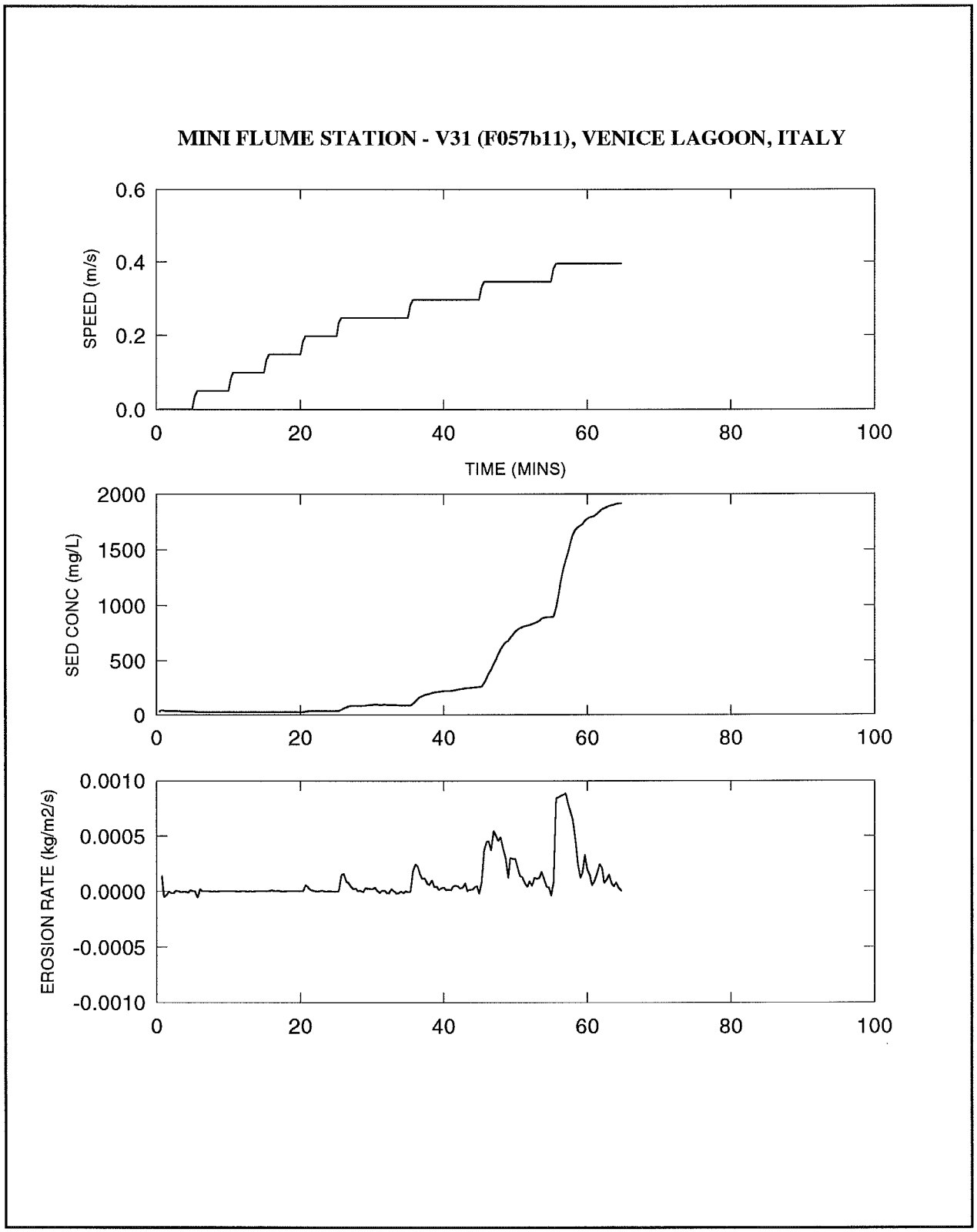

Figure 4.9.4 : Mini Flume time-series from site V31.

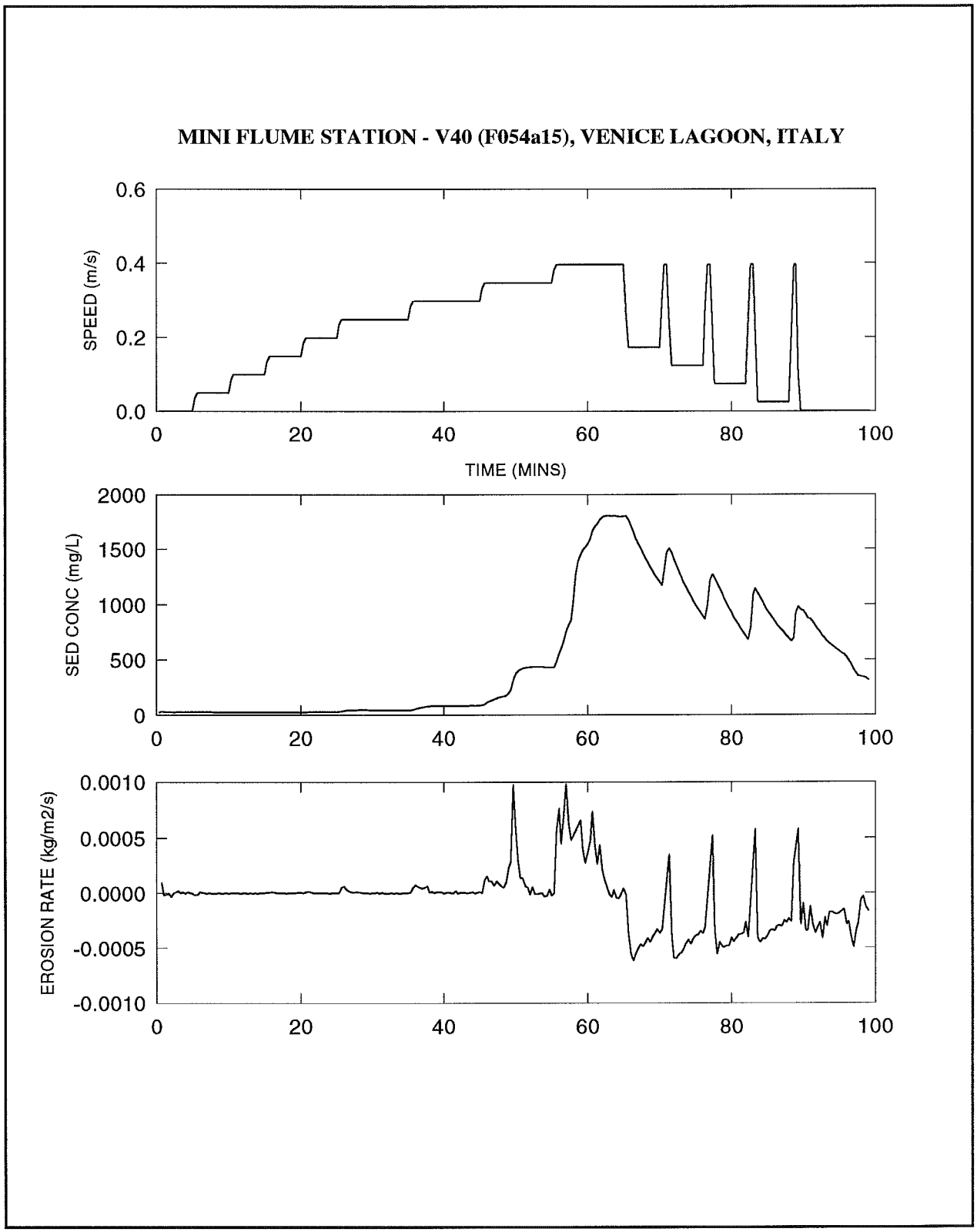

Figure 4.9.5 : Mini Flume time-series from site V40.

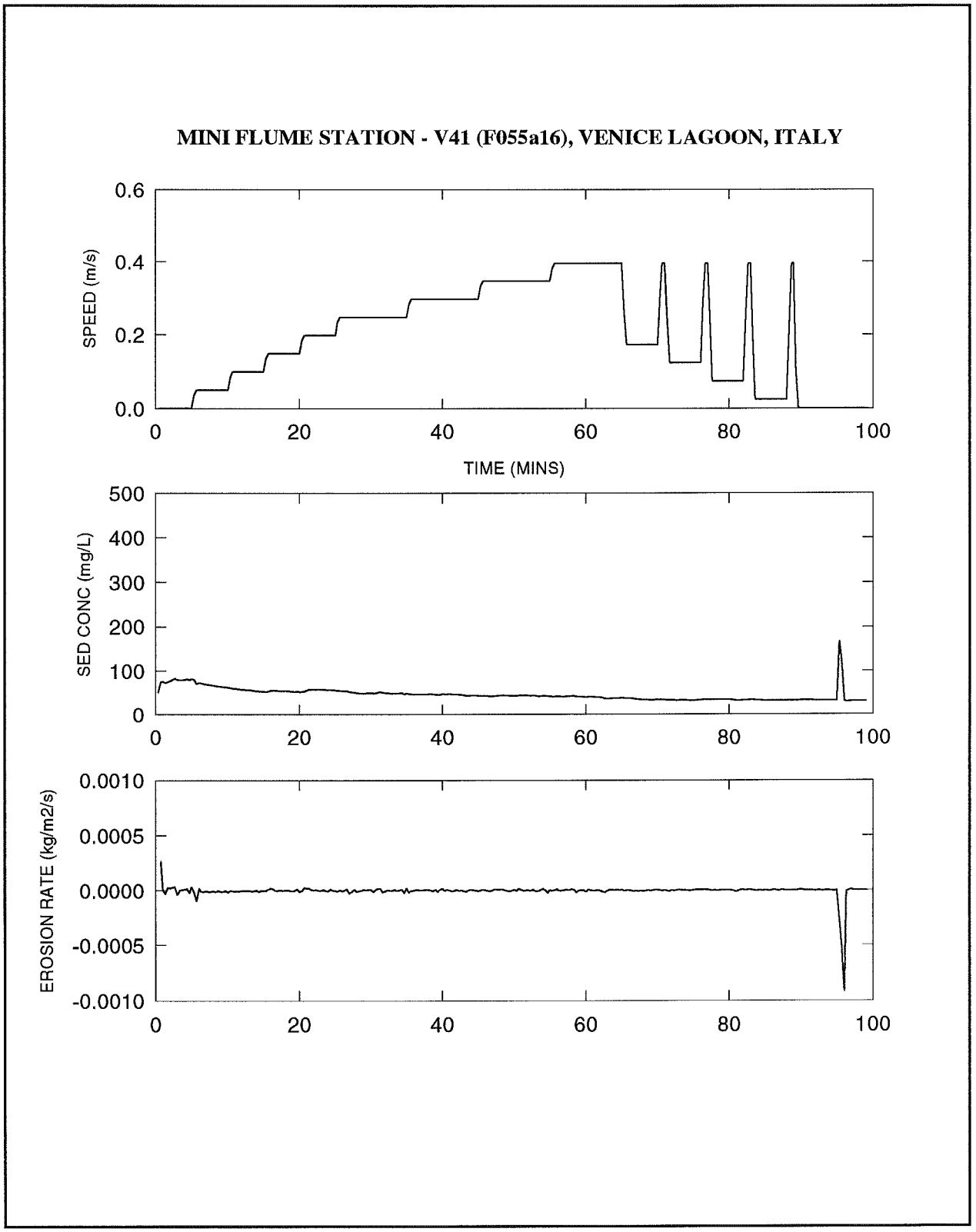

Figure 4.9.6 : Mini Flume time-series from site V41.

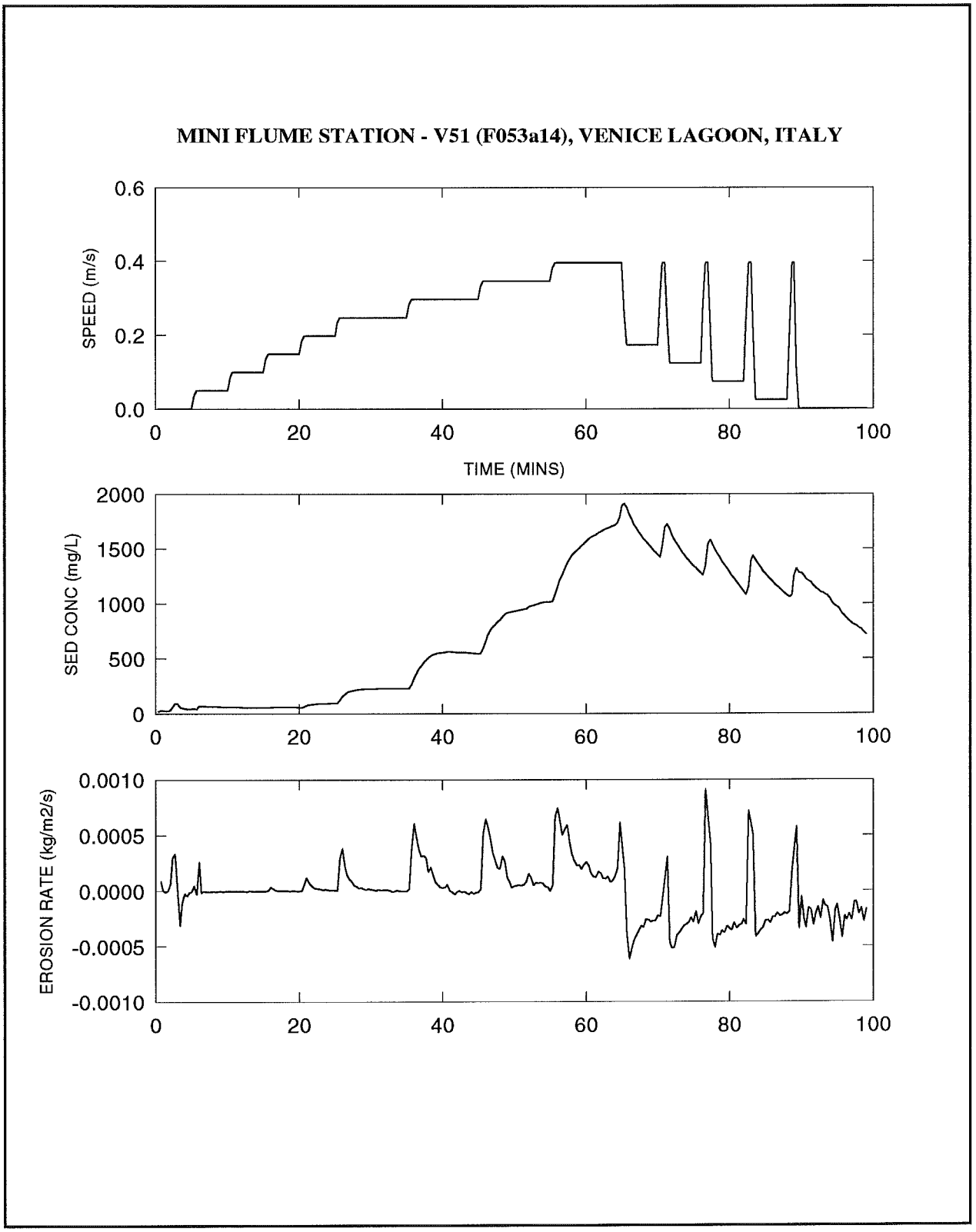

Figure 4.9.7 : Mini Flume time-series from site V51.

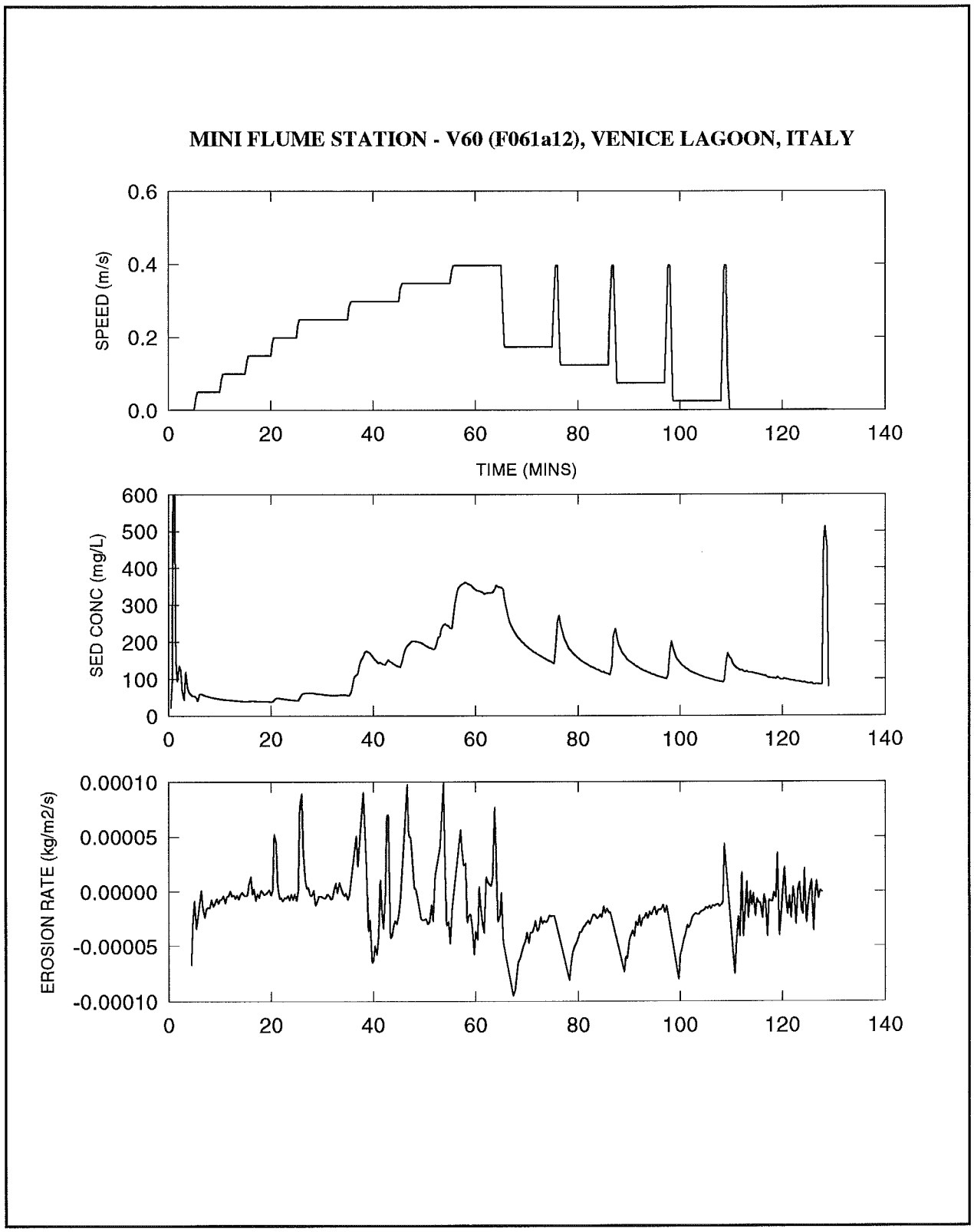

Figure 4.9.8 : Mini Flume time-series from site V60.

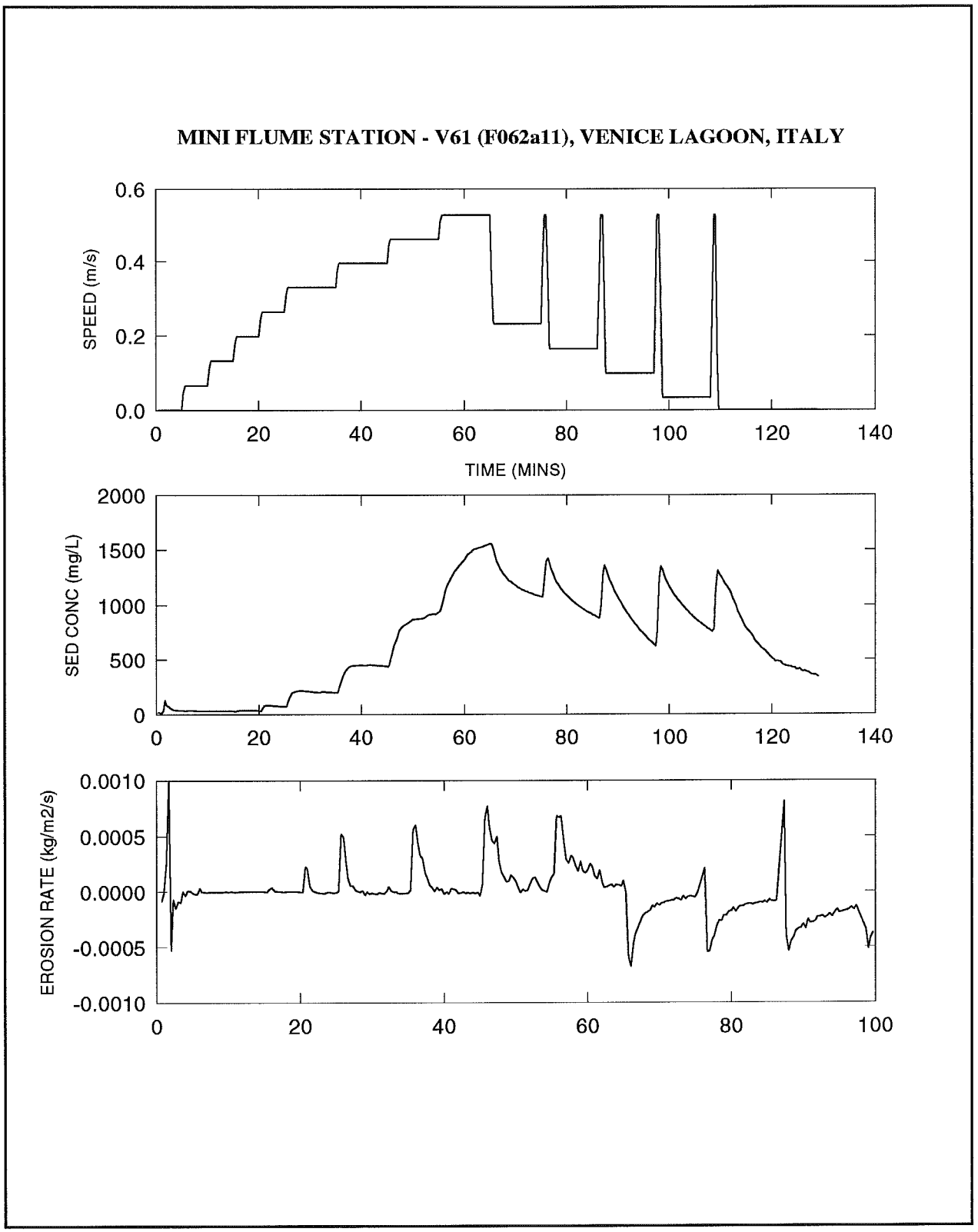

Figure 4.9.9 : Mini Flume time-series from site V61.

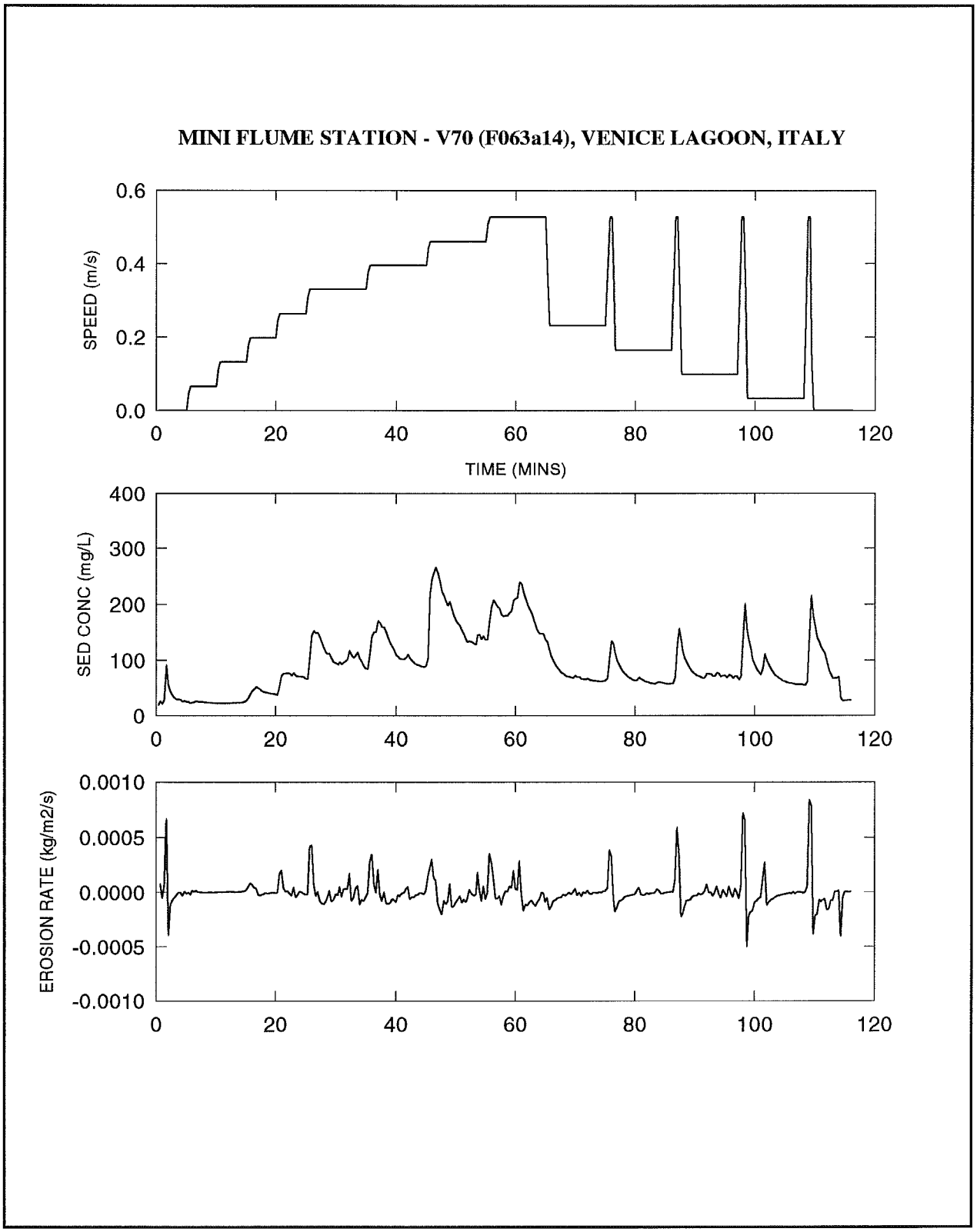

Figure 4.9.10 : Mini Flume time-series from site V70.

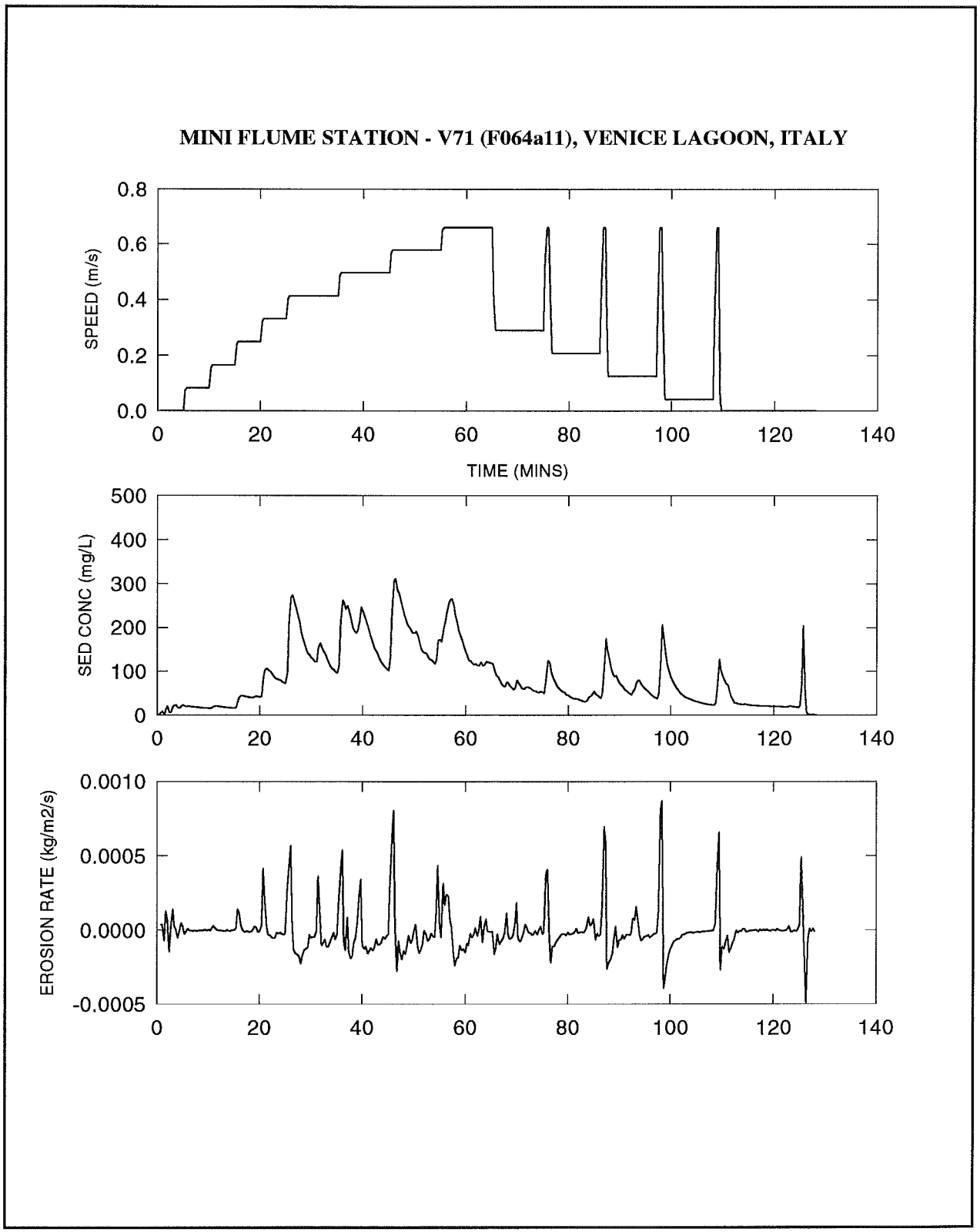

Figure 4.9.11 : Mini Flume time-series from site V71.

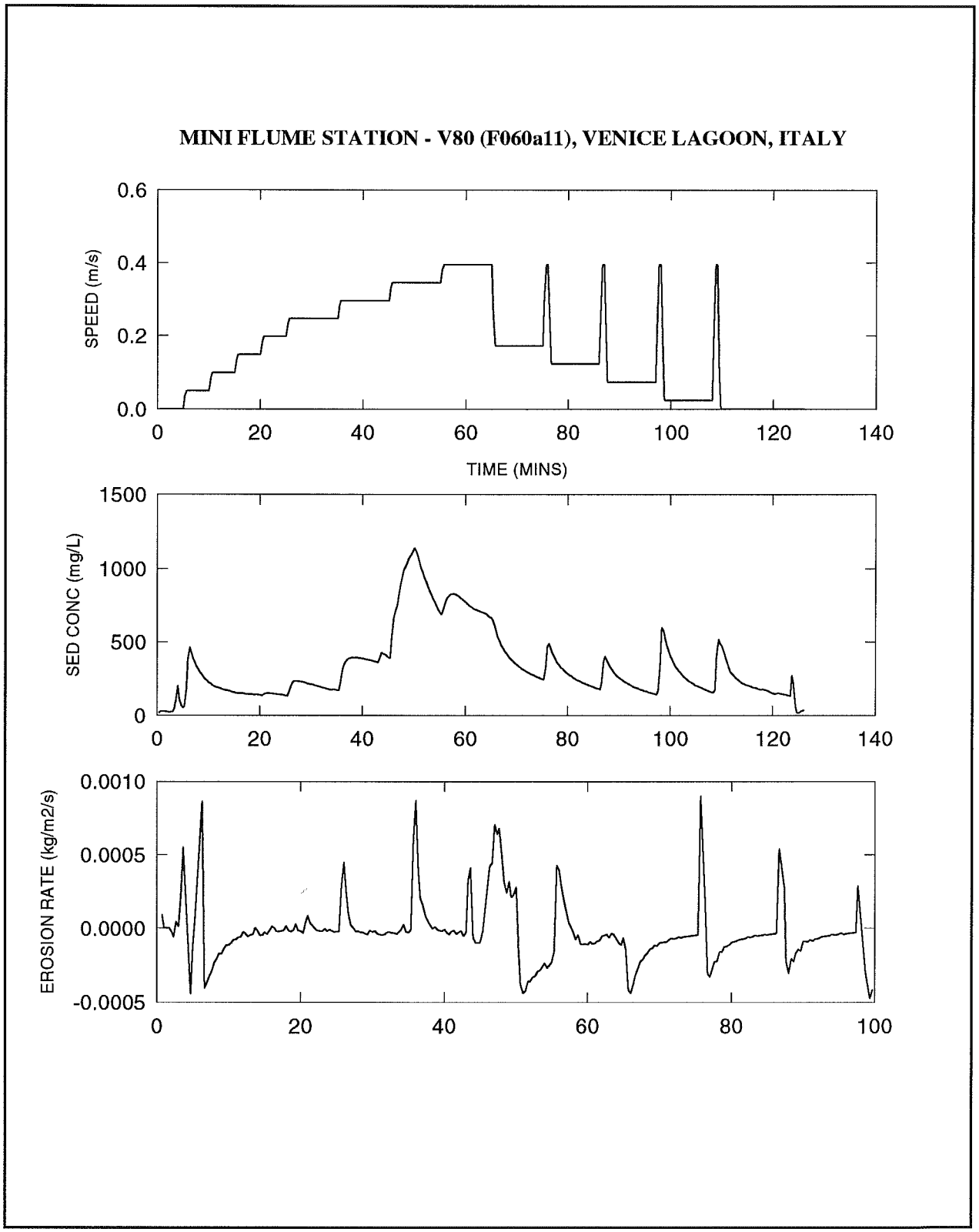

Figure 4.9.12 : Mini Flume time-series from site V80

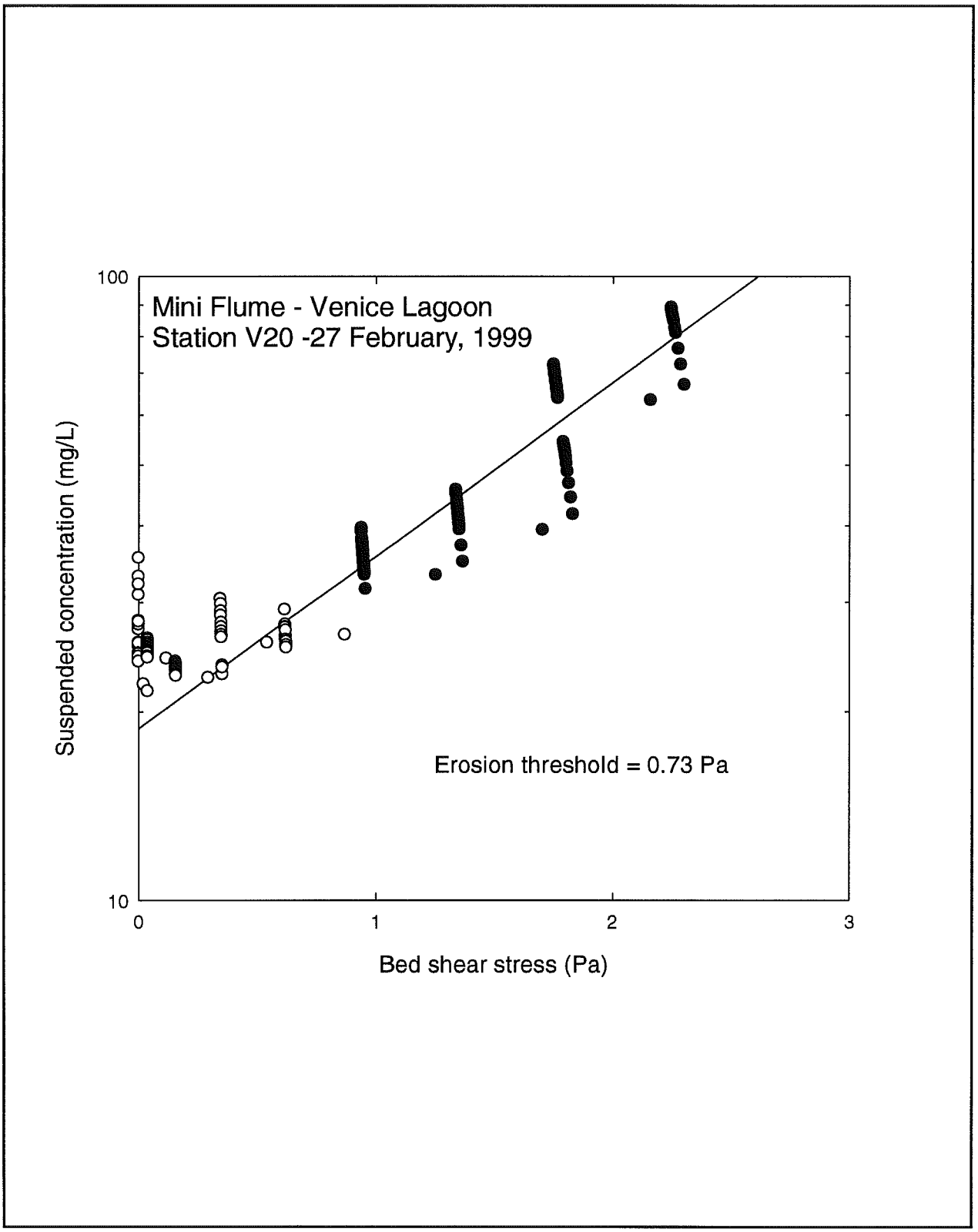

Figure 4.9.1.1 : A regression analysis of applied shear stress for site V20 against suspended sediment concentration for values interpreted as post-erosional (solid dots).

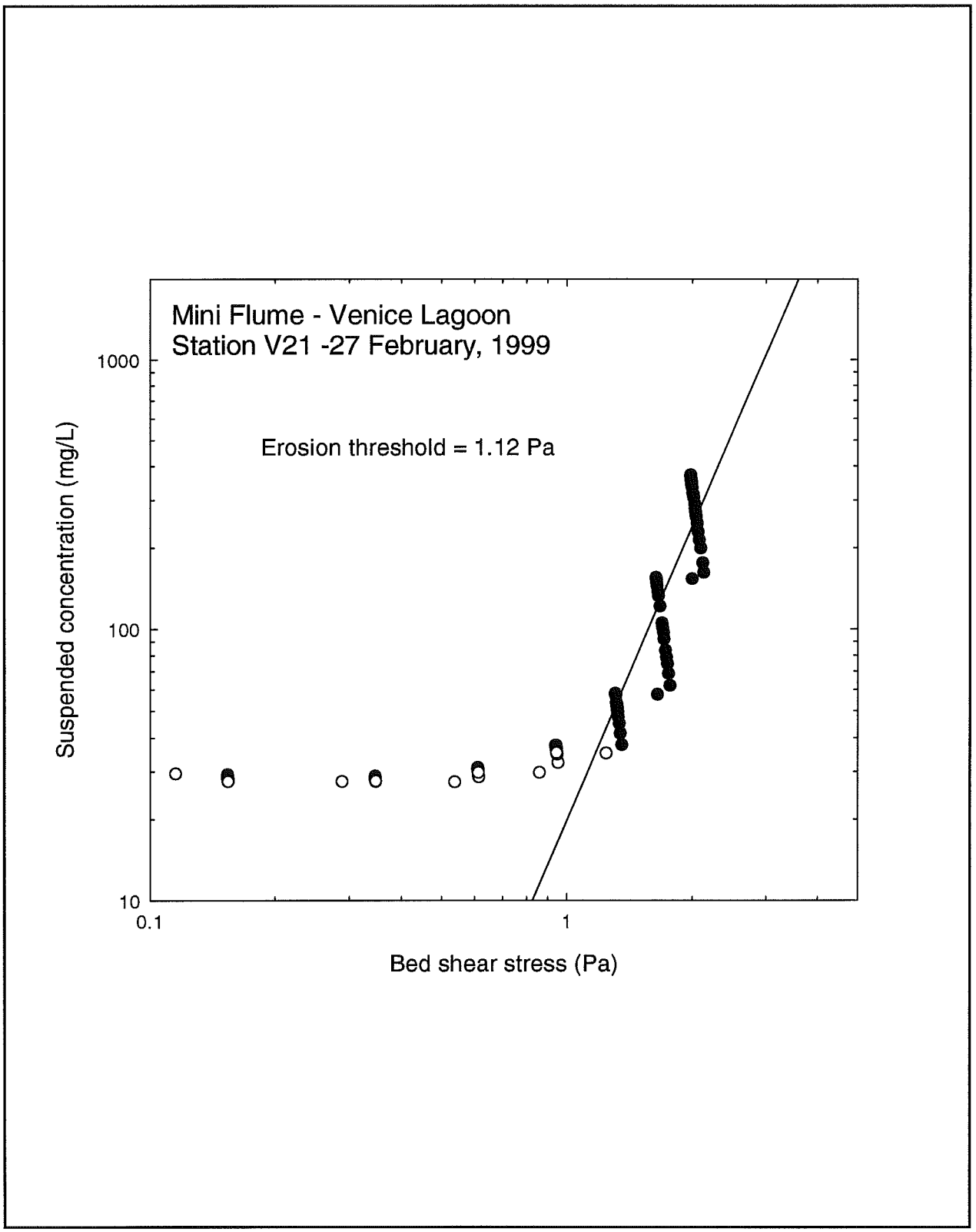

Figure 4.9.1.2 : A regression analysis of applied shear stress for site V21 against suspended sediment concentration for values interpreted as post-erosional (solid dots).

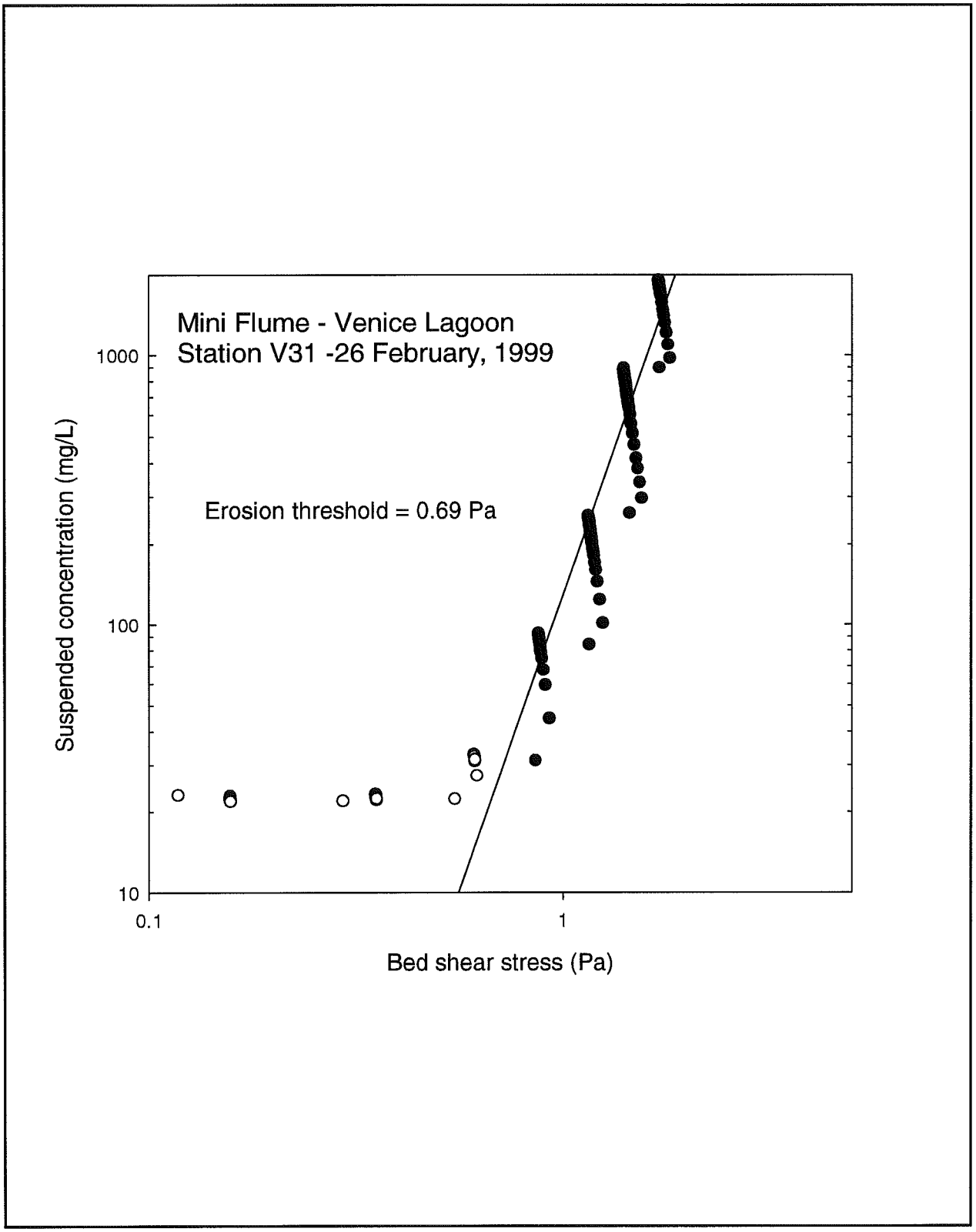

Figure 4.9.1.3 : A regression analysis of applied shear stress for site V31 against suspended sediment concentration for values interpreted as post-erosional (solid dots).

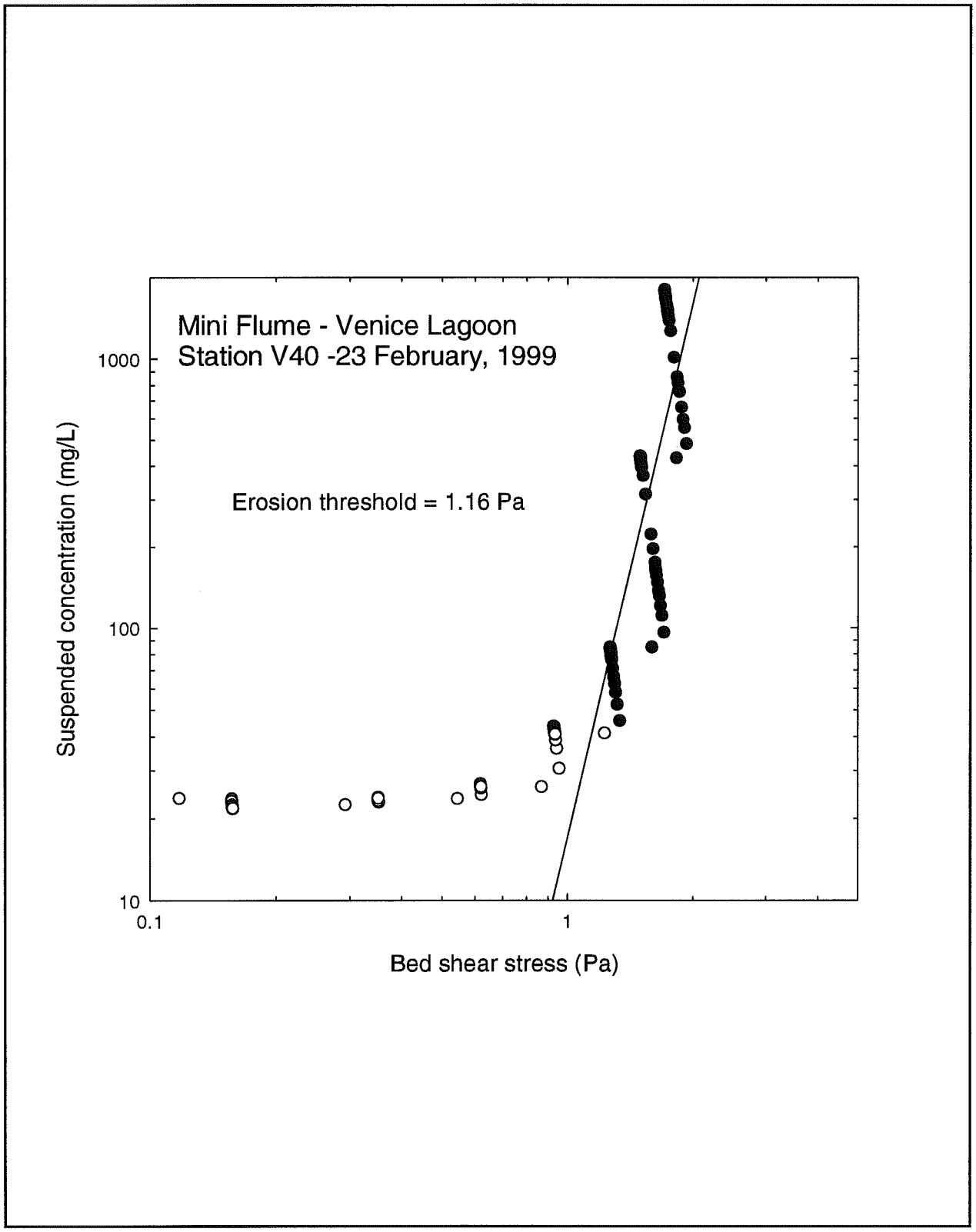

Figure 4.9.1.4 : A regression analysis of applied shear stress for site V40 against suspended sediment concentration for values interpreted as post-erosional (solid dots).

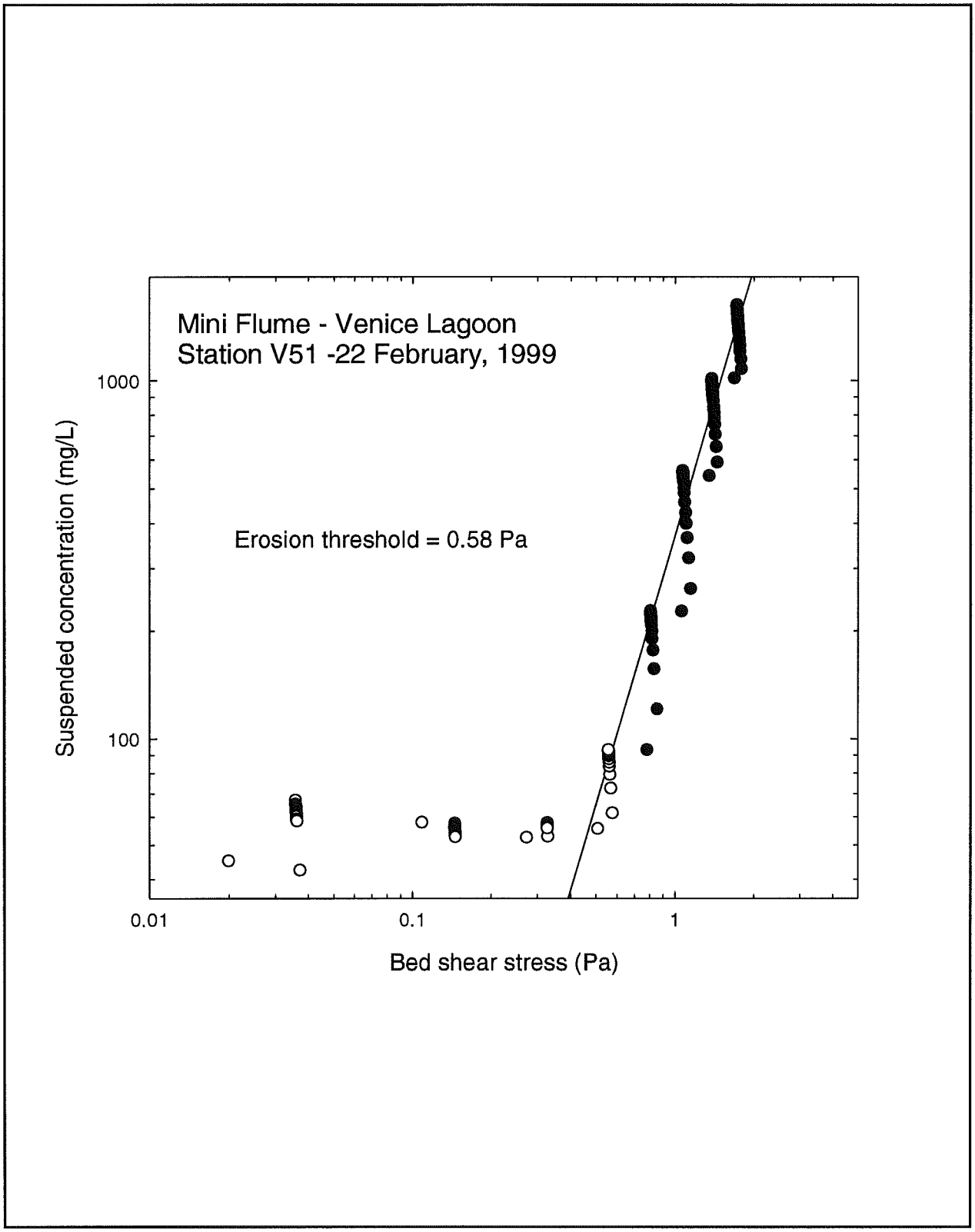

Figure 4.9.1.5 : A regression analysis of applied shear stress for site V51 against suspended sediment concentration for values interpreted as post-erosional (solid dots).

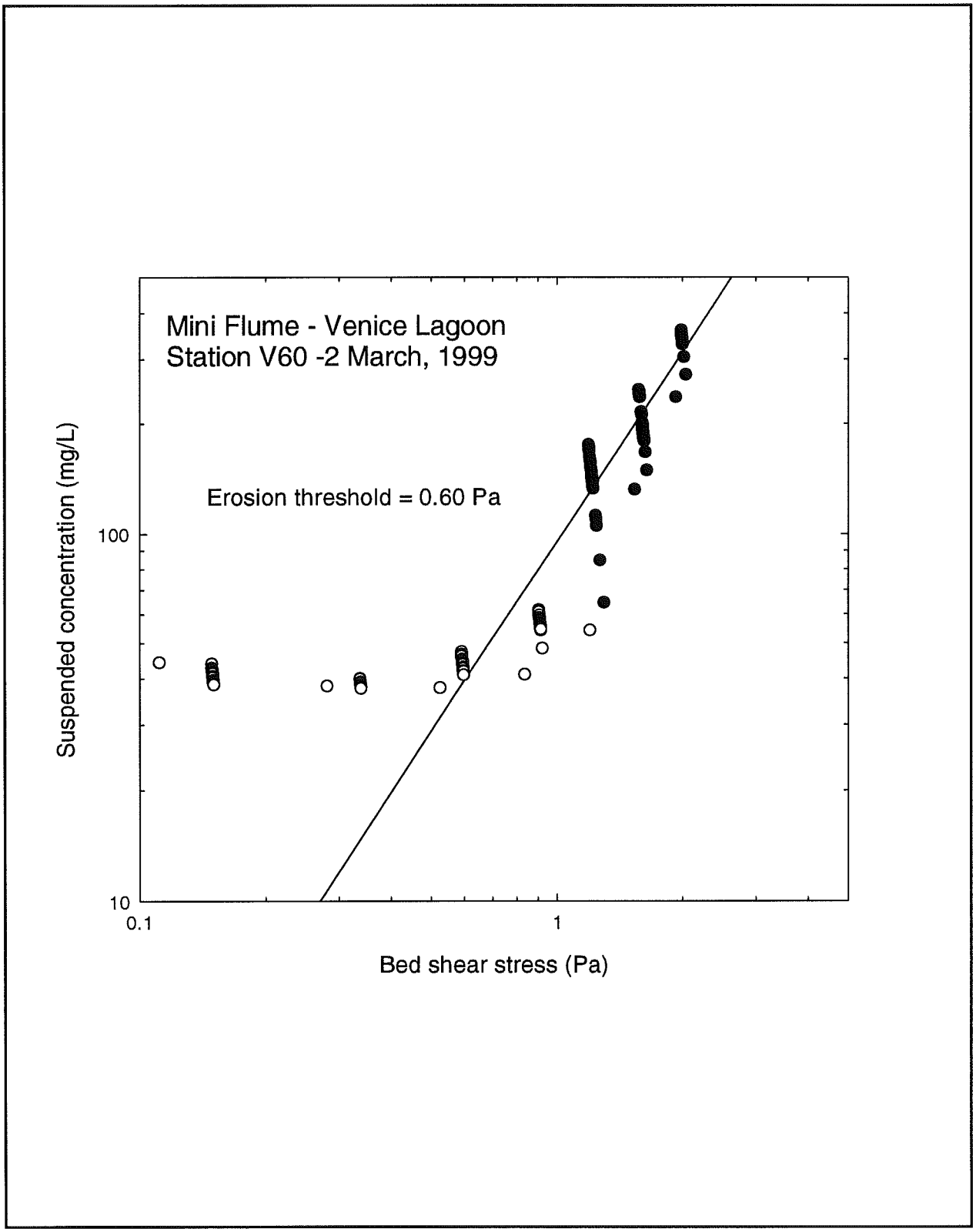

Figure 4.9.1.6 : A regression analysis of applied shear stress for site V60 against suspended sediment concentration for values interpreted as post-erosional (solid dots).

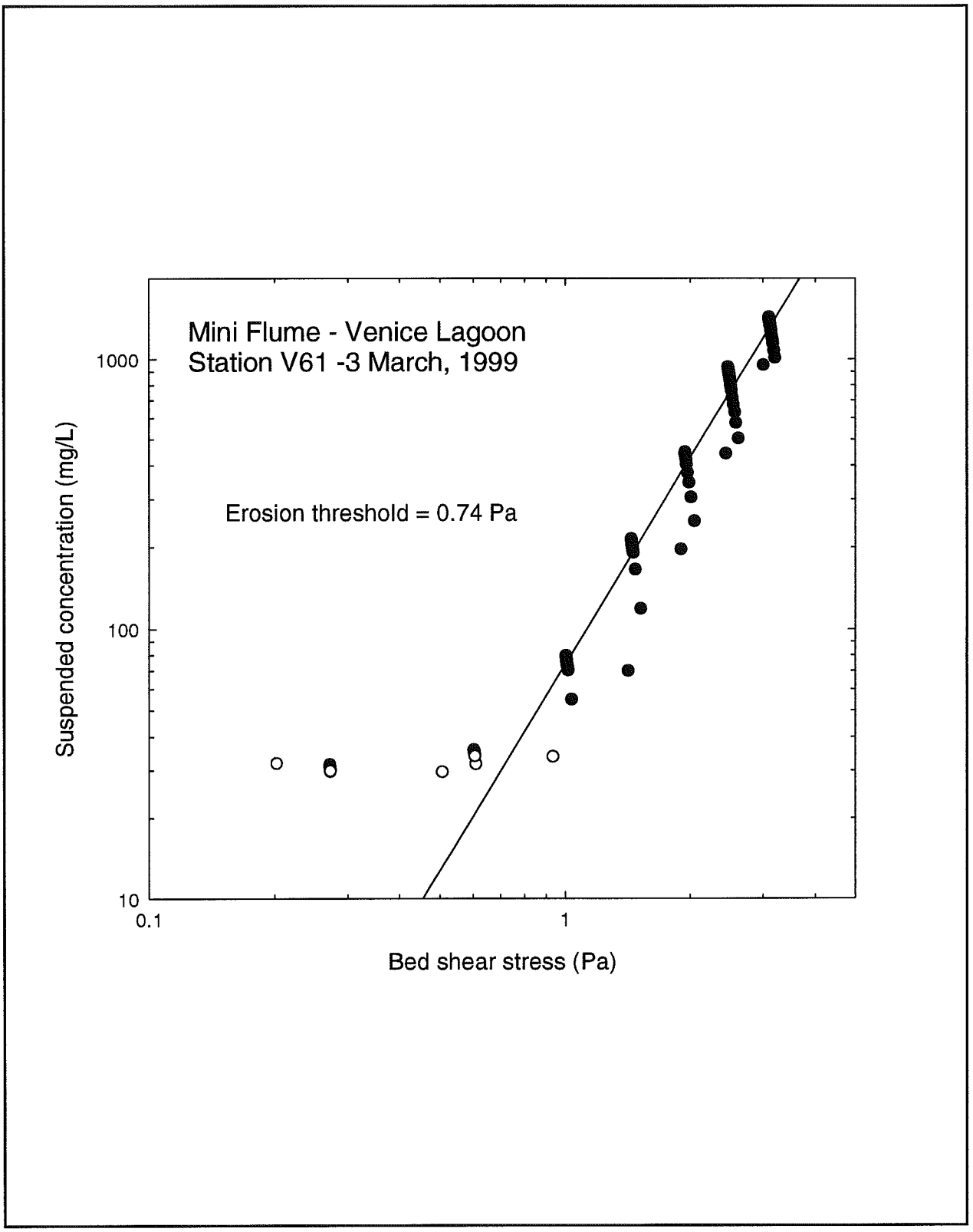

Figure 4.9.1.7 : A regression analysis of applied shear stress for site V61 against suspended sediment concentration for values interpreted as post-erosional (solid dots).

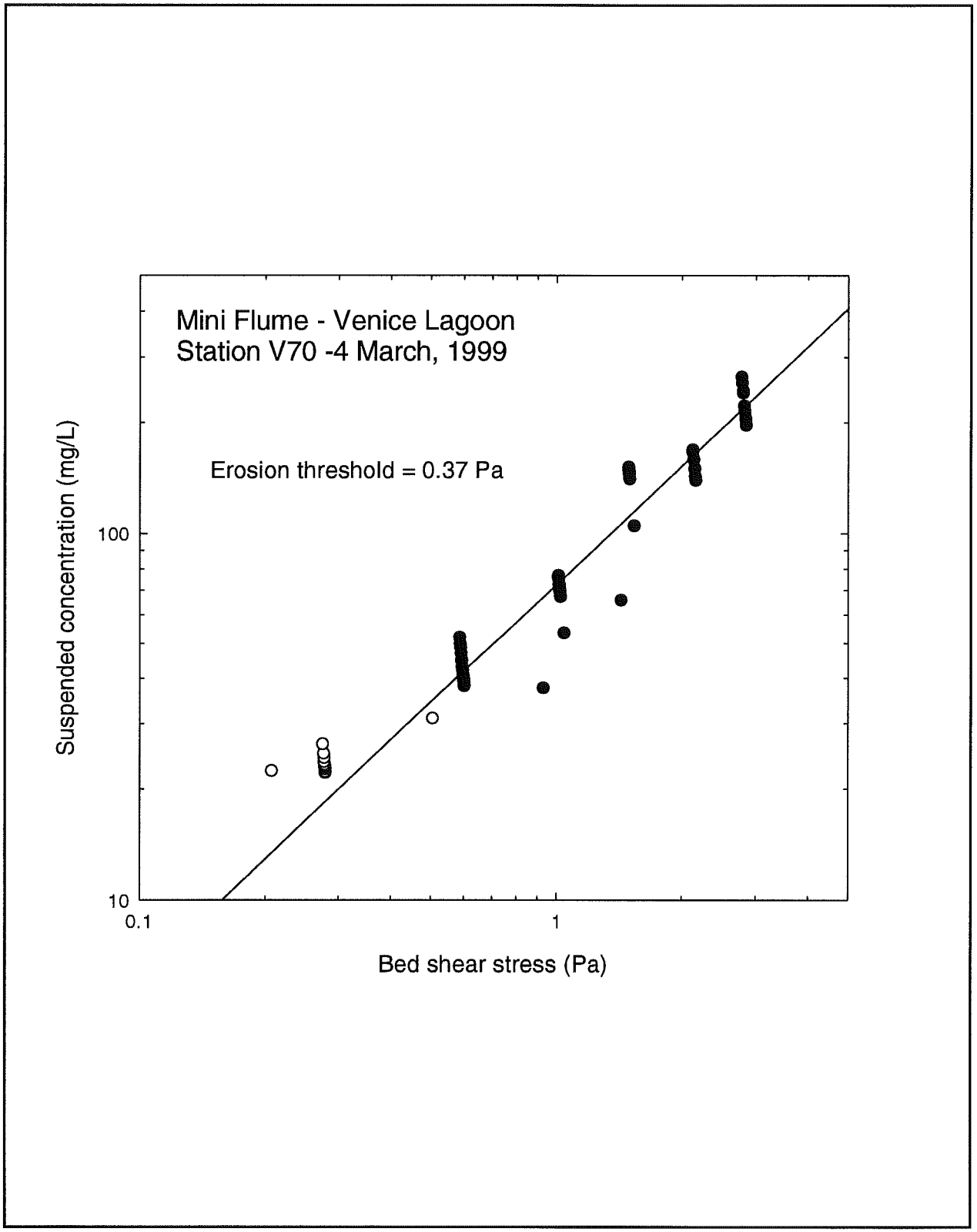

Figure 4.9.1.8 : A regression analysis of applied shear stress for site V70 against suspended sediment concentration for values interpreted as post-erosional (solid dots).

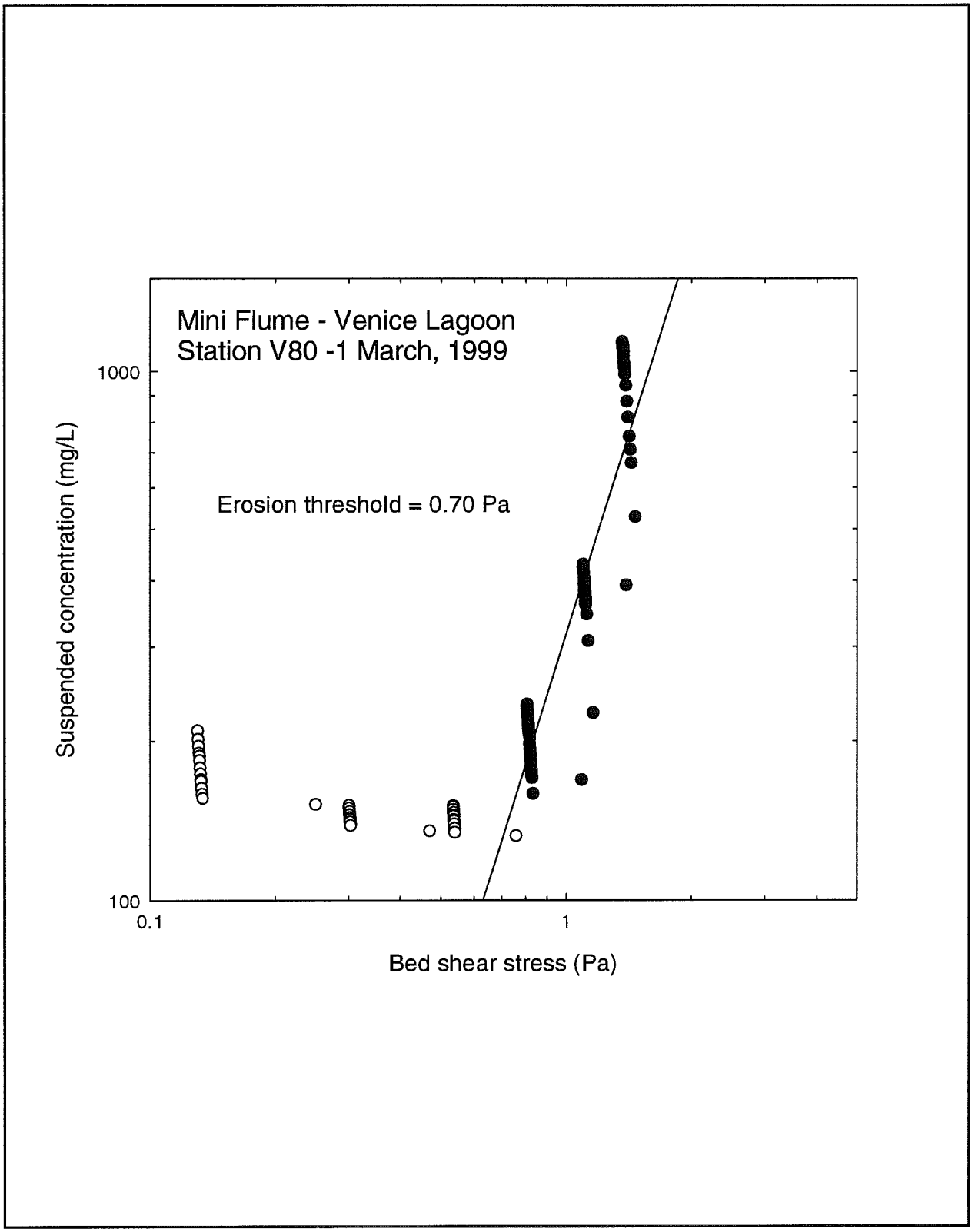

Figure 4.9.1.9 : A regression analysis of applied shear stress for site V80 against suspended sediment concentration for values interpreted as post-erosional (solid dots).

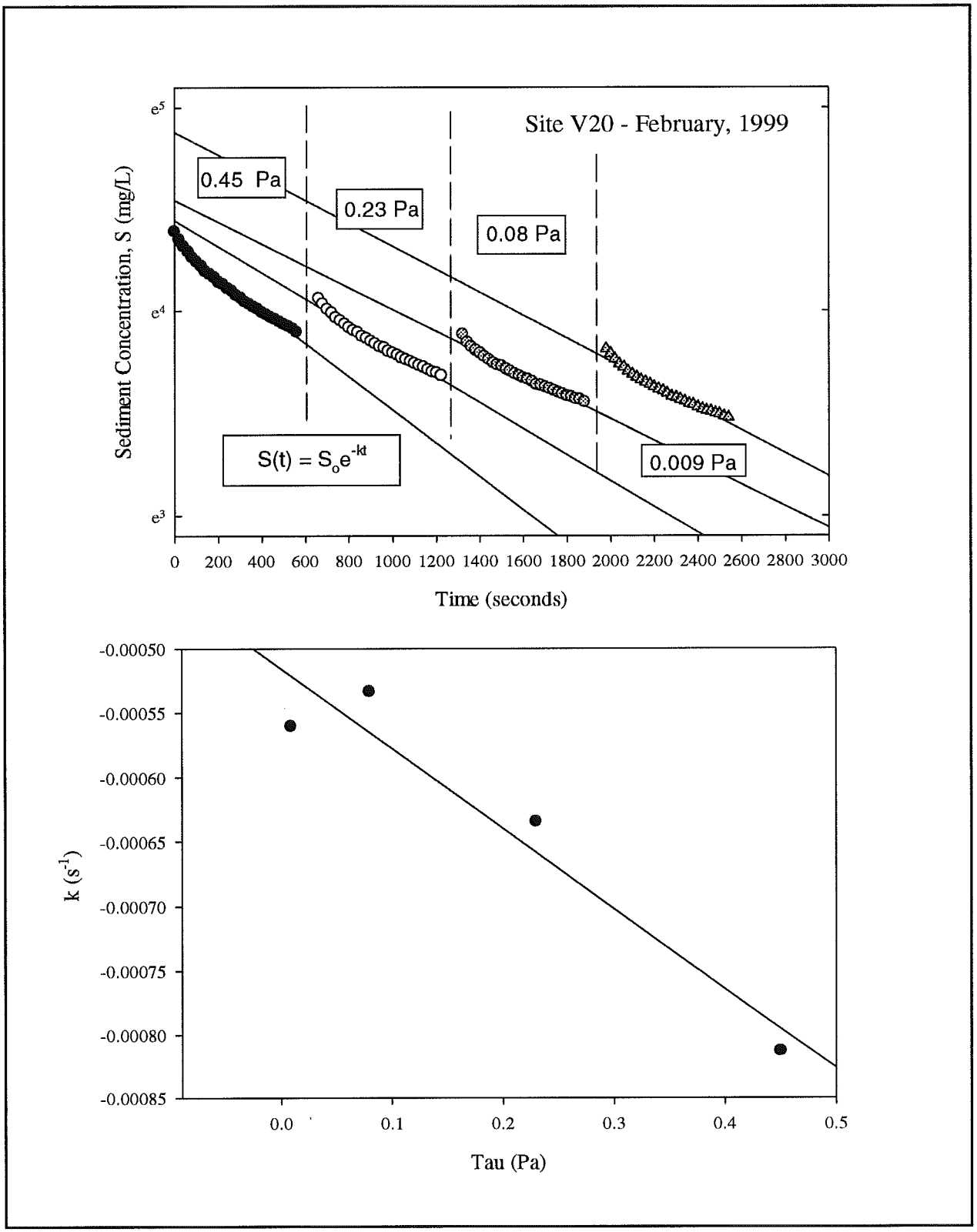

Figure 4.9.2.1 : The settling character of material suspended in the Mini Flume at site V20 measured on 27 February, 1999. The positive correlation of the decay constant, k, with applied shear stress is counter-intuitive and cannot be explained, as a consequence, no deposition

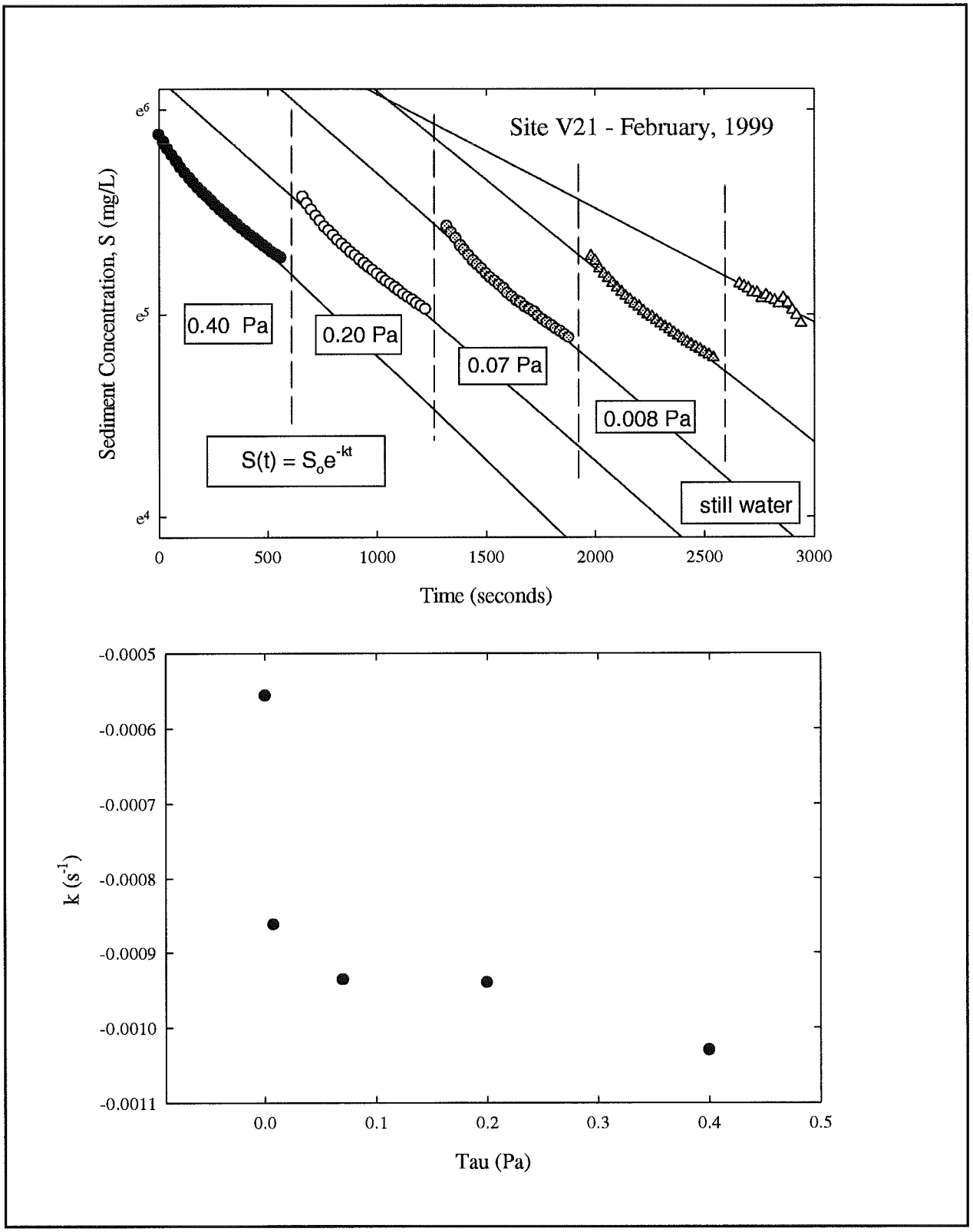

Figure 4.9.2.2 : The settling character of material suspended in the Mini Flume at site V21 measured on 27 February, 1999. The low values of k at low speeds and under still water conditions is noted.

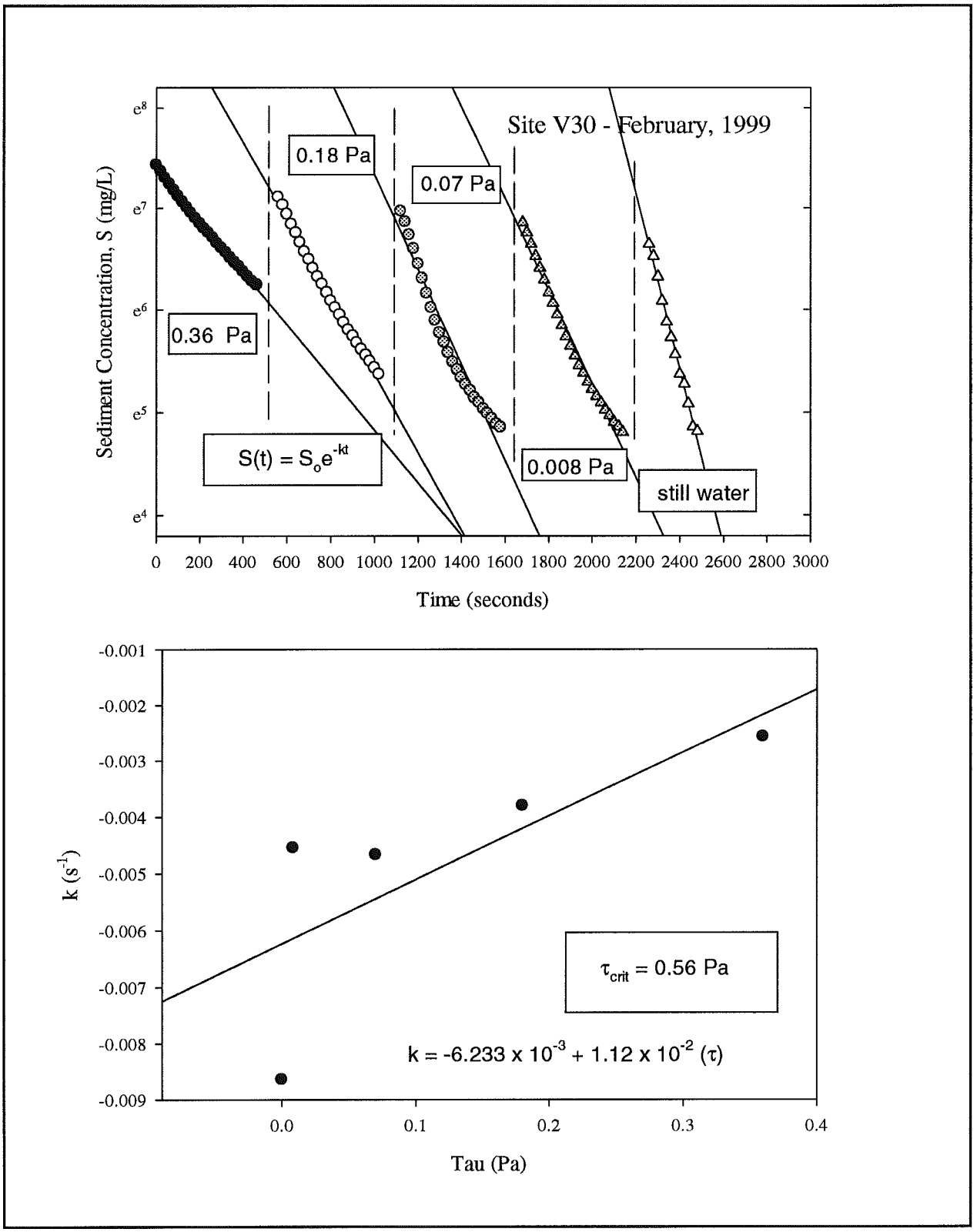

Figure 4.9.2.3 : The settling character of material suspended in the Mini Flume at site V30 measured on 25 February, 1999.

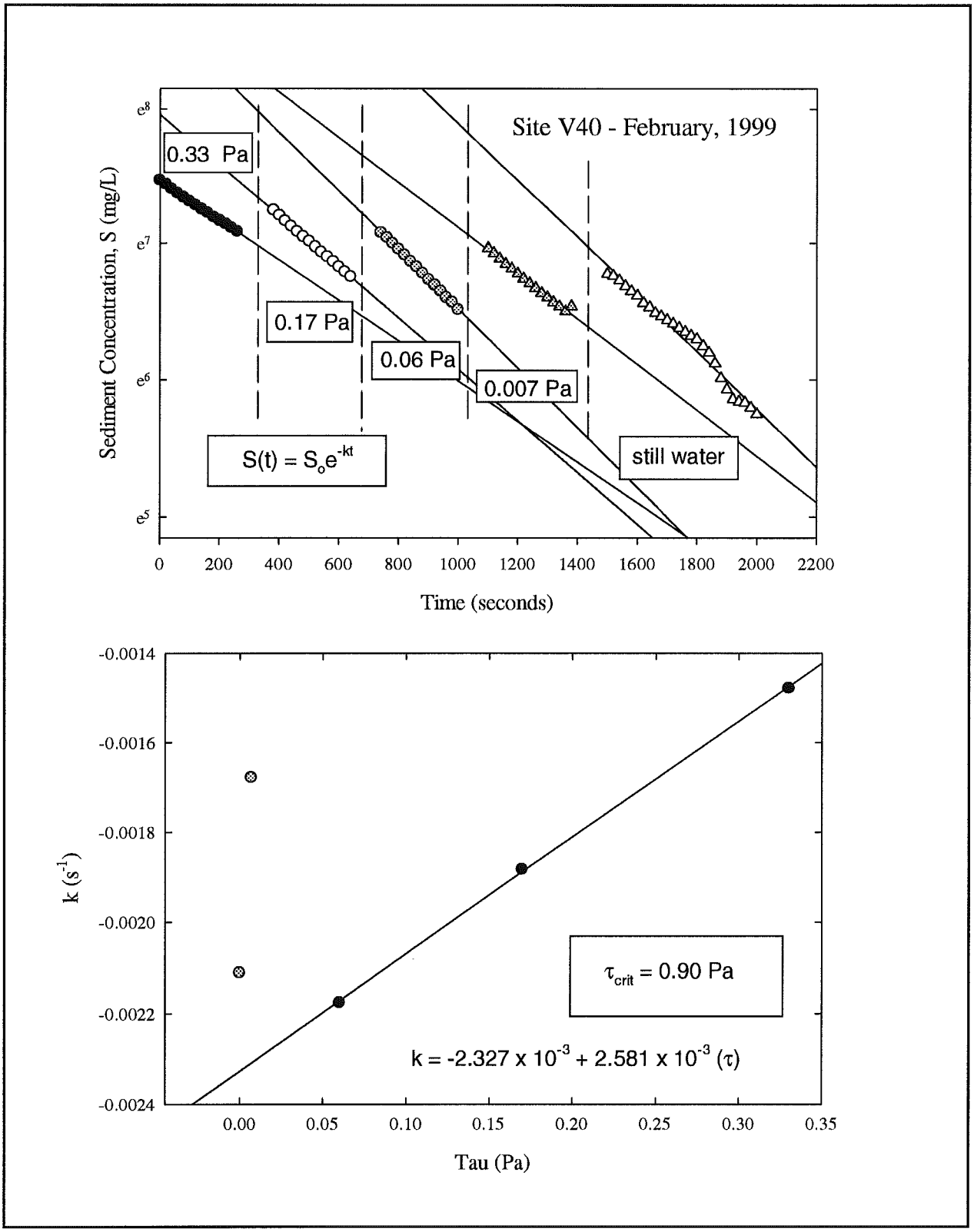

Figure 4.9.2.4 : The settling character of material suspended in the Mini Flume at site V40 measured on 24 February, 1999. The derivation of the deposition threshold is based on the three highest applied stresses for settling. Note that the lowest speed and still water values are below the expected values.

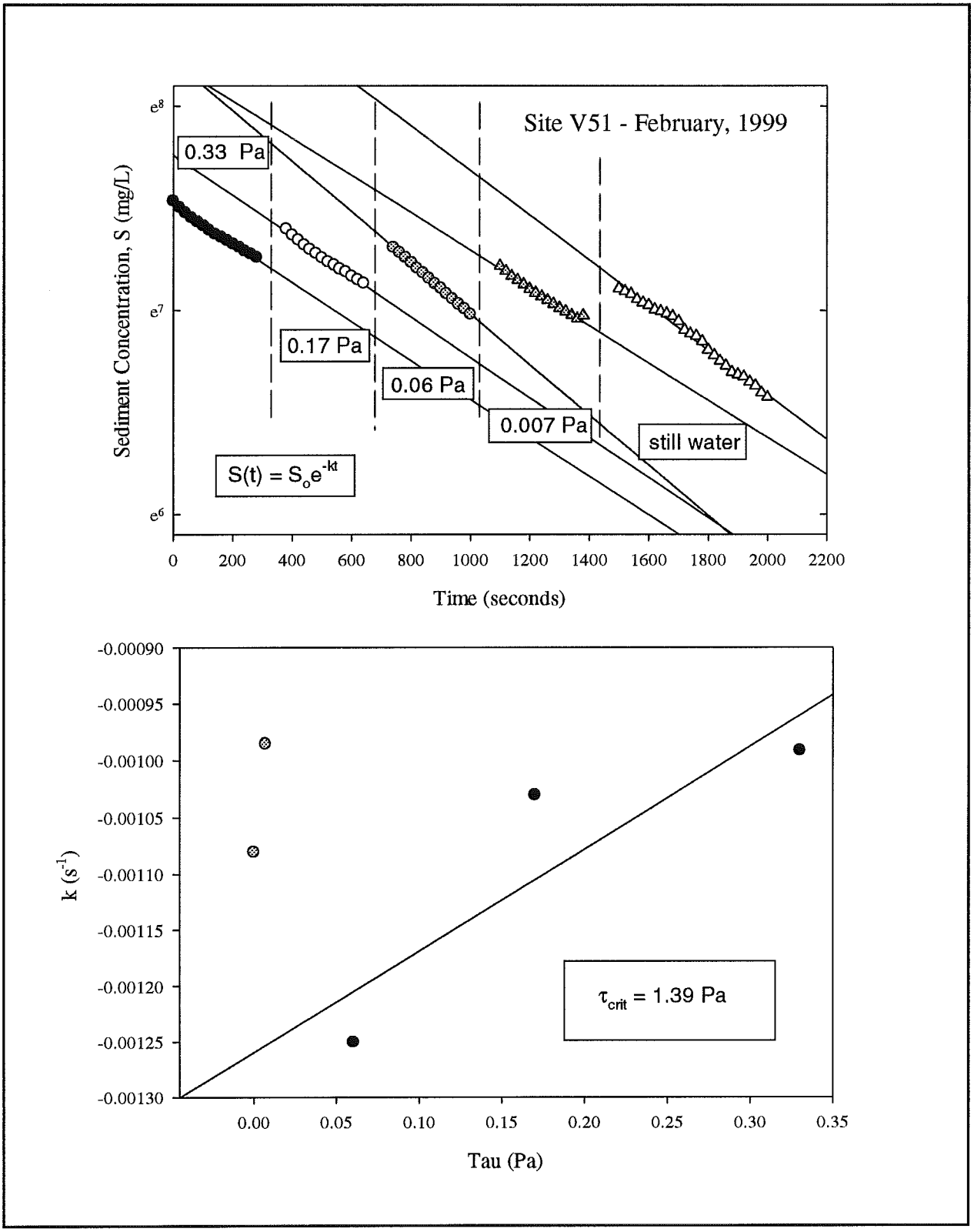

Figure 4.9.2.5: The settling character of material suspended in the Mini Flume at site V51 measured on 22 February, 1999.

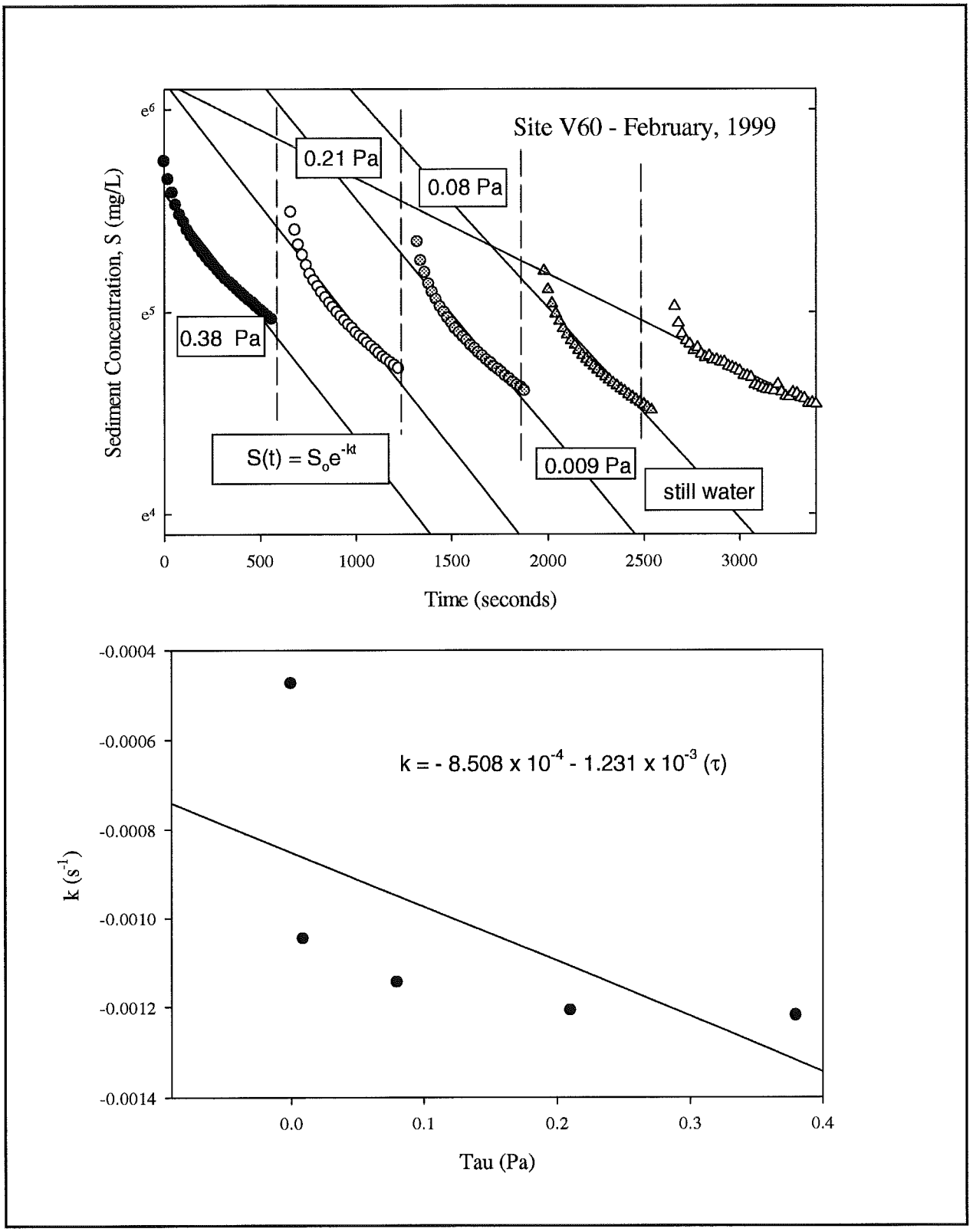

Figure 4.9.2.6 : The settling character of material suspended within Mini Flume at Site V60 measured on 2 March, 1999. The decay constant k does not vary with flow speed and no deposition threshold can be defined. Notice the very low decay constant under still water.

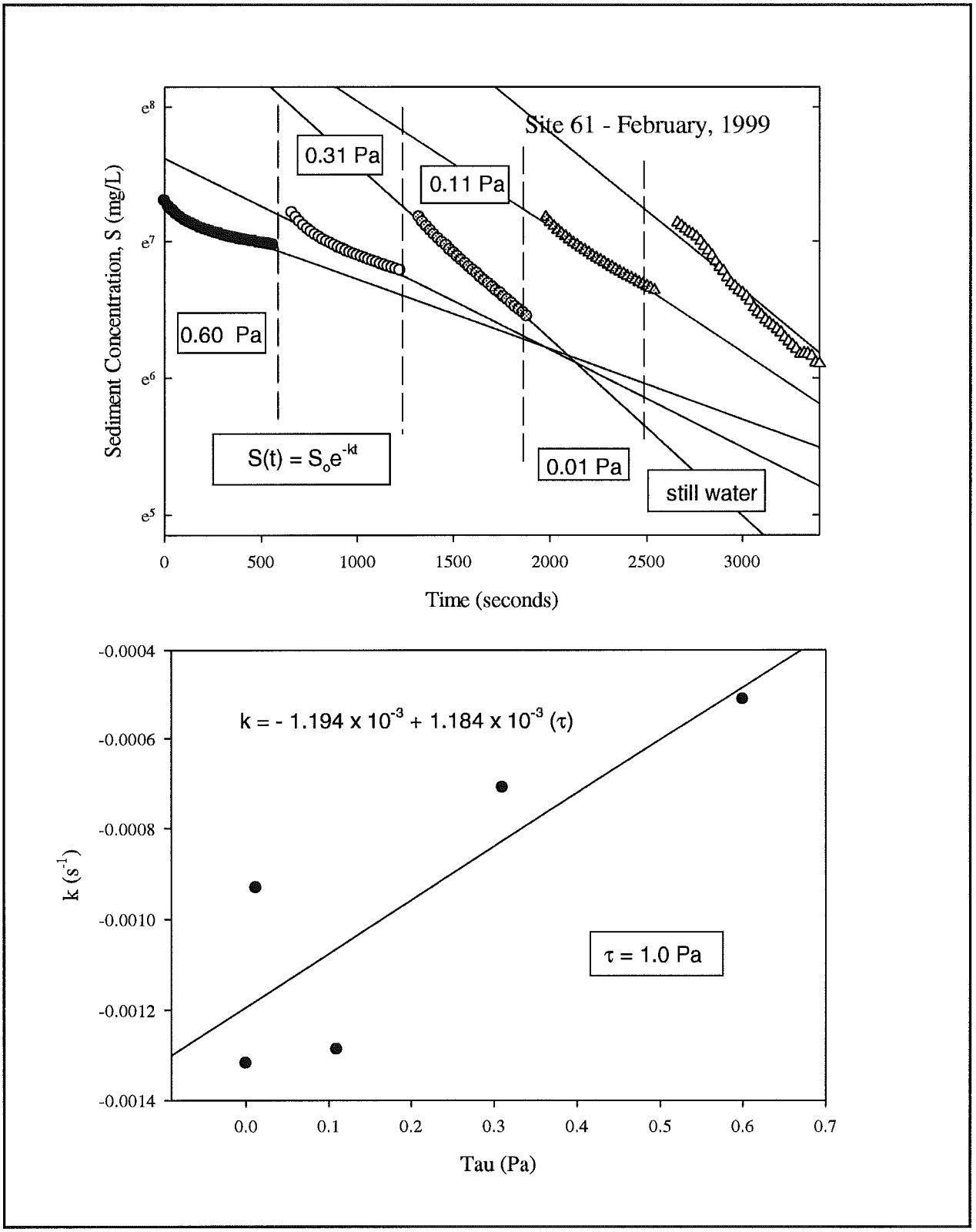

Figure 4.9.2.7 : The settling character of material suspended within Mini Flume at Site V61 measured on 3 March, 1999. The decay constant is inversely related to flow and results in a deposition threshold of 1.0 Pa.

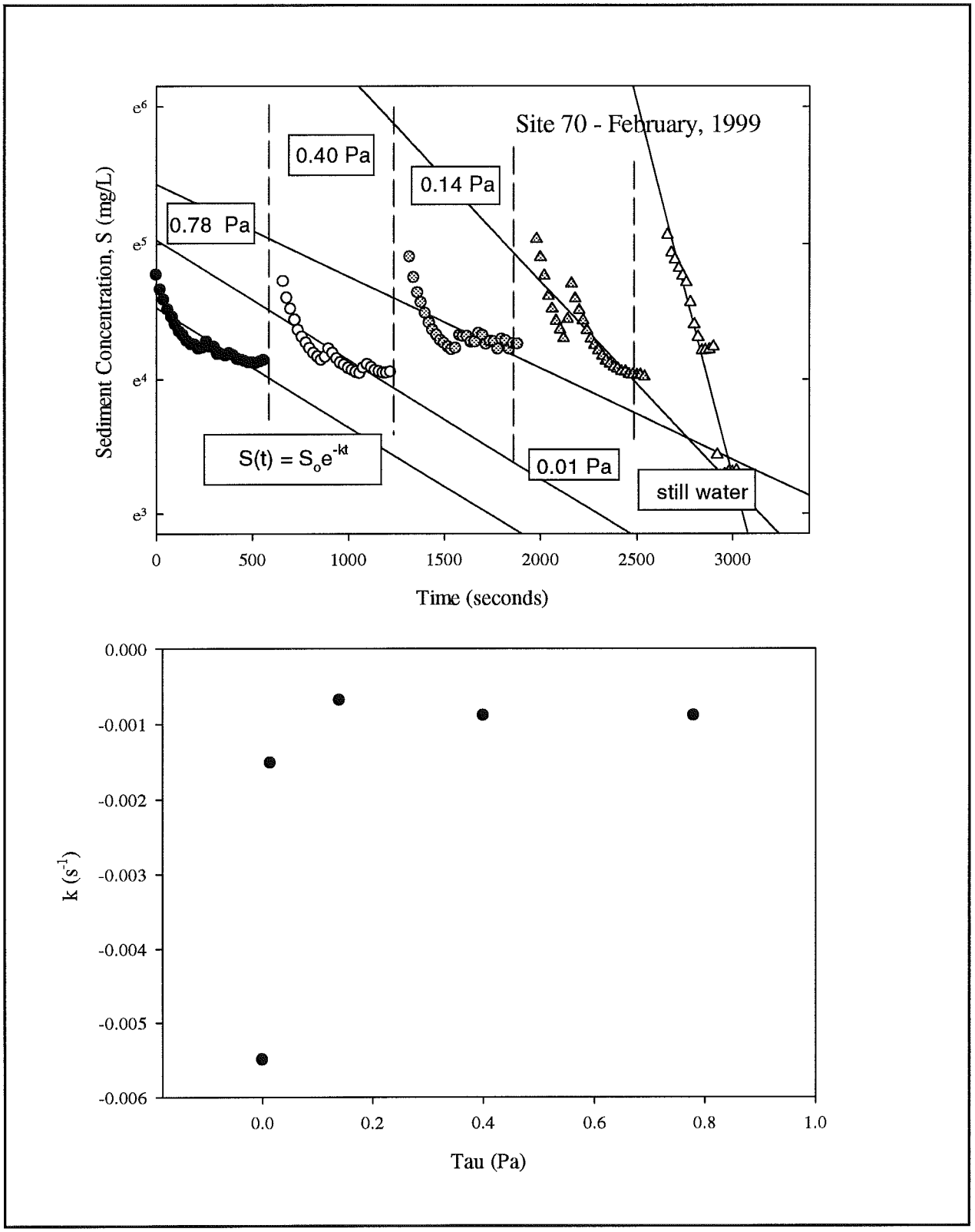

Figure 4.9.2.8 : The settling character of material suspended within Mini Flume at Site V70 measured on 4 March, 1999. k appears independent of applied flow.

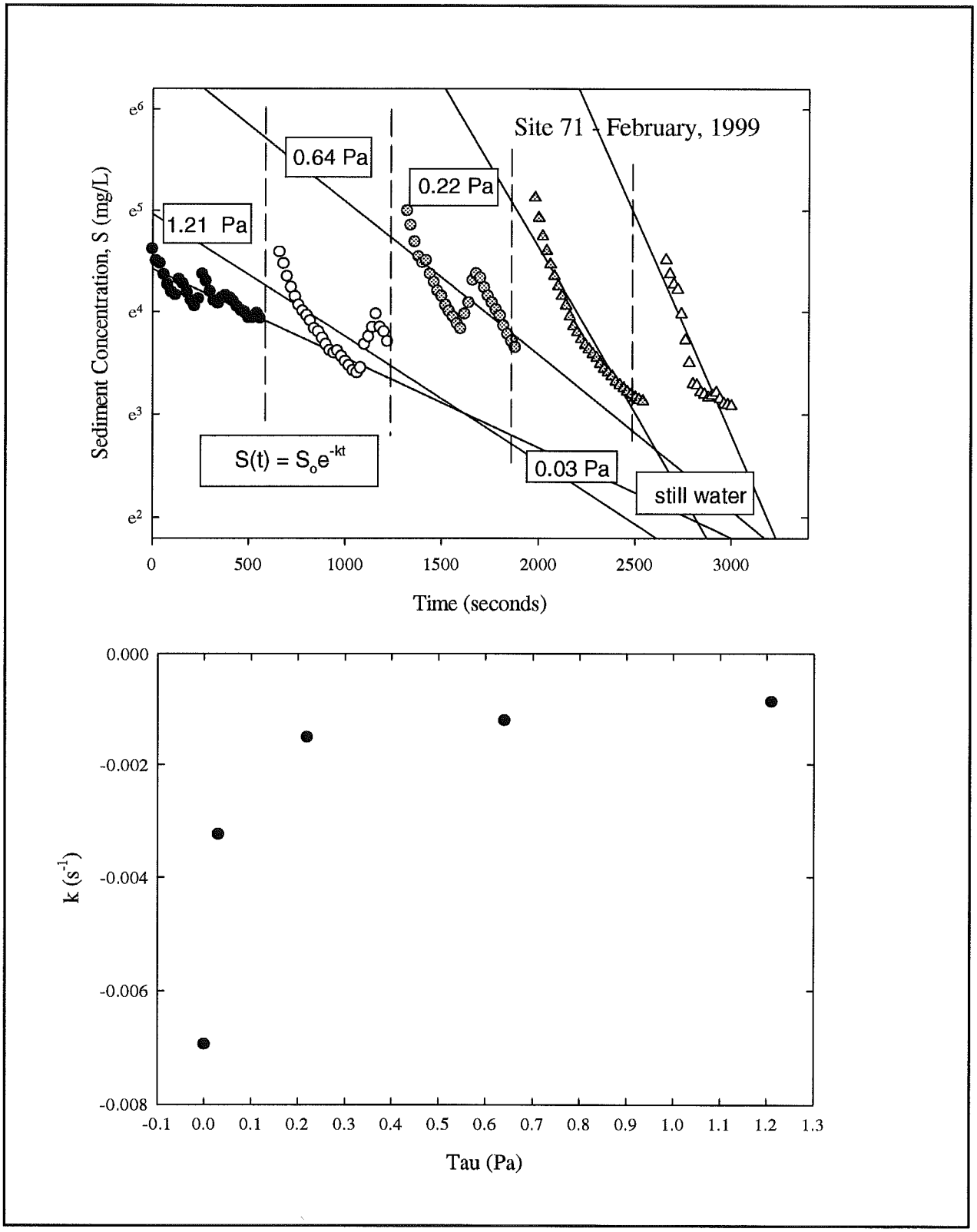

Figure 4.9.2.9 : The settling character of material suspended within Mini Flume at Site V71 measured on 5 March, 1999.

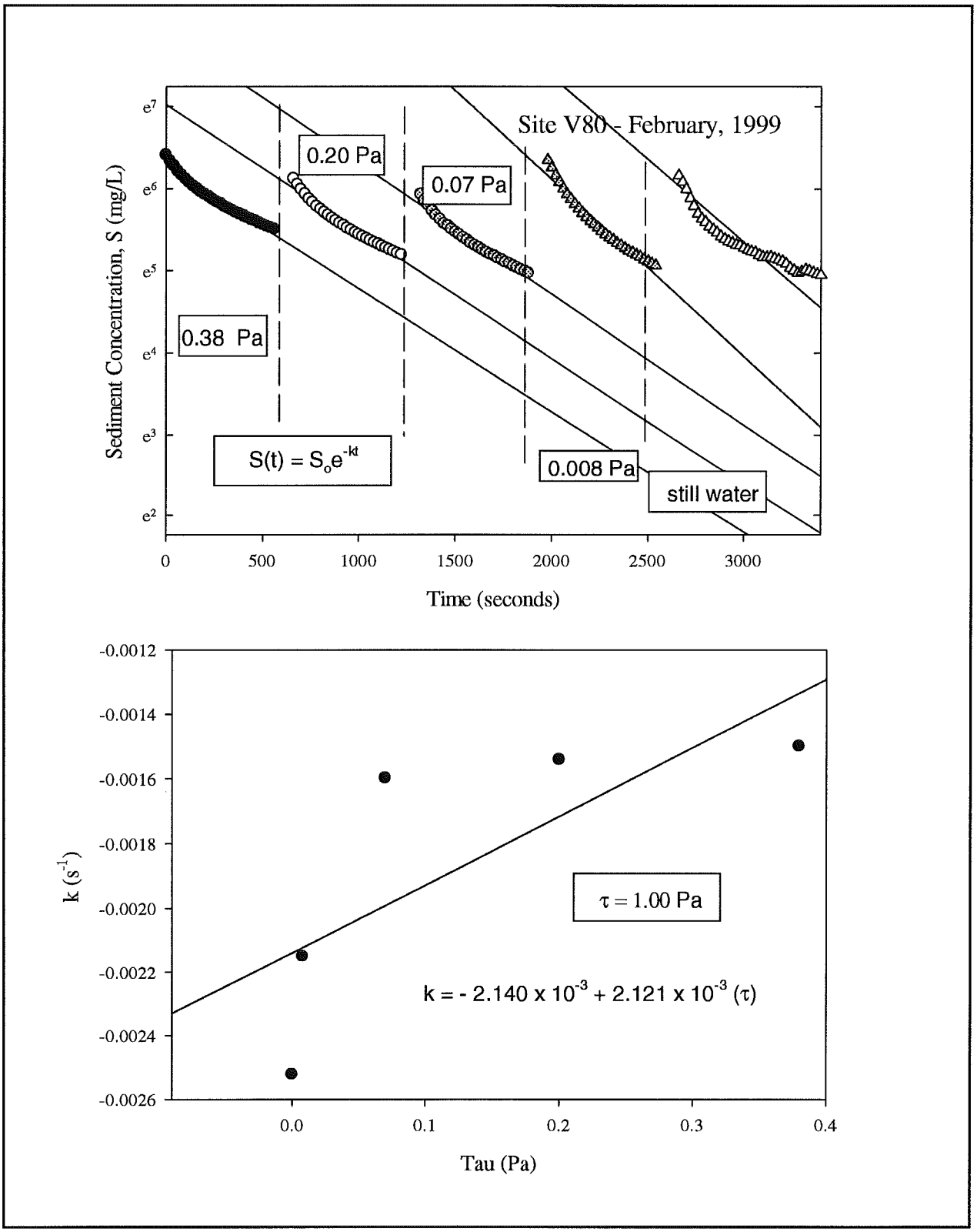

Figure 4.9.2.10: The settling character of material suspended within Mini Flume at Site V80 measured on 1 March, 1999.

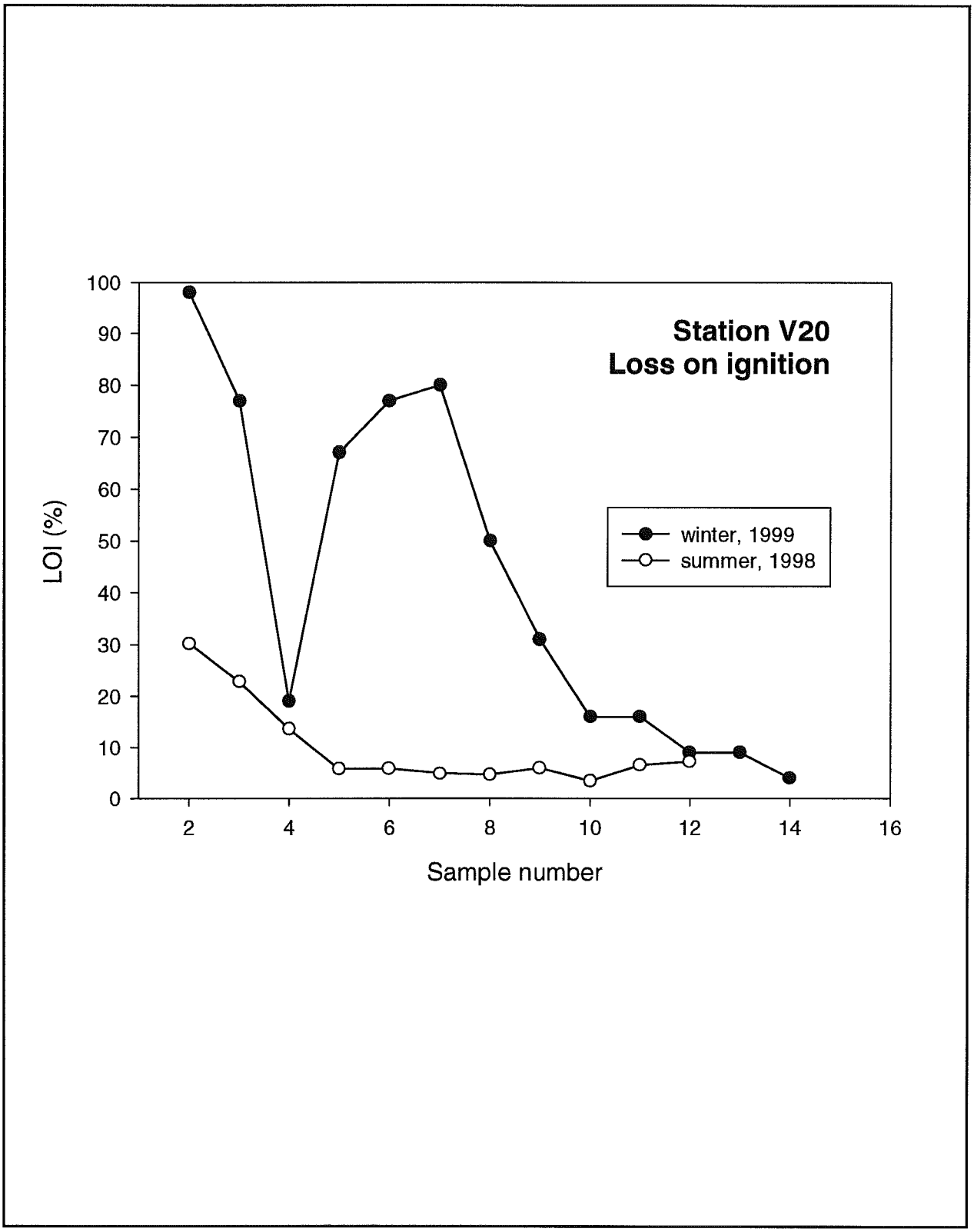

Figure 4.10.1 : Loss on ignition from site V20. The sample numbers refer to each increment of flow in the Sea Carousel (beginning with ambient (no flow)) for the summer (open dots) and winter (solid dots) campaigns. The trends show initial maxima on organic content decreasing with time as bed erosion takes place.

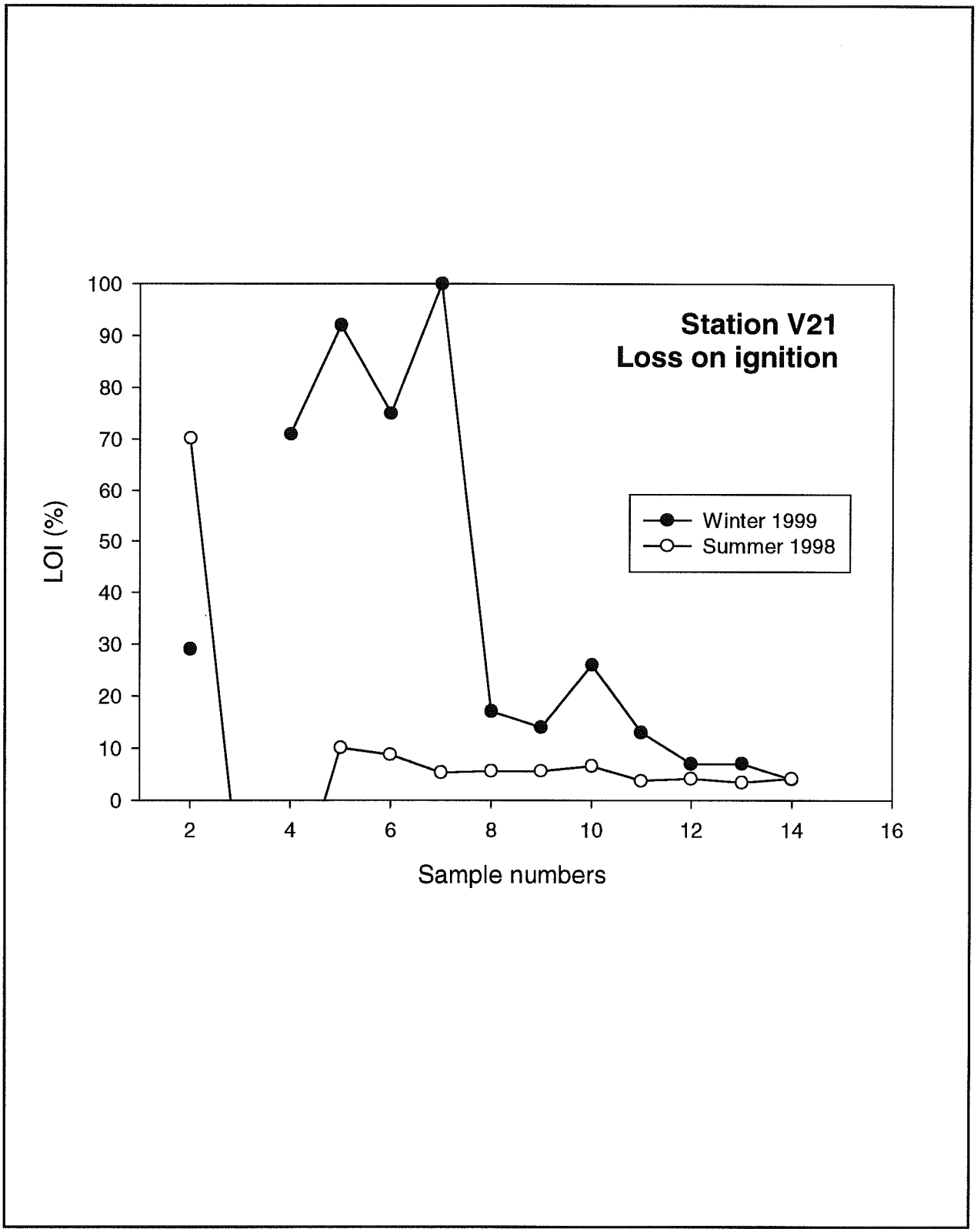

Figure 4.10.2 : Loss on ignition from site V21.

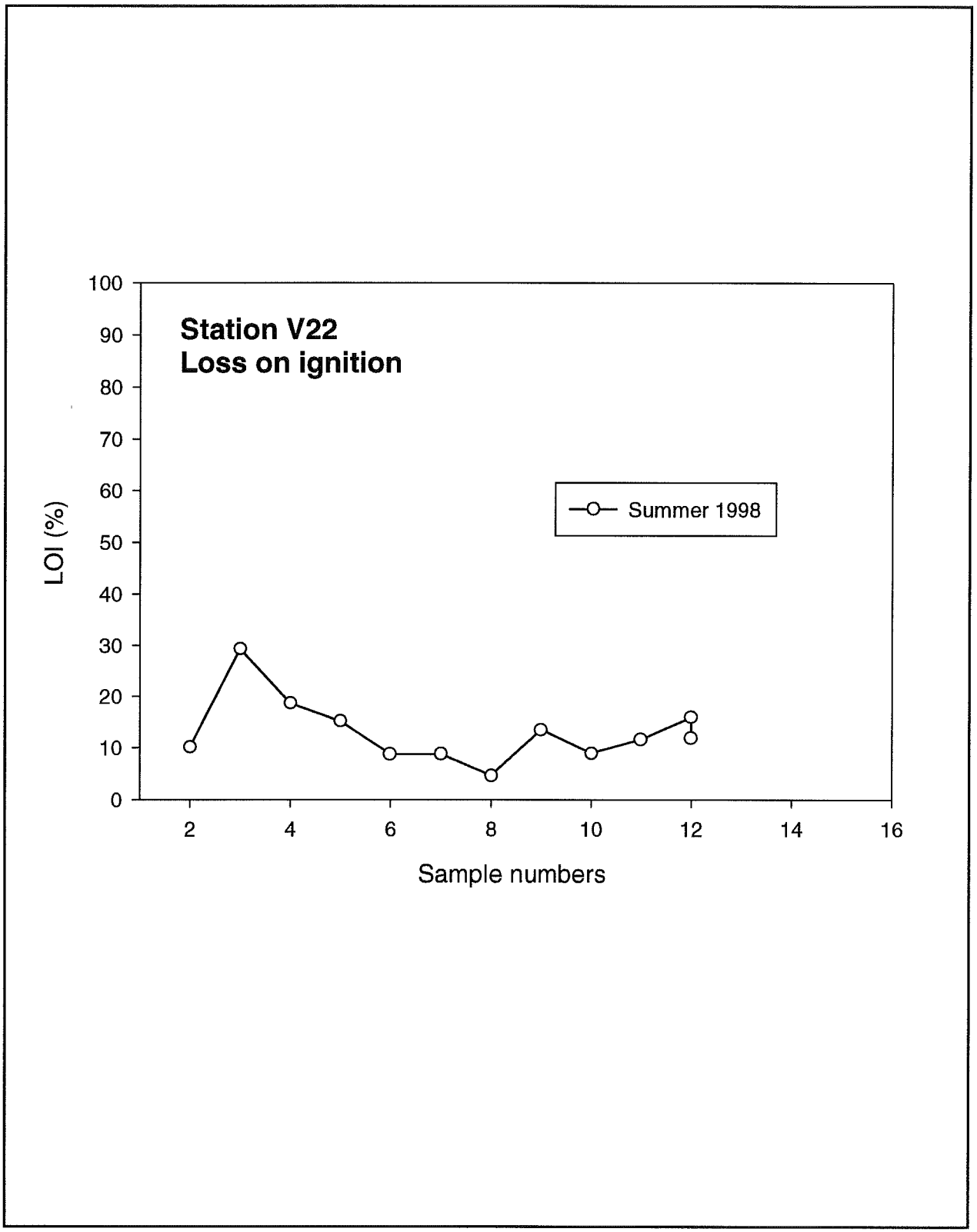

Figure 4.10.3 : Loss on ignition from site V22.

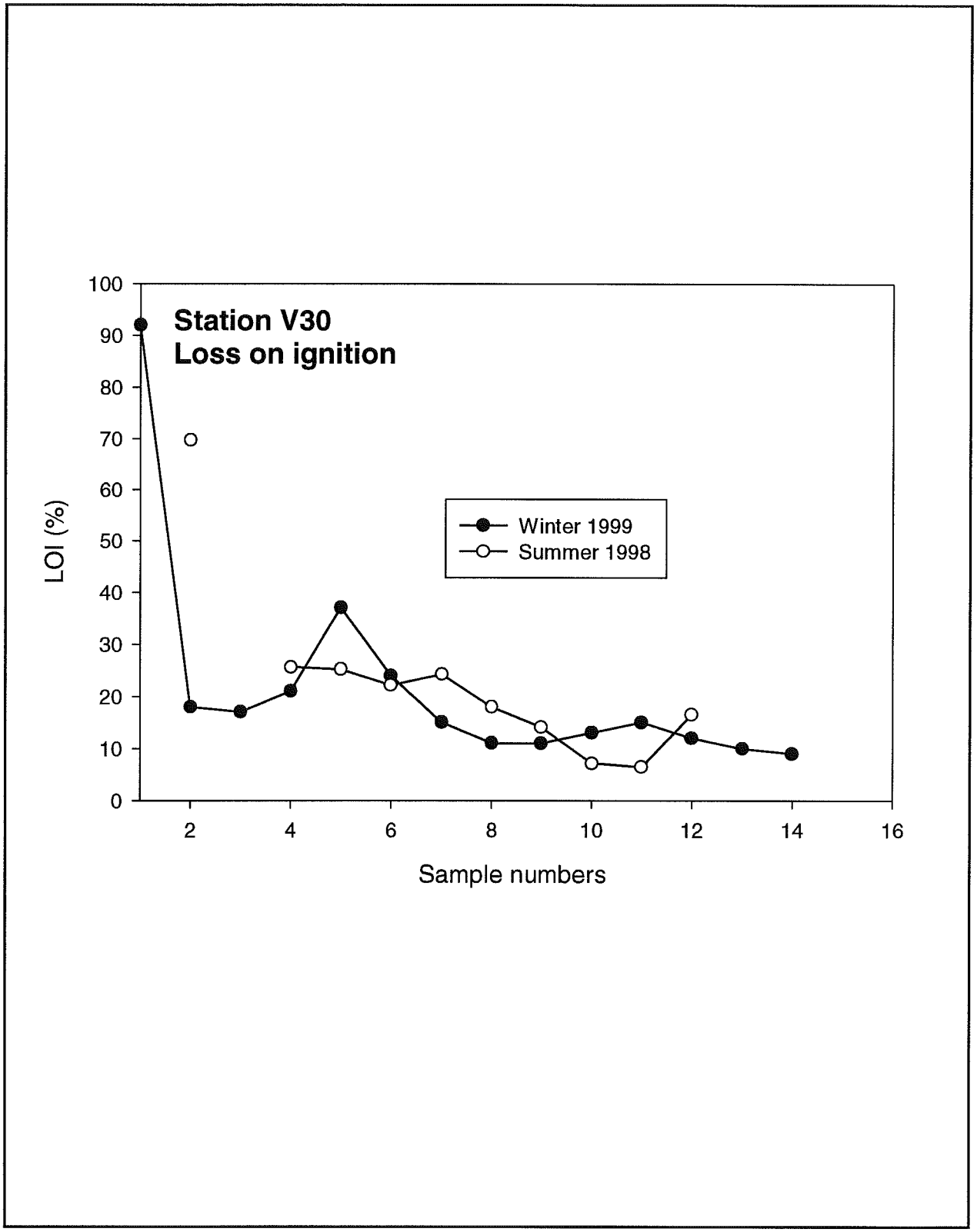

Figure 4.10.4 : Loss on ignition from site V30.

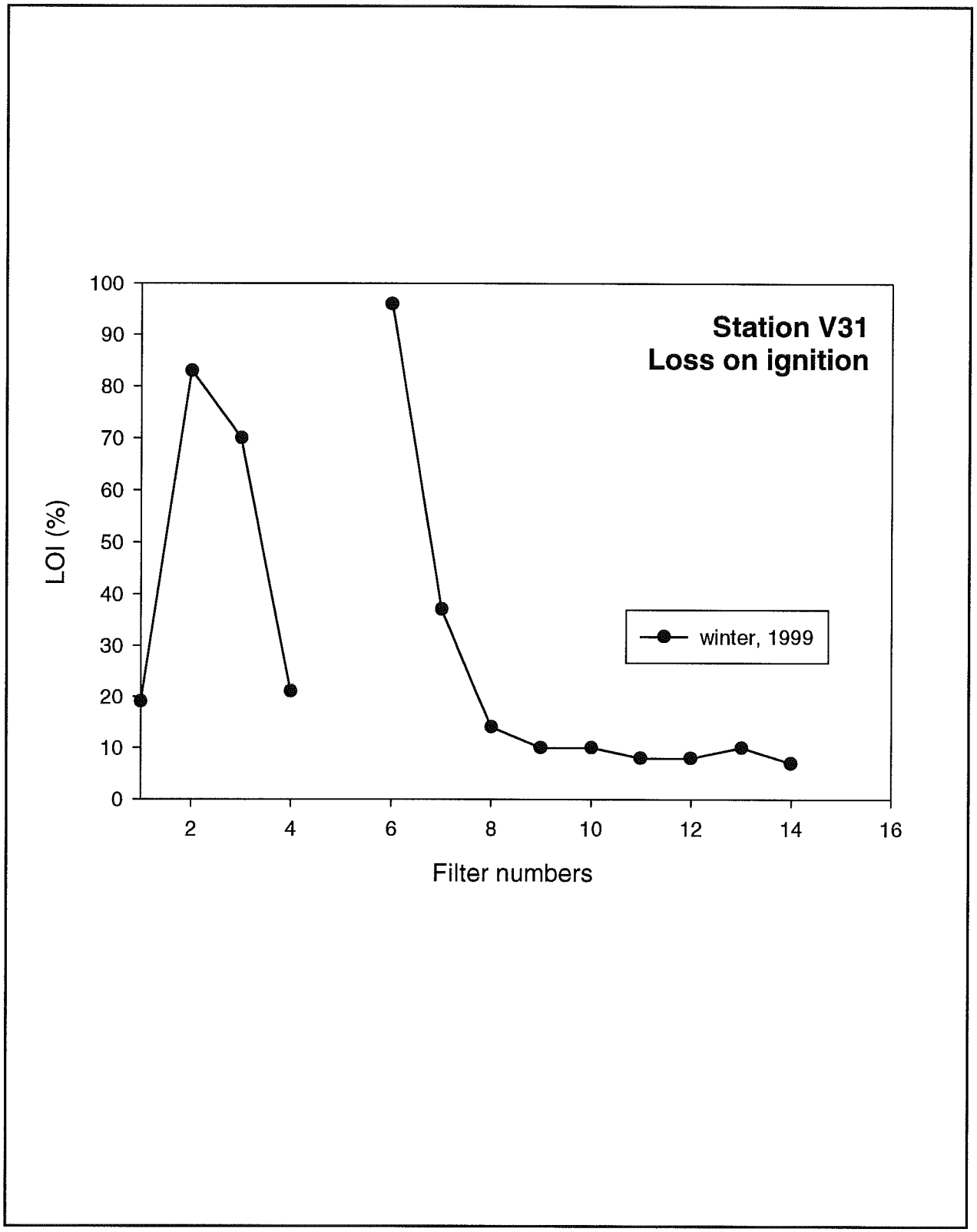

Figure 4.10.5 : Loss on ignition from site V31.

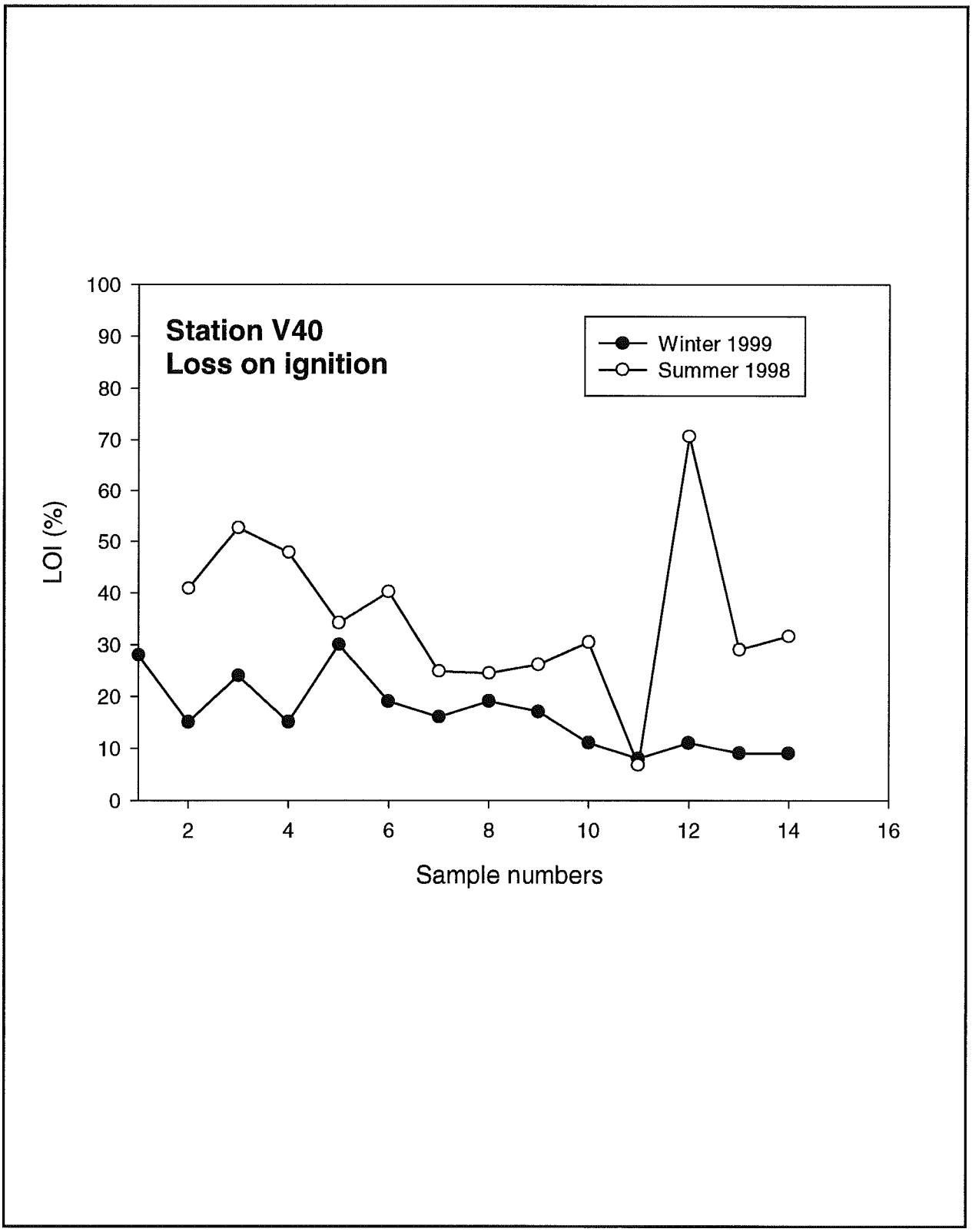

Figure 4.10.6 : Loss on ignition from site V40.

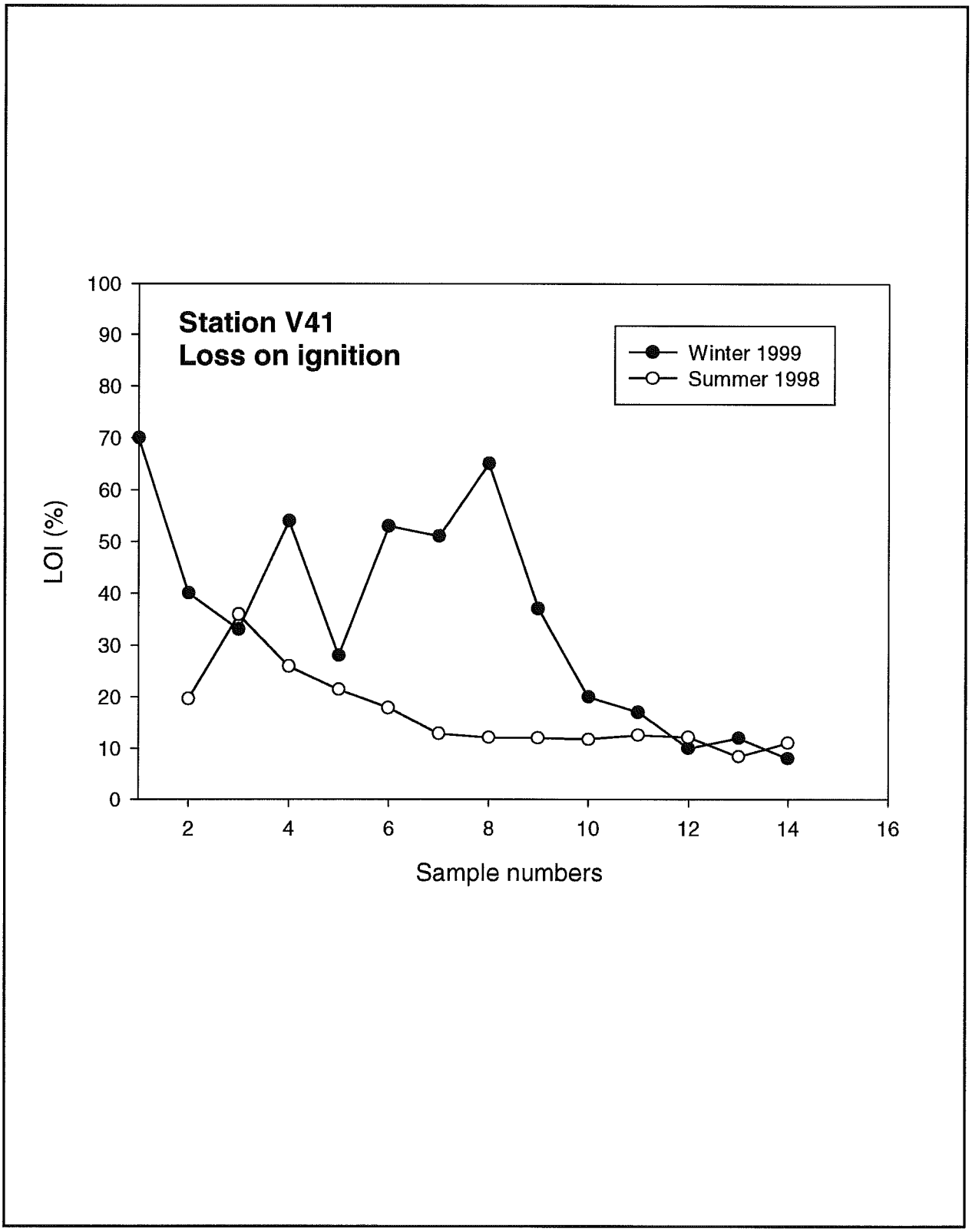

Figure 4.10.7 : Loss on ignition from site V41.

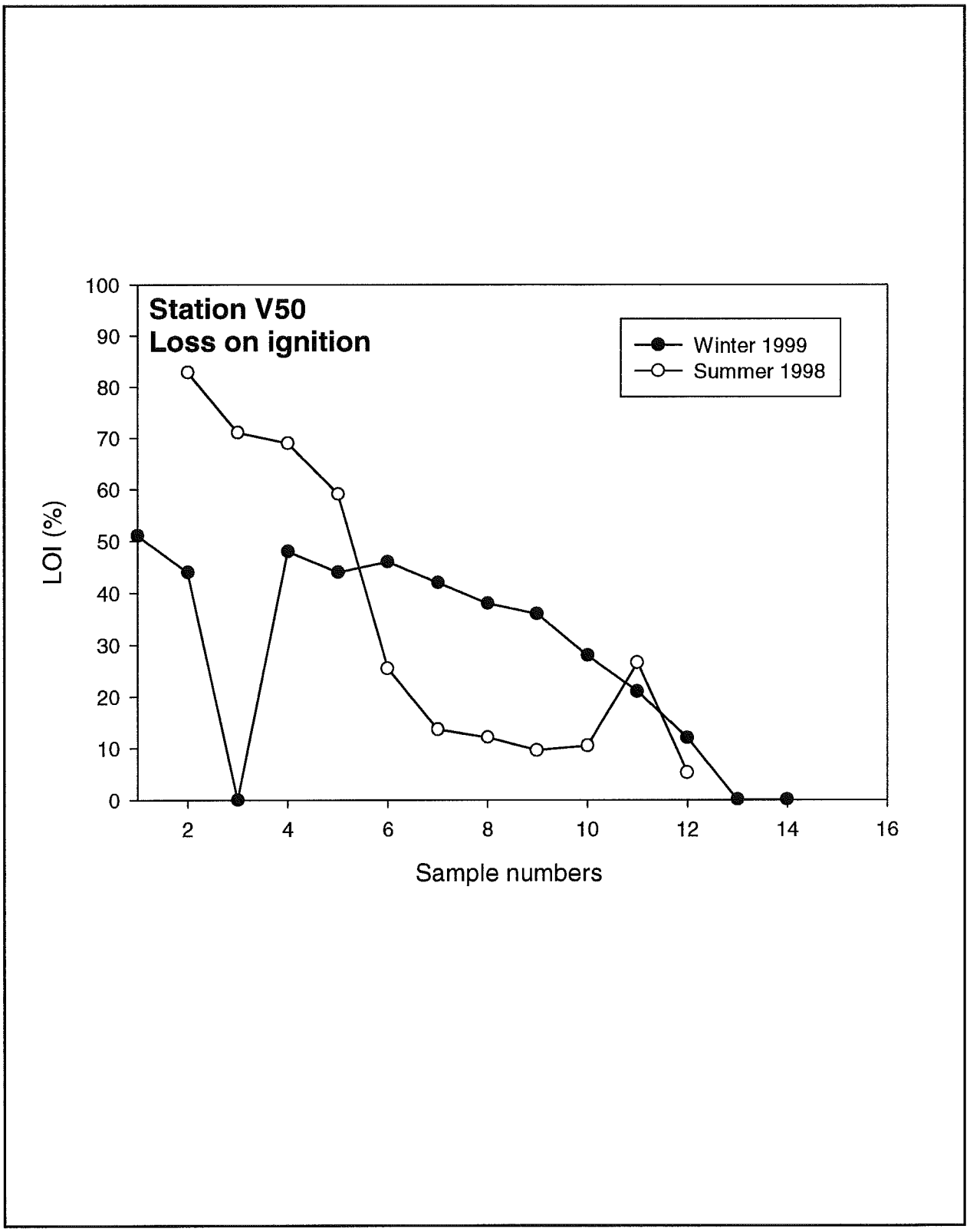

Figure 4.10.8 : Loss on ignition from site V50.

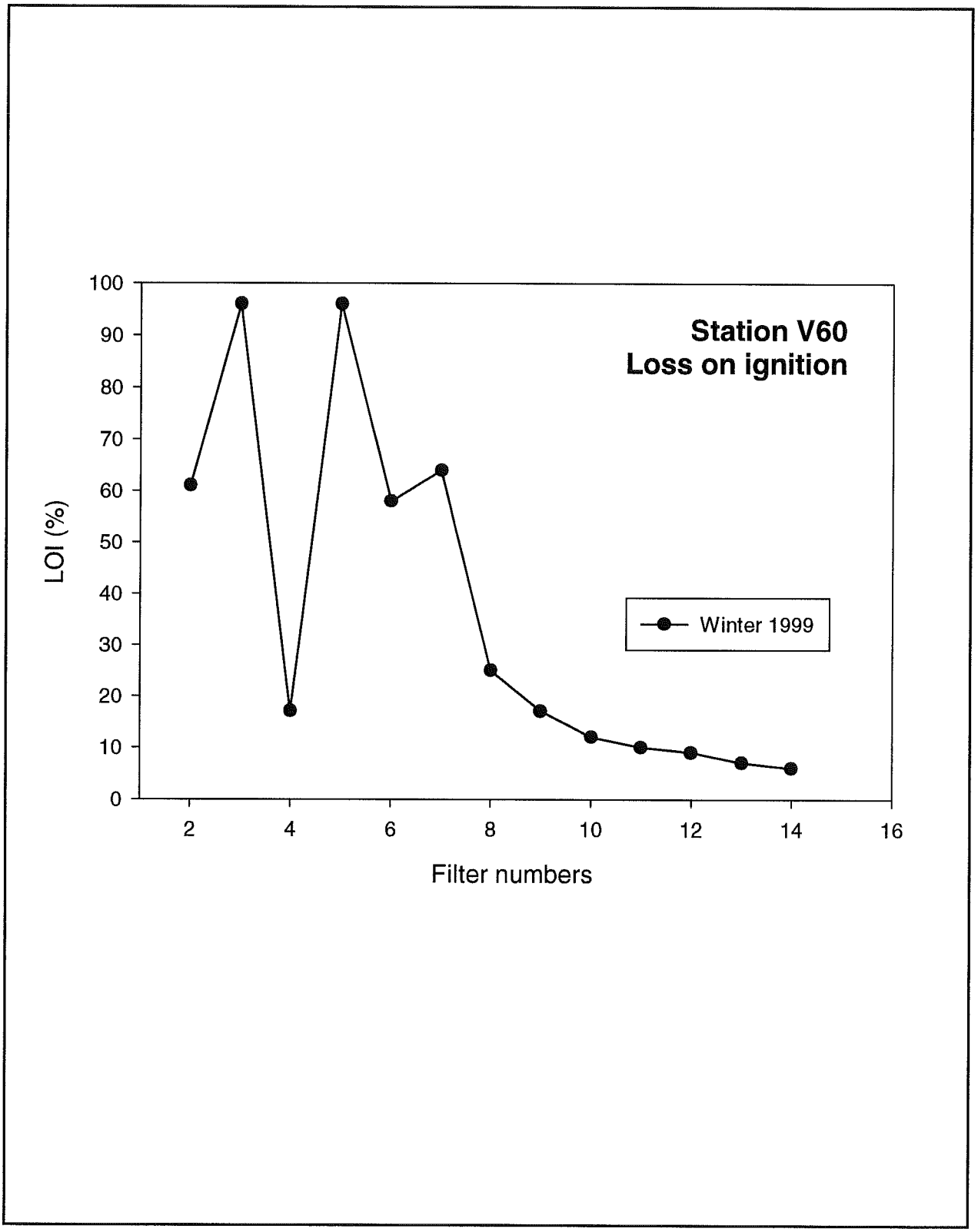

Figure 4.10.9 : Loss on ignition from site V60.

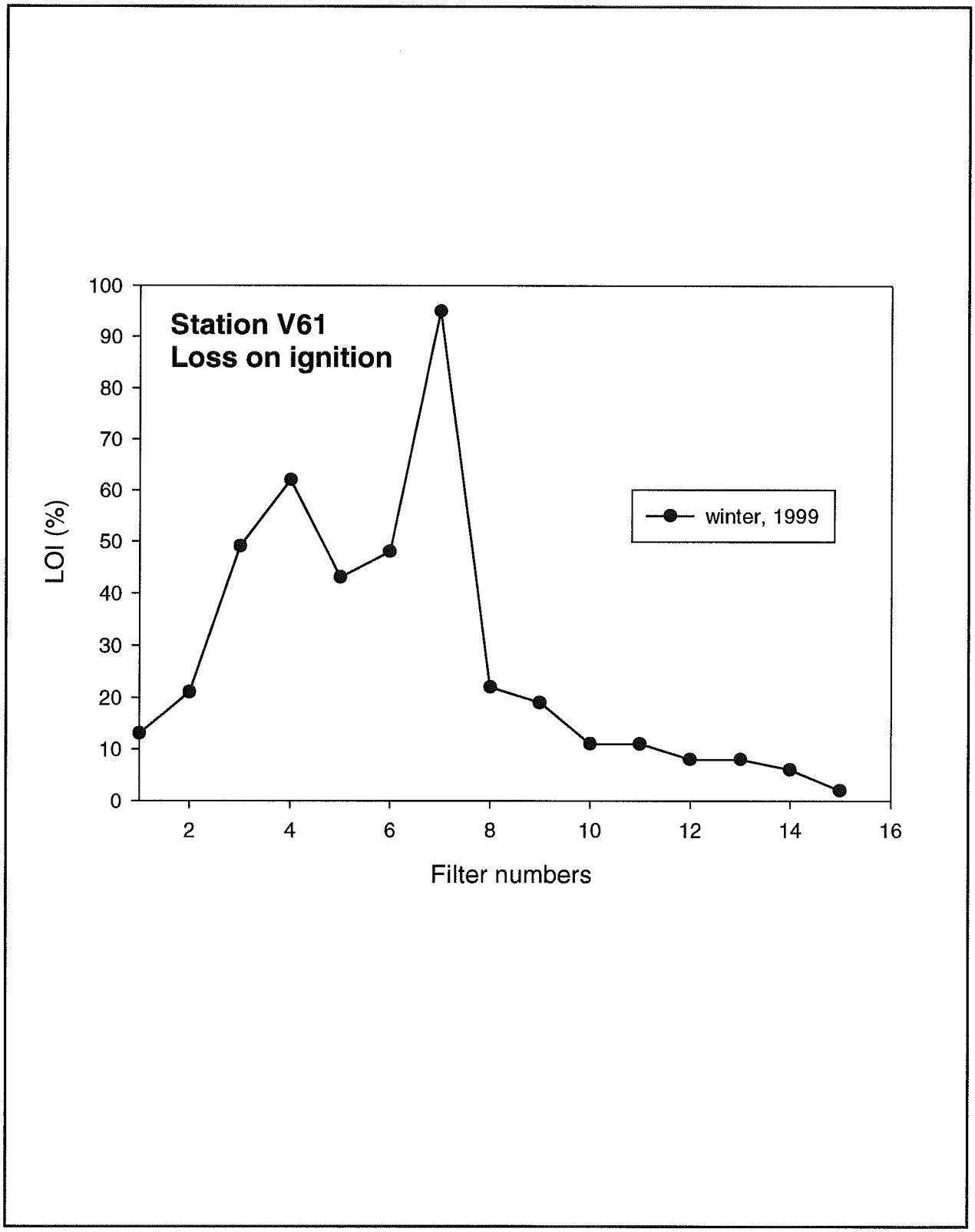

Figure 4.10.10 : Loss on ignition from site V61.

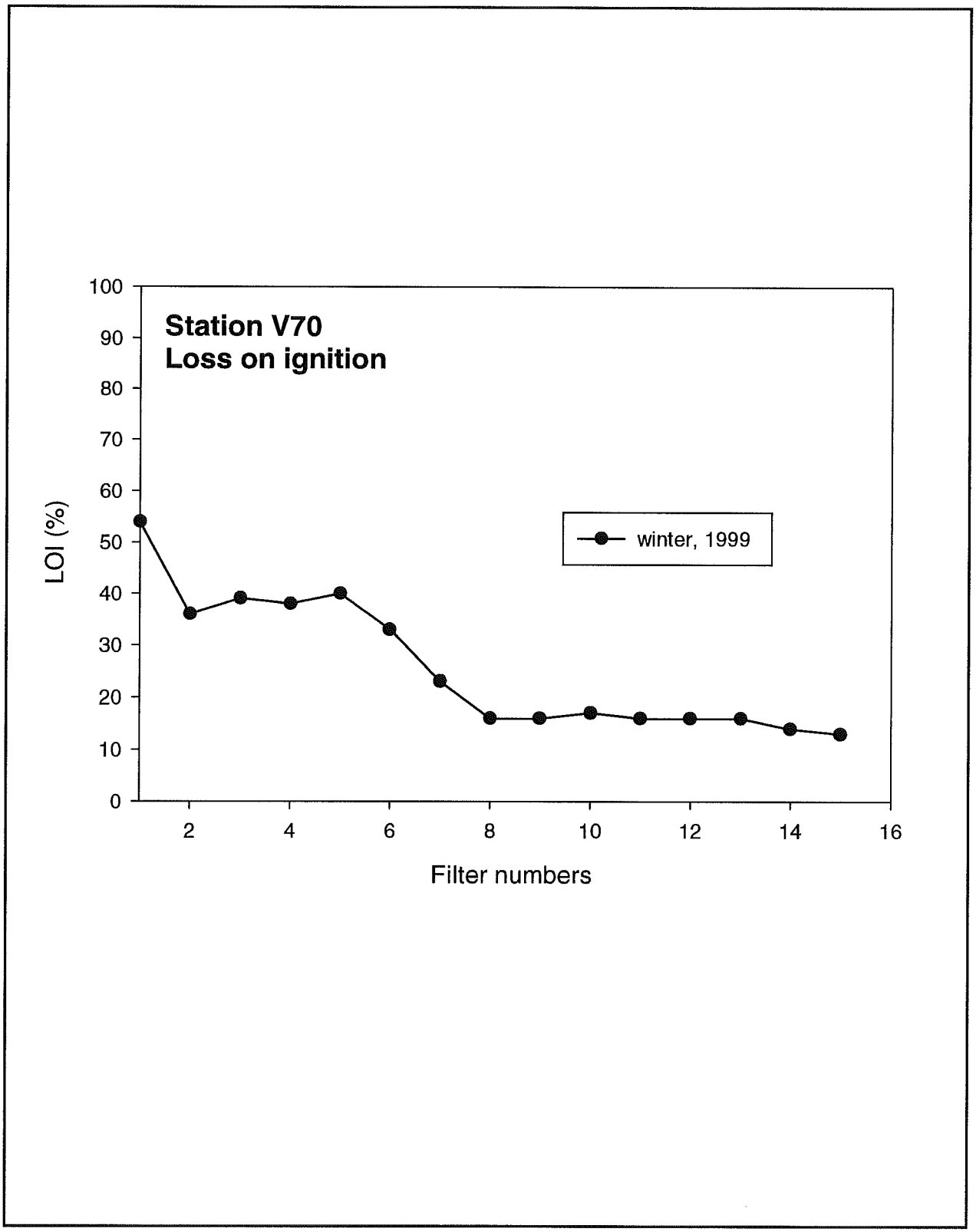

Figure 4.10.11 : Loss on ignition from site V70.

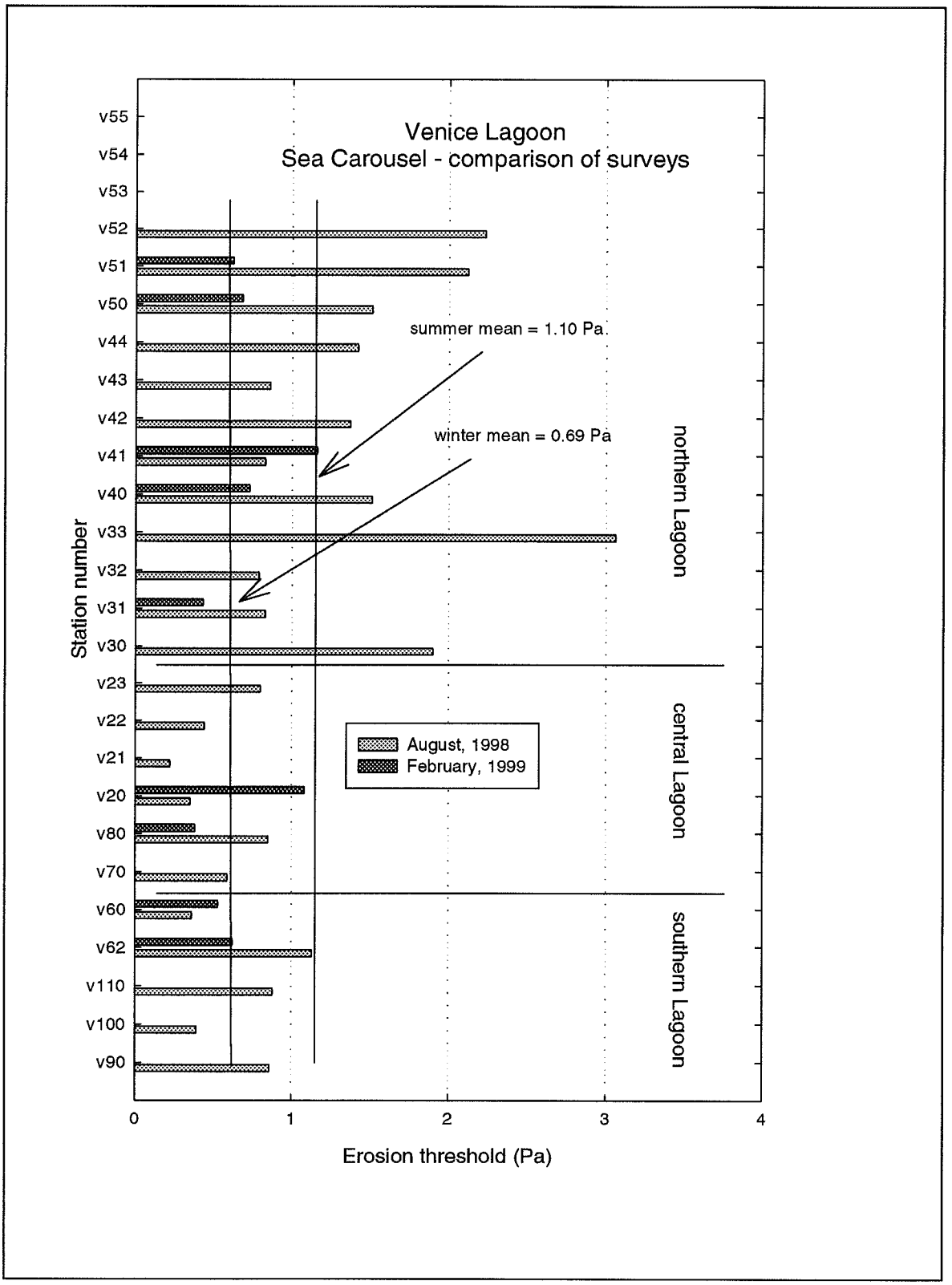

Figure 5.2.1 : A comparison between erosion thresholds determined from Sea Carousel in Venice Lagoon during the August, 1998 and February, 1999 surveys. Notice that the mean threshold during the winter is approximately half that of the summertime.

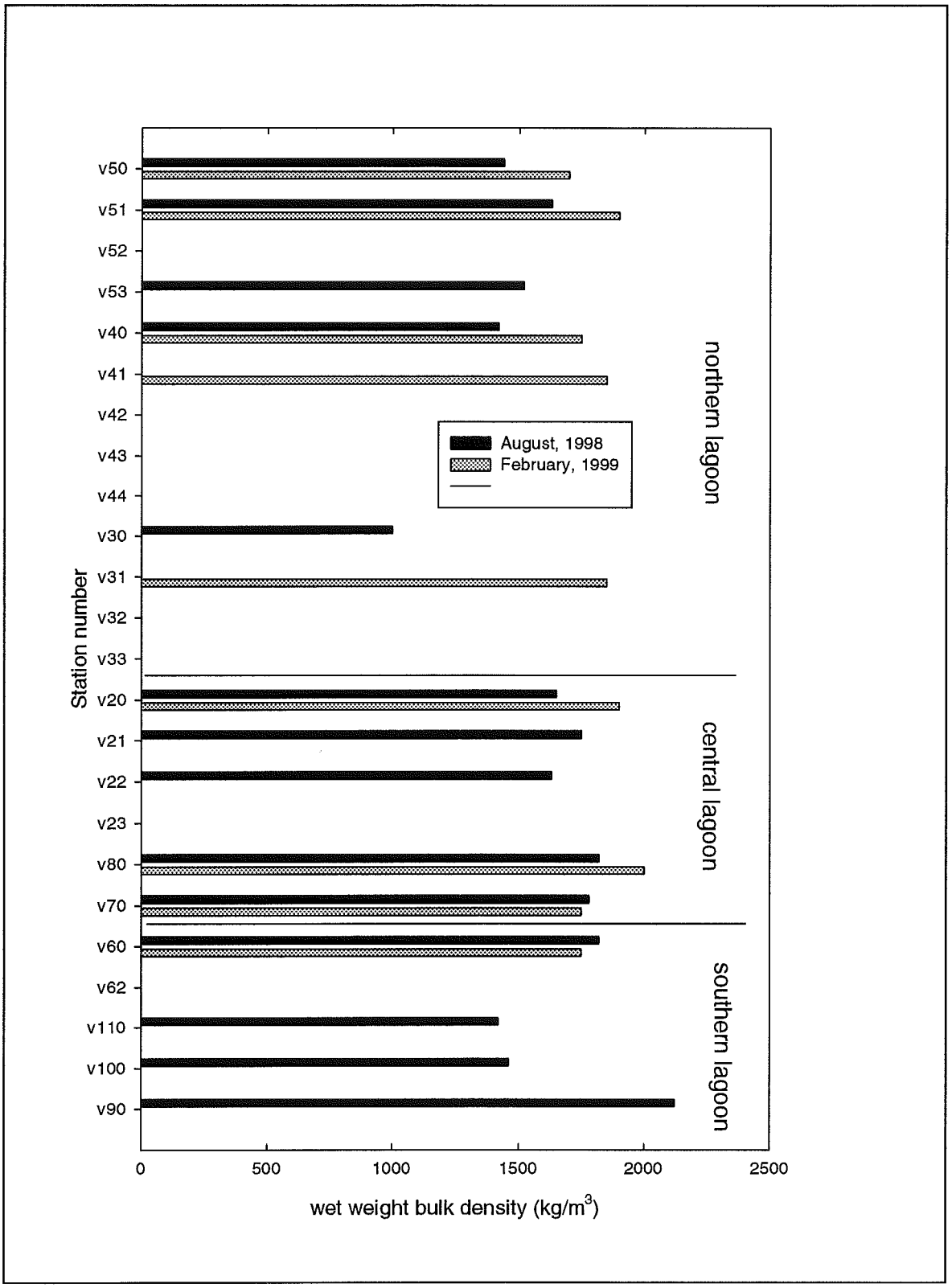

Figure 5.2.2 : Wet weight bulk density of the surface 5 mm of sediment in Venice Lagoon measured on syringe cores collected during the August, 1998 and February, 1999 surveys. The trends are generally similar, though the February values are slightly higher perhaps reflecting bed erosion.

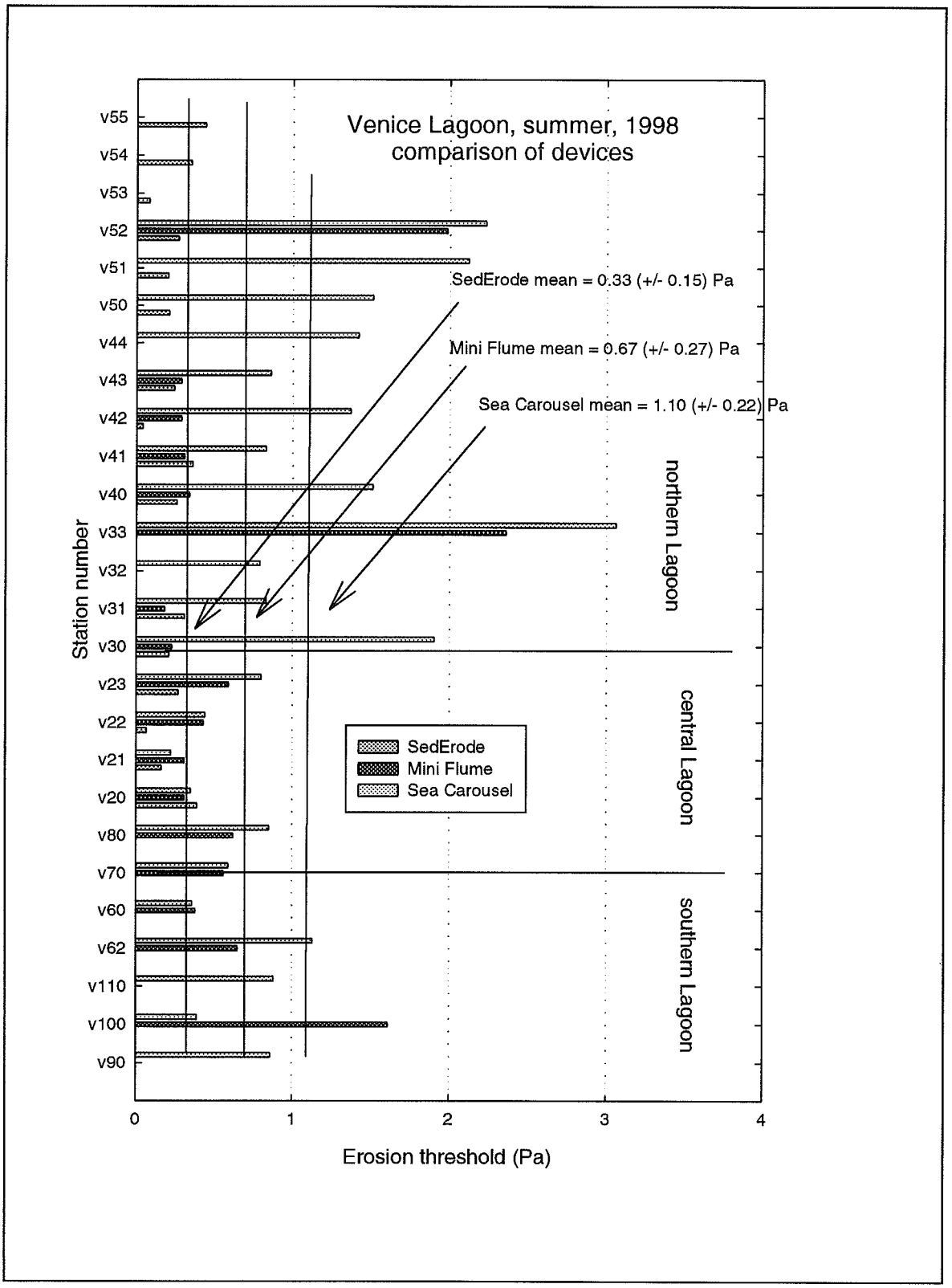

Figure 5.3.1 : A comparison between erosion thresholds determined from (1) Sea Carousel, (2) SedErode, and (3) Mini Flume measured during August, 1998. There is a wide divergence in values.